Addis Ababa University
አዲስ አበባ ዩኒቨርሲቲ
SEEK WISDOM, ELEVATE YOUR INTELLECT AND SERVE HUMANITY !

Synthesis, Characterization and Evaluation of Nanocellulose-based Nanogels from Local Sources for Sustained Drug Delivery

A Dissertation Presented in Partial Fulfilment of the Requirements for the Degree

Doctor of Philosophy (PhD) in Pharmaceutics

Tesfaye Gabriel Dalalo (BPharm, MSc in Pharmaceutics)

Advisors: Prof. Dr. Tsige Gebre-Mariam
Prof. Dr. Dr. h.c. Reinhard H.H. Neubert
Dr. Anteneh Belete

March 2022
Addis Ababa, Ethiopia

ADDIS ABABA UNIVERSITY

College of Health Sciences, School of Pharmacy

PhD Program in Pharmaceutics

Synthesis, Characterization and Evaluation of Nanocellulose-based Nanogels from Local Sources for Sustained Drug Delivery

A PhD Dissertation submitted to the Department of Pharmaceutics and Social Pharmacy, School of Pharmacy, College of Health Sciences, Addis Ababa University

Presented in Partial Fulfilment of the Requirements for the Degree Doctor of Philosophy (PhD) in Pharmaceutics

By: Tesfaye Gabriel Dalalo (BPharm, MSc in Pharmaceutics)

Advisors: Prof. Dr. Tsige Gebre-Mariam

Prof. Dr. Dr. h.c. Reinhard H.H. Neubert

Dr. Anteneh Belete

Mar, 2022

Addis Ababa, Ethiopia

ADDIS ABABA UNIVERSITY

SCHOOL OF GRADUATE STUDIES

Department of Pharmaceutics and Social Pharmacy

School of Pharmacy, College of Health Sciences

Approval by the examining board

This is to certify that the Dissertation titled 'Synthesis, Characterization and Evaluation of Nanocellulose-based Nanogels from Local Sources for Sustained Drug Delivery' is prepared by Tesfaye Gabriel Dalalo, and submitted in partial fulfilment of the requirements for Doctor of Philosophy (PhD) in Pharmaceutics, and complies with the regulations of the University and meets the accepted standards with respect to originality and quality.

Examiners:

Prof. Dr. Dr. h.c. Joachim Ulrich (External) Signature: _____ Date: 01.04.2022

Prof. Dr. Zebene Kiflie (Internal) Signature: _____ Date: 04.04.2022

Advisors:

Prof. Dr. Tsige Gebre-Mariam Signature: _____ Date: 05.04.2022

Prof. Dr. Dr. h.c. Reinhard H.H. Neubert Signature: _____ Date: April 01, 2022

Dr. Anteneh Belete Signature: _____ Date: 05.04.2022

Chair of Department or Graduate Program Coordinator

Declaration of academic integrity

With this statement I declare that I have independently completed the above PhD Dissertation titled ‘Synthesis, Characterization and Evaluation of Nanocellulose-based Nanogels from Local Sources for Sustained Drug Delivery’. The thoughts taken directly or indirectly from external sources are properly marked as such. This Dissertation was not previously submitted to another academic institution and has also not yet been published.

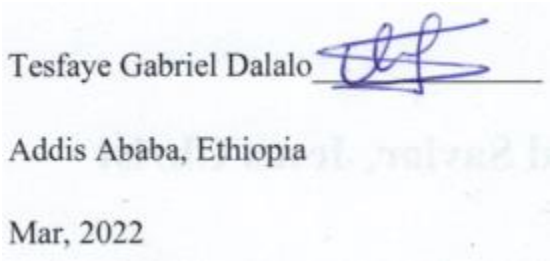

Dedicated to my Lord and Savior, Jesus Christ

Plagiarism test index result

Curiginal

Document Information

Analyzed document	PhD Dissertation Final Thesis_Tesfaye Gabriel Dalalo_Mar 2022 V6.docx (D131283776)
Submitted	2022-03-23T13:51:00.0000000
Submitted by	anteneh belete
Submitter email	anteneh.belete@aau.edu.et
Similarity	6%
Analysis address	anteneh.belete.aauni@analysis.urkund.com

Acknowledgements

First and foremost, all glory and praise go to Almighty God, who reigns above forever and ever for His help and presence in so many ups and downs, and finally for my successful completion of this PhD research work. What an unconditional love, and unending and great mercy Sovereign God showed to me and my family through Jesus Christ in our lives. Nahum 1:7- The LORD is good, a refuge in times of trouble. He cares for those who trust in him.

Next, I feel honored to express my deepest and sincere gratitude and appreciation to my advisors: Prof. Tsige Gebre-Mariam, Prof. Reinhard Neubert, and Dr. Anteneh Belete for their constructive suggestions, guidance, encouragement and support throughout this research work. Dear Prof. Tsige, I know how much you challenged me to utilize my full potential, and to develop such an interesting work and to focus on specific research area in the future, in general. It is exceptionally a unique opportunity you arranged for me to join the Tri-sustain Project and come-up with this thesis. I am actually grateful to you for your scientific as well as personal advice, support, and encouragement. Dear Prof. Neubert, I want to express my gratitude for your scientific guidance, and making my stay in Germany pleasant as well as coordination roles such as arranging access for laboratory facilities and spaces. Dear Dr. Anteneh, I am very much thankful to you for giving me your precious time, insights and direction, and your friendly approach and advice in various ups and downs.

I extend my heartfelt thanks to Institute of Applied Dermatopharmacy (IADP), Department of Pharmaceutical Chemistry and Clinical Pharmacy, and Department of Pharmaceutical Technology and Biopharmaceutics, Institute of Pharmacy, Martin Luther University (MLU) Halle-Wittenberg for providing me access to office and laboratory facilities while I was in Germany. Dr. Gerd Hause and Frank Syrowatka, MLU Halle-Wittenberg are warmly acknowledged for taking the TEM and SEM images of different samples. I would also like to offer my thanks to Prof. Peter Imming and Dr. Lucie Moeller for the coordination roles in the Tri-Sustain Project, and facilitating space, material as well as financial arrangements as well as organizing graduate school workshops in Botswana, Ethiopia, Germany and Tanzania along with country's coordinators. I am also thankful for all colleagues and PhD students in the Project for the nice time and discussions we had together, wishing them all the success in their future endeavors.

I would also like to acknowledge Department of Pharmaceutics and Social Pharmacy, Addis Ababa University (AAU) for providing laboratory space, necessary chemicals and apparatus for the laboratory work in Ethiopia. Cadila Pharmaceuticals PLC and Ethiopian Pharmaceutical Manufacturing Sh. Co. are also acknowledged for providing me the raw active pharmaceutical ingredients and access to FTIR; Department of Materials Science and Engineering, Adama Science and Technology University for providing access to XRD and TGA.

I also wish to extend my special thanks to my family, especially to my beloved and God-fearing wife and darling Mulu Erkalo, and our beloved and precious gifts of God: Kijan Tesfaye, Nathinael Tesfaye and Dibora Tesfaye for giving me their costly time, as well as for their kindness, encouragement and unreserved support extended to me and for successful accomplishment of this research work. I am also grateful to all other family members (especially my father, Gabriel Dalalo Deutche and mother, Amarech Feranso Lafebo as well as my brothers and sisters), relatives as well as colleagues and friends (mainly Fabio Strati, Hans-Jürgen Figur, and Drs. Efrem Nigussu and Getahun Paulos) who contributed directly or indirectly to my study.

Finally, I must acknowledge AAU for sponsoring my PhD study, and Tri-Sustain Project (funded by the Federal Ministry of Education and Research (BmBF) and the German Academic Exchange Service (DAAD)), Germany for the financial support. Ministry of Innovation and Technology, Ethiopia is also acknowledged for the financial support during the initial phase of this research work.

Title

Synthesis, Characterization and Evaluation of Nanocellulose-based Nanogels from Local Sources for Sustained Drug Delivery

Tesfaye Gabriel Dalalo,
Addis Ababa University; Mar, 2022

Abstract

Polysaccharides possess great potential advantages in the development of drug delivery vehicles due to their biocompatibility, biodegradability, and amenability for modifications. Cellulose, a well-known ubiquitous polysaccharide on Earth, and its derivatives are among the most promising and versatile materials with special chemical structure providing a good platform for the synthesis of hydrogel networks. Woody plants and cotton are the major sources of cellulose and its derivatives such as cellulose nanocrystals (CNCs) and carboxymethyl cellulose (CMC), but overutilization of these sources has raised huge economic and environmental concerns forcing researchers and stakeholders to look for other potential substitutes. Nanogels, three-dimensional hydrogel nanomaterials, based on natural biodegradable polymers have recently got considerable attention as effective drug delivery nanocarriers as they include the advantages of hydrogels and nanoparticles. However, the longer preparation time and usage of large amounts of organic solvents and surfactants have limited their applications.

The objectives of this study were to explore *teff* straw (TS), *enset* fiber (EF), sugarcane bagasse (SB) and coffee hull (CH) as alternative sources of cellulose, CNCs and CMC as well as to prepare nanocellulose-based nanogels following a simple and green ecofriendly approach, and evaluate the nanogels for sustained delivery of various model BCS class drugs: acyclovir, carbamazepine and furosemide.

Cellulose fibers were extracted from the aforementioned lignocellulosic sources following various eco-friendly chlorine-free extraction conditions comprising alkaline pretreatment, delignification (using formic acid, acetic acid and hydrogen peroxide) and bleaching (using alkaline hydrogen peroxide) to obtain an optimum condition. CNCs were obtained following sulfuric acid (64% w/w) hydrolysis of cellulose fibers extracted using 5%, 10% and 17.5% sodium hydroxide at the pretreatment stage. CMC was obtained from the as-extracted cellulose fibers, following

mercerization and etherification steps using sodium hydroxide and monochloroacetic acid in isopropyl alcohol. The as-obtained cellulose fibers, CNCs and CMC were investigated and characterized in terms of yield, crystallinity, chemical functionality, morphology, particle diameter/size, and thermal stability.

EF yielded the highest cellulose content (60.0%), whereas CH the least (35.5%). FTIR spectra and SEM morphological studies of the celluloses indicated progressive removal of non-cellulosic constituents. XRD analyses showed EF cellulose had the highest crystallinity index (CrI) (85.56%), crystallite size (5.52 nm), and proportion of crystallite interior chains of 200 plane (0.629), exhibiting unique physicochemical properties. TGA studies revealed enhanced stability of the as-extracted celluloses. All as-isolated cellulose fibers and CNCs maintained a typical Cellulose I_β crystalline structure, but Cellulose I and II allomorphs coexisted in CNCs isolated from TS, EF, and SB pretreated with 17.5% sodium hydroxide. The highest yield (~ 70%), CrI (~ 86%), and crystal size (~ 6 nm) were observed in EF–CNCs, and the least in CH–CNCs (yield: ~25%, crystal size: ~4 nm) and SB-CNCs (CrI: ~65.4%). FTIR spectra of all CNCs indicated typical chemical composition of cellulose. TEM analyses revealed that CNCs isolated from all byproducts pretreated with 5% sodium hydroxide had higher aspect ratios (17.32-36.67) with elongated needle-shaped nanoscale structures than CNCs obtained with 17.5% sodium hydroxide at the pretreatment stage (8.95-16.38). The thermal studies by TGA/DTG revealed the CNCs had a two-step decomposition process at T_{max} ranging from 215–225 °C and 340–355 °C. The CNCs obtained using 5% sodium hydroxide at the pretreatment stage also exhibited high yield, crystal size, crystallinity, length, aspect ratio and colloidal stability. The high alkaline condition, 17.5% sodium hydroxide, might not necessarily contribute to the polymorphic transition in lignocellulosic materials with higher lignin content as evidenced in CH. By and large, the formation of Cellulose I and II allomorphs in the as-obtained CNCs were dependent on the cellulose source and cellulose extraction condition, and less influenced by sulfuric acid hydrolysis. The as-obtained CMC from all plant sources had DS in the range of 0.71-1.18, and with a yield of 1.28-1.55 g/g. The appearance of new bands around 1600 and 1412 cm^{-1} in the FTIR spectra of as-obtained CMC showed efficient attachment of carboxymethyl groups to the cellulose chains. The XRD analyses of the as-obtained CMC samples showed a significant reduction in crystallinity with the main diffraction signal at $2\theta=20°$, showing polymorphic transition to Cellulose II too. From the TGA results, the T_{max} of the as-obtained CMC ranged from 285-296 °C. The SEM results indicated that

the CMC samples existed as more granular and corroded structure. At similar modification condition, CMC obtained from EF had the highest DS, %carboxymethyl, yield and purity.

Based on its unique and superior properties such as yield, purity, and crystallinity, EF was selected for preparation of carboxymethyl (nano)cellulose (CM(N)C) to be included as anionic polysaccharide in the nanogel formulations. CMNC was obtained from EF-CNCs following a similar etherification approach for CMC. The DS and yield of EF-CMNC were 0.56 and 1.11 g/g. The nanogels were prepared from self-assembled anionic CMC- or CMNC- and cationic-lysozyme blends via electrostatic complexation for sustained drug delivery. Three model drugs from different classes of Biopharmaceutics Classification System (BCS): acyclovir (BCS III), carbamazepine (BCS II), and furosemide (BCS IV) were evaluated. The influence of weight ratios of CMNC-lysozyme, pH, sonication and heating times, and storage conditions on the size and polydispersity index (PDI) of the nanogels was studied. The nanogels were characterized by PCS, UV/Vis spectrophotometry, FTIR spectroscopy, TEM, XRD, TGA, and DSC techniques, and also evaluated for drug loading and *in vitro* drug release. Spherical nanogels of small sizes (75-110 nm) and PDI (< 0.2) as well as large zeta potential (-38 to -55 mV) were prepared at optimal condition (at 1:1 weight ratio of CMNC:lysozyme, pH 7.4, and 30-min heating time). CMNC-based nanogels exhibited lower particle size than CMC-based nanogels at all pH points (5.3-10.5) investigated. The results demonstrated high encapsulation efficiency (62-94%) and loading capacity (18-27%), and sustained release profiles of the model drugs from the loaded nanogels for 12 h.

On the basis of the physicochemical characteristics, all the byproducts studied could be considered as alternative sources of cellulose, CNCs, and CMC for potential value-added industrial applications although differences were observed due to variations in cellulose sources. EF showed unique and superior physicochemical properties. From the findings, nanocellulose-based nanogels with potential applications as sustained release nanocarriers for various BCS class drugs were developed following a simple and green approach.

Keywords: *Teff* straw, *Enset* fiber, Sugarcane bagasse, Coffee hull, Cellulose, Chlorine-free extraction, Cellulose nanocrystals, Cellulose I and II allomorphs, Crystallinity, Polymorphic transition, Carboxymethyl cellulose, Physicochemical characterization, Etherification, Synthesis, Nanogels, Carboxymethyl nanocellulose, Lysozyme, Electrostatic complexation, Sustained drug delivery.

Table of contents

Approval by the examining board ..... **ii**
Declaration of academic integrity ..... **iii**
Plagiarism test index result ..... **v**
Acknowledgements ..... **vi**
Abstract ..... **viii**
Table of contents ..... **xi**
Abbreviations ..... **xvi**
List of figures ..... **xviii**
List of tables ..... **xxiv**
1 Introduction **1**
1.1 Biopolymers 1
1.2 Cellulose 1
1.3 Extraction of cellulose 2
1.4 Nanocelluloses 3
1.5 Modification of (nano)celluloses 3
1.6 Nanogels as novel drug delivery systems 4
1.7 Polysaccharide-based nanogels 5
1.7.1 Cellulose-based nanogels 6
1.7.1.1 CMC-based nanogels 6
1.7.1.2 HPMC-based nanogels 8
1.7.1.3 HPC-based nanogels 9
1.7.1.4 MC-based nanogels 10
1.7.1.5 MCC/CMC-based nanogels 11
1.7.1.6 Bacterial cellulose (BC) Whisker/Poly(NIPAM-co-BMA) (PNB) based nanogels 11
1.8 Synthesis techniques of nanogels 11
1.9 The present study 14
1.10 Research questions 15
1.11 Objectives 15
1.11.1 General objective 15
1.11.2 Specific Objectives 15
2 Extraction and characterization of celluloses from various plant byproducts **16**
2.1 Introduction 16

2.2 Materials and methods 17
2.2.1 Materials 17
2.2.2 Cellulose extraction 18
2.2.2.1 Alkaline pretreatment 18
2.2.2.2 Formic acid, acetic acid and hydrogen peroxide treatment 18
2.2.2.3 Bleaching 18
2.2.3 Identification tests and estimation of constituents of the plant materials 19
2.2.3.1 Klason lignin 19
2.2.3.2 Hemicellulose content 19
2.2.3.3 Water soluble components 20
2.2.3.4 Fatty and waxy matters 20
2.2.3.5 Pectic matter 20
2.2.3.6 Cellulose content 20
2.2.4 Fourier-Transform Infrared (FTIR) spectroscopy studies 20
2.2.5 X-ray diffraction (XRD) 21
2.2.6 Thermogravimetric analysis (TGA) 22
2.2.7 Environmental Scanning Electron Microscopy (ESEM) 22
2.3 Results and discussions 22
2.3.1 Identification and composition of the plant materials 22
2.3.2 Efficiency and conditions of the extraction method 24
2.3.3 Chemical functionality 27
2.3.4 Crystallinity 29
2.3.5 Thermal stability 34
2.3.6 Morphological properties 38
2.4 Conclusion 42
3 Isolation and characterization of cellulose nanocrystals from different lignocellulosic residues: A comparative study 43
3.1 Introduction 43
3.2 Materials and methods 45
3.2.1 Materials 45
3.2.2 Cellulose extraction 45
3.2.3 Acid hydrolysis 45
3.2.4 Yield determination 46
3.2.5 Determination of chemical composition 46

3.2.6 XRD analyses 46
3.2.7 FTIR spectroscopy 46
3.2.8 TEM investigation 46
3.2.9 Particle size analysis 47
3.2.10 Zeta potential 47
3.2.11 TGA properties 47
3.3 Results and discussion 47
3.3.1 Effect of isolation conditions and yield of CNCs 47
3.3.2 Crystallinity of the CNCs 50
3.3.3 Chemical functionality studies 56
3.3.4 Dimensional and morphological analyses 58
3.3.5 Particle size and Zeta potential of CNCs 60
3.3.6 Thermal properties of the CNCs 61
3.4 Conclusion 65
4 Is mercerization the only factor for (partial) polymorphic transition of cellulose I to cellulose II in cellulose nanocrystals? 66
4.1 Introduction 66
4.2 Materials and methods 68
4.2.1 Materials 68
4.2.2 Cellulose extraction 68
4.2.3 Isolation of CNCs 68
4.2.4 FTIR spectroscopy 69
4.2.5 XRD 69
4.2.6 TEM studies 70
4.2.7 TGA properties 70
4.3 Results and discussions 71
4.3.1 CNCs isolation condition, and yield 71
4.3.2 Crystallinity investigations 71
4.3.3 Chemical functionality studies 76
4.3.4 Morphological and dimensional analyses 77
4.3.5 Thermal properties 79
4.4 Conclusion 83
5 Physicochemical characterization of carboxymethyl cellulose from local agro-industrial byproducts 84

5.1 Introduction 84
5.2 Materials and methods 86
5.2.1 Materials 86
5.2.2 Cellulose extraction 86
5.2.3 Preparation of CMC 86
5.2.4 Identification tests and properties of CMC 87
5.2.5 Determination of degree of substitution (DS) 87
5.2.6 Rheological properties of CMC 88
5.2.7 FTIR spectroscopy studies 88
5.2.8 XRD investigations 88
5.2.9 TGA analyses 89
5.2.10 SEM studies 89
5.2.11 Statistical analysis 89
5.3 Results and discussions 89
5.3.1 Properties of as-obtained CMC 89
5.3.2 FTIR spectroscopy properties 92
5.3.3 Crystallinity analyses 94
5.3.4 Thermal stability behaviors 96
5.3.5 Morphological properties 99
5.4 Conclusion 102
6 Nanocellulose-based nanogels for sustained drug delivery: Preparation, characterization and evaluation 103
6.1 Introduction 103
6.2 Materials and methods 106
6.2.1 Materials 106
6.2.2 Cellulose extraction 106
6.2.3 Isolation of CNCs 106
6.2.4 Preparation of carboxymethyl nanocellulose (CMNC) 107
6.2.5 Preparation of nanogels 107
6.2.6 Preparation of drug-loaded nanogels 107
6.2.7 Turbidity measurements 107
6.2.8 FTIR spectroscopy 108
6.2.9 Morphological investigations 108
6.2.10 Particle size and polydispersity index (PDI) analyses 108

6.2.11 Zeta potential 108
6.2.12 XRD studies 108
6.2.13 Thermal analyses 109
6.2.14 UV calibration curves of model drugs 109
6.2.15 Determinations of solubilities and partition coefficients of the model drugs 109
6.2.16 Drug encapsulation efficiency (EE) and loading capacity (LC) 110
6.2.17 *In vitro* drug release 110
6.2.18 Short-term stability studies 110
6.2.19 Statistical analysis 111
6.3 Results and discussion 111
6.3.1 Preparation conditions of nanogels 111
6.3.2 FTIR spectroscopy studies 117
6.3.3 Morphological properties 118
6.3.4 Crystallinity analyses 121
6.3.5 Thermal properties 124
6.3.6 Drug loading and *in vitro* release studies 128
6.3.7 Stability profiles of the unloaded and drug-loaded nanogels 131
6.4 Conclusion 133
Summary 134
Suggestions for further work 135
List of publications 135
References 136
Appendix 168

Abbreviations

A-NGs	Acyclovir loaded nanogels
BC	Bacterial cellulose
BP	British Pharmacopoeia
BCS	Biopharmaceutics Classification System
CC	Commercial cellulose
CC-(C)NCs	Cellulose nanocrystals isolated from commercial cellulose
CNCs-I	Cellulose nanocrystals containing only Cellulose I;
CH	Coffee hull
CMC-CC	Carboxymethyl cellulose prepared from commercial cellulose
CM(N)C	Carboxymethyl (nano)cellulose
C-NGs	Carbamazepine loaded nanogels
CrI(s)	Crystallinity index or indexes/indices
C-SCMC	Commercial sodium carboxymethyl cellulose
DLS	Dynamic light scattering
DS	Degree of substitution
DSC	Differential scanning calorimetry
DTG	Differential thermo gravimetry
EE	Encapsulation efficiency
EF	*Enset* fiber
F-NGs	Furosemide loaded nanogels
FTIR	Fourier-transform infrared spectroscopy
HA	Hermans et al. approach
HPC	Hydroxylpropyl cellulose
HPC–SH	Thiolated hydroxylpropyl cellulose
HPMC	Hydroxypropyl methylcellulose
LC	Loading capacity
LDL	Low density lipoprotein
MAA	Methacrylic acid
MC	Methyl cellulose
MCA	Monochloroacetic acid
MCC	Microcrystalline cellulose
MWCO	Molecular weight cut off
NGs0	Unloaded nanogels obtained at pH 5.3
NGs1	Unloaded nanogels obtained at pH 5.3 and ultrasonicated
NGs2	Unloaded nanogels prepared at pH 7.4
PAA	Polyacrylic acid
PCS	Photon correlation spectroscopy
PDI	Polydispersity index
PEC	Polyelectrolyte complex

SA	Segal et al. approach
SB	Sugarcane bagasse
SEM	Scanning electron microscopy
TEM	Transmission electron microscopy
TGA	Thermogravimetric analysis
TS	*Teff* straw
UC1	Unheated complex
UNGs	Unloaded nanogels
USP	United States Pharmacopoeia
UV/Vis	Ultraviolet/visible
XRD	X-ray diffraction

List of figures

Fig. 1.1: Structure of cellulose. 2
Fig. 1.2: Schematic illustration of the nanogel network created by: (a) direct polymerization of monomers; (b) assembling of a polymer precursor (adapted from Chacko et al. 2012; Neamtu et al. 2017). 12
Fig. 1.3: Synthesis of nanogels via miniemulsion technique. (a) Initial two phases mixture. (b) Formation of small droplets in a continuous phase by applying high shear stress, such as ultrasonication. (c) Monodisperse nanosized 50-500 nm template for nanogel synthesis (adapted from Asadian-Birjand et al., 2012). 13
Fig. 1.4: Synthetic approaches for preparation of nanogels via conventional and inverse emulsion polymerization (adapted from Baipaywad et al., 2014). 13
Fig. 2.1: Photographs of A) the four untreated plant byproducts: *teff* straw (TS), *enset* fiber (EF), sugarcane bagasse (SB) and coffee hull (CH) (from left to right), and B) respective cellulose (C2) extracted with extraction Condition B (optimum Condition). 23
Fig. 2.2: FTIR spectra of the four untreated plant byproducts (left), and the corresponding celluloses (C2) extracted with Condition B (optimum Extraction) (right). (Key: 0-untreated plant byproduct; TS-*teff* straw; EF-*enset* fiber; SB-sugarcane bagasse; CH-coffee hull; CC-commercial cellulose included for comparison). 27
Fig. 2.3: FTIR spectra of extracted cellulose C1 (left) following extraction Condition A; C3 (middle) following Condition C, C4 following extraction Condition D (right), and CC. (Key: TS-*teff* straw; EF-*enset* fiber; SB-sugarcane bagasse; CH-coffee hull; CC-commercial cellulose included for comparison). 28
Fig. 2.4: X-ray diffractograms of the four untreated plant byproducts (left) and cellulose (C2) extracted with Condition B (optimum Extraction) (right) and CC. (Key: 0-untreated plant byproduct; TS-*teff* straw; EF-*enset* fiber; SB-sugarcane bagasse; CH-coffee hull; CC-commercial cellulose included for comparison). 29
Fig. 2.5: Comparison of Segal's et al (SM) and Herman's et al (HM) methods for estimation of CrI of the plant materials. (Key: 0-Untreated plant byproducts; C1, C2, C3 and C4-Cellulose extracted using extraction Conditions A, B, C and D, respectively; TS-*teff* straw; EF-*enset* fiber; SB-sugarcane bagasse; CH-coffee hull; CrI - crystallinity index). 31
Fig. 2.6: X-ray diffractograms of extracted cellulose C1 (left) following extraction Condition A; C3 (middle) following Condition C, C4 following extraction Condition D (right), and CC. (Key: TS-*teff* straw; EF-*enset* fiber; SB-sugarcane bagasse; CH-coffee hull; CC-commercial cellulose included for comparison). 33
Fig. 2.7: X-ray diffractograms of Cellulose II of EF-C3, and Cellulose I and II allomorphs of EF-C4 and SB-C4. (Key: EF-C3 and EF-C4--Cellulose extracted from *enset* fiber following extraction Conditions C and D, respectively; SB-C4—Cellulose from sugarcane bagasse following extraction Condition D; Cellulose II—Cellulose with antiparallel chains). 34
Fig. 2.8: Thermal degradation behaviors: TGA (left) and DTG (right) of the four untreated byproducts, and CC. (Key: 0-untreated plant byproduct; TS-*teff* straw; EF-*enset* fiber; SB-sugarcane bagasse; CH-coffee hull; CC-commercial cellulose included for comparison) 35
Fig. 2.9: Thermal degradation behaviors: TGA (left) and DTG (right) of cellulose (C2) extracted with Condition B (optimum Condition), and CC. (Key: TS-*teff* straw; EF-*enset* fiber; SB-sugarcane bagasse; CH-coffee hull; CC-commercial cellulose included for comparison). 36

Fig. 2.10: TGA curves for cellulose C1 (left) following extraction Condition A; C3 (middle) following Condition C, C4 following extraction Condition D (right), and CC. (Key: TS-*teff* straw; EF-*enset* fiber; SB-sugarcane bagasse; CH-coffee hull; CC-commercial cellulose included for comparison). 38
Fig. 2.11: Scanning electron micrographs of untreated plant byproducts with a scale bar of 100 μm (Key: TS-*teff* straw; EF-*enset* fiber; SB-sugarcane bagasse; CH-coffee hull). 40
Fig. 2.12: Scanning electron micrographs of as-extracted cellulose (C2) using Condition B (optimum Condition), and CC with a scale bar of 30 μm. (Key: TS-*teff* straw; EF-*enset* fiber; SB-sugarcane bagasse; CH-coffee hull; CC-commercial cellulose included for comparison)..... 41
Fig. 3.1: Photographs of CNCs a) lyophilized samples b) dispersions in distilled water (0.5%) at the 10th day of storage at 4 °C (CNCs from TS, EF, SB, CH and CC from left to right). (Key: TS-*teff* straw; EF-*enset* fiber; SB-sugarcane bagasse; CH-coffee hull; CNCs-cellulose nanocrystals; CC- commercial cellulose included for comparison)..... 49
Fig. 3.2: XRD patterns of a) CNCs-C1, and b) cellulose (C1) precursors. (Key: TS-*teff* straw; EF-*enset* fiber; SB-sugarcane bagasse; CH-coffee hull; CNCs-C1-Cellulose nanocrystals isolated from cellulose (C1) extracted following Condition 1; CC-CNCs-Nanocrystals isolated from CC (commercial cellulose) included for comparison)..... 51
Fig. 3.3: Comparison of Segal et al. (SA) and Hermans et al. (HA) approaches for estimation of CrIs of the CNCs and cellulose precursors. (Key: CNCs-C1 and CNCs-C2-cellulose nanocrystals isolated from C1 and C2, respectively. TS-*teff* straw; EF-*enset* fiber; SB-sugarcane bagasse; CH-coffee hull)..... 52
Fig. 3.4: FTIR spectra of a) CNCs-C1, and b) cellulose (C1) precursors. (Key: CNCs-C1-cellulose nanocrystals isolated from C1; C1-Cellulose extracted using extraction Condition 1; TS-*teff* straw; EF-*enset* fiber; SB-sugarcane bagasse; CH-coffee hull; CC-CNCs-cellulose nanocrystals isolated from commercial cellulose (CC) included for comparison)..... 57
Fig. 3.5: Transmission electron micrographs of CNCs-1 (TS-CNCs-C1, EF-CNCs-C1, SB-CNCs-C1, CH-CNCs-C1), and CC-CNCs) (Bar scale: 200 nm). (Key: CNCs-C1-cellulose nanocrystals isolated from C1; C1-Cellulose extracted using extraction Condition 1; TS-*teff* straw; EF-*enset* fiber; SB-sugarcane bagasse; CH-coffee hull; CC-CNCs-cellulose nanocrystals isolated from commercial cellulose (CC) included for comparison)..... 59
Fig. 3.6: Thermal degradation behaviors: a) TGA and b) DTG of CNCs (upper two), and c) TGA and d) DTG of cellulose (C1) precursors (lower two) extracted with Condition 1, and CC. (Key: CNCs-C1-cellulose nanocrystals isolated from C1; C1-Cellulose extracted using extraction Condition 1; TS-*teff* straw; EF-*enset* fiber; SB-sugarcane bagasse; CH-coffee hull; CC-CNCs-cellulose nanocrystals isolated from commercial cellulose (CC) included for comparison). 63
Fig. 4.1: X-ray diffractograms of CNCs of EF and SB (a), and their cellulose precursors (b); and CNCs of TS and CH (c), and their cellulose precursors (d). (Key: CNCs-cellulose nanocrystals; Cel-cellulose; TS-*teff* straw; EF-*enset* fiber; SB-sugarcane bagasse; CH-coffee hull; CC-NCs-cellulose nanocrystals isolated from commercial cellulose (CC) included for comparison). 73
Fig. 4.2: FTIR spectra of CNCs isolated (Left), and cellulose precursors (Right). (Key: CNCs-cellulose nanocrystals; Cel-cellulose; TS-*teff* straw; EF-*enset* fiber; SB-sugarcane

bagasse; CH-coffee hull; CC-NCs-cellulose nanocrystals isolated from commercial cellulose (CC) included for comparison). 77
Figure 4.3: Transmission electron micrographs of CNCs isolated from the celluloses extracted (bar scale: 50 nm). (Key: CNCs-cellulose nanocrystals; TS-*teff* straw; EF-*enset* fiber; SB-sugarcane bagasse; CH-coffee hull). 78
Fig. 4.4: Thermal degradation characteristics of as-isolated CNCs using TGA (a) and DTG (b), and their cellulose precursors using TGA (c) and DTG (d). (Key: CNCs-cellulose nanocrystals; Cel-cellulose; TS-*teff* straw; EF-*enset* fiber; SB-sugarcane bagasse; CH-coffee hull; CC-NCs-cellulose nanocrystals isolated from commercial cellulose (CC) included for comparison). 82
Fig. 5.1: (a) Effect of amount of MCA (Cellulose: MCA g/g) on DS (NaOH: 30%; Temp: 55 °C; Time: 3.0 h). (b) Effect of reaction time on DS (NaOH: 30%; Temp: 55 °C; Cellulose to MCA: 1:1.14 g/g). (Key: TS-*teff* straw; EF-*enset* fiber; SB-sugarcane bagasse; CH-coffee hull; CC-commercial cellulose; CMC-Carboxymethylcellulose obtained from the celluloses; CMC-CC:-Carboxymethylcellulose obtained from CC included for comparison)..... 91
Fig. 5.2: Relationship curve between viscosity and shear rate of the samples. (Key: TS-*teff* straw; EF-*enset* fiber; SB-sugarcane bagasse; CH-coffee hull; CC-commercial cellulose; CMC-Carboxymethylcellulose obtained from the celluloses; CMC-CC:-Carboxymethylcellulose obtained from CC included for comparison). 92
Fig. 5.3: FTIR spectra of the celluloses extracted from the four plant byproducts (left), and the as obtained CMC (right). (Key: TS-*teff* straw; EF-*enset* fiber; SB-sugarcane bagasse; CH-coffee hull; Cel-cellulose extracted from the byproducts; CC-commercial cellulose; CMC- Carboxymethylcellulose obtained from the celluloses; CMC-CC:-Carboxymethylcellulose obtained from CC; and C-SCMC:-Commercial sodium carboxymethyl cellulose, the last three included for comparison). 93
Fig. 5.4: X-ray diffractograms of the celluloses extracted from the four plant byproducts (left), and the as-obtained CMC (right). (Key: TS-*teff* straw; EF-*enset* fiber; SB-sugarcane bagasse; CH-coffee hull; Cel-cellulose extracted from the byproducts; CC-commercial cellulose; CMC- Carboxymethylcellulose obtained from the celluloses; CMC-CC:-Carboxymethylcellulose obtained from CC; and C-SCMC:-Commercial sodium carboxymethyl cellulose, the last three included for comparison). 95
Fig. 5.5: Thermal degradation behaviors: TGA (left) and DTG (right) of as-obtained CMC from the cellulose extracted from the four plant byproducts. (Key: TS-*teff* straw; EF-*enset* fiber; SB-sugarcane bagasse; CH-coffee hull; Cel-cellulose extracted from the byproducts; CC-commercial cellulose; CMC:-Carboxymethylcellulose obtained from the celluloses; CMC-CC:-Carboxymethylcellulose obtained from CC; and C-SCMC:-Commercial sodium carboxymethyl cellulose, the last three included for comparison).. 97
Fig. 5.6: Thermal degradation behaviors: TGA (left) and DTG (right) of celluloses extracted from the four plant byproducts, and CC. (Key: TS-*teff* straw; EF-*enset* fiber; SB-sugarcane bagasse; CH-coffee hull; Cel-cellulose extracted from the byproducts; CC-commercial cellulose; CMC:- Carboxymethylcellulose obtained from the celluloses; CMC-CC:-Carboxymethylcellulose obtained from CC; and C-SCMC:-Commercial sodium carboxymethyl cellulose, the last three included for comparison)..... 97
Fig. 5.7: SEM images of as-obtained CMC, CMC-CC and C-SCMC with a scale bar of 20 μm. (Key: TS-*teff* straw; EF-*enset* fiber; SB-sugarcane bagasse; CH-coffee hull; Cel-cellulose extracted from the byproducts; CC-commercial cellulose; CMC:-Carboxymethylcellulose

obtained from the celluloses; CMC-CC:-Carboxymethylcellulose obtained from CC; and C-SCMC:-Commercial sodium carboxymethyl cellulose, the last three included for comparison)..... 100
Fig. 5.8: SEM images of as-obtained CMC, CMC-CC and C-SCMC with a scale bar of 70 μm. (Key: TS-*teff* straw; EF-*enset* fiber; SB-sugarcane bagasse; CH-coffee hull; CMC-As-obtained carboxymethyl cellulose; C-SCMC-Commercial sodium carboxymethyl cellulose and CMC-CC-Carboxymethylcellulose obtained from CC included for comparison)..... 101
Fig. 6.1: a) Size and PDI of CMNC-based unloaded nanogels (UNGs0, UNGs1, and UNGs2), and CMC-based unloaded nanogels (CMC-NGs0, 1, and 2) obtained at 1:1 weight ratio and 30 min heating time, and influence of b) pH and heating time and c) weight ratios of CMNC:lysozyme on the size and PDI of nanogels. (Key:- CMNC: Carboxymethyl nanocellulose; CMC: Carboxymethyl cellulose; NGs0: unloaded nanogels obtained at pH 5.3; NGs1: unloaded nanogels obtained at pH 5.3 and ultrasonicated; NGs2: unloaded nanogels prepared at pH 7.4). Data are presented as the mean ± SD (*n* = 3). 114
Fig. 6.2: a) Particle size, zeta potential and turbidity of unloaded and drug-loaded nanogels prepared at pH 5.3 and 7.4, and b) photographs of unheated complexes (UC1 and UC2) as well as the nanogels (NG1 and NGs2). (Key: - UC1: Unheated complex; 1, and 2: Complexes or nanogels, prepared at pH 5.3, followed by probe-sonication for 5 min, and pH adjusted at 7.4; UNGs: Unloaded nanogels; A-NGs: Acyclovir loaded nanogels; C-NGs: Carbamazepine loaded nanogels; F-NGs: Furosemide loaded nanogels). Data are presented as the mean ± SD (*n* = 3). 116
Fig. 6.3: FTIR spectra of CNCs, CMNC, Lysozyme, and UNGs (Key:- CNCs: cellulose nanocrystals; CMNC: carboxymethyl nanocellulose; UNGs: Unloaded nanogels). 118
Fig. 6.4: a) Transmission electron micrographs of unloaded and drug-loaded nanogels, b) the size of the nanogels from the TEM images (Key:- 1,and 2: Nanogels, their pH prepared at 5.3 and ultrasonicated, and adjusted at 7.4, respectively; UNGs: Unloaded nanogels; A-NGs: Acyclovir loaded nanogels; C-NGs: Carbamazepine loaded nanogels; F-NGs: Furosemide loaded nanogels). (Bar scale: 100 nm). NB: ImageJ Software was used for the determination of the (average) diameters. Data are presented as the mean ± SD (*n* > 10). 121
Fig. 6.5: XRD of a) CNCs, CMNC, lysozyme, unloaded nanogels, b) drug-loaded nanogels: A-NGs, C-NGs, and F-NGs, compared to UNGs c) pure drugs: acyclovir, carbamazepine, and furosemide. (Key:- CNCs: cellulose nanocrystals; CMNC: carboxymethyl nanocellulose; UNGs: Unloaded nanogels; A-NGs: Acyclovir loaded nanogels; C-NGs: Carbamazepine loaded nanogels; F-NGs: Furosemide loaded nanogels)..... 123
Fig. 6.6: Thermal degradation behaviors: TGA (a) and DTG (b) of CNCs, CMNC, lysozyme, unloaded nanogels (UNGs), and TGA (c) and DTG (d) of drug-loaded nanogels (A-NGs, C-NGs and F-NGs) and UNGs. (Key:- CNCs: cellulose nanocrystals; CMNC: carboxymethyl nanocellulose; UNGs: Unloaded nanogels; A-NGs: Acyclovir loaded nanogels; C-NGs: Carbamazepine loaded nanogels; F-NGs: Furosemide loaded nanogels). 125
Fig. 6.7: a) DSC curves of CNCs, CMNC, lysozyme, unloaded nanogels (UNGs), and drug-loaded nanogels (A-NGs, C-NGs and F-NGs), and b) the derived DSC curve counterparts (Key:- CNCs: cellulose nanocrystals; CMNC: carboxymethyl nanocellulose; UNGs: Unloaded nanogels; A-NGs: Acyclovir loaded nanogels; C-NGs: Carbamazepine loaded nanogels; F-NGs: Furosemide loaded nanogels). 128

Fig. 6.8: Loading capacity and encapsulation efficiency of the nanogels. (Key:- 1 and 2: Nanogels pH 5.3 and probe-sonicated, and 7.4, respectively; A-NGs: Acyclovir loaded nanogels; C-NGs: Carbamazepine loaded nanogels; F-NGs: Furosemide loaded nanogels). Data are presented as the mean ± SD (*n* = 3). 129
Fig. 6.9: Cumulative *in vitro* release profiles of the three drugs from the drug-loaded CMNC based nanogels for 12 h in PBS (pH 7.4) (Key- 1, and 2: Nanogels, pH 5.3, and adjusted pH 7.4, respectively; A-NGs: Acyclovir loaded nanogels; C-NGs: Carbamazepine loaded nanogels; F-NGs: Furosemide loaded nanogels). Data are presented as the mean ± SD (*n* = 3). 130
Fig. 6.10: Stability profiles of unloaded and drug-loaded nanogels in terms of particle size and PDI stored at a) 4 °C b) 25 °C and c) 40 °C for 3 months (Key:- NGs: Nanogels, their pH 5.6, followed by ultra-sonication; A-NGs: Acyclovir loaded nanogels; C-NGs: Carbamazepine loaded nanogels; F-NGs: Furosemide loaded nanogels). Data are presented as the mean ± SD (*n* = 3). 133
Fig. A1: Photographs of a) CNCs after initial centrifugation b) CNCs during dialysis (TS, EF, SB, CH and CC from left to right). 168
Fig. A2: XRD patterns of CNCs-C2, and the cellulose (C2) precursors. (Key: CNCs-C2-cellulose nanocrystals isolated from C2; C2-cellulose extracted following extraction Condition B; TS-*teff* straw; EF-*enset* fiber; SB-sugarcane bagasse; CH-coffee hull; CC-CNCs-cellulose nanocrystals isolated from commercial cellulose (CC) included for comparison). 168
Fig. A3: Deconvoluted XRD patterns of the cellulose precursors (left) and as-obtained CNCs-C1 (right) from TS (a), EF (b), SB (c), CH (d) and CC (e). (Key: CNCs-C1-cellulose nanocrystals isolated from C1; C1-Cellulose extracted using extraction Condition A; TS-*teff* straw; EF-*enset* fiber; SB-sugarcane bagasse; CH-coffee hull; CC-CNCs-cellulose nanocrystals isolated from commercial cellulose (CC) included for comparison). 171
Fig. A4: Influence of sulfuric acid ratio and concentration on CrI of hydrolyzed cellulose using cellulose (C1) from each byproduct and CC as precursor (Preliminary work). (Key: CNCs-C1-cellulose nanocrystals isolated from C1 using 64% (w/w) sulfuric acid (1:20); CNCs-C1X and CC-NCsX-cellulose nanocrystals obtained using 64% wt/wt sulfuric acid (1:8.75 g/mL); Cellulose-Y-cellulose hydrolyzed using 58% (w/w) sulfuric acid (1:20); C1-cellulose extracted following extraction condition A; TS-*teff* straw; EF-*enset* fiber; SB-sugarcane bagasse; CH-coffee hull; CC- commercial cellulose included for comparison). 172
Fig. A5: FTIR spectra of CNCs-C2, and cellulose (C2) precursors. (Key: CNCs-C2-cellulose nanocrystals isolated from C2; C2-cellulose extracted following extraction Condition B; TS-*teff* straw; EF-*enset* fiber; SB-sugarcane bagasse; CH-coffee hull; CC-CNCs-cellulose nanocrystals isolated from commercial cellulose (CC) included for comparison). 172
Fig. A6: DTG curve of as-obtained CNCs-C1 from the celluloses extracted from the four plant byproducts, CC-CNCs, and CC. (Key: CNCs-C1-cellulose nanocrystals isolated from C1; C1-Cellulose extracted using extraction Condition A; TS-*teff* straw; EF-*enset* fiber; SB-sugarcane bagasse; CH-coffee hull; CC-CNCs-cellulose nanocrystals isolated from commercial cellulose (CC) included for comparison). 173
Fig. A7: The UV absorption calibration curves of a) acyclovir b) carbamazepine and c) furosemide. Where, Y is absorbance and X is concentration (μg/ml) of the drug solutions. Data are presented as the mean ± SD (*n* = 3). 176
Fig. A8: FTIR spectra of a) UNGs and drug-loaded nanogels, b) UNGs and free model drugs, c) physical mixture of CMNC and Lysozyme (weight ratio of 1:1) in comparison with FTIR

spectra of CNCs, CMNC and Lysozyme, d) the physical mixture with respect to FTIR spectra of pure drugs, e) physical mixture of CMNC and Lysozyme, with respect to FTIR spectra of physical mixture containing the drugs (Key:- CNCs: cellulose nanocrystals; CMNC: carboxymethyl nanocellulose; UNGs: Unloaded nanogels; A-NGs: Acyclovir loaded nanogels; C-NGs: Carbamazepine loaded nanogels; F-NGs: Furosemide loaded nanogels; CMNC:Lysozyme-Physical mixture at a ratio of 1:1; CMNC:Lysozyme:Acy, CMZ, and Fru-Physical mixture containing CMNC, Lysozyme and Acyclovir, Carbamazepine, and Furosemide, respectively at weight ratios of 1:1:1). 178
Fig. A9: Loading capacity and encapsulation efficiency of the nanogels prepared at 15 min heating time. (Key:- 1 and 2: Nanogels pH 5.3 and probe-sonicated, and 7.4, respectively; A-NGs: Acyclovir loaded nanogels; C-NGs: Carbamazepine loaded nanogels; F-NGs: Furosemide loaded nanogels). Data are presented as the mean ± SD (*n* = 3)..... 179
Fig. A10: Certificate of analyses of model drugs: a) Acyclovir, b) Carbamazepine, and c) Furosemide raw materials. 183

List of tables

Table 2.1: Extraction conditions of cellulose from the four plant byproducts (TS-teff straw; EF-enset fiber; SB-sugarcane bagasse; CH-coffee hull) at 1:10 (g/ml) byproduct/reagent ratio. 19
Table 2.2: Chemical composition of the four untreated plant byproducts and as-extracted cellulose (C2). 25
Table 2.3: Parameters obtained from the (deconvoluted) XRD of the four untreated plant byproducts (TS-*teff* straw; EF-*enset* fiber; SB-sugarcane bagasse; CH-coffee hull; as-extracted cellulose (C1, C2, C3 and C4), and CC. 30
Table 2.4: Summary of thermogravimetric characteristics of TGA and DTG of the four plant .. 36
Table 2.5: Average diameters of the four untreated plant byproducts, the respective as-extracted celluloses (C2), and CC. 39
Table 3.1: Yields of celluloses and CNCs from the byproducts 49
Table 3.2: Parameters obtained from the (deconvoluted) XRD of CNCs-C1, CNCs-C2 and cellulose precursors, as well as CC-CNCs 54
Table 3.3: TEM dimensional analysis of CNCs isolated from cellulose (C1) extracted from various raw materials. 60
Table 3.4: Hydrodynamic size using DLS and Zeta potential values 61
Table 4.1: Parameters obtained from the (deconvoluted) XRD of Cellulose II allomorphs in the CNCs from TS, EF and SB, and Cellulose I allomorph in the CNCs from CH, as well as their cellulose precursors. 75
Table 4.2: TEM dimensional analysis of CNCs isolated from celluloses extracted from various plant byproducts. 79
Table 4.3: Summary of thermogravimetric characteristics of TGA and DTG of the CNCs and cellulose precursors. 82
Table 5.1: Properties of CMC obtained from TS, EF, SB and CH. 90
Table 5.2: Summary of thermal characteristics of TGA and DTG of the as-obtained CMC and the 97
Table 5.3: Average diameters of the as-obtained CMC, respective cellulose precursors, as well as CMC-CC and C-SCMC. 102
Table 6.1: Summary of TGA and DTG results of CNCs, CMNC, lysozyme, unloaded and drug-loaded nanogels. 126
Table 6.2: Solubilities and partition coefficients of the model drug molecules 131
Table A1: Summary of TGA and DTG results of the as-obtained CNCs-1, and cellulose (C1) precursors. 173

1 Introduction

1.1 Biopolymers

Biopolymers are defined as biologically degradable polymers, generated by living organisms. Biopolymers have a structural backbone with carbon, oxygen, and nitrogen atoms which makes them easily biodegradable (Gheorghita et al., 2021). Polysaccharides are among essential biomacromolecules found in nature, which exhibit several biological activities and important functional roles in living organisms (Mansur et al., 2017). Recently, renewable natural resources for the development of recyclable and/or biodegradable products have received much attention to protect the environment from pollution. Lignocellulosic materials are among the most important natural sources for the production of value-added materials (El Achaby et al., 2018). Polysaccharides can be divided into several broad groups according their functions i.e. structural polymers (cellulose), protective polysaccharides (pectin and hemicelluloses) and storage polysaccharides (starch) (Singh, 2011). Polymer-based excipients have many pharmaceutical and/or medical applications including sustained/controlled release systems, transdermal patches, encapsulation, tablet coatings and conjugation to biologics, wound dressing, tissue engineering, suture, galenic, vascular implant, medical clothing accessories, osteosynthesis, etc (Gheorghita et al., 2021).

1.2 Cellulose

Cellulose is the major component in the lignocellulosic biomass comprising around 35–50%, and it is a well-known ubiquitous structural polymer in nature. There are many renewable sources of cellulose including plants, animals, algae, bacteria, and amoeba (Dufresne, 2013; Dunlop et al., 2018; Habibi et al., 2010; Malucelli et al., 2017).

Cellulose is an important environmentally-friendly renewable polymer on the earth. Cellulose has been widely used as feedstocks for the synthesis of biomaterials, biofuels and biochemicals. Recently, cellulose and cellulose derivatives have received intense attention in biomedical applications, such as tissue engineering, scaffold, artificial blood vessel, skin grafts, artificial skin, drug carrier, and chronic skin diseases (Meng et al., 2017)

Soft and hard wood, and cotton are the major sources for celluloses of different quality accompanying hemicellulose and lignin. Cellulose is preferred to other polymers because of its biodegradability, abundance, light weight, cost effectiveness, high tensile strength and stiffness

(Poletto et al., 2014). Cellulose has a linear β-(1→4)-linked glucan structure (Fig. 1.1) having the formula $(C_6H_{10}O_5)_n$, enabling strong cooperative intra-and intermolecular hydrogen-bond patterns, stiffening the chain, and forming mechanically stable, insoluble fibrils and fibers (Mischnick and Momcilovic, 2010).

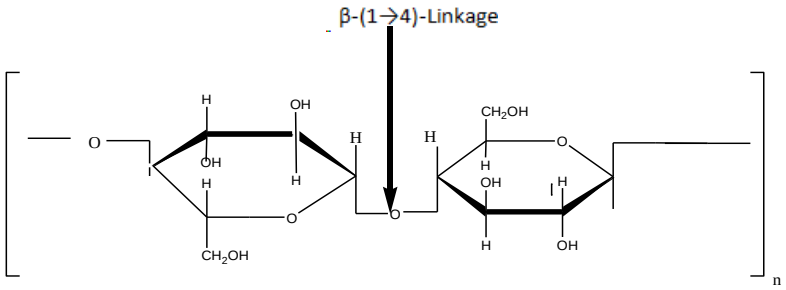

Fig. 1.1: Structure of cellulose.

1.3 Extraction of cellulose

Different cellulose extraction methods have been reported in the literature such as alkaline treatment (Melikoğlu et al., 2019; Xiao et al., 2019), steam explosion pretreatment (Sun et al., 2005), mixed chemical and enzymatic extraction (Reddy and Yang, 2006), ultrasound-assisted extraction (Dinh Vu et al., 2017), liquefaction (Meng et al., 2019b), and ionic liquid methods (Wang et al., 2011) among others. Alkaline treatment facilitates the disruption of cell walls by dissolution of mainly hemicellulose, lignin, and silica, and by hydrolysing uronic and acetic acid esters. Furthermore, alkaline treatment is a preferred process for it does not affect the environment (Abdel-Halim, 2014; Dinh Vu et al., 2017).

Bleaching the pulps using sodium chlorite or hypochlorite solutions in acidic media is widely reported to remove the lignin and remaining hemicellulose (Park et al., 2019; Zhanhong Wang et al., 2019; Zhang et al., 2020). Hydrogen peroxide is also used as an effective oxidizing/bleaching agent to improve the degree of whiteness and achieve a good delignification rate in an alkaline medium. The lignin chromophore groups are removed by the hydroperoxide anion (HOO-), preferentially attacking ethylenic and carbonyl groups. Moreover, eco-friendly radical species are generated, such as hydroxyl (OH-), which results from the alkaline decomposition of the hydrogen

peroxide and is responsible for the solubilization of hemicelluloses and removal of lignin (Ditzel et al., 2017).

1.4 Nanocelluloses

Nanocelluloses are natural materials isolated from cellulose having defined nano-scale structural dimensions, less than 100 nm in diameter and several micrometers in length. The three main classes of nanocelluloses are a) cellulose nanocrystals (CNCs), also referred to as nanocrystalline cellulose and cellulose nanowhiskers, b) cellulose nanofibrils, also referred to as nano-fibrillated cellulose, c) bacterial cellulose (Abitbol et al., 2016; Du et al., 2019; Gabriel et al., 2021; Klemm et al., 2018).

CNCs have captured the interest of researchers and industries due to their unique properties such as high crystallinity, large specific surface area, high mechanical strength and stiffness, low density, biocompatibility, and degradability as well as reactive hydroxyl group on the surface (Kupnik et al., 2020). Consequently, they are suitable for many advanced functional applications such as drug delivery, tissue engineering, reinforcement of composite materials, template for nanomaterial synthesis, protein or enzyme immobilization, emulsion stabilizer etc. (Mariano et al., 2014; Trache et al., 2020).

CNCs have different morphological shapes such as rod-like, ribbon-like, or sphere-like and dimensions ranging from 5–30 nm in diameter and 100–500 nm in length (Kamelnia et al., 2019; Park et al., 2019). Various other approaches such as deep eutectic solvent (Fan et al., 2020), ammonium persulfate and 2,2,6,6-tetramethylpiperidine 1-oxyl (TEMPO)-mediated oxidation (Zhang et al., 2020), ball mill assisted solid acid hydrolysis (Song et al., 2018), enzyme-assisted hydrolysis, mechanical disintegration and high-pressure homogenization (Park et al., 2019) have been reported for isolation of CNCs. However, the acid hydrolysis approach especially using sulfuric acid is reported to be the most effective method for CNCs isolation in literature due to higher colloidal stabilities (Dai et al., 2020, 2018; Meng et al., 2019a).

1.5 Modification of (nano)celluloses

Chemical modification of (nano)celluloses is performed to impart new steric or electrostatic effects to the particles and to improve processability, which can be tailored for specific

industrial/pharmaceutical applications. The typical modifications of cellulose are etherification and esterification at the hydroxyl groups of cellulose. Most water-soluble and organic solvent-soluble cellulose derivatives are prepared by these substitution reactions (Kamel et al., 2008).

Chemical modification of CNCs can be classified into two major groups: a) physical adsorption to the surface, and b) covalent bond formation or derivatization of the surface (Tortorella et al., 2020). The covalent chemical modification of CNC surfaces includes sulfonation, oxidation, cationization, silylation, esterification, carboxylation, and carbidation. CNCs can be modified hydrophobically using different types of surfactants such as cetyl trimethylammonium bromide (CTAB); longer or short chain; linear or branched chains; or ionic liquids (Raghav et al., 2021).

The basic chemical reactions used industrially for etherification of (nano)celluloses are confined largely to the ether synthesis by (a) Williamson and (b) base catalysed oxyalkylation. The Williamson synthesis is the most common method for etherification of cellulose. In this case, the alkali (nano)cellulose is reacted with alkyl or aryl halides (or sulfates), alkene oxides, and unsaturated compounds activated by electron-attracting groups. In the reaction, a cellulose ether and a salt are formed (Kamel et al., 2008; Wüstenberg, 2015). Carboxymethylation of (nano)cellulose is a versatile modification by etherification because it provides access to water-swellable or water-soluble polymers and intermediates with various valuable features (Varshney et al., 2006). Carboxymethyl (nano)cellulose (CM(N)C) is a linear, long chain, water soluble, and anionic semi-synthetic polysaccharide produced by aqueous alkali swollen cellulose reaction with monochloroacetic acid (MCA) in surplus of organic solvent (e.g. isopropanol, butanol or ethanol) (Mansur et al., 2017; Singh and Singh, 2013).

1.6 Nanogels as novel drug delivery systems

Drug delivery systems are approaches by which active drug molecules are delivered using a variety of drug carriers to desired body sites like tissues, organs, cells and subcellular organs (Li et al., 2019). Novel drug delivery systems are engineered according to a rational design to enhance the delivery and the performance of existing drugs with respect to traditional systems. The main rationale for the advancement of novel drug delivery systems is to enable a sustained and controlled drug delivery, to maintain efficient drug level and simultaneously reduce adverse effects (Laffleur and Keckeis, 2020). Polymeric nanocarriers such as nanogels represent one of the most

innovative approaches for drug delivery applications. The main objective of such nanocarriers is to convey the therapeutic molecule be they drugs, proteins, or nucleic acids directly into the target organ or tissue (Begines et al., 2020).

For the first time, Vinogradov et al. (1999) introduced the term "nanogel" (NanoGel™) as a novel type of drug delivery system. They defined NanoGel™ to represent particles of cross-linked bifunctional networks of polyethyleneimine and carbonyldiimidazole-activated poly(ethylene glycol) prepared using emulsification-solvent evaporation technique for delivery of antisense phosphorothioate oligonucleotides.

Nanogels are three-dimensional hydrogel materials in the nanoscale size range formed by crosslinked swellable polymer networks with a high capacity to hold water, without actually dissolving into the aqueous medium. Nanogels can be composed of a variety of naturally occurring polymers, synthetic polymers or a combination thereof (Kabanov and Vinogradov, 2009; Soni et al., 2016).

Nanogels, also known as hydrogel nanoparticles, are new generation gel systems for drug delivery. They have gained lots of attention as promising drug delivery systems because of their unique potentials by combining the advantages of gel systems and nanoparticles (Demirel and Von Klitzing, 2013; Eckmann et al., 2014; Neamtu et al., 2017; Quinn, 2016; Raemdonck et al., 2009; Zhang et al., 2016). Drug delivery systems using nanoparticles only exhibit several drawbacks such as low loading efficiency and low intracellular uptake capacity (Neamtu et al., 2017; Yang et al., 2015). However, nanogels exhibit the physiological property which resembles tissues. Drug loading is relatively high and drugs are incorporated into the systems without any chemical reaction, thus their activity could be preserved for longer durations.

1.7 Polysaccharide-based nanogels

Polysaccharide-based nanogels exhibit excellent properties such as large tunable size, high surface area, large interior network for the incorporation of different drugs, lack of toxicity, high water content, high stability, high drug-loading capacity, biocompatibility, stable network structure, and responsiveness to environmental factors such as temperature and pH in drug delivery systems (Baipaywad et al., 2014). These unique properties offer great potential for the utilization of polysaccharide-based nanogels in the drug delivery systems. Extensive review was conducted on

different polysaccharide-based nanogels in drug delivery including chitosan, heparin, hyaluronic acid, alginate, pullulans, pectin, chondroitin sulfate, cyclodextrin, dextran, starch, and cellulose-based nanogels (Debele et al., 2016).

1.7.1 Cellulose-based nanogels

Cellulose derivatives are among the promising and versatile materials with special chemical structure which provides a good platform for the construction of hydrogel/nanogel networks with distinctive properties in terms of swelling ability and sensibility to external stimuli. Indeed, the high density of free hydroxyl groups in the cellulose structure makes them become a solid substrate that can undergo functionalization, allowing the production of new materials for novel and advanced applications. Consequently, cellulose based hydrogels/nanogels are promising materials, biodegradable, biocompatible, and of low cost, which exhibit properties that make them attractive in many applications, particularly in biomedical applications (Onofrei and Filimon, 2016).

Studies on cellulose-based nanogels have emerged within the last two decades for pharmaceutical applications. Developments on carboxymethyl cellulose (CMC), hydroxypropyl methylcellulose (HPMC), hydroxypropyl cellulose (HPC), and methyl cellulose (MC) based nanogels have got wide attention, and microcrystalline cellulose (MCC)-CMC and bacterial cellulose (BC) based nanogels are also reported.

1.7.1.1 CMC-based nanogels

Ernsting and coworkers (2012) developed a polymer conjugate composed of acetylated CMC, docetaxel, and polyethylene glycol, designed to enhance the pharmacokinetics and antitumor efficacy of docetaxel. Their design placed an emphasis on nanoparticle self-assembly to protect docetaxel during blood transport, stability of the nanocarrier, and PEGylation to enhance pharmacokinetics.

Zhu et al (2013) fabricated nanogels from lysozyme and CMC by a convenient method without using any chemical treatment except simple heating to achieve the denaturation temperature of lysozyme. The nanogels were of spherical shape with average hydrodynamic diameter of 241 nm and the swelling ratio of nanogels was about 5. They reported that the release of the model drug, 5-fluorouracil, in simulated gastric fluid was more slowly compared with that in simulated intestinal fluid.

Bio-reductive nanogels were developed based on methacrylated carboxymethyl cellulose combined with cystamine bisacrylamide by radical polymerization for delivery of doxorubicin *in vitro* and *in vivo* (Qian et al., 2014). Cystamine bisacrylamide was synthesized by dissolving cystamine dihydrochloride in water and adding an acryloyl chloride solution and a NaOH aqueous solution dropwise simultaneously at 0 °C. Methacrylated carboxymethyl cellulose was synthesized by dissolving carboxymethyl cellulose in water and adding methacrylic anhydride and then adjusting the pH of the mixture to around 8 with NaOH solution.

Wen & Oh (2014) also synthesized CMC-based bionanogels for dual stimuli-responsive drug release and cancer therapy. pH/reduction-responsive CMC-based bionanogels were synthesized by aqueous crosslinking polymerization of oligo(ethylene oxide) monomethyl ether methacrylate in the presence of CMC and a disulfide labeled crosslinker dithiopropionyl poly(ethylene glycol) dimethacrylate. The resulting bionanogels had a mean diameter of approx..25 nm as confirmed by DLS and TEM. Doxorubicin was physically encapsulated within the nanogels through electrostatic interactions. Bionanogels exhibit enhanced drug release in response to acidic pH due to reduced interaction between doxorubicin and the bionanogels, and reducing agent due to the reductive cleavage of disulfide bonds. Furthermore, their ability to facile conjugating with cell-targeting ligands was demonstrated using a water-soluble UV-active dye as a model cell-targeting biomolecule.

Yang and co-workers (2015) prepared CMC nanogels with branched poly(ethyleneimine) for inhibition of cytotoxicity in human mesenchymal stem cells as a plasmid DNA encapsulation. The nanogel networks they developed had various advantages including prolonged drug stability during storage, prolonged drug uptake, and lower cytotoxicity.

Wen & Oh (2015) also developed the dual temperature/acidic pH-responsive bionanogels by aqueous crosslinking polymerization assisted with temperature-driven self-association method, yielding narrow-size distribution of bionanogels with diameter of approx. 11 nm. The bionanogels had good colloidal stability in physiological and acidic pH conditions. For biological perspective, bionanogels show negligible non-specific protein absorption with model protein bovine serum albumin for up to 72 hrs. In response to high temperature and acidic pH, bionanogels underwent changes in volume or ionic interactions triggering rapid drug release.

Another study by Li et al (2015) also reported the development of lysozyme and CMC nanogels through a green self-assembly method of electrostatic interaction using methotrexate as a model drug. They indicated that slow release and increased bioavailability of the loaded drug were observed from the nanogels, with about 14.2% of drug loading capacity and 40% encapsulation efficiency.

The work of He and co-workers (2015) showed the development of pH sensitive nanogels from low density lipoprotein (LDL)/CMC through self-assembly to target cancer cells by doxorubicin. The nanogels were spherical with an average diameter of about 90 nm. Additionally, the cationic doxorubicin was effectively loaded into LDL/CMC nanogels with exceptionally high encapsulation efficiency of about 98%.

In the work reported elsewhere, nanogels based on the self-assembly of CMC and bovine serum albumin was prepared for co-delivery of radionuclide ^{131}I and chemotherapeutic drug camptothecin to achieve the combined chemo-radioisotope therapy of cancer. The nanogels were prepared by a simple and green electrostatic interaction, showing typical spherical shape with average size about 120 nm, high drug loading capacity, robust stability and low hemolysis (Liu et al., 2018).

1.7.1.2 HPMC-based nanogels

The work of Yao and coworkers showed the development of HPMC/polyacrylic acid (PAA) hybrid nanogels by surfactant-free polymerization in aqueous solution for controlled delivery of insulin. They studied the effect of temperature, reaction time, and amount of cross-linker on the size and morphology of the nanogels. Their results showed that when the reaction temperature was higher than the lower critical solution temperature, the particle size increased with increasing temperature (Yao et al., 2014). Similar synthesis mechanism for HPMC/PAA hybrid nanogels was also reported (Yao et al., 2011).

Zhao and the team developed HPMC hybrid nanogels as controlled-release delivery system by surfactant-free polymerization of methacrylic acid in aqueous solution. The obtained nanogels possessed an average particle size of 170 nm with PDI of 0.06. The HPMC nanogels loaded with insulin had a high drug loading of 21.3 % and a high entrapment efficiency of 95.7 %. The effects of reaction time and cross-linker concentration on the size of the nanogels have been studied. The

results showed that in a certain range, the particle size decreased with increasing reaction time and increasing concentration of cross-linker (Zhao et al., 2016).

1.7.1.3 HPC-based nanogels

A redox and thermosensitive HPC was synthesized by conjugating cysteamine to HPC and they controlled the degree of thiol groups by the feed ratio of the reactants (Tan et al., 2011). The thiolated HPC (HPC–SH) maintained the thermosensitivity of HPC and the thiol groups on the HPC chain can be oxidized to disulfide bonds. Cytotoxity tests performed on MG-63 cells proved that HPC–SH was not harmful to the cells. The crosslinking degree of the nanogels was controlled by the degree of substitution of thiol groups (–SH) in the thiolated HPC. The hydrodynamic radius of the nanogels was tuned by adjusting the degree of crosslinking and the concentration of the initial thiolated HPC solution in the self-association process. The hydrodynamic radius of the nanogels was changed with temperature and the dissociation process by adding the reducing agent dithiothreitol.

HPC-based PAA nanogels were prepared by inverse emulsion polymerization (Liao et al., 2012b). Through the hydrogen bonding interaction of AA with HPC, AA absorbed on the HPC to form PAA, the much stronger interpolymer hydrogen bonding triggered the phase transition of HPC at a temperature around room temperature, causing HPC coil-globular phase transition to collapse and form nanospheres at room temperature, and formed nanogels chemically crosslinked by poly(ethylene glycol) diacrylate & bisacrylamide. The results showed that all the PAA nanogels demonstrated a narrow size distribution with diameters ranging from 60 nm to 600 nm.

Methacrylic acid (MAA)-triggered phase transition properties of thermosensitive HPC were also investigated (Liao et al., 2012a). They reported that the phase transition temperature of 0.1 wt.% HPC aqueous solutions was dramatically reduced from 41 °C to 8 °C as the MAA concentration increased from 0 wt% to 4 wt%. MAA attaching on HPC polymer chains was polymerized to form surfactant-free nanogels around ambient temperature when HPC collapsed forming PMAA nanogels.

Surfactant-free HPC/PMAA nanogels were developed by polymerization and crosslinking (An et al., 2015). It was reported that the average size of HPC nanogels varied little with increasing polymerization temperature below 26 °C, whereas it greatly increased above 26 °C. Besides, high

crosslinker bisacrylamide concentration resulted a low size, and the nanogels had the narrowest size distribution when its concentration was 0.1 wt%. The formulated nanogels were both thermo-sensitive and pH sensitive due to the coexistence of HPC and PMAA.

HPC-based disulfide-crosslinked nanogels exhibiting dual reduction-responsive and thermoresponsive properties were also synthesized by grafting from method utilizing atom transfer radical polymerization of a mixture of two methacrylate monomers containing pendant disulfide linkage (HMssEt) and Oligo(ethylene oxide) monomethyl ether methacrylate. Their thermal properties are tuned with pendant hydrophobic/hydrophilic balance (Rahimian et al., 2015).

Tahara et al (2016) prepared a thermoresponsive nanogel from cholesterol-bearing HPC by self-assembly and cross-linking. Recently, pH and thermosensitive nanogels were synthesized by Hassanpour & Bagheri (2017) by polymerization of itaconic acid and copolymerization with MA in aqueous solution of HPC and cross-linking with N, N′-methylenebisacrylamide.

1.7.1.4 MC-based nanogels

Zhang et al (2014) synthesized MC-based nanogels of PMAA. MC is a thermo sensitive polymer, having a phase transition temperature or a lower critical solution temperature of about 65 °C. When the investigators added MAA to the MC solution, the phase transition of MC occurred at a lower temperature less than 65 °C, and a higher concentration of MAA led to a lower phase transition temperature of MC. Based on the phase transition of MC solution triggered by MAA, the surfactant-free nanogels were synthesized by using MC as a template in an aqueous media. The resulting PMAA nanogels were characterized by using DLS and FTIR. The nanogels were affected by the concentration of both MC and MAA. A higher concentration of MAA led to a higher polymerization rate, and the higher concentration of MC resulted in the formation of the smaller size of PMAA nanogels.

Jamard and co-workers (2016) synthesized a copolymer made of MC hydrophobized with poly(N-tert-butylacrylamide), MC-g-PNtBAm, that self-assembles in aqueous media to form nanogels of 140 nm in diameter to target the ocular surface, and thus prolong corneal retention.

1.7.1.5 MCC/CMC-based nanogels

Keshavarz & Kaffashi (2014) synthesized nanogel bioadhesives based on cellulose derivatives of MCC/CMC. They used clay, fumed porous silica and porous starch as reinforcing nanofillers and additives. In their study, a monomer solution of sodium polyacrylate was prepared by mixing sodium hydroxide, acrylic acid and distillated water. Then, N,N'-methylenebisacrylamide (as the cross-linking agent), N,N,N',N'-tetramethylethylenediamine (as accelerator) and ammonium peroxydisulfate (as initiator) were added. It was reported that the drug (pentoxifylline) release pattern indicated the biopolymer-clay nanocomposites had better controlled release properties compared to the other nanogel formulations.

1.7.1.6 Bacterial cellulose (BC) Whisker/Poly(NIPAM-co-BMA) (PNB) based nanogels

Nanogels based on complex dispersions of poly(N-isopropylacrylamide-cobutyl methacrylate) (PNB) with BC were developed (Wu et al., 2013). The nanogels exhibited reversible thermosensitive sol-gel phase behavior to be utilized in a wide range of biomedical applications. In their study, TEM, DSC, and rheological investigations indicated that the formation of shishkebab crystals, oriented molecular chains.

1.8 Synthesis techniques of nanogels

The three major aspects to be considered for the successful synthesis of nanogels include: (1) the particles size, (2) the polymer nature and composition, and (3) the cross-linking strategy within the polymer chains. These parameters cause significant influence on the stability of the particles and determine their suitability for biomedical applications (Asadian-Birjand et al., 2012).

Different approaches of nanogels synthesis techniques are reported by different researchers. Chacko and co-workers (2012), Khoee & Asadi (2016) and Neamtu et al (2017) divided the synthesis techniques into two major classes (Fig. 1.2): (1) production of nanogels via heterogeneous monomer polymerization; and (2) preparation of nanogels from polymer precursors.

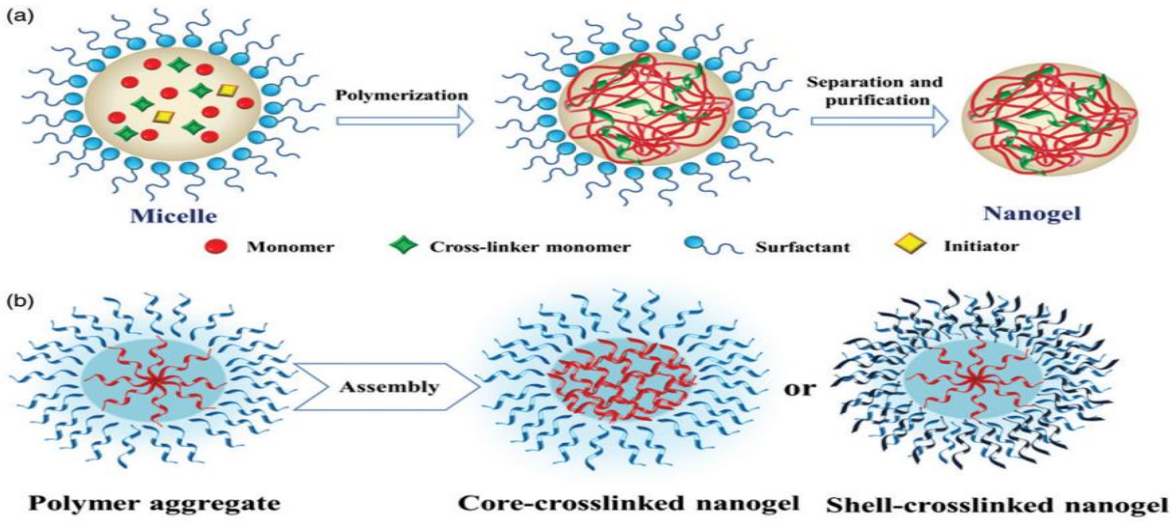

Fig. 1.2: Schematic illustration of the nanogel network created by: (a) direct polymerization of monomers; (b) assembling of a polymer precursor (adapted from Chacko et al. 2012; Neamtu et al. 2017).

Heterogeneous free radical polymerization, precipitation polymerization, heterogeneous controlled/living radical polymerization, atom-transfer radical polymerization, reversible addition–fragmentation chain transfer and nanogels synthesis by inverse reversible addition-fragmentation chain transfer polymerization (RAFT) miniemulsion are also among the methods for preparation of nanogels via heterogeneous monomer polymerization. Synthesis of nanogels via miniemulsion technique is illustrated in Fig. 1.3.

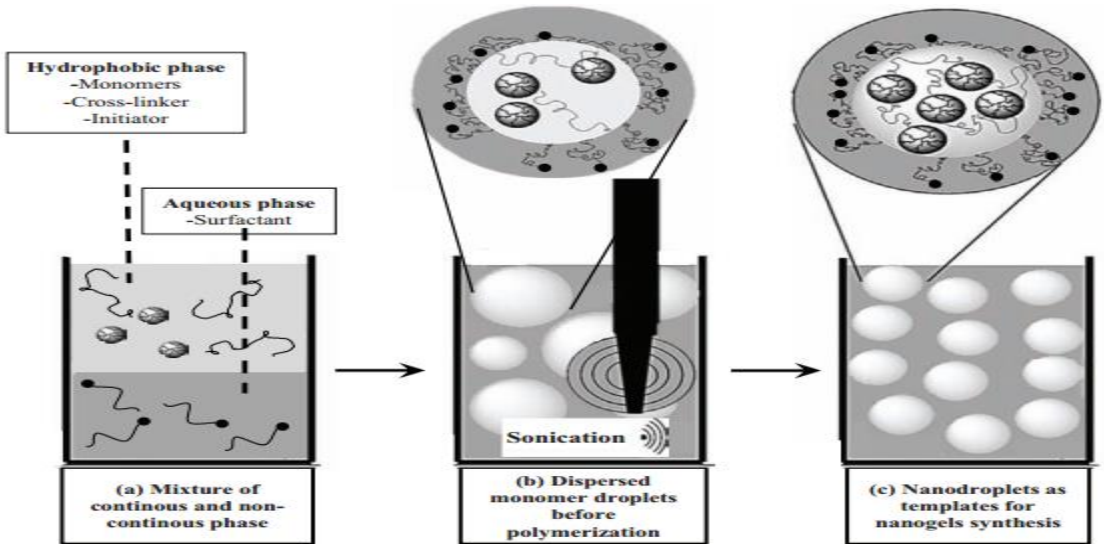

Fig. 1.3: Synthesis of nanogels via miniemulsion technique. (a) Initial two phases mixture. (b) Formation of small droplets in a continuous phase by applying high shear stress, such as ultrasonication. (c) Monodisperse nanosized 50-500 nm template for nanogel synthesis (adapted from Asadian-Birjand et al., 2012).

In the studies of Baipaywad et al (2014) and Tan et al (2010), similar approaches for the preparation of nanogels were also described, including free radical polymerization, controlled/living radical polymerization, and self-assembly. Depending on the phase in which this process occurs, free radical polymerization includes either as dispersion polymerization and precipitation or emulsion polymerization (Fig. 1.4). Controlled/living radical polymerization techniques such as atom transfer radical polymerization, RAFT, and stable free radical polymerization have been developed for the synthesis of nanogels with precisely controlled dimensions, topology, composition, and functionality.

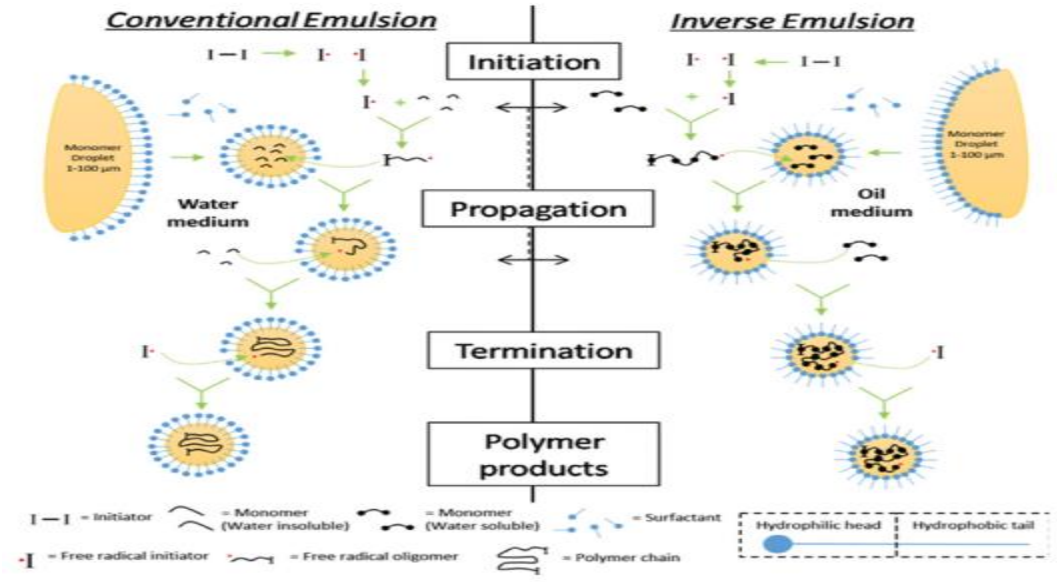

Fig. 1.4: Synthetic approaches for preparation of nanogels via conventional and inverse emulsion polymerization (adapted from Baipaywad et al., 2014).

However, various researchers (Hamidi et al., 2008; Sasaki and Akiyoshi, 2010; Sivaram et al., 2015) preferred to classify the major techniques of synthesis of nanogels into two categories according to their cross-linking structure: chemically (covalent) cross-linked nanogels which form cross-linking points by covalent bonds, and physically cross-linked nanogels with non-covalent

bonds, such as hydrogen bonds, electrostatic and hydrophobic interactions. It was mentioned in the work of Sasaki & Akiyoshi (2010) that chemically cross-linked nanogels are prepared by either nano- or micro-emulsion polymerization, cross-linking of block copolymer micelle, nano template method, top-down methods using lithography (PRINT (Particle Replication in Non-Wetting Templates)), and physically cross-linked nanogels are prepared by self-assembled nanogels formed by amphiphilic associating polymers as also indicated in another work of development of a nanogel formed by self-association of cholesterol-bearing pullulans (Sekine et al., 2016).

1.9 The present study

Woody plants and cotton are the major sources of cellulose and its derivatives such as CNCs and CMC, but different factors such as economic and environmental concerns have forced researchers and stakeholders to look for other potential substitutes. Furthermore, its origin determines the physicochemical properties such as: yield, length of cellulose chains, the degree of crystallinity and morphology and dimensions of the microfibrils. This PhD research work will explore *teff* straw (TS), *enset* fiber (EF), sugarcane bagasse (SB), and coffee hull (CH) as alternative sources of celluloses, CNCs and CMC, and undertake physicochemical and morphological characterization of the untreated byproducts, as-extracted cellulose, CNCs, and CMC. Biocompatible and biodegradable nanocarriers such as nanogels have recently received considerable attention in drug delivery systems. However, the longer preparation time and usage of large amounts of organic solvents and surfactants have limited their application. In this work, nanogels were prepared from self-assembled CMC- and carboxymethyl nanocellulose (CMNC)-lysozyme blends via electrostatic complexation following a simple and green ecofriendly preparation approach for sustained drug delivery. To the author's knowledge, the CMNC-lysozyme based nanogels for sustained drug delivery were presented for the first time. Furthermore, no single work has reported on comparative loading of drugs from different classes of Biopharmaceutics Classification System (BCS) into nanogels except the work reported by Paulos et al (2019) who developed hydrophobically modified starch-based nanoparticles for loading of various BCS class drugs. In this study, three model drugs: acyclovir (Class III, poorly permeable), carbamazepine (Class II, poorly soluble), and furosemide (Class IV, poorly soluble and permeable) from different BCS classes were selected on the basis of their solubility and permeability profiles.

1.10 Research questions

a) Can TS, EF, SB, and CH be exploited as alternative sources of cellulose, CNCs and CMC?
b) Do the plant sources and extraction conditions have impact on the physicochemical properties of cellulose, CNCs, and CMC?
c) Which plant source has superior and promising physicochemical properties in terms of cellulose content, yield, and crystallinity?
d) Can nanogels be prepared from self-assembled CMNC-lysozyme blends following a simple and green ecofriendly preparation approach for sustained drug delivery?
e) Do the preparation conditions such weight ratio, pH, and heating time of nanogels affect the physicochemical properties?
f) Do CMNC-based nanogels have superior properties over CMC-based nanogels?

1.11 Objectives

1.11.1 General objective

- To explore TS, EF, SB and CH as alternative sources of cellulose, CNCs and CMC as well as to synthesize nanocellulose-based nanogels via electrostatic complexation for sustained drug delivery.

1.11.2 Specific Objectives

- To extract and characterize cellulose fibers from TS, EF, SB and CH;
- To isolate and characterize CNCs from TS, EF, SB and CH;
- To prepare and characterize CMC and CMNC from TS, EF, SB and CH;
- To prepare, characterize and evaluate CMNC-based nanogels for sustained delivery of various model BCS class drugs: acyclovir, carbamazepine and furosemide, and investigate the drug loading and *in vitro* release profiles;

2 Extraction and characterization of celluloses from various plant byproducts

2.1 Introduction

Lignocellulosic-based materials in the green industry have received much attention because they are abundant, relatively cheaper and eco-friendly (Naceur Abouloula et al., 2018; Veeramachineni et al., 2016). A large amount of cellulosic waste is generated by agro-industries (Rosa et al., 2010), utilizing these cellulose-rich byproducts can address both ecological and economic concerns (Mischnick and Momcilovic, 2010).

Cellulose is the most abundant polysaccharide produced in nature by plants and microorganisms (Khan et al., 2017; Mischnick and Momcilovic, 2010). Celluloses are obtained from the major conventional sources such as cotton and wood. These sources have been used for years in the production of cellulose and its derivatives for different industrial applications mainly in pharmaceutical, textile and paper industries. However, the overutilization of such sources by competing industries, such as energy and construction, and/or deforestations globally has increased the need for alternative cellulose sources from herbaceous plants, agricultural crops and/or non-woody plants (Jmel et al., 2019; Klemm et al., 2005).

Teff (*Eragrostis tef* (Zucc.) Trotter) is among the most widely cultivated staple cereal crops in Ethiopia and its grains are rich in starch. Ethiopia is the largest *teff* producer in the world and TS is the solid waste byproduct. Traditionally, TS is used as a binding material for muddy walls of huts and fodder for livestock (Lee, 2018; Minten et al., 2016). *Enset* (*Ensete ventricosum* (Welw.) Cheesman), known as *false banana* due to its striking resemblance to the banana plant, is also a traditional staple crop in the South and South-West Ethiopia. EF is harvested from the leaves, pseudostems, and the inner inflorescence stalks of *enset* plant as a byproduct of *kocho*. Traditionally, EF is used in the production of sacks and ropes for house and fence constructions (Berhanu et al., 2018; Gebre-Mariam and Schmidt, 1996). Sugarcane is a tall perennial grass of the genus Saccharum, Family Poaceae, and SB is the byproduct obtained from sugarcane after sucrose extraction and bioethanol production (Bhattacharya et al., 2008). Coffee, the most popular beverage and the second-largest traded good after crude oil worldwide, traces its origin to the mountains of Ethiopia (Alghooneh et al., 2017; Alves et al., 2017). CHs are agro-industrial

residues available in huge quantities in coffee processing enterprises across Ethiopia, which is among the top 5 coffee producing countries in the world (Collazo-Bigliardi et al., 2018).

Despite their huge abundance, there have not been any significant value-added applications of these four plant byproducts in Ethiopia. Even though extraction of cellulose from SB has been reported elsewhere (Abdel-Halim, 2014; Golbaghi et al., 2017), to the best of the authors' knowledge, no work has been reported on the exploration and full characterization of celluloses from TS, EF and CH. SB was considered in this study because sugar producing factories are booming in the country which are expected to generate even more massive amounts of cellulose-rich SB as byproduct.

The aim of the present work was to explore alternative sources of cellulose fibers from the aforementioned plant byproducts using simple, ecofriendly and chlorine-free extraction conditions, and characterize their physicochemical properties for potential value-added industrial applications.

2.2 Materials and methods

2.2.1 Materials

Brown TS was purchased from Merkato, a local market in Addis Ababa, Ethiopia. EF was purchased from a local market in Kambata Tembaro Zone, South Ethiopia. SB was donated by the Metehara Sugar Factory, East Shoa Zone, Ethiopia. CH was collected from the Ethiopian Coffee Processing and Warehouse Enterprise in Addis Ababa, Ethiopia. Glacial acetic acid (Riedel-de Haën), acetone and sodium hydroxide 97% (HiMedia, Mumbai, India), sulfuric acid 97% (BDH, England), formic acid (98%) (Central Drug House (P) Ltd. New Delhi, India), copper sulfate pentahydrate 98.5%, commercial cellulose (CC), n-hexane 99% and zinc chloride (LOBA CHEMIE-Laboratory, India), toluene (Fisher Scientific, UK), potassium iodide (Reagent chemical services Ltd Runcorn, Cheshire), ammonium oxalate 99.5% (UNI-Chem, Chemical Reagents), iodine 99%, methanol 99.9%, ammonia solution 28% and hydrogen peroxide 30% (CARLO ERBA Reagents, France) and ethanol absolute (Fisher Scientific, UK) were used as received.

2.2.2 Cellulose extraction

The plant byproducts were washed to remove dust, dried in an oven (Kottermann® 2711, Germany) at 80 ^{o}C, cut and then treated with extraction solvents in three stages (Jahan et al., 2011; Mariano et al., 2016; Melikoğlu et al., 2019; Nazir et al., 2013; Nuruddin et al., 2016, 2011; Veeramachineni et al., 2016; Watkins et al., 2015) as described below. Four solvent extraction conditions (A, B, C and D) were followed to extract the celluloses from the byproducts, and the extracted celluloses were designated as C1, C2, C3 and C4, respectively, as shown in Table 2.1.

2.2.2.1 Alkaline pretreatment

Alkaline pretreatment was conducted in 3 L flask with 5%, 10% and 17.5% NaOH solutions in 1:10 (g/ml) solid to liquid ratio of dry material on a water bath at 90 °C for 1.5 h. Residues of the byproducts were filtered and washed continuously with hot distilled water.

2.2.2.2 Formic acid, acetic acid and hydrogen peroxide treatment

The pulps were further treated with a mixture of 20% formic acid (FA)/20% acetic acid/7.5% H_2O_2 (2:1:2) solution on the water bath at 90 °C for 1.5 h, at a byproduct to liquor ratio of 1:10 (g/ml). Finally, the delignified pulps were filtered to separate the cooking liquor (which contains lignin and hemicellulose) from cellulose and washed with hot water.

2.2.2.3 Bleaching

Bleaching was done by treating the pulps with 7.5% H_2O_2 in alkaline media of 4% and 10% NaOH solutions at 1:10 (g/ml) fiber ratio separately, first at room temperature for 30 min, then on a water bath at 70 °C for 30 min. Finally, the pulps were washed repeatedly with hot distilled water to remove residual lignin, and dried in an oven (Kottermann® 2711, Germany) at 60 °C until constant weight. The bleaching step was repeated once for CH when alkaline pretreatment was performed using 5% NaOH.

Table 2.1: Extraction conditions of cellulose from the four plant byproducts (TS-teff straw; EF-enset fiber; SB-sugarcane bagasse; CH-coffee hull) at 1:10 (g/ml) byproduct/reagent ratio.

Stage	Extraction condition (Cellulose extracted)			
	A (C1)	**B (C2)**	**C (C3)**	**D (C4)**
I.	5% NaOH	10% NaOH	10% NaOH	17.5% NaOH
II.	20% FA/20% Ace/7.5% H_2O_2 (2:1:2)	20% FA/20% Ace/7.5% H_2O_2 (2:1:2)	20% FA/20% Ace/7.5% H_2O_2 (2:1:2)	20% FA/20% Ace/7.5% H_2O_2 (2:1:2)
III.	7.5% H_2O_2 in 4% NaOH	7.5% H_2O_2 in 4% NaOH	7.5% H_2O_2 in 10% NaOH	7.5% H_2O_2 in 10% NaOH

NB: For stage I and stage II each, a treatment time of 90 min was required; and for stage III, 60 min was required. Key: FA-formic acid; Ace-acetic acid, C1-4-kind of cellulose extracted.

2.2.3 Identification tests and estimation of constituents of the plant materials

Appearance, solubility, color test, pH, ash values and moisture content of the celluloses (C2) obtained from the four byproducts using extraction Condition B were determined according to the methods described in different pharmacopoeias (BP, 2016a; EP, 2013; USP41-NF36, 2019a). The compositions of the untreated plant byproducts and the as-extracted celluloses (C2), such as lignin, hemicellulose, aqueous extracts, fatty and waxy matters, pectic matters and cellulose content were determined according to the methods stated elsewhere (Abdel-Halim, 2014; Lin et al., 2010; Smyth et al., 2017; Yeasmin and Mondal, 2015).

2.2.3.1 Klason lignin

To determine klason lignin, methods reported elsewhere were followed (Abdel-Halim, 2014; Smyth et al., 2017; Yeasmin and Mondal, 2015). First, defatted and dewaxed sample was treated with 72% wt/wt H_2SO_4 in a ratio of 1:20 by adding drop-wise with constant stirring. Then, the mixture was allowed to stand for 2 h and then diluted to 3% acid concentration and boiled for 4 h under reflux, and allowed to stand overnight. The lignin was filtered on a pre-weighed filter paper and washed with hot distilled water till neutrality. The lignin was then dried at 105 °C for 6 h and gravimetrically estimated after subtracting the ash value.

2.2.3.2 Hemicellulose content

The amount of hemicellulose content was determined according to the method described elsewhere (Lin et al., 2010). The defatted and dewaxed sample (1:10 (g/ml)) was treated after drying using 0.5 M of NaOH solution at 80 °C for 3.5 h. Then, the sample was repeatedly washed with distilled

water till neutral pH and dried to a constant weight. The difference between sample weight before and after treatment was taken as the amount of hemicellulose.

2.2.3.3 Water soluble components

To estimate water soluble components, the plant material was treated with boiling distilled water for 2 h on hot plate, filtered and dried at 105 °C until a constant weight was obtained. % Water soluble components = W_1 x 100%/W_0, where W_1 is the loss in weight and W_0 is the initial weight of the sample (before treatment) (Yeasmin and Mondal, 2015).

2.2.3.4 Fatty and waxy matters

To estimate fatty and waxy matters, the sample was immersed in an n-hexane–alcohol mixture (2:1, v/v), in the solid to liquor ratio of 1:100 (g/ml), and then allowed to stand for 10 h with occasional stirring. The sample was washed with fresh n-hexane–alcohol mixture and finally with alcohol. The sample was then dried at 105 °C until it had a constant weight. The amount of fatty and waxy matter was estimated as follows: % Fatty and waxy matters = W_1 x 100%/W_0, where W_1 is the loss in weight and W_0 is the initial weight of the sample (before treatment) (Yeasmin and Mondal, 2015).

2.2.3.5 Pectic matter

To determine the pectic matter, the defatted and dewaxed sample was heated in 0.5% ammonium oxalate solution, in the solid to liquor ratio of 1:100 (g/ml), at 70–80 °C for 3 days on a heating mantle. The sample was filtered, washed thoroughly with hot distilled water and then dried at 105 °C until a constant weight was obtained. The percentage of pectic matters was then calculated as: % Pectic matters = W_1 x 100%/W_0, where W_1 is the loss in weight and W_0 is the initial weight of the sample (before treatment) (Yeasmin and Mondal, 2015).

2.2.3.6 Cellulose content

The content of cellulose in the as-extracted cellulose was calculated by difference, assuming that water soluble extractives, hemicellulose, lignin, fatty and waxy matter, and pectic matter, and cellulose are the only components (Abdel-Halim, 2014).

2.2.4 Fourier-Transform Infrared (FTIR) spectroscopy studies

FTIR spectroscopy experiments were conducted using a PerkinElmer FTIR spectrometer (L1600400 Spectrum TWO DTGS, SN: 108152, LIantrisant, UK). The FTIR spectra of the plant byproducts, as-extracted celluloses and CC were recorded in the range from 4000 to 450 cm^{-1}, with no further sample preparation.

2.2.5 X-ray diffraction (XRD)

XRD analyses were performed using an XRD-7000 X-ray Diffractometer MAXima (SHIMADZU Corporation, Japan) at 40 kV, 30 mA with monochromatic Cu-Kα radiation, typically with scan speed of 3.0000 °/min and sampling pitch of 0.0200 °. Data acquired were plotted in Origin Pro 8.5.1 in a 2θ scale from 10 to 40. Raw plant byproducts, as-extracted celluloses as well as CC were examined.

The crystalline indices (CrI) were determined using the following two approaches (Poletto et al., 2014; Segal et al., 1959):

a) equation proposed by Segal *et al.* (Empirical method):

$$CrI = \frac{(I_{200} - I_{am})}{I_{200}} x100\% \text{----------2.1}$$

Where, I_{200} is the maximum intensity (in arbitrary units) of the diffraction from the 200 plane, and I_{am} is the intensity of the background scatter.

b) Hermans *et al.* equation (Peak deconvolution method):

$$CrI = \frac{A_{cry}}{A_{total}} \text{x}100\% \text{ ----------2.2}$$

Where, A_{cry} is the sum of crystalline band areas; and A_{total} is the total area under the diffractograms.

After deconvolution of respective XRD diffractograms following Gaussian profile, parameters such as d-spacings (d), apparent crystallite size or thickness for the 200 plane (τ_{200}), the proportion of crystallite interior chains for the 200 plane (X_{200}), fractional variation in the plane spacing for the 200 plane $(\Delta d/d)_{200}$, and Z-values were obtained using equations described elsewhere (Aguayo et al., 2018; Poletto et al., 2014; Popescu et al., 2011).

The d-spacings were calculated using the Bragg equation:

$$d = \frac{\lambda}{2sin\theta} \text{----------2.3}$$

Where, λ is the wavelength of the incident X-rays, d is the interplanar spacing of the crystal and θ is the angle of incidence.

The average thickness of cellulose crystallites was estimated from the XRD patterns by using Scherrer's equation:

$$\tau = \frac{\kappa\lambda}{\beta_{1/2} cos\theta} \text{----------2.4}$$

where τ is the crystallite dimension/size, κ is the correction factor and usually taken to be 0.94, λ is the radiation wavelength (0.1542 nm), θ is the diffraction angle corresponding to 200 plane and $\beta_{1/2}$ is the peak width at half maximum intensity.

The proportion of crystallite interior chains (X) is calculated using the equation:

$$X = \frac{(\tau - 2h)^2}{\tau^2} \text{----------2.5}$$

where τ is the apparent crystallite size for the reflection of plane (200), and h = 0.57 nm is the layer thickness of the surface chain.

Also, the fractional variation in the plane spacing Δd/d for the 200 plane was calculated following the equation:

$$\frac{\Delta d}{d} = \frac{\beta}{2tan\theta} \text{----------2.6}$$

The Z-value indicates whether cellulose is I_α or I_β. The function that discriminates between I_α or I_β is given by equation:

$$Z = 1693d1 - 902d2 - 549 \text{----------2.7}$$

Where, d_1 is the d-spacing of the $(1\bar{1}0)$ peak and d_2 is the d-spacing of the (110) peak.

2.2.6 Thermogravimetric analysis (TGA)

TGA was performed using DTG (Differential Thermo Gravimetry)-60H (SHIMADZU Corporation, Japan) to study the degradation characteristics of the plant byproducts, as-extracted celluloses and CC. The samples were heated from room temperature to 700 °C at a heating rate of 10 ^oC/min and a nitrogen gas flow rate of 60 mL/min.

2.2.7 Environmental Scanning Electron Microscopy (ESEM)

The ESEM images of the plant byproducts, as-extracted celluloses and CC were obtained using ESEM FEI/Philips XL-30 ESEM (Leuven, Belgium) at an accelerating voltage of 2.00 KV. All the samples were coated with chromium using vacuum sputter prior to SEM analysis.

2.3 Results and discussions

2.3.1 Identification and composition of the plant materials

The celluloses obtained from the plant byproducts following the series of extraction conditions were white in appearance, fluffy and fibrous in nature. The as-extracted celluloses were insoluble in water, acetone, anhydrous ethanol, and toluene but soluble in cuprammonium hydroxide 'Cuam'

solution. All the as-extracted celluloses became violet-blue when dispersed in iodinated zinc chloride solution on a watch-glass, fulfilling the parameters specified in pharmacopoeias (BP, 2016a; EP, 2013; USP41-NF36, 2019a). The digital macroscopic images of the plant byproducts, and as-extracted celluloses (C2) from the byproducts are shown in Fig. 2.1.

Fig. 2.1: Photographs of A) the four untreated plant byproducts: *teff* straw (TS), *enset* fiber (EF), sugarcane bagasse (SB) and coffee hull (CH) (from left to right), and B) respective cellulose (C2) extracted with extraction Condition B (optimum Condition).

Table 2.2 presents the composition of the untreated byproducts and the as-extracted celluloses (C2); namely, cellulose, hemicellulose, lignin contents and other materials. Cellulose percentage in the extracted materials was significantly higher than the respective byproducts as a result of the removal of lignin and hemicellulose after the three stages treatment. This is in agreement with previous studies (Alghooneh et al., 2017; Candido and Gonçalves, 2016). EF yielded the highest cellulose content (60.0%), followed by SB (39.5%), TS (36.7%) and CH (35.5%). TS contained comparable hemicellulose content as SB (~23%), but much higher than EF (~17%) and CH (~15%). The highest lignin content existed in the CH (~31%), and the lowest in EF (~13%). Accordingly, double bleaching was required for cellulose extraction from CH and consequently, its cellulose content was the lowest. It has been reported that alkaline treatment is very effective in increasing the digestibility of hardwood and agricultural residues with low lignin content (Abd El-Fattah et al., 2018). Evidently, the brightness and yield of CH cellulose were considerably higher when 70% FA and GAA (70:30) was used instead of NaOH in the preliminary work.

EF-C2 had the highest cellulose content (~95%), whereas CH-C2 contained the least (~80%). Furthermore, the cellulose contents of untreated SB and SB-C2 in the current study were comparable to the cellulose contents of untreated SB (40.6%) and extracted cellulose (89.2%) of a work reported elsewhere (Candido and Gonçalves, 2016).

2.3.2 Efficiency and conditions of the extraction method

There are different cellulose isolation methods such as steam explosion pretreatment (Sun et al., 2005), ultrasound-assisted extraction (Dinh Vu et al., 2017), mixed chemical and enzymatic extraction (Reddy and Yang, 2006), liquefaction (Meng et al., 2019b) and ionic liquid methods (Wang et al., 2011), among others.

In the cellulose extraction process, the alkaline treatment disrupts the cell wall by dissolving hemicellulose, lignin, and silica, by hydrolysing uronic and acetic acid esters, and by swelling the cellulose. Furthermore, the alkaline solution breaks alpha-ether bonds between lignin and hemicellulose and ester bonds between lignin and hydroxycinnamic acids such as p-coumaric acid and ferulic acid, fragments connecting lignin and hemicellulose (Abdel-Halim, 2014; Dinh Vu et al., 2017).

Table 2.2: Chemical composition of the four untreated plant byproducts and as-extracted cellulose (C2).

Plant materials		Composition (%w/w) on dry basis						
		Cellulose	**Hemicellulose**	**Klason lignin**	**Pectic matters**	**Fatty and waxy matters**	**Aqueous extractives**	**Ash**
Teff straw	0	36.7 ± 0.55	23.6 ± 0.88	19.5 ± 1.02	5.2 ± 0.34	5.1 ± 0.37	5.7 ± 0.07	4.3 ± 0.33
	C2	89.9 ± 0.50	4.6 ± 0.20	3.1 ± 0.06	0.3 ± 0.02	0.4 ± 0.01	2.2 ± 0.12	0.6 ± 0.01
Enset fiber	0	60.0 ± 1.25	18.5 ± 0.68	10.7 ± 0.65	1.4 ± 0.15	3.6 ± 0.14	4.0 ± 0.07	1.8 ± 0.15
	C2	95.7 ± 0.41	2.3 ± 0.18	0.7 ± 0.01	0.3 ± 0.01	0.2 ± 0.01	0.3 ± 0.02	0.7 ± 0.28
Sugarcane bagasse	0	39.5 ± 1.08	23.4 ± 1.24	21.0 ± 0.95	3.4 ± 0.22	5.1 ± 0.50	4.4 ± 0.56	3.2 ± 0.14
	C2	90.8 ± 0.58	4.0 ± 0.38	2.8 ± 0.16	0.7 ± 0.09	0.5 ± 0.01	0.6 ± 0.00	0.7 ± 0.01
Coffee hull	0	35.5 ± 1.80	14.8 ± 1.10	30.7 ± 0.36	6.2± 0.03	6.9 ± 0.20	4.5 ± 0.15	1.5 ± 0.06
	C2	79.9 ± 0.46	8.8 ± 0.03	7.9 ± 0.14	1.0 ± 0.05	0.9 ± 0.45	0.7 ± 0.01	1.0 ± 0.01

Key: 0-Raw (untreated byproduct); C2-Cellulose extracted with Condition B (optimum extraction Condition).

The delignification process is facilitated by the presence of H_2O_2 in organic acid solutions: formic acid (FA) and acetic acid (AA) (Watkins et al., 2015). The acids used in the process are relatively cheaper, eco-friendly, less corrosive and can be easily recovered by distillation and reused in the process when compared to mineral acids such as sulfuric acid (Ditzel et al., 2017; Jahan et al., 2011; Nuruddin et al., 2011). The combined effect of FA/AA/H_2O_2 is used as an oxidizing agent to dissolve the lignin. The OH^+ ion produced is a strong electrophilic agent which reacts with lignin to enhance the delignification process (Watkins et al., 2015).

Bleaching the mass with a solution of H_2O_2 in an alkali medium, a chlorine-free bleaching agent, is carried out to eliminate the chromophore compounds so as to enhance the whiteness of the cellulose, and reduce the residual chlorinated organic matters, which are important characteristics to produce cellulose derivatives. During bleaching, oxidation of lignin through cleavage of side chains occurs due to the formation of the perhydroxyl anion (OOH^-), a nucleophile intermediate. The action of radicals formed during the bleaching process is responsible to a large extent for the delignification. The bleaching with peroxide causes degradation of lignin molecules into smaller and water soluble parts (Watkins et al., 2015). Basically, the chromophore compounds constitute fragments of lignin. Therefore, it is expected that in this process mainly lignin is removed most, preserving the polysaccharides (Candido and Gonçalves, 2016).

In this study, extraction Condition B which employed 10% NaOH (in byproduct to liquor ratio of 1:10 (g/ml)) in the pretreatment stage, 20% FA/20% AA/7.5% H_2O_2 (2:1:2) for delignification, and 7.5% H_2O_2 in 4% NaOH for bleaching the materials was considered the 'optimum' condition based on the higher or comparable degree of crystallinity (Section 2.3.4), cellulose content and whiteness of the celluloses (C2) resulting from the treatment condition regardless of the sources of the cellulose, and used as a comparison.

With sequential decrease of the percentage ratio of FA/AA/H_2O_2 from 85%/100%/10% to 40%/40%/10% and then to 20%/20%/7.5% in the preliminary work, no significant change was observed in the cellulose content, crystallinity and whiteness. However, when the percentage of FA/AA/H_2O_2 was lower than 20%/20%/7.5%, or one of the acids was removed, the cellulose content, crystallinity and color were all negatively affected. Hence, the percentage ratio of FA/AA/H_2O_2 was fixed at 20%/20%/7.5% (2:1:2) in Stage II for optimizing other extraction conditions.

The extraction method employed in this study takes approximately 4 h. This is significantly shorter than many other extraction methods that range from 10.5-20 h (Abd El-Fattah et al., 2018; Naceur Abouloula et al., 2018; Nazir et al., 2013). The method is also desirable as it employs less-corrosive reagents and a chlorine-free extraction technique.

2.3.3 Chemical functionality

The FTIR spectra of the untreated byproducts and the as-extracted celluloses (C2) are shown in Fig. 2.2. All the samples displayed two main regions: at high wave numbers (2800–3500 cm^{-1}) and low wave numbers (500–1700 cm^{-1}), respectively. Furthermore, the figure shows similarities in the spectra indicating similar chemical compositions of the samples.

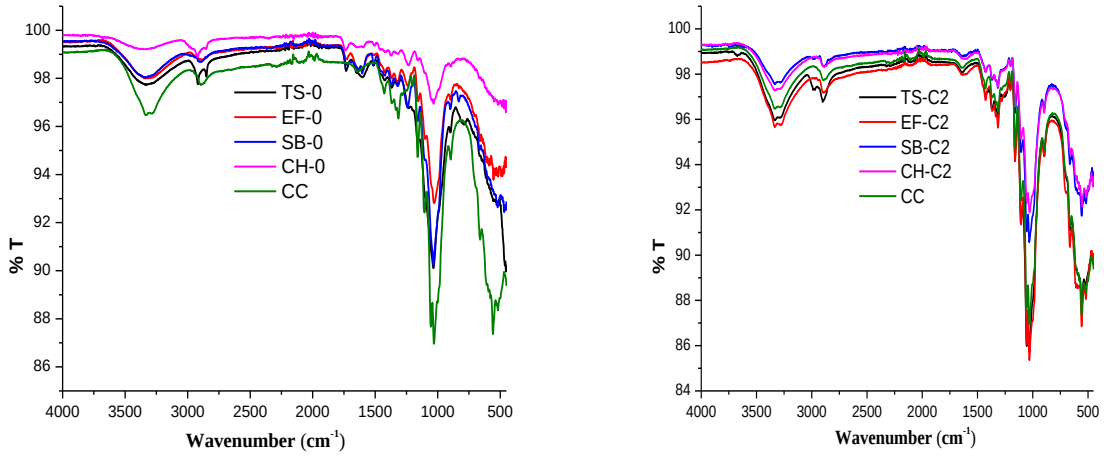

Fig. 2.2: FTIR spectra of the four untreated plant byproducts (left), and the corresponding celluloses (C2) extracted with Condition B (optimum Extraction) (right). (Key: 0-untreated plant byproduct; TS-*teff* straw; EF-*enset* fiber; SB-sugarcane bagasse; CH-coffee hull; CC-commercial cellulose included for comparison).

The broad band around 3338 cm^{-1} represents the stretching vibration of OH which contributes to the formation of hydrogen bonds in the polyhydroxylated saccharide backbone, and the weak band around 2907 cm^{-1} is attributed to the asymmetric stretching vibration of CH in hemicellulose, lignin and each glucose unit of cellulose (Tarchoun et al., 2019).

A band around 1425 cm^{-1} is related to CH and CH_2 bending. The peak around 1323 cm^{-1} region of the spectra is due to the in-plane bending vibration of the CH and C-O groups of the hexose ring

in the cellulose. The peak around 896 cm^{-1} is related to glycosidic C_1H deformation, a ring vibration, and OH bending where these characters infer the β-glycosidic linkages between anhydroglucose units. The increase in peak intensity at 1030 cm^{-1} reveals that the cellulose content of the material increases as a result of the various chemical treatments. The transmittance peaks around 3338, 2907, 1425, 1323, 896 cm^{-1} are associated with the characteristics of native Cellulose I as seen in all cellulose spectra, except for EF-C4 and SB-C4, showing chemical similarity and, therefore, the treatment stages did not affect the chemical structure of the cellulosic fragments (Mohamad Haafiz et al., 2013; Veeramachineni et al., 2016; Yang et al., 2007). However, intense double peaks appeared in EF-C4 and SB-C4 around 2900 cm^{-1} where higher alkaline condition was used, suggesting formation of Cellulose II. The FTIR spectra of as-extracted cellulose (C1, C3 and C4) are shown in Fig. 2.3.

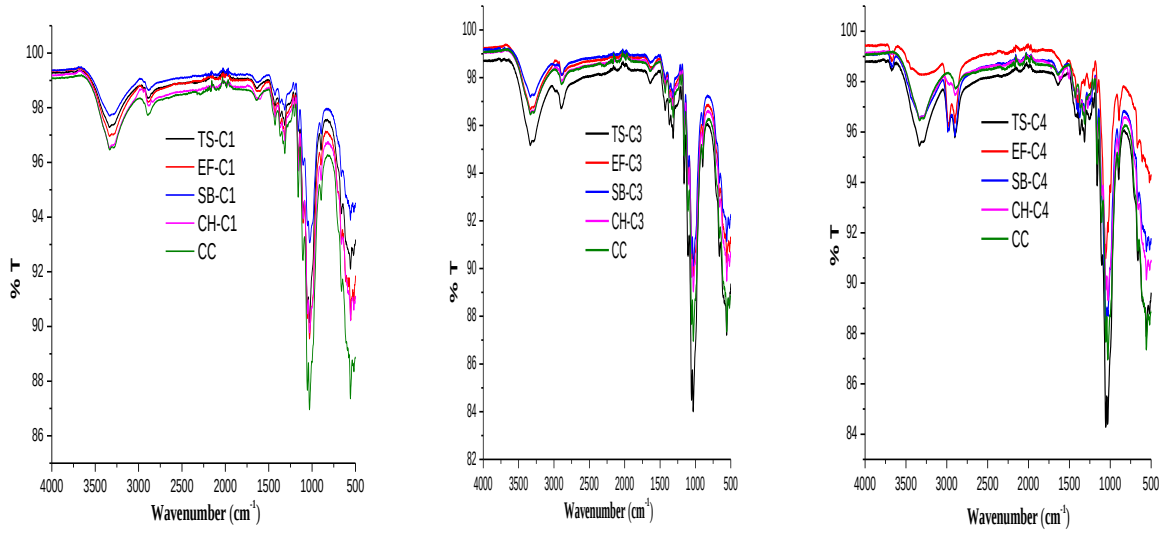

Fig. 2.3: FTIR spectra of extracted cellulose C1 (left) following extraction Condition A; C3 (middle) following Condition C, C4 following extraction Condition D (right), and CC. (Key: TS-*teff* straw; EF-*enset* fiber; SB-sugarcane bagasse; CH-coffee hull; CC-commercial cellulose included for comparison).

Unlike the spectra of the extracted celluloses, the untreated plant byproducts showed characteristic peaks around 1736 cm^{-1}, 1516 cm^{-1}, and 1235 cm^{-1}. The peak around 1736 cm^{-1} is due to the acetyl and uronic ester groups of hemicellulose, and indicates the linkages between ferulic acid or p-coumaric acid or (p-) hydroxycinnamic acids and lignin. The dissociation of the key ester linkages between lignin and carbohydrates leads to the dissolution of lignin into the solvents. The bands

around 1516 cm^{-1} and 1235 cm^{-1} indicate lignin functional groups such as aromatic rings. The characteristic bands of lignin (1516, 1235 cm^{-1}) were absent in the spectra of the extracted celluloses, suggesting removal of lignin from the byproducts. Similar findings were also reported by different research groups indicating removal of non-cellulosic materials using different treatment conditions (Abdel-Halim, 2014; Alghooneh et al., 2017; Jahan et al., 2011; Rosa et al., 2010; Tarchoun et al., 2019; Xie et al., 2016).

2.3.4 Crystallinity

The X-ray diffractograms of the untreated byproducts (TS-0, EF-0, SB-0 and CH-0) and celluloses (C2) are shown in Fig. 2.4. Parameters obtained from the (deconvoluted) XRD of the untreated byproducts and as-extracted celluloses are given in Table 2.3.

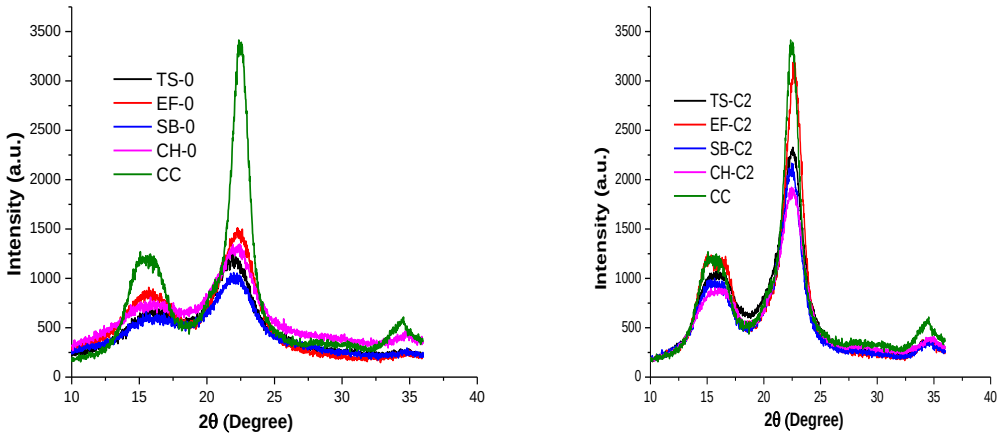

Fig. 2.4: X-ray diffractograms of the four untreated plant byproducts (left) and cellulose (C2) extracted with Condition B (optimum Extraction) (right) and CC. (Key: 0-untreated plant byproduct; TS-*teff* straw; EF-*enset* fiber; SB-sugarcane bagasse; CH-coffee hull; CC-commercial cellulose included for comparison).

Table 2.3: Parameters obtained from the (deconvoluted) XRD of the four untreated plant byproducts (TS-*teff* straw; EF-*enset* fiber; SB-sugarcane bagasse; CH-coffee hull; as-extracted cellulose (C1, C2, C3 and C4), and CC.

Materials	d-spacings (nm)				τ_{200} (nm)	X_{200}	$\Delta d/d_{200}$	CrI (SM) (%)	Z-Values
	$1\bar{1}0$	110	200	400					
TS-0	0.591	0.543	0.405	0.271	2.512	0.298	0.1515	58.95	-37.67
TS-C1	0.577	0.557	0.394	0.257	2.922	0.372	0.1268	73.90	-74.22
TS-C2	0.608	0.562	0.395	0.257	3.689	0.477	0.1006	78.00	-27.64
TS-C3	0.608	0.548	0.394	0.259	2.966	0.379	0.1250	76.73	-13.81
TS-C4	0.732	0.563	0.396	0.259	2.935	0.374	0.1269	74.13	182.95
EF-0	0.592	0.569	0.399	0.264	2.925	0.372	0.1282	66.44	-60.66
EF-C1	0.580	0.559	0.392	0.270	3.973	0.509	0.0928	77.78	-50.54
EF-C2	0.587	0.544	0.392	0.260	5.515	0.629	0.0668	85.56	-45.84
EF-C3	0.716	0.560	0.403	0.263	4.582	0.564	0.0826	80.67	158.42
EF-C4	0.716	0.560	0.401	0.258	4.091	0.520	0.0920	76.42	156.88
SB-0	0.575	0.567	0.403	0.266	3.024	0.388	0.1252	55.77	-87.31
SB-C1	0.559	0.558	0.396	0.260	3.600	0.467	0.1035	72.90	-105.00
SB-C2	0.582	0.542	0.395	0.259	3.939	0.505	0.0944	80.92	-52.41
SB-C3	0.600	0.543	0.397	0.260	3.926	0.504	0.0950	78.86	-22.92
SB-C4	0.731	0.547	0.394	0.257	3.881	0.499	0.0954	77.32	195.85
CH-0	0.598	0.566	0.402	0.262	2.471	0.290	0.1528	55.87	-47.17
CH-C1	0.606	0.560	0.397	0.259	3.618	0.469	0.1031	74.87	-49.29
CH-C2	0.609	0.554	0.394	0.261	3.946	0.506	0.0938	77.59	-16.75
CH-C3	0.609	0.538	0.395	0.259	3.931	0.504	0.0944	74.43	-2.28
CH-C4	0.613	0.539	0.397	0.261	3.483	0.453	0.1071	66.41	2.48
CC	0.608	0.554	0.395	0.260	6.480	0.679	0.0573	87.23	-19.85

Key: 0-Raw (untreated byproduct); C2-Cellulose extracted with Condition B(optimum extraction Condition); C3 and C4-Cellulose extracted using Condition C and D at higher alkaline condition, respectively; CC-commercial cellulose included for comparison; d-the interplanar spacing of the crystal; τ_{200}-average thickness of cellulose crystallites; X_{200}-the proportion of crystallite interior chains for the 200 plane; $\Delta d/d_{200}$-the fractional variation in the plane spacing for the 200 plane; CrI (SM)-crystallinity index following Segal's et al. method.

Increasing the concentration of NaOH from 5% to 10% in the pretreatment stage of all byproducts significantly enhanced the degree of crystallinity of the extracted celluloses (Table 2.3). Such enhancement of crystallinity was due to the removal of hemicellulose and lignin existing in the amorphous regions, leading to the realignment of the cellulose molecules (Veeramachineni et al., 2016).

The approaches by Segal *et al.* and Herman *et al.* were employed for the determination of CrI (Poletto et al., 2014; Segal et al., 1959). The CrI for SB-C4, however, was estimated following

only the Segal *et al.* approach as the peaks could not fit accurately on deconvolution for the estimation of the (total) area under the peaks with Herman *et al*. approach. It was observed that the Segal *et al.* approach exhibited higher values of CrI than Herman *et al.* approach for the same plant materials. Both methods indicated the removal of non-cellulosic materials from the extracted celluloses, as confirmed by the increase in the respective CrI (Fig. 2.5). The Segal *et al.* and Herman *et al.* approaches showed the highest CrI in EF-C2 (85.56%; 66.74%), and the least was observed in CH-C2 (77.90%; 57.81%), respectively. In the literature, the Segal *et al.* approach is most frequently used to estimate CrI, since it is a simple approach providing useful information (Aguayo et al., 2018; Naduparambath and Purushothaman, 2016; Prado and Spinacé, 2019; Taflick et al., 2017).

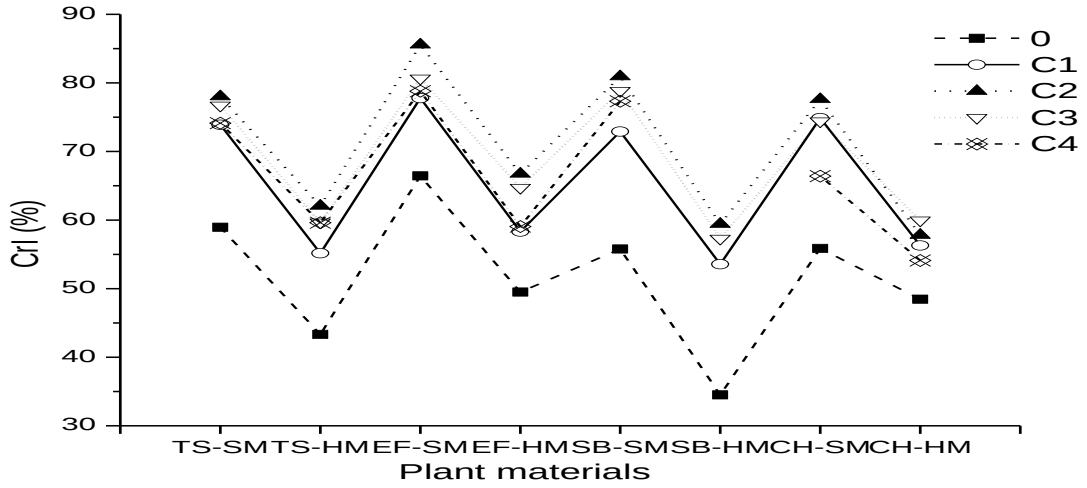

Fig. 2.5: Comparison of Segal's et al (SM) and Herman's et al (HM) methods for estimation of CrI of the plant materials. (Key: 0-Untreated plant byproducts; C1, C2, C3 and C4-Cellulose extracted using extraction Conditions A, B, C and D, respectively; TS-*teff* straw; EF-*enset* fiber; SB-sugarcane bagasse; CH-coffee hull; CrI - crystallinity index).

The CrI of all celluloses (C2) (77.90%-85.56%) in this study were higher than those reported elsewhere using Segal *et al.* approach for other biomasses such as *Posidonia oceanica* brown algae (60.50%) (Tarchoun et al., 2019), apple pomace (67%) (Melikoğlu et al., 2019), potato pulp (62.54%) (Cheng et al., 2019), corn stalk (77.45%) (Reddy and Yang, 2005), wheat straw (57.85%) (Tsegaye et al., 2019), and *Ulva lactuca* cellulose (59%) and Avicel® (82%) (Jmel et al., 2019).

Cellulose may consist of several types of polymorphs (namely I_α, I_β, II, III, and IV cellulose) depending on the origin of cellulose and the type of chemicals used in the treatments (Alghooneh et al., 2017). The peak intensities and CrI are different from one plant source to another. After deconvolution, all XRD patterns showed ~15°, ~16°, ~22°, ~34° 2θ with assigned crystallographic plane of $1\bar{1}0$, 110, 200 and 400, respectively, of Cellulose I, except for celluloses extracted in higher alkaline conditions which suggested formation of Cellulose II. The sharpness of the diffraction peak around 22° for all Cellulose I forms indicates an increase in crystallinity. The more pronounced difference occurs around the peak 200 plane 2θ reflection (Tarchoun et al., 2019; Veeramachineni et al., 2016; Xie et al., 2016). The absence of any peak around 29° 2θ in all materials of this study showed nil or minimal mineral impurities like silica and weddellite.

The increment of the τ and X-values in the celluloses (C2) is due to decreased chain mobility permitting a lower percentage of the chains to move into the perfect register of the crystals (Table 2.3) (Newman, 1999; Popescu et al., 2011). Subsequently, the cellulose content and the CrI increased because of the reduction of amorphous cellulose regions (Kim et al., 2010). The results indicate that EF-C2 contained the most ordered cellulose structure when compared to other extracted celluloses. This can lead to higher hydrogen bond intensity among neighboring cellulose chains resulting in a more packed cellulose structure besides higher crystallinity. However, the τ and X-values and cellulose content were reduced in Cellulose II of EF-C3, C4 and SB-C3, due to the polymorphic transition in higher alkaline conditions which decreased the crystallinity of the celluloses and increased the exposure of the cellulose chains (Table 2.3). A similar finding was reported in regenerated cellulose film from a solution in lithium bromide molten salt hydrate indicating the transformation of Cellulose I to Cellulose II (Zhang et al., 2018).

A greater value of the fractional variation, a measurement for the dispersion of the crystalline plane values, shows higher microstresses. All the as-extracted celluloses (C2) of this study had lower fractional variations. It was also reported that smaller crystallite sizes are associated with a high fractional variation in its interplanar distance (Aguayo et al., 2018).

The d-spacings of the Cellulose I of the plant materials ranged from 0.575-0.613 (except for EF-C3, EF-C4, SB-C4 and TS-C4 which ranged from 0.716-0.732), 0.538-0.569, 0.392-0.405, and 0.257-0.266 for the planes of $1\bar{1}0$, 110, 200, and 400, respectively (Table 2.3). Three lattice planes with approximate d-spacings of 0.39 nm, 0.53 nm and 0.61 nm correspond to the I_α lattice planes

(110), (010), and (100) for the triclinic structure, and to the I_β lattice planes (200), (110) and ($1\bar{1}0$) for the monoclinic structure, which is in line with cellulose (C2) indicating the cellulose extracted with the optimum Condition B is I_β type (Table 2.3) (Poletto et al., 2013; Wada and Okano, 2001). This is further substantiated by the negative numbers of the Z-Values, except the celluloses extracted following Condition D (C4) (Table 2.3) (Kim et al., 2010; Poletto et al., 2012). It is usually possible to categorize cellulose as belonging to the I_α or I_β predominant form. The Z-value indicates whether Cellulose is I_α or I_β. When Z>0, it indicates that the Cellulose is rich in the I_α form and when Z<0, it indicates that I_β is the predominant form (Poletto et al., 2014). The XRD of the extracted celluloses (C1, C3 and C4) are given in Fig. 2.6.

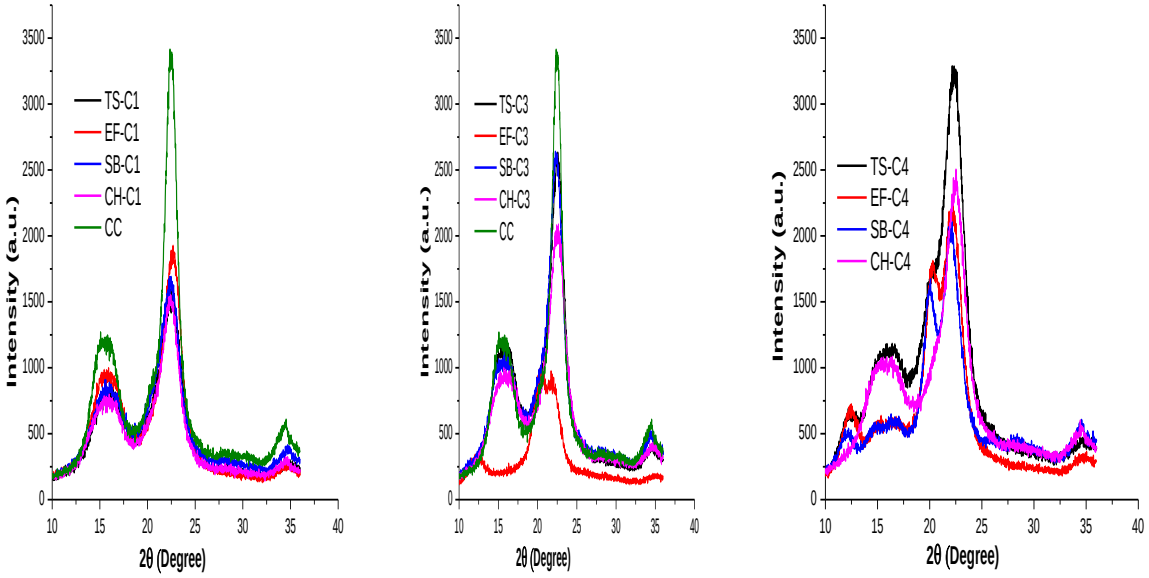

Fig. 2.6: X-ray diffractograms of extracted cellulose C1 (left) following extraction Condition A; C3 (middle) following Condition C, C4 following extraction Condition D (right), and CC. (Key: TS-*teff* straw; EF-*enset* fiber; SB-sugarcane bagasse; CH-coffee hull; CC-commercial cellulose included for comparison).

The τ values ranged from 2.512 nm for TS-0 to 5.52 nm for EF-C2, and respective X values ranged from 0.298 for TS-0 to 0.629 for EF-C2. Elsewhere, it has been reported the τ values ranged from 2.6 nm for *Asplenium* frond fiber to 7.8 nm for cotton fabric (Newman, 1999). The celluloses (C2) had higher τ and X values when compared to untreated byproducts and other extracted celluloses.

Appearance of doublet in the main peak around 22° 2θ of the diffractograms of EF-C3, EF-C4 and SB-C4 indicates polymorphic transformation due to the chemical treatment and (partial) formation of Cellulose II (Fig. 2.7). The XRD patterns of EF-C3, EF-C4 and SB-C4, exhibit three sharp high diffraction peaks at around 12.0°, 20.0° and 22.0° 2θ for the plane indices of $(1\bar{1}0)$, (110) and (200), respectively, which were assigned to Cellulose II (Gong et al., 2018; Xing et al., 2018), where a complete formation of Cellulose II was observed in EF-C3. By increasing the alkaline condition in EF-C3, EF-C4 and SB-C4, the intermolecular bonds are weakened by swelling and penetration of sodium hydrates inside the cellulose fiber matrix. This leads to the realignment and complete recrystallization of celluloses to break the already existing intermolecular chain links to produce new crystalline lattice structures, due to rearrangement resulting from the swelling and decrystallization of intra and intermolecular bonds of the cellulose lattice structures. Similarly, it has been reported that there is a shift in the main peak of original cellulose to a Cellulose II structure for the fibers treated with 17.5% NaOH, and the highest CrI was observed when 5% NaOH was used (Soyekwo et al., 2016), which is contrary to our finding where highest CrIs were obtained using 10% NaOH.

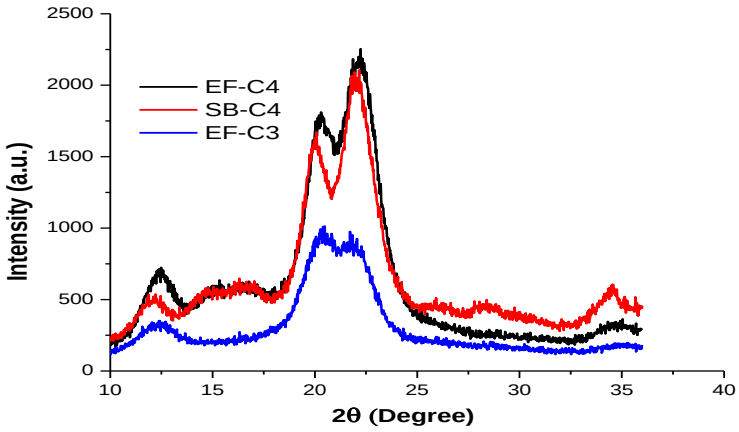

Fig. 2.7: X-ray diffractograms of Cellulose II of EF-C3, and Cellulose I and II allomorphs of EF-C4 and SB-C4. (Key: EF-C3 and EF-C4--Cellulose extracted from *enset* fiber following extraction Conditions C and D, respectively; SB-C4—Cellulose from sugarcane bagasse following extraction Condition D; Cellulose II—Cellulose with antiparallel chains).

2.3.5 Thermal stability

The untreated plant byproducts, and as-extracted celluloses were thermogravimetrically analyzed and compared with the degradation characteristics of CC. The as-extracted cellulose samples

presented three weight loss regions, as shown in Figs. 2.8, 2.9 and Table 2.4. The initial weight loss (3 to 9%) in the region 29–130 °C is mainly due to moisture evaporation; loss of water adsorbed to the plant materials. The extracted celluloses contained relatively lower moisture when compared to their respective untreated byproducts as shown in Table 2.4, due to the removal of hemicellulose and lignin. Elsewhere, it has also been suggested that hemicellulose, lignin, and other non-cellulosic components of untreated byproducts are hydrophilic in nature, which help to maintain high amounts of moisture (Nuruddin et al., 2016).

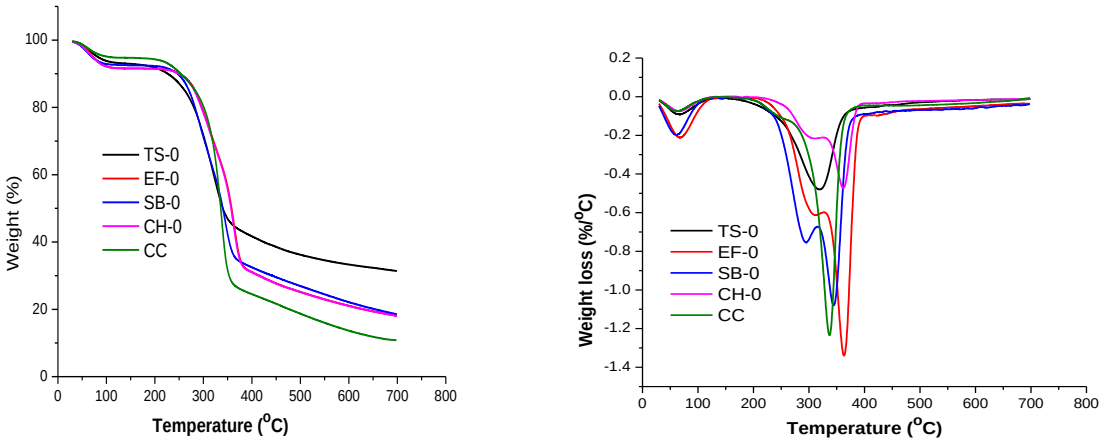

Fig. 2.8: Thermal degradation behaviors: TGA (left) and DTG (right) of the four untreated byproducts, and CC. (Key: 0-untreated plant byproduct; TS-*teff* straw; EF-*enset* fiber; SB-sugarcane bagasse; CH-coffee hull; CC-commercial cellulose included for comparison).

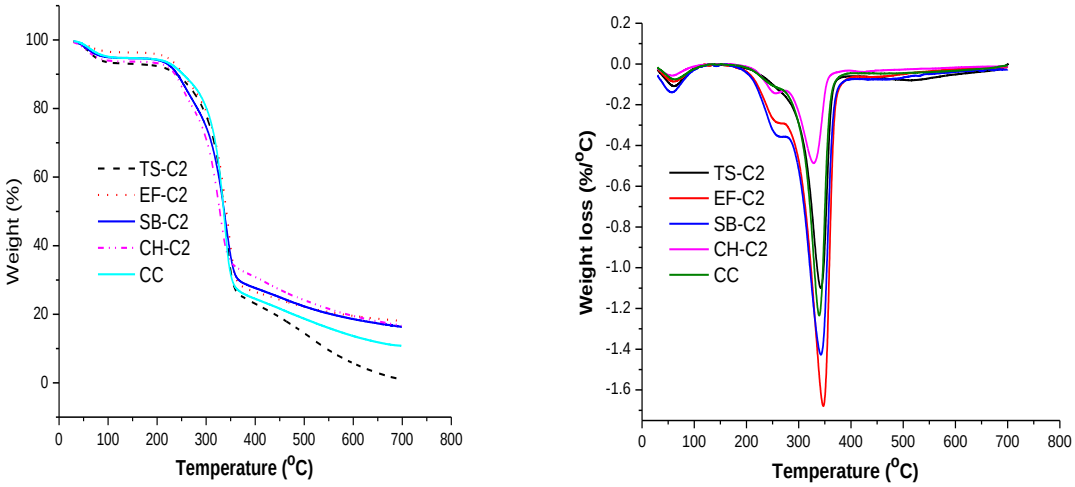

Fig. 2.9: Thermal degradation behaviors: TGA (left) and DTG (right) of cellulose (C2) extracted with Condition B (optimum Condition), and CC. (Key: TS-*teff* straw; EF-*enset* fiber; SB-sugarcane bagasse; CH-coffee hull; CC-commercial cellulose included for comparison).

Table 2.4: Summary of thermogravimetric characteristics of TGA and DTG of the four plant byproducts, respective celluloses (C2), and CC.

Material	ΔT (°C)	T_{max} (°C)	Weight loss (%)	Weight loss rate (%/°C)	T_i (°C)	Residue at 550 °C (%)	Residue at 700 °C (%)
TS-0	30.16-109.04	69.54	9.24	0.0916	203.37	34.62	31.40
	203.37-375.47	321.29	44.44	0.4800			
	375.47-550.00	452.31	8.99	0.0433			
TS-C2	29.70-109.04	61.69	6.25	0.1081	207.15	9.73	1.16
	207.15-390.23	342.88	47.52	1.0979			
	390.23-550.00	517.18	14.11	0.0797			
EF-0	29.78-116.41	69.22	6.20	0.2108	234.16	23.03	18.09
	234.16-329.74	309.04	23.82	0.6088			
	333.86-400.32	365.05	34.21	1.3340			
	400.32-550.00	423.51	7.92	0.0996			
EF-C2	29.99-121.38	65.62	3.15	0.0846	210.43	20.66	18.07
	210.43-400.22	346.67	69.04	1.6778			
	400.22-550.00	438.86	5.81	0.0637			
SB-0	29.72-107.45	60.78	6.79	0.1979	215.69	24.47	18.57
	215.69-311.53	293.41	26.37	0.7515			
	315.53-392.42	345.44	30.84	1.0791			
	392.42-550.00	447.63	6.37	0.0797			
SB-C2	29.72-125.25	57.64	4.85	0.1382	199.76	20.26	16.31
	199.76-399.47	340.68	66.59	1.4264			
	399.47-550.00	469.58	7.40	0.0759			
CH-0	29.77-120.56	67.26	7.92	0.0746	245.05	22.91	18.03
	245.05-330.94	300.45	24.96	0.2082			
	330.94-399.46	361.67	34.33	0.4730			
	399.46-550.00	421.55	11.43	0.0350			
CH-C2	29.77-109.00	56.35	5.48	0.0568	282.45	21.56	16.61
	282.45-390.20	327.57	46.24	0.4862			
	390.20-550.00	423.13	9.91	0.0392			
CC	30.16-108.49	62.60	4.70	0.0749	268.93	15.91	10.81
	268.93-378.50	338.76	62.20	1.2165			
	378.50-550.00	463.49	9.85	0.0470			

Key:-ΔT-Temperature change where main weight loss occurs; T_{max}-Maximum degradation (maximum weight loss)temperature; T_i-Initial degradation temperature (Onset temperature); TGA-Thermogravimetric analysis; DTG-Differential thermogravimetry; 0-Raw (untreated byproduct); C2-Cellulose extracted with extraction Condition B (optimum Condition); TS-*teff* straw; EF-*enset* fiber; SB-sugarcane bagasse; CH-coffee hull; CC-commercial cellulose included for comparison.

The differential thermogravimetry (DTG) thermograms of the untreated products show two degradation peaks (Fig. 2.8). A sudden reduction in weight loss in all thermograms of the materials occurred between 192-284 °C, mainly due to the loss of hemicellulose. The low thermal stability of hemicellulose is due to the presence of acetyl groups. The degradation of hemicellulose was more visible in the untreated byproducts of EF and SB at 309.04 °C and 293.41 °C, respectively. A second and more pronounced weight loss was observed between 320-400 °C due to the main degradation of cellulose (Flauzino Neto et al., 2013; Poletto et al., 2012). The major cellulosic chain degradation is due to several steps such as depolymerisation, dehydration and decomposition of the glycosidic units (Bano and Negi, 2017).

On the contrary, peak(s) corresponding to lignin did not appear in any of the untreated plant byproducts even in CH, where the lignin content was very high (Fig. 2.8). This could be due to the slow and resistant decomposition of lignin which results in poorly identifiable peaks in the TGA/DTG thermograms (Melikoğlu et al., 2019; Meng et al., 2019b; Poletto et al., 2012; Yang et al., 2007). Yang *et al*. investigated the degradation behaviors of commercial lignin, hemicellulose and cellulose separately, and reported significant differences among them. As lignin is the most difficult component to decompose, its decomposition ranged from ambient temperature to 900 °C, but at a very low mass loss rate (<0.14 %/°C) and highest residue (45.7%), and no peak was observed in the DTG curve unlike for hemicellulose and cellulose (Yang et al., 2007). Elsewhere, it was also reported that commercial lignin decomposition ranged from 200-700 °C (Morán et al., 2008). However, Kaushik and Singh reported a small identifiable tail peak at 343 °C (mass loss 30%) which attributed to the degradation of wheat straw lignin (Kaushik and Singh, 2011), and Watkins *et al*. also reported the maximum degradation temperature (T_{max}) appeared between 320 and 340 °C for all lignin samples obtained from flax fiber, alfalfa, pine straw and wheat straw (Watkins et al., 2015).

The higher thermal stability of the celluloses (C2) of each byproduct is related to its higher crystallinity. The T_{max} of the as-extracted celluloses (C2) ranged from 327-357 °C. The weight loss rate of the as-extracted celluloses in the cellulose degradation region ranged from 0.4627 %/°C for CH-C4 (at 327.73 °C) to 1.6778 %/°C for EF-C2 (at 346.67 °C). The residual mass of all untreated byproducts at 700 °C was higher than the respective extracted celluloses due to the inorganic impurities. The different thermal behaviors were possibly due to differences in the inherent

structures and chemical nature of the four plant byproducts and as-extracted celluloses. The thermal degradation behaviors of the as-extracted celluloses (C1, C3 and C4) are displayed in the Supplemental material (Fig. 2.10).

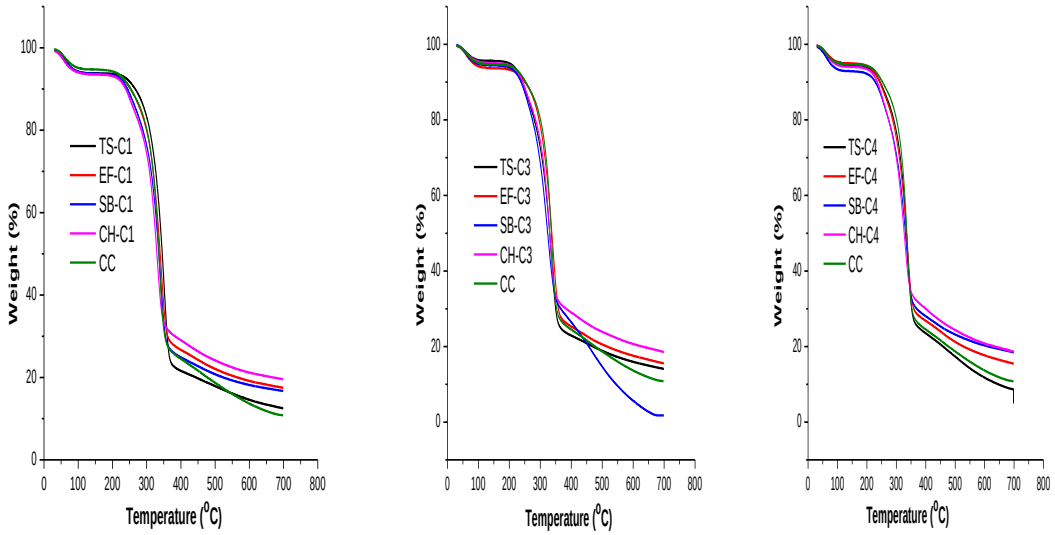

Fig. 2.10: TGA curves for cellulose C1 (left) following extraction Condition A; C3 (middle) following Condition C, C4 following extraction Condition D (right), and CC. (Key: TS-*teff* straw; EF-*enset* fiber; SB-sugarcane bagasse; CH-coffee hull; CC-commercial cellulose included for comparison).

2.3.6 Morphological properties

The morphological analysis of the ESEM images reveals that the untreated byproducts exhibit rough and compact fibrillar packing while the extracted celluloses (C2) exhibit smaller and isolated fibrils following the dissolution of non-cellulosic materials and removal of fatty and waxy matters, pectins, hemicellulose and lignin (Figs. 2.11 and 2.12). Other studies also reported the removal of non-cellulosic and cementing materials such as hemicelluloses, lignin, and wax during treatment of lignocellulosic materials using different chemicals for extraction of isolated fibrils of cellulose (Deepa et al., 2011; Nazir et al., 2013).

The average diameters of the cellulose microfibrils as well as the untreated byproducts are shown in Table 2.5. The diameters of the untreated plant byproducts ranged from 160 μm (TS-0) to 965 μm (CH-0), showing that CH-0 exists as the most compact structure when compared to other

untreated byproducts. The diameters of the as-extracted celluloses were found to be significantly smaller (6–24 μm) than the respective untreated plant byproducts, indicating the removal of non-cellulosic components during the treatment conditions. The as-extracted celluloses (C2) obtained from CH had the highest diameter (24 μm); and the least was recorded for TS-C2 (6 μm). Moran *et al*. reported the diameter of untreated sisal fibers ranged from 100–500 μm and the fiber diameter was reduced to 7–31 μm in the extracted cellulose (Morán et al., 2008). In another study, untreated banana pseudostem presented rough longitudinal surface and relatively intact structures, with a diameter of 83.3 ± 4.4 μm. Cellulose fibers with a diameter of 5.5–7.2 μm and rough surfaces were isolated from the banana pseudostem (Meng et al., 2019b). The average diameters of cellulose microfibrils obtained from dhaincha, rice straw, wheat straw and corn stalks were reported to be 6.8, 8.7,9.3 and 6.6 μm, respectively (Nuruddin et al., 2011).

Table 2.5: Average diameters of the four untreated plant byproducts, the respective as-extracted celluloses (C2), and CC.

Samples	**Diameters average (μm)**				
	TS	**EF**	**SB**	**CH**	**CC**
Untreated byproducts (0)	160.38 ± 53.65	258.80 ± 19.38	213.02 ± 14.82	964.99 ± 120.23	--
As-extracted cellulose (C2)/CC	6.389 ± 2.24	13.37 ± 2.45	19.19 ± 5.18	24.06 ± 7.37	11.93 ± 3.08

Key: 0-Raw (untreated plant byproducts); C2-Cellulose extracted with extraction Condition B (optimum Condition); TS-*teff* straw; EF-*enset* fiber; SB-sugarcane bagasse; CH-coffee hull; CC-commercial cellulose included for comparison. NB: ImageJ Software was used for the determination of the (average) diameters.

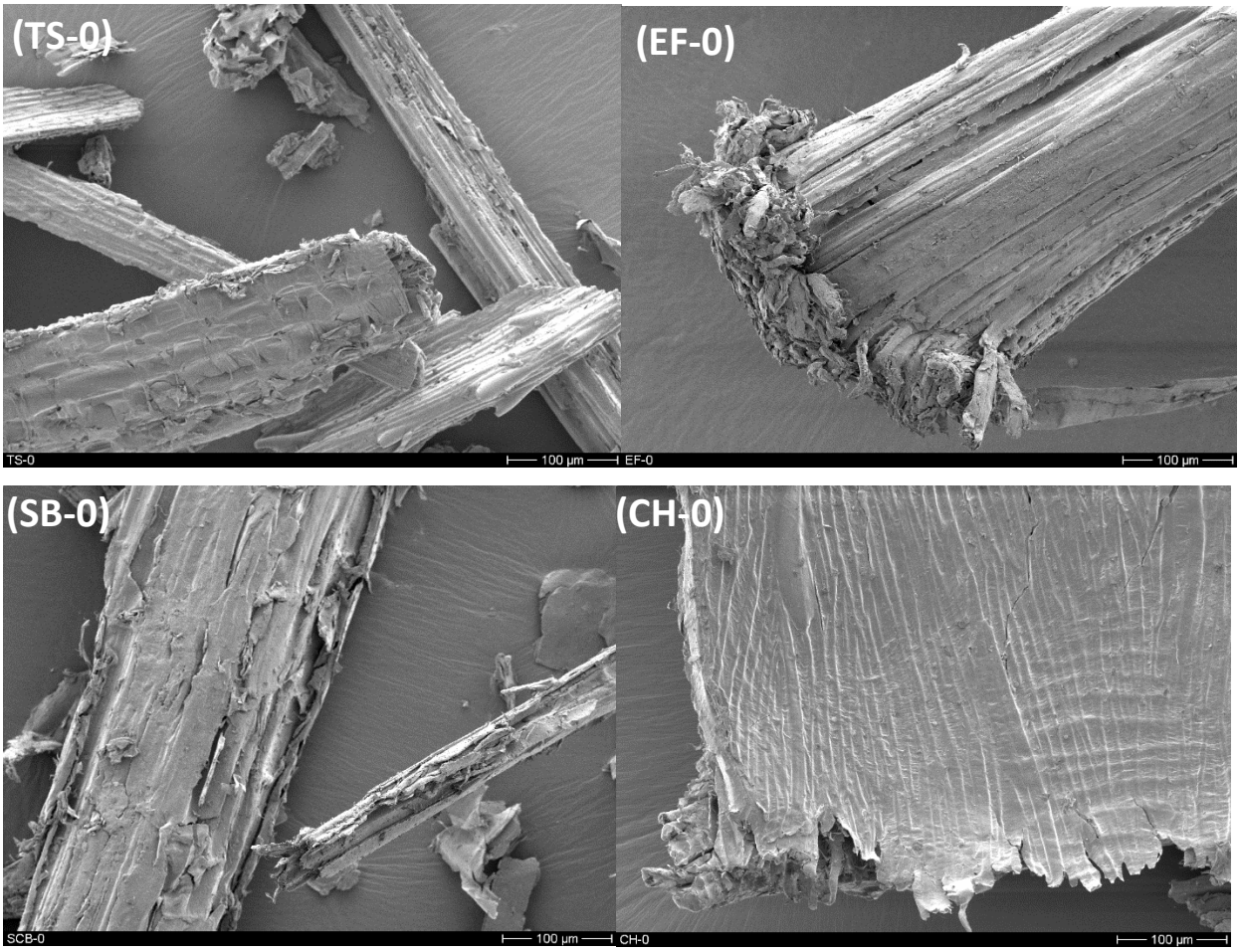

Fig. 2.11: Scanning electron micrographs of untreated plant byproducts with a scale bar of 100 µm (Key: TS-*teff* straw; EF-*enset* fiber; SB-sugarcane bagasse; CH-coffee hull).

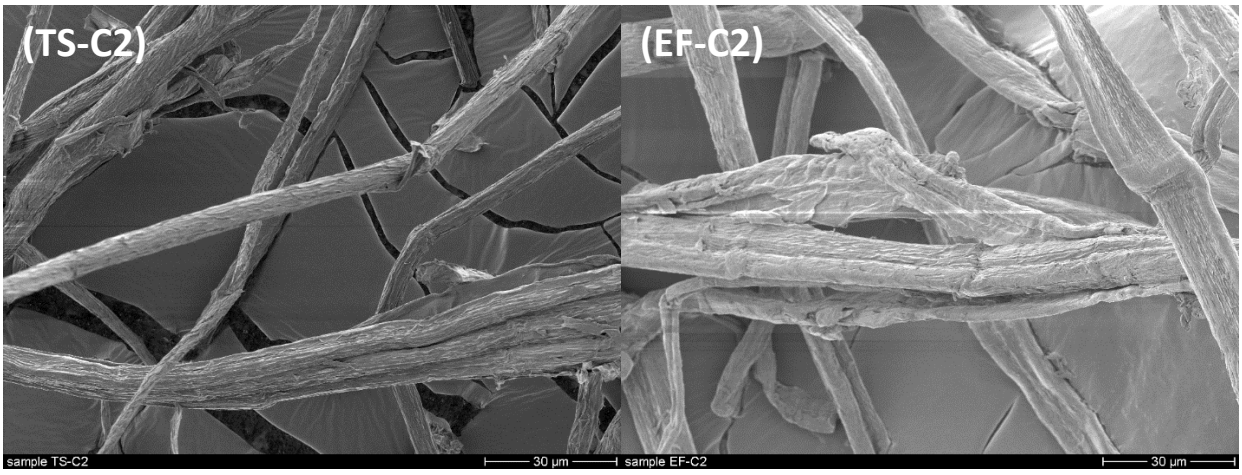

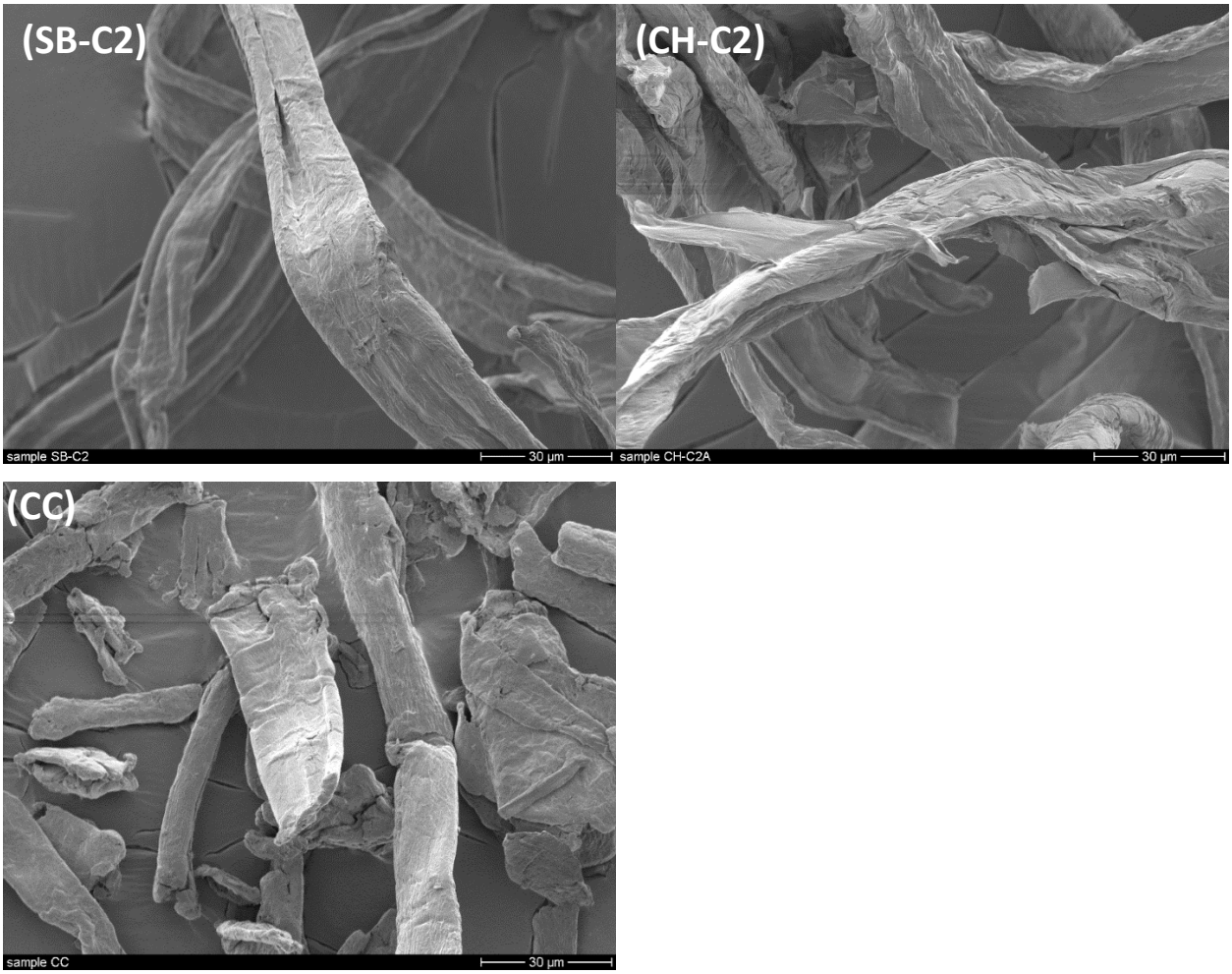

Fig. 2.12: Scanning electron micrographs of as-extracted cellulose (C2) using Condition B (optimum Condition), and CC with a scale bar of 30 µm. (Key: TS-*teff* straw; EF-*enset* fiber; SB-sugarcane bagasse; CH-coffee hull; CC-commercial cellulose included for comparison).

2.4 Conclusion

Celluloses were isolated from four plant byproducts; namely, TS, EF, SB and CH using eco-friendly and chlorine-free method, and optimum extraction conditions. EF yielded the highest cellulose content, and CH the lowest. The FTIR spectra of the extracted celluloses were significantly different from those of the untreated byproducts, confirming removal of hemicellulose and lignin upon successive chemical treatment. The XRD spectra of the celluloses exhibited the characteristic peaks of Cellulose I_β around 15, 16, 22 and 34^o 2θ, as confirmed by the d-spacings and Z-values. Highest CrI was observed in the cellulose extracted from EF (85.56 %). The CrI increased in all celluloses as the NaOH concentration increased from 5% to 10% in the extraction medium. Further increase in NaOH concentration, however, caused (partial) polymorphic transition of Cellulose I to Cellulose II in EF-C3, EF-C4 and SB-C4; which was evidently dependent on both the source of the cellulose and the alkaline condition. Morphological studies revealed that there was dissolution of non-cellulosic materials to form separate smaller fibrils of cellulose. In general, the physicochemical properties of the extracted celluloses were dependent on the source of cellulose and treatment conditions. From the foregoing, it is apparent that the byproducts could be potential sources of cellulose that can find various value-added industrial applications.

3 Isolation and characterization of cellulose nanocrystals from different lignocellulosic residues: A comparative study

3.1 Introduction

Cellulose, the most abundant polysaccharide on Earth, is the biosynthetic product from plants, animals, or bacteria. Because of its unique properties such as abundance, biodegradability, cost effectiveness, light weight, high tensile strength and stiffness, cellulose is widely used in various industries (El Achaby et al., 2018; Poletto et al., 2014).

Woody plants and cotton are the major sources of cellulose and cellulose derivatives for different industrial applications mainly in pharmaceutical, textile, energy and paper industries, but different factors such as economic and environmental concerns have forced researchers and stakeholders to look for other potential substitutes (Adel et al., 2011). Additionally, it is reported that agro-industrial fibers have low cost, huge availability, and are easy to collect and are attractive alternative materials to wood, cotton, and linter (Nascimento et al., 2016).

Nanocelluloses are natural materials with defined nano-scale structural dimensions. The three main classes of nanocelluloses are a) CNCs, also referred to as nanocrystalline cellulose and cellulose nanowhiskers, b) cellulose nanofibrils, also referred to as nano-fibrillated cellulose, and c) bacterial cellulose (Abitbol et al., 2016; Klemm et al., 2018).

CNCs are biopolymeric materials with diameter of 5-30 nm and length of 100-500 nm having needle- or rod-like crystal structure. CNCs have unique physicochemical properties such as higher surface area, reactive hydroxyl group in the surface, biocompatibility, etc. Consequently, CNCs have captured the interest of researchers and industries as they are suitable for many advanced functional applications such as tissue engineering, drug delivery, reinforcement of composite materials, template for nanomaterial synthesis, protein or enzyme immobilization, emulsion stabilizer, etc (Abitbol et al., 2016; Wijaya et al., 2017).

CNCs have been isolated from different lignocellulosic resources such as cotton gin motes and cotton gin waste (Jordan et al., 2019), pineapple crown waste or peel (Dai et al., 2018; Pereira et al., 2020; Prado and Spinacé, 2019), banana pseudo-stem residue (Meng et al., 2019a), sago fronds (Arnata et al., 2020), oil palm empty fruit bunch pulp (Al-Dulaimi and Wanrosli, 2017), wheat bran (Xiao et al., 2019), *Posidonia oceanica* waste biomass (Benito-González et al., 2019),

seaweed (*Gelidiella aceroso*) (Singh et al., 2017), mandacaru (*Cereus jamacaru* DC.) spines (Nepomuceno et al., 2017), lemon seeds (Zhang et al., 2020) and so on.

CNCs are isolated by various methods such as acid hydrolysis, ammonium persulfate and 2,2,6,6-tetramethylpiperidine 1-oxyl (TEMPO)-mediated oxidation (Zhang et al., 2020), deep eutectic solvent (Fan et al., 2020), ball mill assisted solid acid hydrolysis (Song et al., 2018), enzyme-assisted hydrolysis, mechanical disintegration and high-pressure homogenization (Park et al., 2019). Acid hydrolysis is the most effective method for CNCs isolation. Most authors reported the use of sulfuric acid for preparation of CNCs due to its versatile tuning of the surface charge density that endows CNCs suspensions higher colloidal stabilities (Dai et al., 2020, 2018; Meng et al., 2019a), but others also reported nitric acid (Orasugh et al., 2019), phosphoric acid (Kassab et al., 2020; Zhanhong Wang et al., 2019), phosphotungstic acid (Liu et al., 2014), hydrochloric acid (Hastuti et al., 2018; Yu et al., 2013), citric/hydrochloric acid hydrolysis (Kassab et al., 2020) and hydrobromic acid (Sadeghifar et al., 2011).

CNCs are usually prepared from extracted cellulose fibers or highly refined cellulose products. The chemical treatment process can alter the physicochemical properties of the cellulose fibers (Jordan et al., 2019). In most studies, alkaline treatment and bleaching with sodium chlorite solutions are commonly employed for extraction of cellulose fibers prior to isolation of CNCs (Couret et al., 2017; Jordan et al., 2019; Kassab et al., 2020; Xiao et al., 2019; Zhang et al., 2020).

In this study, four abundantly available lignocellulosic byproducts namely, TS, EF, SB and CH were used for chlorine-free extraction of cellulose fibers and CNCs. *Teff* (*Eragrostis tef*, Poaceae) is one of the most commonly cultivated staple food crops for the majority of people in Ethiopia. TS is the solid byproduct generated in large quantities during threshing to obtain starch-rich tiny *teff* grains (Esayas et al., 2018; Minten et al., 2016). *Enset* (*Ensete ventricosum*, Musaceae), a unique crop and perennial herb plant resembling banana, provides the staple food for around 20 million Ethiopians. EF is extracted mainly from the pseudostem and leaves, largely as a byproduct (Borrell et al., 2019; Gebre-Mariam and Schmidt, 1996). Sugarcane (*Saccharum officinarum*, Poaceae) plays a significant role in the Ethiopian economy. The booming sugar industries in Ethiopia aiming for annual production of 3.9-4.17 million tons of sugar, and 181 million L ethanol will generate massive cellulose-rich SB (Tena Gashaw et al., 2018). Ethiopia, a leading coffee (*Coffea arabica*, Rubiaceae) producer (441,000 metric tons) in Africa, ranks the fifth largest

producer and tenth exporter globally (Bickford, 2019). During coffee bean processing, large amounts of byproducts mainly CH, are generated and discarded or dumped into a landfill (Zhihao Wang et al., 2019).

To the best of our knowledge, no work has been reported on extraction and characterization of CNCs from the abundant lignocellulosic materials: TS, EF, and CH for potential value-added applications. Isolation of CNCs from SB was included due to its massive abundance and for comparison purposes.

3.2 Materials and methods

3.2.1 Materials

Previously collected untreated samples: TS, EF, SB and CH were used (in section 2.2.1). Chemicals and solvents mentioned in section 2.2.1 were used as received.

3.2.2 Cellulose extraction

Cellulose fibers were extracted from the four plant byproducts: TS, EF, SB and CH following a three-stage treatment reported in our previous work (Gabriel et al., 2020) in section 2.2.2. Briefly, the plant byproducts (each 20 g) were pretreated with 5% NaOH (for extraction condition 1) or 10% NaOH (for extraction condition 2), 1/10 (w/v) solid/liquid ratio of dry material on a water bath at 90 °C for 1.5 h. Similar steps for delignification and bleaching were followed (as mentioned in section 2.2.2). The extracted celluloses following extraction condition 1 and 2 were designated as C1 and C2, respectively.

3.2.3 Acid hydrolysis

First, the extracted celluloses (C1 or C2) from the plant byproducts, and CC were hydrolyzed with 64% (w/w) sulfuric acid (1:20 g/mL) at 45 °C for 30 min under vigorous stirring at 1500 rpm (the resulting NCs designated as CNCs-C1 and CNCs-C2, CC-CNCs). Immediately following the hydrolysis, the suspension was diluted 10-fold with chilled distilled water to quench the hydrolysis reaction, and centrifuged successively at 4 °C (Beckman Coulter Avanti J-20 XP Centrifuge, USA) for 10 min each at 9,000 rpm to remove the excess acid. The precipitate was then dialyzed in dialysis sacks (Avg. flat width 35 mm, MWCO 12,000 Da, Sigma-Aldrich, USA) with distilled water to remove non-reactive sulfate groups, salts and soluble sugars, until neutral pH was reached (5 days). Subsequently, the resulting suspension of dialysis process was treated using a disperser

type UltraTurrax (Janke and Kunkel IKA-Labortechnik, Ultra-Turrax T50) for 5 min at 10,000 rpm twice and sonicated (Bandelin SONOREX Digital 10P, Sigma-aldrich) for 5 min. The aqueous suspension thus obtained was freeze-dried in a lyophilizer (Martin Christ Gefrieetrocknungsanlagen GmbH, CHRIST, An der UnterenSöse 50, 37520 Osterode am Harz, Germany) and dried for 72 h to obtain CNCs powder (Coelho et al., 2018; de Oliveira et al., 2019; El Achaby et al., 2018; Fortunati et al., 2013).

3.2.4 Yield determination

The yields of CNCs were estimated gravimetrically, following successive extractions of celluloses from the byproducts, and CNCs from as-extracted cellulose fibers.

3.2.5 Determination of chemical composition

The chemical compositions of the untreated plant byproducts and the as-extracted celluloses, such as cellulose, lignin, and hemicellulose contents were determined according to the methods stated elsewhere (Abdel-Halim, 2014; Gabriel et al., 2020; Lin et al., 2010; Yeasmin and Mondal, 2015), as described in section 2.2.3.

3.2.6 XRD analyses

The crystallinity of as-isolated CNCs and cellulose precursors was analyzed according to the method mentioned in section 2.2.5. The crystalline indexes (CrI), d-spacings (d), apparent crystallite size or thickness for the 200 plane (τ_{200}), the proportion of crystallite interior chains for the 200 plane (X_{200}), fractional variation in the plane spacing for the 200 plane $(\Delta d/d)_{200}$, and Z-values were determined using equations described in section 2.2.5 (Equations 2.1-2.7) (Aguayo et al., 2018; Hermans et al., 1948; Poletto et al., 2014; Popescu et al., 2011; Segal et al., 1959).

3.2.7 FTIR spectroscopy

The FTIR spectra of the as-isolated CNCs as well as cellulose precursors, and CC were examined with a Perkin Elmer FTIR spectrometer (L1600400 Spectrum TWO DTGS, SN: 108152, LIantrisant, UK) in the infrared range from 4000 to 450 cm^{-1}, with no further sample preparation.

3.2.8 TEM investigation

A diluted CNC suspension of 0.05% (w/v) was prepared by sonication and then a drop of the suspension was deposited on a formvar-coated copper grid. The specimen was negatively stained

with 1% (w/v) phosphotungstic acid solution and dried at room temperature. Images of CNCs-1 samples were taken with an EM 900 TEM (Carl Zeiss Microscopy, Jena, Germany; acceleration voltage 80 kV). Electron micrographs were taken with a slow scan camera (Variospeed SSCCD camera SM-1k-120, TRS, Moorenweis, Germany).

3.2.9 Particle size analysis

The hydrodynamic size of the CNCs was measured using Malvern Instruments Zetasizer Nano ZS, dynamic light scattering (DLS) in backscattering mode at an angle of 173° and wavelength of 659 nm. The aqueous suspension of CNCs (0.05% w/v) were prepared from the freeze-dried samples. The results were averaged over three measurement cycles of 16 runs each at 25 °C after 120 s equilibration time.

3.2.10 Zeta potential

The zeta potential of aqueous suspension of CNCs (0.05% w/v) in 0.1N PBS was measured with Malvern Instruments Zetasizer Nano ZS working on electrophoretic mobility. The measurements were carried out at a temperature of 25 °C after 120 s equilibration time at a wavelength of 659 nm.

3.2.11 TGA properties

Thermal stability of the as-obtained CNCs and cellulose precursors was determined with TGA/DTG (Differential Thermo Gravimetry)-60H (SHIMADZU Corporation, Japan). The samples were heated from room temperature to 700 °C at a heating rate of 10 °C/min and a nitrogen gas flow rate of 60 mL/min.

3.3 Results and discussion

3.3.1 Effect of isolation conditions and yield of CNCs

The two concentrations of sodium hydroxide (5% and 10%) were used in the pretreatment step to investigate the effect of OH- concentration on the crystallinity of as-prepared cellulose, and then on CNCs, and the details are discussed in the following section: 3.3.2. The key process parameters in the isolation of CNCs are mainly acid concentration, hydrolysis temperature and time. The optimal CNCs extraction condition reported by several researchers is hydrolysing the bleached or as-extracted cellulose with 64-65% sulfuric acid at 45 °C for 30-40 min (Gong et al., 2018;

Hemmati et al., 2018; Kargarzadeh et al., 2012), at fiber to acid ratio of 1:20 (g/ml), and homogenizer speed of 10,000 rpm (Hemmati et al., 2018).

The yield of CNCs decreases as temperature and reaction time increase. This is attributed to the additional hydrolysis of the amorphous regions of the cellulose as well as the degradation of the crystalline structures during the process (Hafemann et al., 2019; Kargarzadeh et al., 2012; Shaheen and Emam, 2018). XRD analyses revealed that the crystallinity first increases upon hydrolysis and then decreases after long duration of hydrolysis (Haafiz et al., 2014; Kargarzadeh et al., 2012; Korolovych et al., 2018). Thermal stability was found to decrease as the hydrolysis time increase (Kargarzadeh et al., 2012). Furthermore, other cellulose extraction conditions also influence the properties of the CNCs to be isolated (Di Giorgio et al., 2020; Fortunati et al., 2013).

A turbid white mixture of materials from TS, EF and SB cellulose fibers and yellowish dark mixture from CH cellulose were formed during acid hydrolysis. White gel-like materials from TS, EF and SB celluloses are obtained after first centrifugation as shown in the Appendix (Fig. A1), however, the dark brown color of CH-CNCs may indicate the presence of relatively higher lignin content in the extracted cellulose. Apparently, untreated CH has 31% lignin content and the extracted cellulose fiber (CH-cellulose) has 8%, the highest in the studied samples (Gabriel et al., 2020). Similar observations on the influence of lignin content on the color of CNCs suspensions has been reported elsewhere (de Oliveira et al., 2019). Cellulose degradation with concomitant color-change occurs due to the formation of carbonyl groups in the cellulose chains, and also due to the formation of colored low-molecular furan-type compounds during the thermal degradation of carbohydrates (Heggset et al., 2017). Additionally, the impact of sulfuric acid ratio and concentration on crystallinity was investigated by hydrolyzing celluloses (C1) from each byproduct, and commercial cellulose (CC) with 64% (w/w) sulfuric acid (1:8.75 g/mL) (the resulting NCs designated as CNCs-C1X and CC-NCsX). Cellulose (C1) and CC were also hydrolyzed by 58% (w/w) sulfuric acid (1:20 g/mL) (the resulting hydrolyzed cellulose designated as Cellulose-C1Y and CC-Y) in a preliminary work.

The CNCs suspensions are found to be dispersed well with a milky white colloidal appearance after ten days of storage at cold temperature as shown in Fig. 3.1, due to the repulsive forces of negative charge of sulfate in CNCs. The lyophilized CNCs are also showed in Fig. 3.1a.

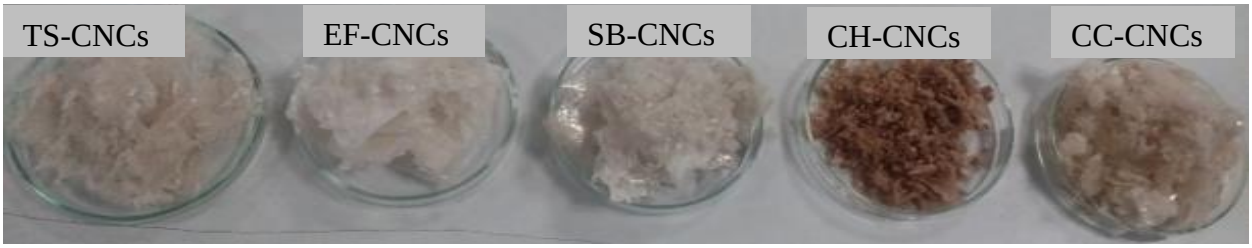

a)

b)

Fig. 3.1: Photographs of CNCs a) lyophilized samples b) dispersions in distilled water (0.5%) at the 10th day of storage at 4 °C (CNCs from TS, EF, SB, CH and CC from left to right). (Key: TS-*teff* straw; EF-*enset* fiber; SB-sugarcane bagasse; CH-coffee hull; CNCs- cellulose nanocrystals; CC- commercial cellulose included for comparison)

The yields of the isolated CNCs from the cellulose fibers are given in Table 3.1. As shown in the Table, the CNCs yield depends on the source of cellulose.

Table 3.1: Yields of celluloses and CNCs from the byproducts

Plant byproducts	Yields (%)		
	Cellulose	CNCs from cellulose	CNCs from byproducts
TS	36.7 ± 0.55	50.0 ± 3.32	18.4
EF	60.0 ± 1.25	70.0 ± 1.49	42.0
SB	39.5 ± 1.08	64.0 ± 2.79	25.3
CH	35.5 ± 1.80	25.0 ± 2.11	8.9

(Key: TS-*teff* straw; EF-*enset* fiber; SB-sugarcane bagasse; CH-coffee hull); Data are presented as the mean ± SD (*n* = 3).

3.3.2 Crystallinity of the CNCs

The as-isolated CNCs-C1 and CNCs-C2 like their cellulose precursors displayed a typical crystal lattice of Cellulose I, with the main diffraction signals around 2θ values of 15°, 16°, 22° and 34° with assigned crystallographic plane of $1\bar{1}0$, 110, 200 and 040, respectively after deconvolution using Gaussian profile as reported elsewhere (Haafiz et al., 2014). The XRD patterns of CNCs-C1, and their cellulose precursors (C1) are shown in Fig. 3.2. The XRD patterns of CNCs-C2, and their cellulose (C2) precursors are also depicted in the Appendix (Fig. A2).

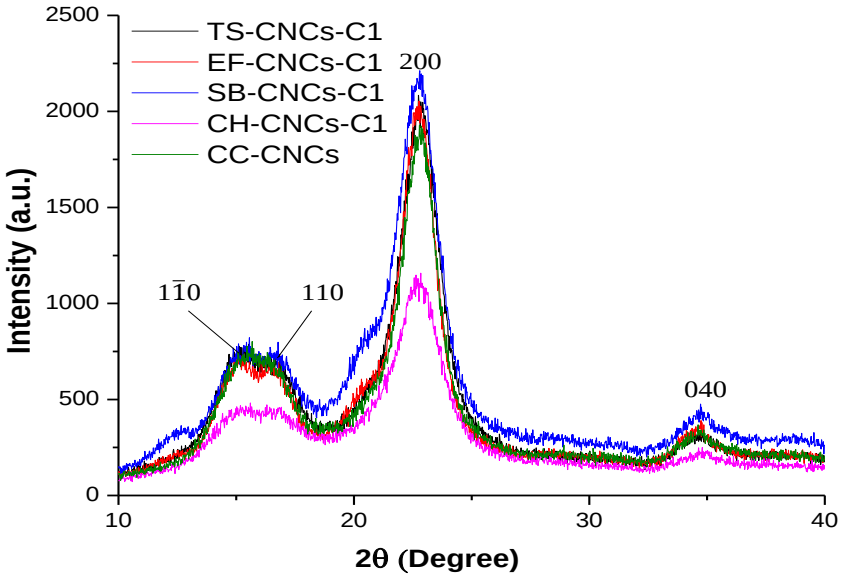

a)

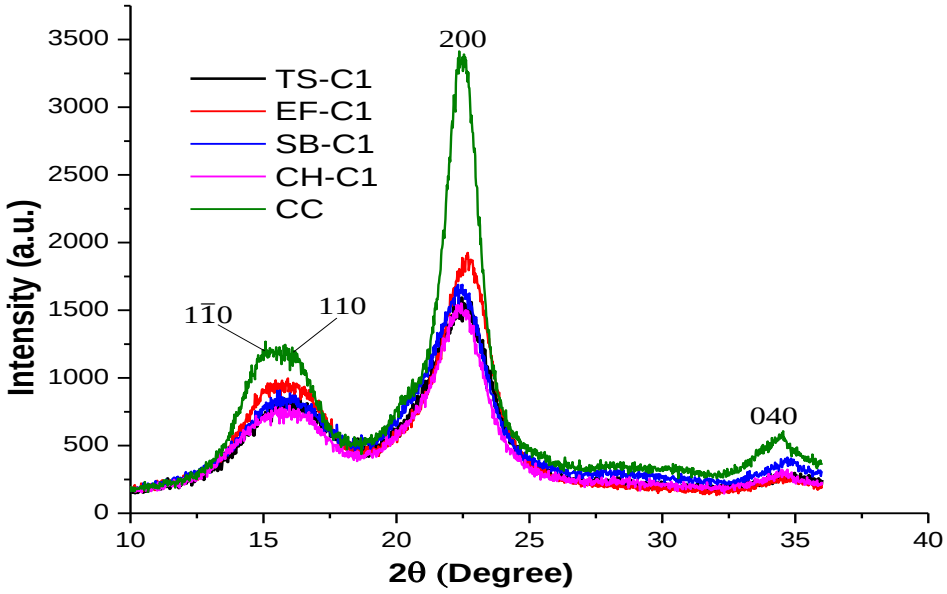

b)

Fig. 3.2: XRD patterns of a) CNCs-C1, and b) cellulose (C1) precursors. (Key: TS-*teff* straw; EF-*enset* fiber; SB-sugarcane bagasse; CH-coffee hull; CNCs-C1-Cellulose nanocrystals isolated from cellulose (C1) extracted following Condition 1; CC-CNCs-Nanocrystals isolated from CC (commercial cellulose) included for comparison)

In this study, CrIs were determined following both Segal et al. and Hermans et al. approaches (Hermans et al., 1948; Poletto et al., 2014; Segal et al., 1959). Higher values of CrIs were recorded following Segal et al. approach when compared to Hermans et al. approach for similar plant samples. Both approaches indicate distinct variation of CrIs during hydrolysis of cellulose using sulfuric acid (Fig. 3.3). As the Segal et al. approach is simple and provides useful information, it is the most frequently used approach to estimate CrI in the literature (Aguayo et al., 2018; Naduparambath and Purushothaman, 2016; Prado and Spinacé, 2019).

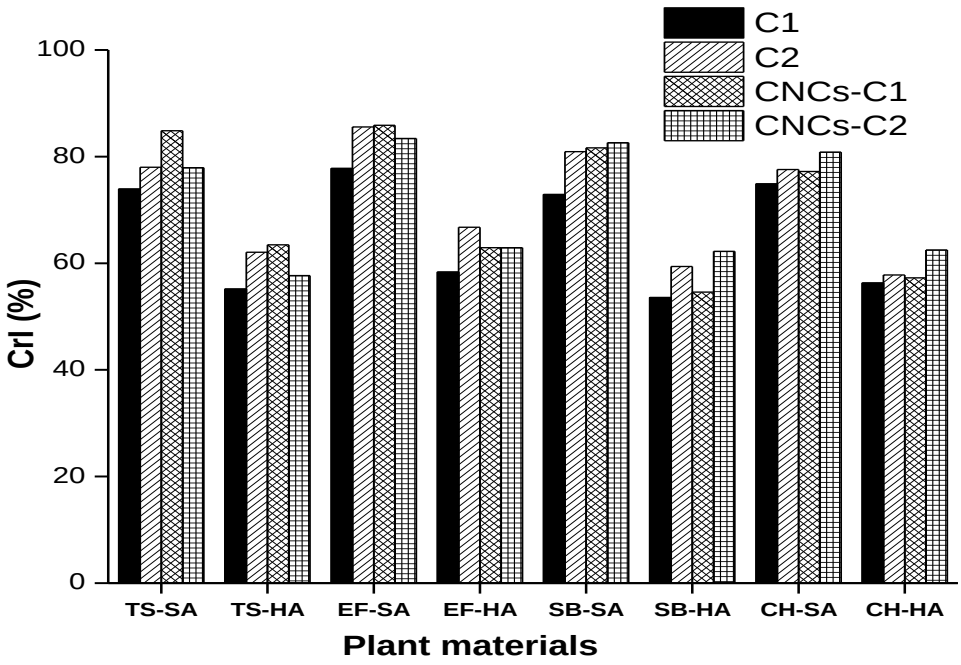

Fig. 3.3: Comparison of Segal et al. (SA) and Hermans et al. (HA) approaches for estimation of CrIs of the CNCs and cellulose precursors. (Key: CNCs-C1 and CNCs-C2-cellulose nanocrystals isolated from C1 and C2, respectively. TS-*teff* straw; EF-*enset* fiber; SB-sugarcane bagasse; CH-coffee hull).

CNCs-C1 isolated from EF exhibited the highest CrI (85.88%), a fibrous plant material (Musaceae) followed by TS and SB (84.84% and 81.64%) (Grass/Poaceae) and CH (77.20%) (Rubiaceae) using 5% NaOH in the pretreatment stage. Generally, CrIs increased in all isolated CNCs when compared to their cellulose precursors, except in CNCs isolated from TS-C2, EF-C2 and CC. Such an increment of CrI was due to the hydrolytic scission of the glycosidic bonds releasing individual crystals and removing the amorphous domains (García-García et al., 2018; Singh et al., 2017).

There was significant increment of the CrI of the cellulose fibers when the raw materials were pretreated with 10% NaOH instead of 5% NaOH, showing removal of considerable amount of non-cellulosic materials when the raw materials were treated with 10% NaOH, without degrading cellulose. However, no significant difference in CrI was observed in the obtained CNCs employing either of the NaOH concentrations, 5% or 10%. Hence, 10% NaOH may be used in the pretreatment stage to obtain crystalline-rich cellulose; and 5% NaOH to obtain highly crystalline CNCs.

Fig. 3.3 and Table 3.2 show slight reduction of crystallinity in TS-CNCs-C2 and EF-CNCs-C2, compared to CrI of their cellulose precursors extracted with 10% NaOH. Such slight reduction in crystallinity may occur upon strong acid hydrolysis of highly pure and crystalline cellulose, showing that the amorphous regions have already been degraded and the acid started to partially attack the crystalline portions. Similar findings were also reported elsewhere in CNCs isolated from different sources such as MCC (Haafiz et al., 2014; Korolovych et al., 2018), and onion skin (Rhim et al., 2015). The CrI of all CNCs-1 increased when compared with the respective cellulose precursors extracted with 5% NaOH as depicted in Fig. 3.3 and Table 3.2. As CNCs isolated from cellulose (C1) exhibited higher crystallinity and comparable yield, CNCs-C1 were considered for full characterization.

Table 3.2: Parameters obtained from the (deconvoluted) XRD of CNCs-C1, CNCs-C2 and cellulose precursors, as well as CC-CNCs

Materials	d-spacings (nm)				τ_{200} (nm)	X_{200}	$\Delta d/d_{200}$	CrI (SA) (%)	Z-Values
	$1\bar{1}0$	110	200	040					
TS-CNCs-C1	0.589	0.523	0.389	0.258	5.233	0.612	0.0699	84.84	-23.69
TS-C1	0.577	0.557	0.394	0.257	2.922	0.372	0.1268	73.90	-74.22
TS-CNCs-C2	0.593	0.544	0.395	0.259	3.682	0.477	0.1007	76.61	-36.57
TS-C2	0.608	0.562	0.395	0.262	3.689	0.477	0.1006	78.00	-27.64
EF-CNCs-C1	0.590	0.528	0.390	0.260	5.799	0.645	0.0633	85.88	-26.53
EF-C1	0.580	0.559	0.392	0.270	3.973	0.509	0.0928	77.78	-50.54
EF-CNCs-C2	0.600	0.540	0.394	0.260	5.502	0.630	0.0674	83.41	-21.08
EF-C2	0.587	0.544	0.394	0.260	5.515	0.629	0.0668	85.56	-45.84
SB-CNCs-C1	0.578	0.519	0.390	0.258	5.320	0.617	0.0690	81.64	-38.84
SB-C1	0.559	0.558	0.396	0.260	3.600	0.467	0.1035	72.90	-105.00
SB-CNCs-C2	0.589	0.528	0.394	0.260	5.366	0.620	0.0690	82.60	-27.94
SB-C2	0.582	0.542	0.395	0.259	3.939	0.505	0.0944	80.92	-52.41
CH-CNCs-C1	0.590	0.524	0.391	0.257	4.438	0.552	0.0827	77.20	-21.92
CH-C1	0.606	0.560	0.397	0.259	3.618	0.469	0.1031	74.87	-49.29
CH-CNCs-C2	0.591	0.526	0.393	0.260	5.042	0.599	0.0732	80.86	-22.78
CH-C2	0.609	0.554	0.394	0.261	3.946	0.506	0.0938	77.59	-16.75
CC-CNCs	0.604	0.541	0.394	0.260	4.415	0.550	0.1287	74.91	-14.18
CC	0.608	0.554	0.395	0.260	6.480	0.679	0.0573	87.23	-19.85

Key: C1 and C2-Cellulose extracted with Conditions A and B, respectively; CNCs-C1 and CNCs-C2- cellulose nanocrystals isolated from C1 and C2, respectively; TS-*teff* straw; EF-*enset* fiber; SB-sugarcane bagasse; CH-coffee hull; CC-Commercial cellulose included for comparison; CC-CNCs-cellulose nanocrystals isolated from commercial cellulose included for comparison; d-the interplanar spacing of the crystal; τ_{200}-average thickness of cellulose crystallites; X_{200}-the proportion of crystallite interior chains for the 200 plane; $\Delta d/d_{200}$-the fractional variation in the plane spacing for the 200 plane; CrI (SA)-crystallinity index following Segal et al. approach.

The CrI of EF-CNCs-C1 (85.88%) reported in this study was higher when compared to CrIs of CNCs isolated from other sources: pseudostems of banana plants (74-75%) (Meng et al., 2019a; Mueller et al., 2014), mandacaru (*Cereus jamacaru* DC.) spines (60.0-62.7%) (Nepomuceno et al., 2017), oil palm fronds (*Elaeis guineensis*) (78.5%) (Dungani et al., 2017), passion fruit (82.8%) peels waste (77.96%) (Wijaya et al., 2017), *Nypa Fruticans* trunk (76.6%), coconut husk fber (79.3%), and rice husk (Nang An et al., 2020), pineapple crown waste (73%) (Prado and Spinacé, 2019), post-consumer wood fiberboard waste (61-71%) (Couret et al., 2017), pueraria root residue (60%) (Zhanhong Wang et al., 2019) and macrophyte *Typha domingensis* (74-80%) (César et al., 2015) following the Segal et al. approach. The CrI of SB-CNCs-C1 (81.64%) in this study is much higher than reported elsewhere 51% (Ferreira et al., 2018) and less than 86% (Oliveira et al., 2016) which may be attributed to variation in cellulose extraction conditions.

Parameters obtained from the (deconvoluted) XRD of CNCs-C1, CNCs-C2 and cellulose precursors are given in Table 3.2. The deconvoluted XRD patterns of the cellulose precursors and as-obtained CNCs-C1 from the lignocellulose sources are shown in Fig. A3 (Appendix). A direct relationship was observed among CrI, crystallite sizes at the 200 plane (τ_{200} values) and the proportion of crystallite interior chains for the 200 plane (X_{200}) unlike the fractional variation in the plane spacing for the 200 plane ($\Delta d/d_{200}$) (Table 3.2). The X-values were used as estimates of the fraction of cellulose chains contained in the interior of the crystallites (Newman, 1999). EF-CNCs-C1 exhibited the highest τ and X-values due to decreased chain mobility permitting a lower percentage of the chains to move into the perfect register of the crystals (Table 3.2) (Newman, 1999; Popescu et al., 2011) and contained the most ordered cellulose structure when compared to other CNCs. However, an inverse relationship between CrI and τ_{200} values was reported elsewhere for CNCs isolated from onion skin (Rhim et al., 2015). A greater value of the $\Delta d/d_{200}$, a measurement for the dispersion of the crystalline plane values, shows higher microstresses. EF-CNCs-C1 of this study had the lowest $\Delta d/d_{200}$ (0.0633), but the highest was recorded for TS-CNCs-C2 (0.1007). It was also reported that smaller τ_{200} value is associated with a high $\Delta d/d_{200}$ in its interplanar distance (Aguayo et al., 2018).

The τ values of the CNCs ranged from 4.438 nm for CH-CNCs-C1 to 5.799 nm for EF-CNCs-C1, obtained from lignocellulosic byproducts pretreated with 5% NaOH, and X values ranged from 0.552 for CH-CNCs-C1 to 0.645 for EF-CNCs-C1. The CNCs-C1 had higher τ and X values when

compared to their cellulose precursors as well as CNCs-C2 except for SB-CNCs. The d-spacings of the isolated CNCs ranged from 0.541-0.600, 0.519-0.544, 0.389-0.395, and 0.257-0.260 for the planes of $1\bar{1}0$, 110, 200, and 040, respectively as shown in Table 3.2. The d-spacing values indicated that the CNCs isolated from cellulose (C1 and C2) in this study are all I_{β}-type cellulose (French, 2014; Kim et al., 2010; Wada and Okano, 2001) stating that the monoclinic structure is dominant in the CNCs, supported by the negative numbers of the Z-Values (He et al., 2018; Poletto et al., 2012).

Influence of sulfuric acid ratio and concentration on CrI was investigated using cellulose (C1) as a precursor, and CC in the preliminary work. The CrI increases when the cellulose (C1) from each byproduct is hydrolyzed with sulfuric acid at 64% (w/w) (1:20 and 1:8.75), and 58% (w/w) (1:20), as depicted in Fig. A4 (Appendix). A ratio of Cellulose to Acid 1:8.75 (64% (w/w) sulfuric acid) gave comparable or slightly higher CrI than using 1:20 ratio, except for TS-CNCs-C1X, and CC-NCsX, and the CrI of EF-CNCs-C1X was 86.34%; 67.54%, which would be the highest CrI using the two approaches, respectively. The amount of acid does not rinse the cellulose fibers at 1:8.75 g/ml ratio initially for about 10 min and the slurry becomes very viscous, making stirring difficult and causing uneven hydrolysis of cellulose. Though the CrI increased using 58% (w/w) sulfuric acid (1:20 g/ml), the celluloses were not well hydrolyzed and the resulting materials were not considered CNCs.

3.3.3 Chemical functionality studies

FTIR spectra of the isolated CNCs-1, and the cellulose precursors (C1) are shown in Fig. 3.4. The broad band around 3333 cm^{-1} corresponds to the stretching vibrations of the OH groups in the CNCs and cellulose molecules, indicating the hydrophilic tendency of the materials. The weak transmittance band around 2890 cm^{-1} is attributed to the asymmetric stretching vibration of the CH bond (Meng et al., 2019a; Zhanhong Wang et al., 2019). The peak at ~1645 cm^{-1} in all the spectra corresponds to the OH bending of water absorbed into the CNCs and cellulose fiber structure (Aguayo et al., 2018).

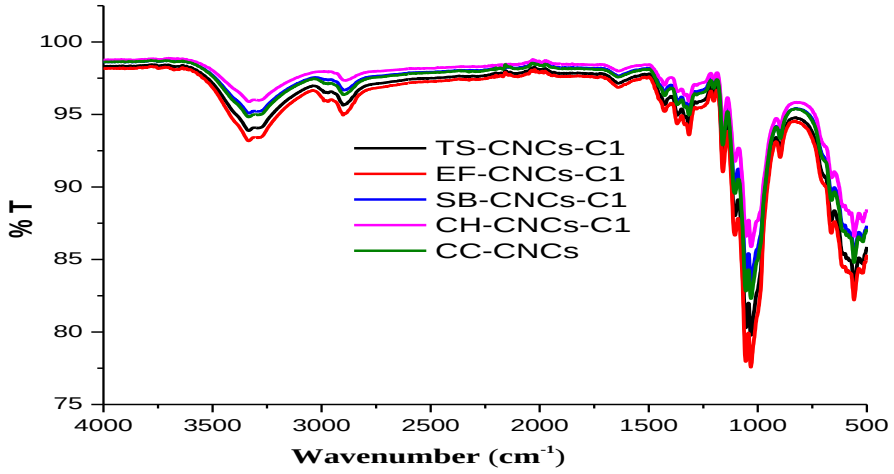

a)

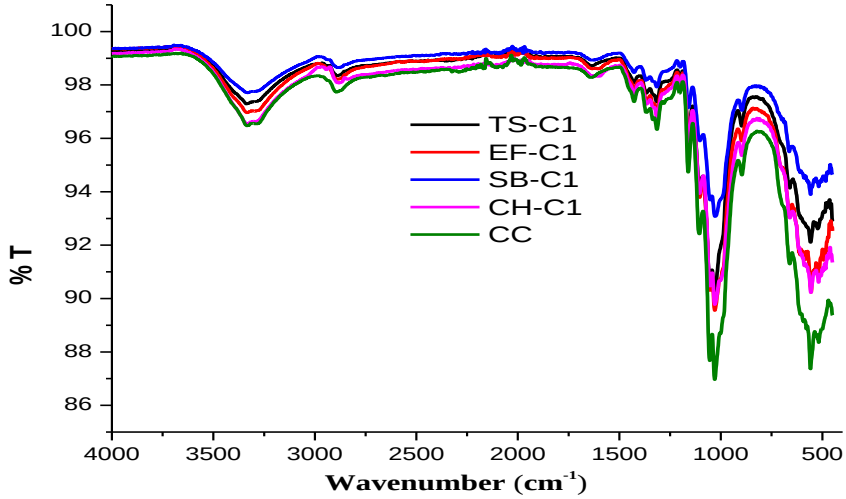

b)

Fig. 3.4: FTIR spectra of a) CNCs-C1, and b) cellulose (C1) precursors. (Key: CNCs-C1-cellulose nanocrystals isolated from C1; C1-Cellulose extracted using extraction Condition 1; TS-*teff* straw; EF-*enset* fiber; SB-sugarcane bagasse; CH-coffee hull; CC-CNCs-cellulose nanocrystals isolated from commercial cellulose (CC) included for comparison)

A band around 1428 cm^{-1} indicates the alkane deformations relating to CH and CH_2 bending. The peak around 896 cm^{-1} is related to glycosidic C_1H deformation, a ring vibration, and OH bending where these characters infer the β-glycosidic linkages between anhydroglucose units. The transmittance peaks around 3333, 2890, 1428, 1323, 896 cm^{-1} are associated with the

characteristics of native Cellulose I as seen in all cellulose and CNCs spectra, showing chemical similarity and, therefore, the acid hydrolysis did not affect the chemical structure of the cellulosic fragments (Mohamad Haafiz et al., 2013; Yang et al., 2007). The FTIR spectra of CNCs-C2, and their cellulose (C2) precursors are shown in the Appendix (Fig. A5).

3.3.4 Dimensional and morphological analyses

Appearance of needle-shaped CNCs on TEM images shows the acid hydrolysis is effective in isolating the CNCs with a scale bar of 200 nm (Fig. 3.5). Relatively clear images were taken for the CNCs when phosphotungstic acid solution was used rather than uranyl acetate during TEM imaging (images using uranyl acetate not shown). From the TEM analysis, the length and diameter of the CNCs isolated from the byproducts ranged from 106.78-193.06 nm and 5.16-11.79 nm, respectively. Generally, the plant CNCs range from 100–250 nm in length and 5–70 nm in diameter.

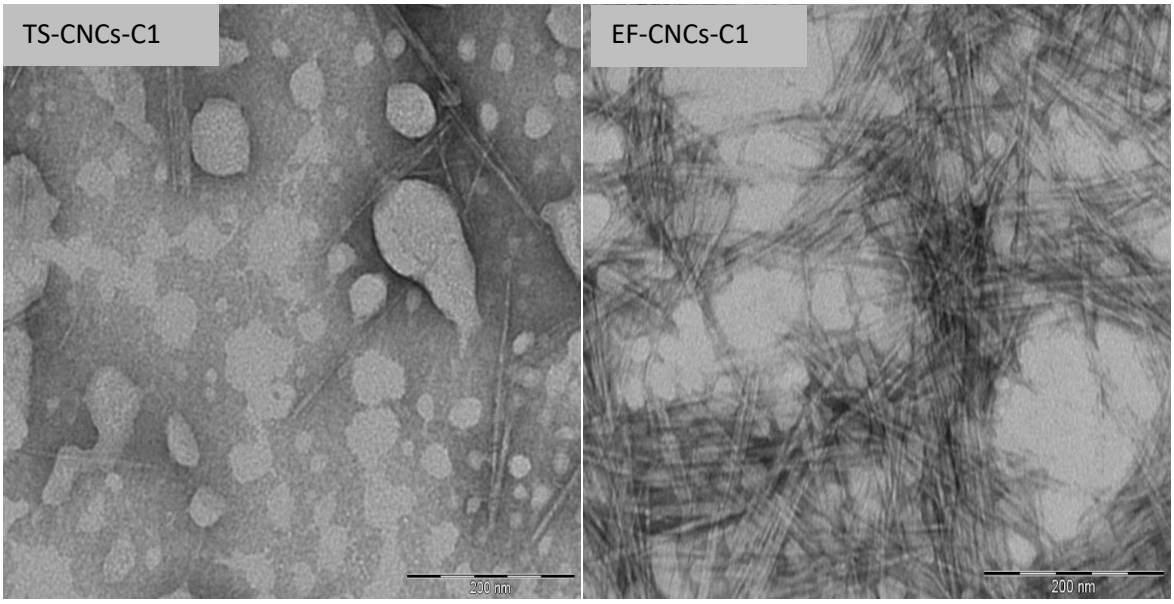

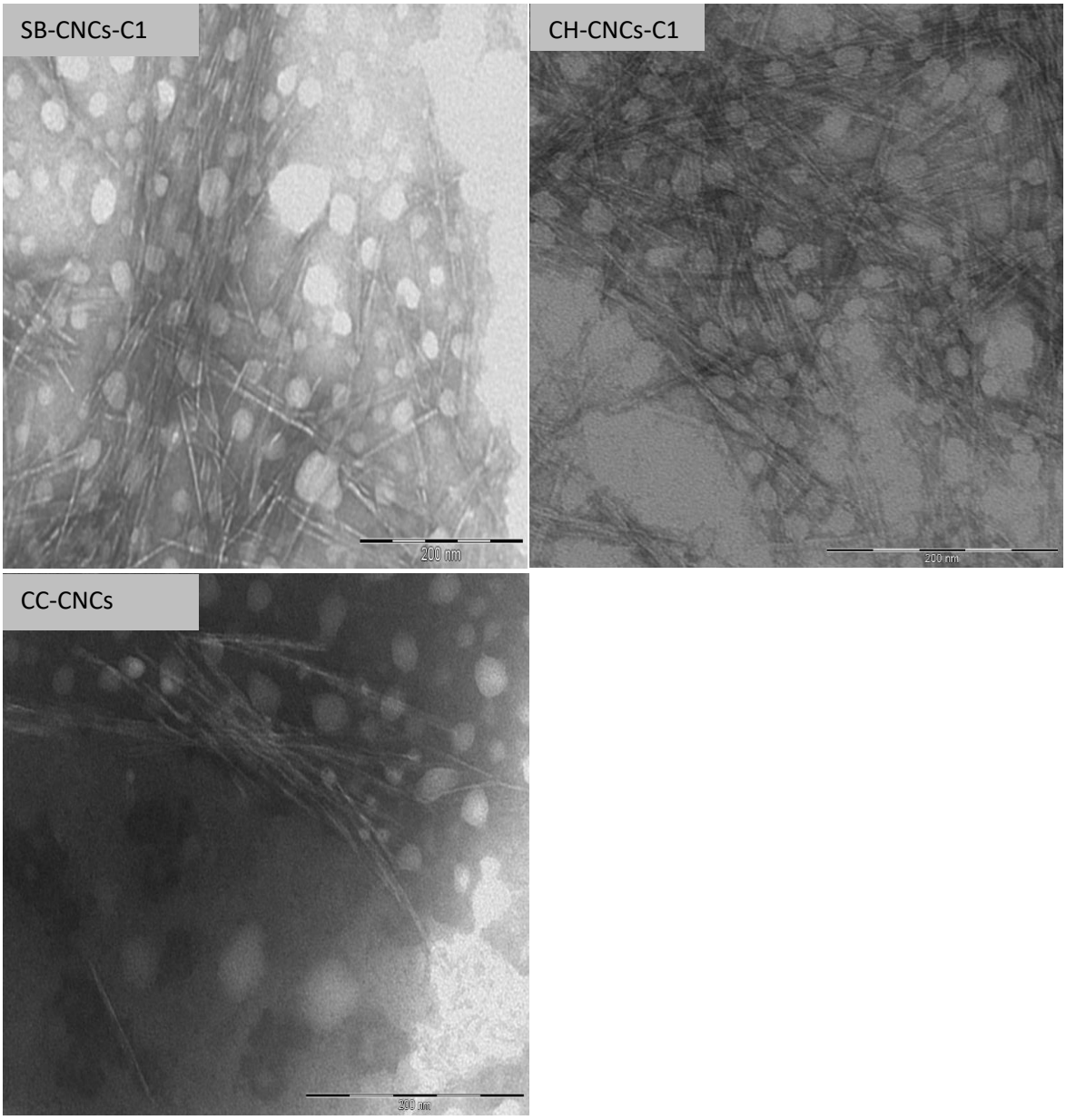

Fig. 3.5: Transmission electron micrographs of CNCs-1 (TS-CNCs-C1, EF-CNCs-C1, SB-CNCs-C1, CH-CNCs-C1), and CC-CNCs) (Bar scale: 200 nm). (Key: CNCs-C1-cellulose nanocrystals isolated from C1; C1-Cellulose extracted using extraction Condition 1; TS-*teff* straw; EF-*enset* fiber; SB-sugarcane bagasse; CH-coffee hull; CC-CNCs-cellulose nanocrystals isolated from commercial cellulose (CC) included for comparison)

In this study, the highest aspect ratio (36.68) is observed in SB-CNCs-C1 (Table 3.3), which is higher than the values reported by Lam et al. 2017 (20-25) and Mueller et al. 2014 (28). Elsewhere, the CNCs obtained from SB were short and needle-shaped in the range 200–300 nm in length and 20–40 nm in diameter (Sukyai et al., 2018). Reports indicate that CNCs with high aspect ratios

(above 10) exhibit good mechanical properties (bending strength, tensile strength and Young's modulus) (Ferreira et al., 2018).

Table 3.3: TEM dimensional analysis of CNCs isolated from cellulose (C1) extracted from various raw materials.

Source (CNCs)	Length (L) range; $L_{average}$ (nm)	Diameter (D) range; $D_{average}$ (nm)	Aspect ratio
TS-CNCs-C1	76.96-300.08; 193.06 ± 52.41	2.25-10.88; 6.7 ± 2.08	28.82
EF-CNCs-C1	88.67-242.35; 154.28 ± 36.712	3.22-16.14; 8.889 ± 3.043	17.32
SB-CNCs-C1	110.68-301.66; 189.29 ± 49.928	2.20-8.97; 5.16 ± 1.91	36.68
CH-CNCs-C1	116.51-232.41; 188.07 ± 25.86	3.65-13.97; 7.268 ± 3.25	25.88
CC-CNCs	50.871-147.211; 106.78± 21.211	4.17-11.31; 6.141 ± 1.567	17.39

(Key: CNCs-C1-cellulose nanocrystals isolated from C1; C1-Cellulose extracted using extraction Condition 1; TS-*teff* straw; EF-*enset* fiber; SB-sugarcane bagasse; CH-coffee hull; CC-CNCs-cellulose nanocrystals isolated from commercial cellulose (CC) included for comparison, $L_{average}$-average length; $D_{average}$-average diameter of CNCs estimated using ImageJ Software)

Needle-shaped particles were observed at 30 min of hydrolysis time in the current study. It was reported an increase in the acid hydrolysis time more than 60 min resulted in a significant decrease in the average length and diameter of the CNC due to the destruction of amorphous regions and even partial crystalline regions of cellulose (Xiao et al., 2019).

3.3.5 Particle size and Zeta potential of CNCs

The DLS results also revealed that the isolated CNCs were in nanoscale range, and their hydrodynamic size ranged from 96.96 nm of CH-CNCs-C1 to 157.2 nm of EF-CNCs-C1 with the polydispersity index (PDI) ranging from 0.209-0.524 (Table 3.4). Elsewhere, the hydrodynamic size of CNCs from SB ranged from 18.17-220 nm, with most particles accumulated beyond 37.84 nm (Mandal and Chakrabarty, 2011) and from 115-130 nm (Saha and Ghosh, 2019). The zeta potential values of the CNCs suspensions ranged from -28.8 to -38.6 mV in neutral water (Table 3.4), and resulted in stable colloidal suspensions as the absolute values obtained are higher than -15 mV which is the minimum value to represent the onset of agglomeration (Benini et al., 2018;

Thomas et al., 2018). The negatively charged surfaces on CNCs were due to the insertion of sulfate during sulfuric acid hydrolysis (Dungani et al., 2017; Kassab et al., 2020).

Table 3.4: Hydrodynamic size using DLS and Zeta potential values

SN	Source (CNCs)	Hydrodynamic size (nm); PDI (DLS)	Zeta Potential (mV)
1.	TS-CNCs-C1	137.0; 0.209	-28.8
2.	EF-CNCs-C1	157.2; 0.524	-29.9
3.	SB-CNCs-C1	106.8; 0.285	-38.6
4.	CH-CNCs-C1	96.96; 0.261	-33.5
5.	CC-CNCs	184.9; 0.426	-37.8

(Key: CNCs-C1-cellulose nanocrystals isolated from C1; C1-Cellulose extracted using extraction Condition 1; TS-*teff* straw; EF-*enset* fiber; SB-sugarcane bagasse; CH-coffee hull; CC-commercial cellulose; CC-CNCs-cellulose nanocrystals isolated from commercial cellulose included for comparison)

CNCs at the zeta potential values near or lower than -20 mV at low concentrations remain stable (Stinson-Bagby et al., 2018). The zeta potential absolute value of SB-CNCs-C1 (-38.6 mV) was slightly higher than the zeta potential of CNCs isolated from SB in other studies: -32.3 mV (Ferreira et al., 2018) and -18.3 to -20.97 mV (Saha and Ghosh, 2019). The zeta potential absolute values greater than 30 are regarded as highly stable, indicating all the CNCs except TS-CNCs are colloidally very stable, and TS-CNCs with zeta potential value of -28.8 mV are considered to be moderately stable (Table 3.4) (Kassab et al., 2020). It was reported elsewhere that the zeta potential absolute value increased significantly from -8.7 to -95.3 mV when the acid hydrolysis time increased from 20 to 120 min (Kargarzadeh et al., 2012).

3.3.6 Thermal properties of the CNCs

The thermal properties of the CNCs-1, and cellulose precursors (C1) from each byproduct were investigated with TGA/Differential thermogravimetry (DTG). The isolated CNCs presents three main weight loss regions, as shown in Fig. 3.6a and b, and the Appendix (Fig. A6 and Table A1). The initial small (3.8-5.7%) weight loss in the region 30-110 °C (with maximum weight loss temperature from 60-64 °C) is mainly due to moisture evaporation; water adsorbed to the isolated CNCs (Silvério et al., 2013; Zhanhong Wang et al., 2019; Xiao et al., 2019; Xing et al., 2018).

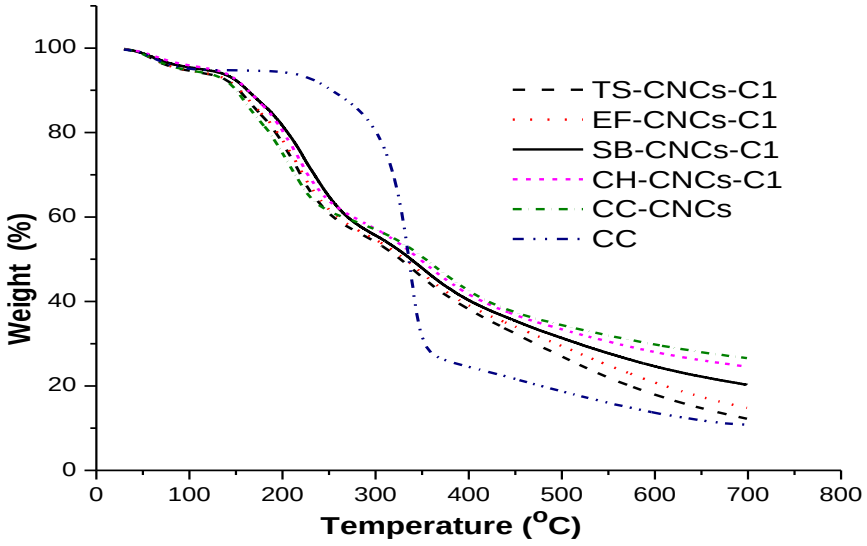
Weight (%)
Temperature (°C)
TS-CNCs-C1
EF-CNCs-C1
SB-CNCs-C1
CH-CNCs-C1
CC-CNCs
CC

a)

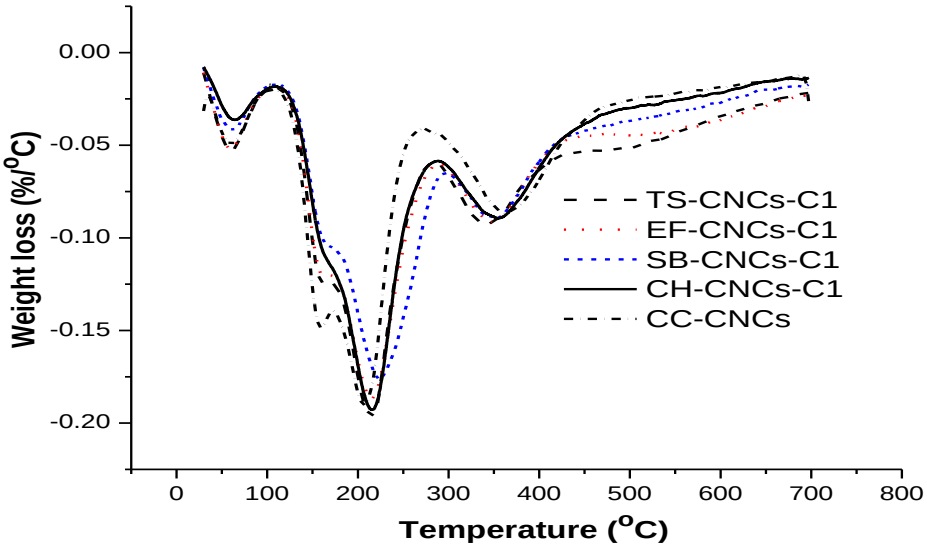
Weight loss (%/°C)
Temperature (°C)
TS-CNCs-C1
EF-CNCs-C1
SB-CNCs-C1
CH-CNCs-C1
CC-CNCs

b)

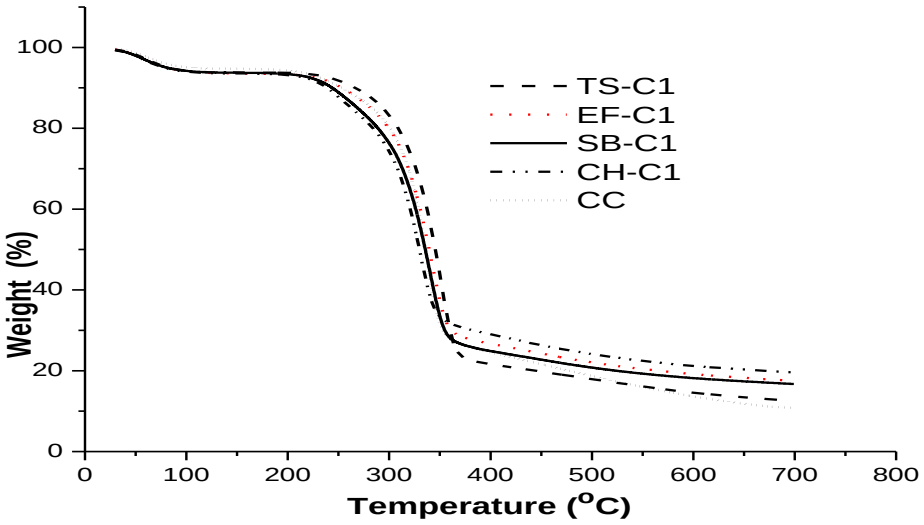

c)

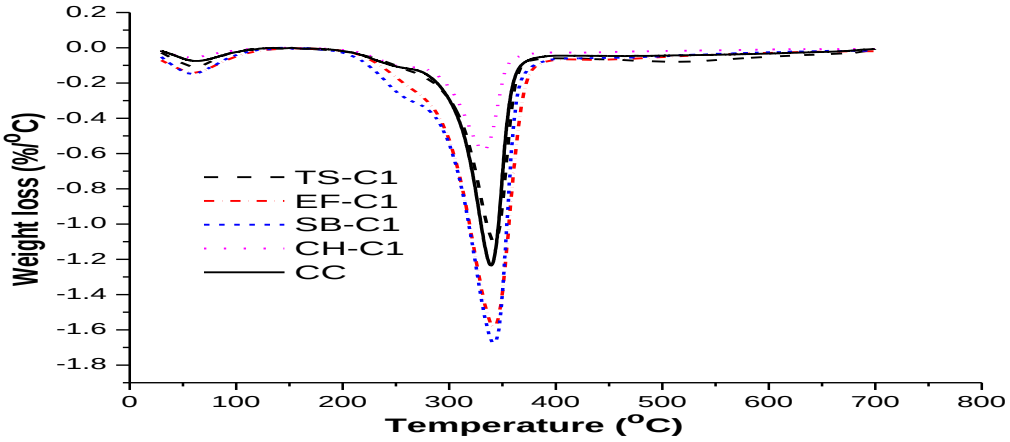

d)

Fig. 3.6: Thermal degradation behaviors: a) TGA and b) DTG of CNCs (upper two), and c) TGA and d) DTG of cellulose (C1) precursors (lower two) extracted with Condition 1, and CC. (Key: CNCs-C1-cellulose nanocrystals isolated from C1; C1-Cellulose extracted using extraction Condition 1; TS-*teff* straw; EF-*enset* fiber; SB-sugarcane bagasse; CH-coffee hull; CC-CNCs-cellulose nanocrystals isolated from commercial cellulose (CC) included for comparison).

All CNCs displayed a two-step decomposition process, along with the appearance of small shoulders around 160 °C in DTG (evident in TS-CNCS, EF-CNCs and CC-CNCs). A weight loss of 29-38% was observed in the first step decomposition temperature of the CNCs (T_{max} 215-225 °C) and this is due to the degradation of both surface sulfate groups and CNCs. Other studies have shown the lower thermal stability of CNCs is due to its large specific surface area and the sulfated group of the CNCs (Lam et al., 2017; Xiao et al., 2019; Xing et al., 2018).

The second decomposition step exhibited at T_{max} ranging from ~340-355 °C (the major cellulose degradation temperature), due to breakdown of the interior non-sulfated cellulose crystals and a few studies in the literature also reported similar behavior for CNCs isolated from plant materials such as SB (Lam et al., 2017), Tetra pak Cellulose I (Xing et al., 2018), corncob (Silvério et al., 2013) and pineapple crown waste (Prado and Spinacé, 2019). The weight loss ranged from 18.5-25.4%, which is slightly lower than the former phase of decomposition. All the isolated CNCs exhibited lower maximum weight loss rates (0.1760-0.2050%/°C) in the sulfated cellulose groups than cellulose precursors. The charred residues at 550 °C of all CNCs showed higher values than cellulose counterparts because of a dehydration effect of the sulfate group as flame retardants (Rhim et al., 2015; Silvério et al., 2013; Xing et al., 2018).

The thermal degradation properties of as-extracted cellulose fibers are depicted in Fig. 3.6c and d, and Table A1. A maximum weight loss of the cellulose fibers (50-70%) was observed at the maximum degradation temperatures ranging from 330-360 °C. This might be due to several degradation factors such as depolymerization, dehydration and decomposition of the glycosidic units of the cellulose chains as reported elsewhere (Bano and Negi, 2017). The higher thermal stability of the as-extracted cellulose fibers from the raw materials is related to their high crystallinity. The maximum weight loss rate of the cellulose fibers ranged from 0.5795%/°C for CH-C1 (at 329.73 °C) to 1.6756%/°C for EF-C1 (at 340.30 °C). The TGA/DTG curves of as-extracted cellulose fibers showed the removal of hemicelluloses and lignin by the chlorine-free extraction conditions confirming successful cellulose extraction process (Wijaya et al., 2019).

3.4 Conclusion

Highly crystalline CNCs were obtained from the four abundant byproducts: TS, EF, SB and CH with chlorine-free cellulose extraction and sulfuric acid hydrolysis. The highest yield, CrI and crystal size were exhibited in EF-CNCs, and the least in CH-CNCs. No polymorphic transition occurred during cellulose extraction and acid hydrolysis. A direct relationship was observed among CrIs, crystallite sizes (τ_{200}) and the proportion of crystallite interior chains (X_{200}) in the as-obtained CNCs. A two-step decomposition process of CNCs was observed and this was due to degradation of surface sulfate groups and large specific surface area, and breakdown of the interior non-sulfated cellulose crystals. Based on the findings (high yield, CrI and aspect ratio), the four lignocellulosic materials can be used as alternative sources of CNCs.

4 Is mercerization the only factor for (partial) polymorphic transition of cellulose I to cellulose II in cellulose nanocrystals?

4.1 Introduction

Cellulose, a homopolymer with a linear β-(1→4)-linked glucan structure, is the most abundant polysaccharide produced in nature (Poletto et al., 2014; Sun et al., 2004). Woody plants and cotton are the major and conventional sources of cellulose. Recently, different agricultural wastes such as wheat straw, fibers of curaua, ramie, kenaf, jute, sisal and buiti, and passion fruit peels, sunflower stalks, *etc*. are considered as potential sources of cellulose (Durmaz and Ateş, 2021; Poletto et al., 2014; Sun et al., 2004; Wijaya et al., 2017). Other sources of cellulose include algae, marine creatures (tunicates), and bacteria (Sun et al., 2004). Cellulose exists in different polymorphs (I_α, I_β, II, III_1, III_{11}, IV_1 and IV_{11}), and naturally occurs as either Cellulose I_α or I_β. The Cellulose I_β (monoclinic) crystalline plane is usually present in higher plants, while Cellulose I_α (triclinic) exists in algae, tunicates and bacteria. Cellulose II, which comprises antiparallel chains, can be prepared from Cellulose I by regeneration or mercerization with NaOH. Both cellulose chains of I_α and I_β adopt parallel configurations without intersheet hydrogen bonding. The crystal lattice gradually changes from cellulose I to cellulose II at higher alkaline concentration, and the degree of polymerisation gradually decreases (Khan et al., 2017; Sun et al., 2004; Wijaya et al., 2017). In contrast to cellulose I, cellulose II has a more stable structure, which makes it preferable for various applications (Gong et al., 2017).

Cellulose nanocrystals (CNCs), also known as nanocrystalline cellulose or cellulose nanowhiskers, are unique biopolymeric materials with nanometers size and needle-like crystal structure. CNCs are produced from plant sources with diameter of 5-20 nm and 100-500 nm in length, mainly by heat controlled acid hydrolysis followed by mechanical treatment (Abitbol et al., 2016; Durmaz and Ateş, 2021; Varma and Vasudevan, 2022; Wijaya et al., 2017). In the acid hydrolysis process, the amorphous regions in the cellulose are removed as they undergo hydrolytic cleavage, which is promoted by hydronium ions, with the release of the individual crystallites (Ditzel et al., 2017).

The CNCs usually retain Cellulose I allomorph after acid hydrolysis of disordered regions of Cellulose I materials. Cellulose II nanocrystals (CNCs-II) are usually produced from acid hydrolysis of mercerized cellulose. Additionally, CNCs-II are also prepared from Cellulose I sources under controlled reaction conditions such as mercerization conditions and acid hydrolysis

time (Xing et al., 2018). There are also reports indicating formation of CNCs-II from Cellulose I nanocrystals (CNCs-I), mercerizing the latter ones (Jin et al., 2016). Cellulose I and II nanocrystal polymorphs are different in morphology, crystal structure, self-assembling structure, and performances of their derived composites for different industrial applications (Xing et al., 2018). There are few studies which focus on the influence of preparation conditions of CNCs on polymorphic transformation of the nanocrystals (Delepierre et al., 2020; Gong et al., 2017; Xing et al., 2018).

In this study, factors such as source of cellulose, cellulose extraction and acid hydrolyis conditions were investigated on the partial polymorphic transition of cellulose to form Cellulose I and II allomorphs. Accordingly, four different lignocellulosic materials: *teff* straw (TS), *enset* fiber (EF), sugarcane bagasse (SB) and coffee hull (CH) were considered in the current study.

TS is a byproduct of one of the most common staple plants, *Teff* (*Eragrostis tef* (Zuccagni) Trotter), in Ethiopia (Lee, 2018; Minten et al., 2016). EF is a byproduct of *kocho*, a common local food in South and South West Ethiopia obtained from *Enset* plant (*Ensete ventricosum* (Welw.) Cheesman) (Berhanu et al., 2018; Gebre-Mariam and Schmidt, 1996). Sugar industries after sucrose extraction and bioethanol production generate large quantities of SB as a byproduct (Bhattacharya et al., 2008). Ethiopia, among top five coffee producers in the world, is the place of origin (Kaffa province) of *Coffee arabica*, which accounts for 65%–70% of the world's coffee production followed by *Coffee canephora* Pierre (Robusta). Coffee is among the most popular beverages on Earth (Alves et al., 2017; Aristizábal-Marulanda et al., 2017). CH is an agro-industrial residue available in huge quantities in coffee processing enterprises across Ethiopia causing significant environmental impact on the government as well as coffee processing enterprises (Gabriel et al., 2020).

4.2 Materials and methods

4.2.1 Materials

Brown TS, EF, SB and CH were collected from different parts of Ethiopia as mentioned in section 2.2.1 (Gabriel et al., 2020). Those chemicals and solvents indicated in section 2.2.1 were used as received.

4.2.2 Cellulose extraction

The cellulose extraction method reported previously (in section 2.2.2) was followed to extract cellulose fibers from the four agro-industrial byproducts following a three-stage treatment (Gabriel et al., 2020). In brief, alkaline pretreatment of the biomass with 17.5% NaOH at 1/10 (w/v) solid/liquid ratio of dry material on a water bath at 90 °C for 1.5 h, was followed by delignification with a mixture of 20% formic acid (FA)/20% acetic acid (AA)/7.5% H_2O_2 (2:1:2) and finally bleaching the pulps with 7.5% H_2O_2 in alkaline media of 10% NaOH at 1:10 (g/ml) fiber ratio. The extracted cellulose fibers were designated as -Cel.

4.2.3 Isolation of CNCs

CNCs were obtained following our previous method described in section 3.2.3 (Gabriel et al., 2021). Briefly, cellulose fibers extracted from the four plant byproducts were hydrolyzed with 64% wt/wt sulphuric acid (1:20 g/mL) at 45 °C for 30 min under vigorous stirring at 1500 rpm using magnetic stirrer. The suspension was immediately diluted 10-fold with chilled distilled water to quench the hydrolysis reaction, and centrifuged successively at 5 °C (Beckman Coulter Avanti J-20 XP Centrifuge, USA) for each 10 min at 9,000 rpm until a cloudy suspension was obtained. The precipitate was then dialyzed through dialysis sacks (Avg. flat width 35 mm, MWCO 12,000 Da, Sigma-Aldrich, USA) against distilled water until the suspension had neutral pH (5 days). Subsequently, the resulting suspension was homogenized by a disperser type Ultra-Turrax (Janke and Kunkel IKA-Labortechnik, Ultra-Turrax T50) for 5 min at 10,000 rpm twice and sonicated (BandelinSONOREX Digital 10P, Sigma-Aldrich) for 5 min. The aqueous suspension thus obtained was freeze-dried in a lyophilizer (Martin Christ Gefrieetrocknungsanlagen GmbH, CHRIST, An der UnterenSöse 50, 37520 Osterode am Harz, Germany) and dried for 72 h to obtain CNCs powder.

4.2.4 FTIR spectroscopy

The FTIR spectra of the CNCs and cellulose precursors were recorded in the range from 4000 to 450 cm^{-1} using a PerkinElmer FTIR spectrometer (L1600400 Spectrum TWO DTGS, SN: 108152, LIantrisant, UK), with no further sample preparation.

4.2.5 XRD

The crystallinity of as-obtained CNCs and cellulose precursors was performed by an XRD-7000 X-ray Diffractometer MAXima (SHIMADZU Corporation, Japan) at 40 kV, 30 mA with monochromatic Cu-Kα radiation, typically with scan speed of 3.0000°/min and sampling pitch of 0.0200°. Data acquired were plotted in Origin Pro 8.5.1 in a 2θ scale from 10 to 40.

The crystalline indices/indexes (CrIs) were calculated by the following three approaches (a-c) (Kljun et al., 2011; Poletto et al., 2014; Segal et al., 1959; Zhang et al., 1993):

a) equation proposed by Segal *et al* (Empirical method) also called Peak height method,

b) Hermans *et al* equation (Peak deconvolution method) (as shown also in Eq. 2.1 and 2.2), and

c) Zhang *et al* equation: the degree of crystallization (DoC) of the samples was also estimated by Zhang *et al* equation (Zhang et al., 1993)

$$DoC = n\frac{I_k}{I_o}x100\%; n = 0.75 \qquad (4.1)$$

where, I_o shows the intensities of the maximum diffraction from the baseline of the X-ray pattern and I_k indicates the Intensity at the base level subtracted from this value I_o. So, I_o shows Intensity at the 200 plane; and I_k is obtained by subtracting Intensity at the amorphous region from Intensity at the 200 reflection.

Additionally, the extent of conversion of Cellulose I to Cellulose II in crystalline areas was derived from the equations described elsewhere (4.2-4.5) (Mansikkamäki et al., 2007; Rånby, 1952; Zhang et al., 1993).

$$I_r = \frac{2I_{II}}{I_I+2I_{II}} \qquad (4.2)$$

where, I_r is relative intensity number; I_I and I_{II} ($I_I + I_{II} = 1.0$) are the estimated intensity ratios of diffraction peaks with Miller indices of (110) and $(1\bar{1}0)$ of Cellulose I to that of (110) Cellulose I_I. I_r is defined as zero for pure native cellulose and one for completely mercerized cellulose, intermediate values of I_r indicating partially mercerized cellulose. The intensity of I_{II} is estimated from diffraction peak (110) on C_{II} and I_I arises from lattice planes (110) and $(1\bar{1}0)$ on C_I. I_I can be

interpreted as the sum of intensities $I_{14.7} + I_{16.1}$ and I_{II} corresponds to the intensity $I_{12.0}$, then the equation is analogous to Eq. (5).

The percentage of the Cellulose II form in the crystalline aggregation, equivalent to I_r according to literature described elsewhere (Mansikkamäki et al., 2007; Zhang et al., 1993) is

$$C_{II} = \frac{I_{12.0}}{I_{12.0}+0.5(I_{14.7}+I_{16.1})} \quad (4.3)$$

Where, $I_{12.0}$, $I_{14.7}$ and $I_{16.1}$ represent the intensities of diffraction peaks around 12.0, 14.7 and 16.1 (2θ), respectively.

The percentage of Cellulose II in the samples is

$$X_{II} = DoC * C_{II} \quad (4.4)$$

The percentage of Cellulose I in the samples is, therefore,

$$X_I = DoC * (1- C_{II}) \quad (4.5)$$

After deconvolution of the respective XRD diffractograms following Gaussian profile, parameters such as d-spacings (d), apparent crystallite size or thickness for the 200 plane (τ_{200}), the proportion of crystallite interior chains for the 200 plane (X_{200}), fractional variation in the plane spacing for the 200 plane $(\Delta d/d)_{200}$, and Z-values were obtained from equations described previously and elsewhere (Aguayo et al., 2018; Poletto et al., 2014; Popescu et al., 2011).

4.2.6 TEM studies

A droplet of the diluted CNC suspension of 0.05% (w/v) after sonication was deposited on a formvar-coated copper grid. The specimen was negatively stained with 2% (w/v) uranyl acetate or a 1% (w/v) phosphotungstic acid solution and dried at room temperature. The CNC samples were observed with a LIBRA 120 PLUS TEM (Carl Zeiss Microscopy, Jena, Germany) operating at 120 kV. Images were taken with a BM-2k-120 Dual-Speed on axis SSCCD-camera (TRS, Moorenweis, Germany). ImageJ was used to estimate the average length, diameter and aspect ratio, the ratio of the length to the diameter, of respective CNCs isolated from each plant material.

4.2.7 TGA properties

The thermal degradation properties of the CNCs and cellulose precursors were performed with TGA/DTG (Differential Thermo Gravimetry)-60H (SHIMADZU Corporation, Japan) to study the degradation characteristics. The samples were heated from room temperature to 700 °C at a heating rate of 10 °C/min and a nitrogen gas flow rate of 60 mL/min.

4.3 Results and discussions

4.3.1 CNCs isolation condition, and yield

During the process of isolation of CNCs, white gel-like materials from TS, EF and SB cellulose fibers were obtained after hydrolysis followed by centrifugation. However, the color of the material obtained from CH cellulose was yellowish black which may indicate carbonization during the hydrolysis process or presence of lignin in the extracted cellulose. It was also reported elsewhere that the yellowish color of CNCs could be due to carbonization of cellulose during hydrolysis and/or the presence of residual organic substrates, including lignin and hexenuronic groups (de Oliveira et al., 2019). Additionally, formation of colored low-molecular furan-type compounds or carbonyl groups in the cellulose chains might also be a reason for yellowish black color of CNCs (Heggset et al., 2017). The highest CNCs yield was obtained from TS cellulose (56.3%), and the least from CH cellulose (30.0%). The yields of EF-CNCs (II) and SB-CNCs (II) were 54.7% and 42.0%, respectively.

4.3.2 Crystallinity investigations

From the XRD patterns, the isolated CNCs from EF and SB cellulose displayed a co-existence of Cellulose I and Cellulose II like their cellulose precursors. The partial conversion of Cellulose I to Cellulose II in the EF-CNCs and SB-CNCs was confirmed by the presence of additional three sharp high diffraction peaks at around 12.0°, 20.0° and 22.0° 2θ, for the plane indices of $(1\bar{1}0)$, (110) and (200), respectively, which were assigned to Cellulose II (Ahmadzadeh et al., 2018; Ahuja et al., 2018; Gong et al., 2018). Additionally, the appearance of doublet in the main peak around 22° 2θ also confirmed the CNCs from EF and SB cellulose contained Cellulose II type. Formation of diffraction peak at around 12.0° 2θ in TS-CNCs like TS cellulose precursors showed presence of small fraction of Cellulose-II. However, no formation of CNCs-II was observed from CH cellulose in similar cellulose extraction as well as acid hydrolysis conditions. The XRD patterns of CNCs from TS, EF, SB and CH, and their cellulose precursors are shown in Fig. 4.1.

Generally, the formation of Cellulose I and II allomorphs in the as-obtained CNCs was dependent on the cellulose source and cellulose extraction condition, and less influenced by sulfuric acid hydrolysis. From the results, it is evident that sulfuric acid hydrolysis did not induce complete or partial polymorphic transition of Cellulose I to II in the CNCs isolated except in TS. However, the higher alkaline condition during the process of cellulose extraction mainly in EF and SB caused

the partial conversion both in as-extracted cellulose and the respective CNCs (Fig. 4. 1). A similar finding was reported elsewhere where the acid hydrolysis of cellulose did not influence the crystallographic structure of CNCs (Borysiak and Grząbka-Zasadzińska, 2016). However, few studies indicate the contribution of sulfuric acid hydrolysis for the formation of Cellulose II or a mixture of Cellulose I and II allomorphs in the CNCs isolated from different sources such as oil palm microcrystalline cellulose (MCC) I, eucalyptus cellulose I and Tetra pak cellulose fibers, and *Pongamia pinnata* oil meal (Flauzino Neto et al., 2016; Haafiz et al., 2014; Nataraj et al., 2022; Xing et al., 2018).

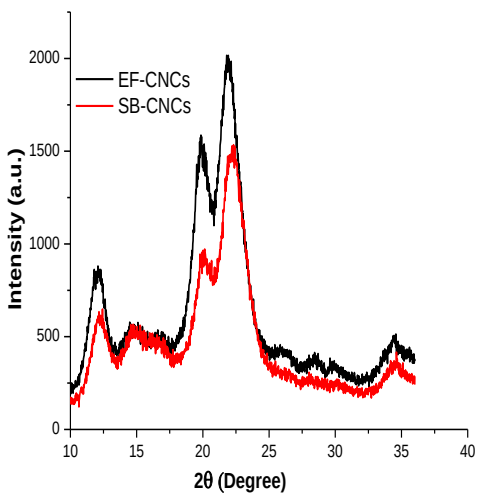

(a)

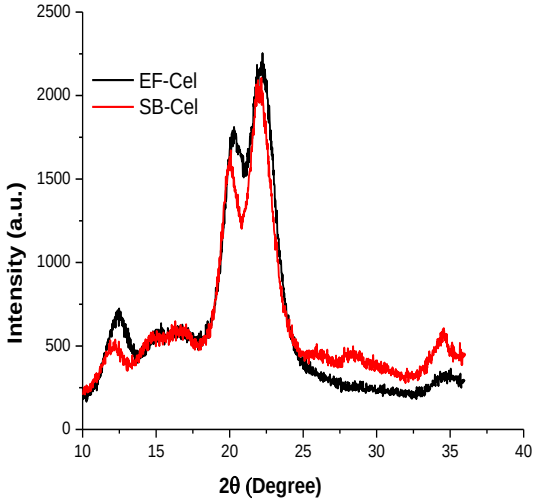

(b)

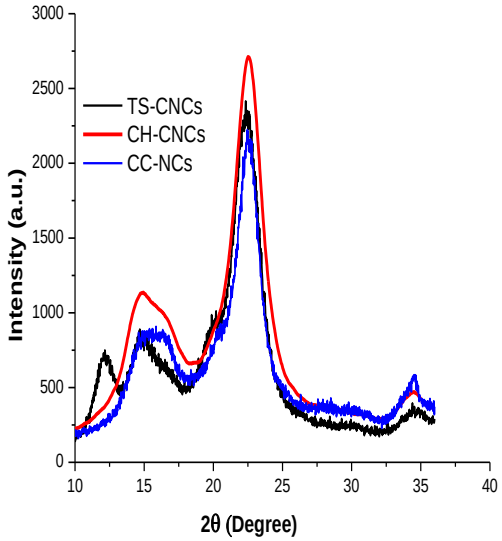

(c)

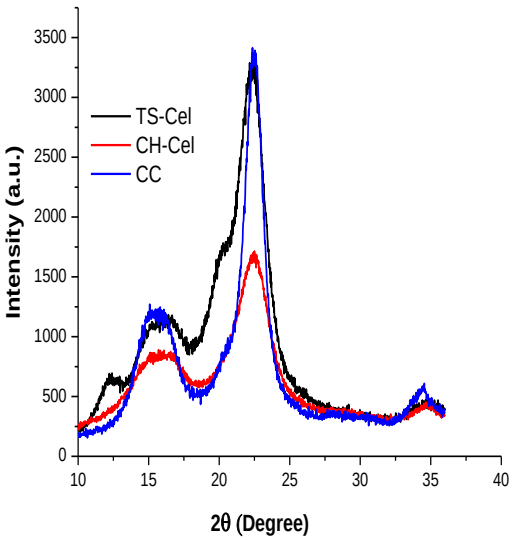

(d)

Fig. 4.1: X-ray diffractograms of CNCs of EF and SB (a), and their cellulose precursors (b); and CNCs of TS and CH (c), and their cellulose precursors (d). (Key: CNCs-cellulose nanocrystals; Cel-cellulose; TS-*teff* straw; EF-*enset* fiber; SB-sugarcane bagasse; CH-coffee hull; CC-NCs-cellulose nanocrystals isolated from commercial cellulose (CC) included for comparison).

Crystallinity indices (CrIs) were determined following three approaches by Segal *et al*, Herman *et al* and Zhang *et al* in this study (Eqs. 2.1, 2.2, and 4.1). Higher values of CrI for each material was observed in Segal *et al* method (Park et al., 2010). Almost equivalent values of CrI for each sample were observed according to the Herman *et al* and Zhang *et al* approaches. For comparison purpose, Segal *et al* method for estimation of CrI is used in the literature, which is simple and gives helpful information (Aguayo et al., 2018; Naduparambath and Purushothaman, 2016; Prado and Spinacé, 2019; Taflick et al., 2017).

From the CNCs containing considerable fraction of Cellulose II allomorphs, EF-CNCs (76.4%; 56.7%) had higher CrI than SB-CNCs (65.4%; 44.8%) following the Segal *et al* and Hermans *et al* approaches, respectively. No drastic decrement of CrIs was recorded in the CNCs-II of EF and SB when compared to CrIs of their cellulose precursors. Other studies also reported (slight) reduction of crystallinity of as-obtained CNCs (Haafiz et al., 2014; Korolovych et al., 2018), which could be due to the partial degradation of the crystalline regions (Ventura-Cruz and Tecante, 2019). However, the CrIs of CNCs-I isolated from CH containing only Cellulose I, and TS-CNCs showed increment which could be due to the hydrolytic scission of the glycosidic bonds releasing individual crystals and removing the amorphous domains only (García-García et al., 2018).

Thus, cellulose extraction at higher alkaline condition resulted with both partial polymorphic transition from Cellulose I to Cellulose II in the native cellulose and the respective CNCs isolated from TS, EF and SB. Furthermore, lower CrIs of CNCs obtained from EF and SB were recorded as compared to CNCs isolated from cellulose fibers extracted at lower alkaline condition (5% and 10% NaOH) (Gabriel et al., 2021). Generally, CrI continuously decreases in the CNCs with an increase in alkali concentration used in the treatment (Jin et al., 2016).

Table 4.1 shows different parameters obtained from the (deconvoluted) XRD of CNCs and their cellulose precursors such as CrIs by the three approaches, d-spacings, crystallite sizes at the 200 plane (τ_{200} values), the proportion of crystallite interior chains for the 200 plane (X_{200}) as well as the fractional variation in the plane spacing for the 200 plane ($\Delta d/d_{200}$) and Z-Values (equations

mentioned under section 2.2.5). The Cellulose II fraction present in the EF-CNCs (78.9%) was the highest followed by SB-CNCs (63.4%), TS-CNCs (41.9%), and CH-CNCs (0%) when considering the intensities at the diffraction lattices of 200 and 110 around 22 and 20^{o} 2θ, respectively. Moreover, the percentage of the Cellulose II form in the crystalline aggregation and the cellulose samples were estimated employing the equations described elsewhere (under section 2.2.5) (Zhang et al., 1993). The highest Cellulose II form was found in EF-CNCs (62.1%, 35.6%) in the crystalline aggregation and the samples, respectively and the Cellulose I in the EF-CNCs was (37.8%, 21.8%), respectively. However, no fraction of Cellulose II was observed in CH-CNCs which could be due to high lignin content in CH hindering polymorphic transition even at higher alkaline conditions in the pretreatment stage (Gabriel et al., 2020).

The d-spacings of the CNCs ranged from 0.599-0.732, 0.449-0.528, 0.394-0.404, and 0.257-0.260 for the planes of $1\bar{1}0$, 110, 200, and 040 as shown in Table 4.1. Higher values of d-spacings for the plane of $1\bar{1}0$, and lower values for 110 plane were recorded for EF-CNCs and SB-CNCs where partial polymorphic transformation occurred. In a study reported elsewhere, the d-spacings of the $1\bar{1}0$, 110, 200 lattice planes for cellulose I are 0.601 ± 0.06, 0.535 ± 0.05 and 0.392 ± 0.02, respectively. These values shifted to 0.741 ± 0.06, 4.43 ± 0.03 and 0.408 ± 0.04 for cellulose II (Jin et al., 2016). The τ_{200} values of CNCs from the four plant sources ranged from 3.86-4.09 nm, and X_{200} and $\Delta d/d_{(200)}$ ranged from 0.496-0.520; 0.0917-0.0980, respectively. There is inverse relationship between CrIs and $\Delta d/d_{(200)}$ of the CNCs (Table 4.1). Hydroxide ions penetrate easily into the matrix and therefore shift the concentration required for polymorphic transformation of CNC to a lower value and within a narrower range (Jin et al., 2016). The negative numbers of the Z-Values in the CNCs isolated from CH indicated that no complete or partial polymorphic transformation happened (Kim et al., 2010; Poletto et al., 2012), as indicated in Table 4.1 and from the XRD patterns (Fig.4.1).

Table 4.1: Parameters obtained from the (deconvoluted) XRD of Cellulose II allomorphs in the CNCs from TS, EF and SB, and Cellulose I allomorph in the CNCs from CH, as well as their cellulose precursors.

Materials	d-spacings (nm)				τ_{200} (nm)	X_{200}	$\Delta d/d_{200}$	CrIs (%) according to			Z-Values
	$1\bar{1}0$	110	200	040				Segal *et al*	Hermans *et al*	Zhang *et al*	
TS-CNCs	0.732	0.587	0.396	0.259	3.861	0.497	0.0963	81.21	53.96	60.91	160.76
TS-Cel	0.732	0.563	0.396	0.259	2.935	0.374	0.1269	74.13	59.62	55.60	182.95
EF-CNCs	0.734	0.449	0.404	0.257	3.876	0.498	0.0980	76.42	56.72	57.32	258.83
EF-Cel	0.716	0.560	0.401	0.258	4.091	0.520	0.0920	78.79	59.05	59.09	156.88
SB-CNCs	0.724	0.444	0.399	0.258	4.089	0.520	0.0917	65.43	44.84	49.07	276.33
SB-Cel	0.731	0.547	0.394	0.257	3.881	0.499	0.0954	77.32	55.61	57.99	195.85
CH-CNCs	0.599	0.528	0.394	0.260	3.859	0.496	0.0959	75.67	60.30	56.75	-11.15
CH-Cel	0.613	0.539	0.397	0.261	3.483	0.453	0.1071	66.41	54.10	49.81	2.48
CC-NCs	0.604	0.541	0.394	0.260	4.415	0.550	0.1287	74.91	54.776962	56.18	-14.18
CC	0.608	0.554	0.395	0.260	6.480	0.679	0.0573	87.23	64.77	65.42	-19.85

(Key: CNCs-cellulose nanocrystals; Cel-cellulose; TS-*teff* straw; EF-*enset* fiber; SB-sugarcane bagasse; CH-coffee hull; CC-NCs-cellulose nanocrystals isolated from commercial cellulose (CC) included for comparison).

4.3.3 Chemical functionality studies

As observed in Fig. 4.2, the peak in the region around 3333 cm^{-1} represents stretching vibration of the OH groups of cellulose in the CNCs and cellulose precursors. The transmittance bands around 2988-2900 cm^{-1} correspond to the CH stretching of methyl and methylene groups in cellulose (Aguayo et al., 2018; García-García et al., 2018), but intensified in the CNCs and celluloses extracted from TS and EF at higher alkaline conditions with formation of double peaks in the same region (Ventura-Cruz and Tecante, 2019). The peak around 1642 is due to the adsorbed water in the CNCs as well as cellulose precursors. The bands around 1473 and 1380 cm^{-1} reflect CH symmetric and asymmetric deformations, respectively. The absorbance at 1327cm^{-1} is attributed to the CC and CO skeletal vibrations (Sun et al., 2005). The relative increase in the intensity of the band near 895 cm^{-1} (C1 group frequency) in CNCs obtained at lower acid hydrolysis time indicates the coexistent of cellulose II (Xing et al., 2018). In studies by Oh and research group(Oh et al., 2005a, 2005b), most FTIR bands including 2901, 1431, 1282, 1236, 1202, 1165, 1032, and 897 cm^{-1} were shifted to higher wave number (by 2–13 cm^{-1}) during transformation of Cellulose I to Cellulose II by the mercerization conditions (15–20 w/w % NaOH) and carbon dioxide treatment. However, the bands at 3352, 1373, and 983 cm^{-1} were shifted to lower wave number (by 3–95 cm^{-1}).

The bands observed at ~1160 cm^{-1} and ~1101 cm^{-1} are attributed to the ring CC bending vibration and COC glycoside ether bond of the β-1,4-glycosidic ring linkages between the D-glucose units in cellulose. The absorption in the range ~1024–1047 cm^{-1} observed in the spectra of CNCs corresponds to the CH stretching vibration of the cellulose component. Peaks at 1061 cm^{-1} refer to the CO stretching (Smyth et al., 2017). The peak around 890 cm^{-1} in the spectra of cellulose and respective CNCs is attributed to the interactions between β-glycosidic C_1H deformation linkages and glucose units of cellulose (Aguayo et al., 2018; Zhanhong Wang et al., 2019).

The appearance of a new small peak around 1205 cm^{-1} in the CNCs spectra is related to S=O vibration, and shows the esterification reaction during the hydrolysis process (García-García et al., 2018). The acid hydrolysis did not change the cellulose molecular structure in the formation of CNCs, rather intensified few peaks around 2900, 1370, 1230, 1060 and 890 cm^{-1} (Gao et al., 2020; Xiao et al., 2019).

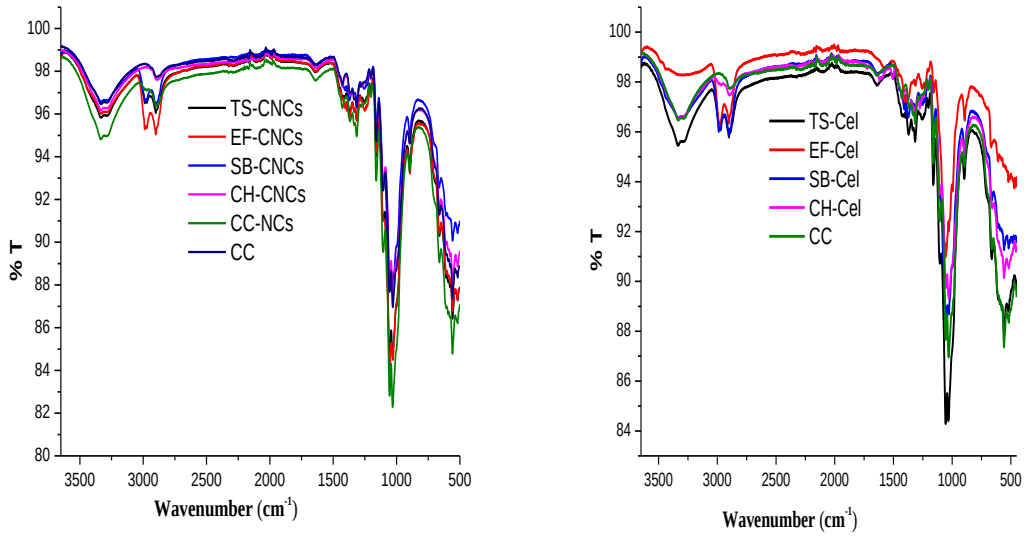

Fig. 4.2: FTIR spectra of CNCs isolated (Left), and cellulose precursors (Right). (Key: CNCs-cellulose nanocrystals; Cel-cellulose; TS-*teff* straw; EF-*enset* fiber; SB-sugarcane bagasse; CH-coffee hull; CC-NCs-cellulose nanocrystals isolated from commercial cellulose (CC) included for comparison).

4.3.4 Morphological and dimensional analyses

The morphological studies by TEM showed that all the CNCs obtained from the cellulose fibers extracted from the plant byproducts were needle-shaped (Fig. 4.3). TEM images showed the acid hydrolysis was effective for isolating CNCs. Relatively clear images were taken for most CNCs when phosphotungstic acid solution was used rather than uranyl acetate (images by uranyl acetate not shown).

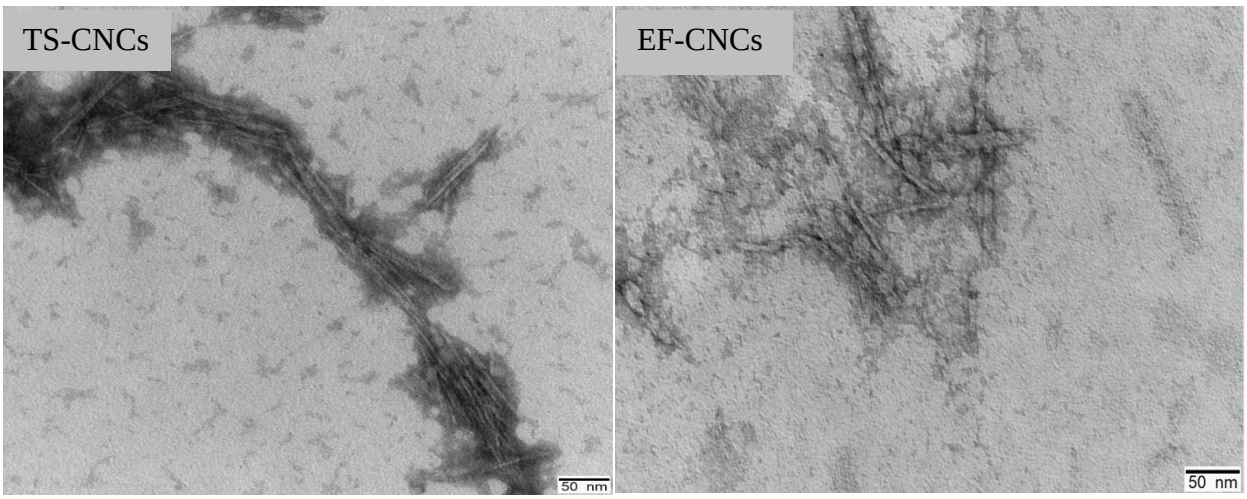

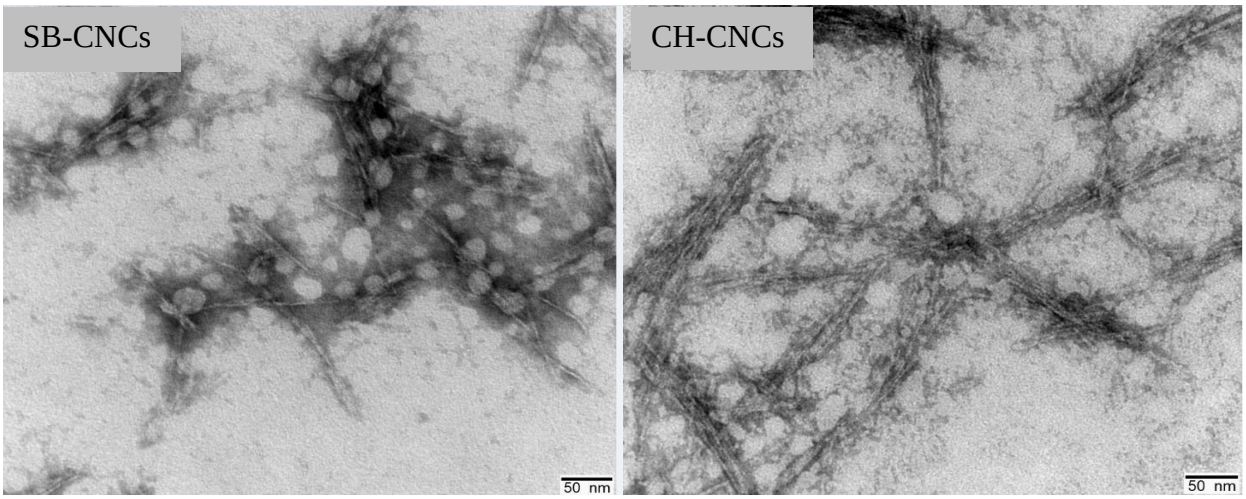

Figure 4.3: Transmission electron micrographs of CNCs isolated from the celluloses extracted (bar scale: 50 nm). (Key: CNCs-cellulose nanocrystals; TS-*teff* straw; EF-*enset* fiber; SB-sugarcane bagasse; CH-coffee hull).

The average length, diameter and aspect ratio of the CNCs ranged from 62 to 121 nm, 5.5 to 10.9 nm, 8.95-16.38, respectively (Table 4.2). In our previous study, higher aspect ratios of CNCs from the four plant samples (17.32-36.68) were recorded when the CNCs were isolated from the cellulose fibers extracted with lower NaOH concentration (5%) at the pretreatment stage (Gabriel et al., 2021). In the literature, it was reported that higher alkaline concentration as well as an increase in the acid hydrolysis time resulted in a significant decrease in the average length and diameter of the CNCs due to the destruction of amorphous regions and even partial crystalline regions of cellulose (Gong et al., 2018, 2017; Jin et al., 2016; Taflick et al., 2017; Xiao et al., 2019). According to studies reported elsewhere (Borysiak and Grząbka-Zasadzińska, 2016; Delepierre et al., 2020), the Cellulose II of the CNCs had a smaller particle size than Cellulose I of the CNCs, which could be due to partial depolymerization of cellulose chains by mercerization. CNCs particles with short-length can be easily obtained when Cellulose I is converted to cellulose II before sulfuric acid hydrolysis (Gong et al., 2017). Reports indicate that CNCs with high aspect ratios (above 10) exhibit good mechanical properties (bending strength, tensile strength and Young's modulus) (Ferreira et al., 2018).

Table 4.2: TEM dimensional analysis of CNCs isolated from celluloses extracted from various plant byproducts.

Source (CNCs)	$L_{average}$(nm)	Diameter D; $D_{average}$(nm)	Aspect ratio
TS-CNCs	62.306 ± 13.166	2.5-15.05; 6.82 ± 3.25	9.14
EF-CNCs	89.534 ± 21.401	6.67-18.15; 5.47 ± 1.939	16.38
SB-CNCs	120.59 ± 24.576	6.22-17.46; 10.864 ± 3.21	11.10
CH-CNCs	86.4 ± 17.469	3.54-13.31; 9.651±2.36	8.95

(Key: $L_{average}$-average length; $D_{average}$-average diameter of CNCs estimated by ImageJ Software; CNCs-cellulose nanocrystals; TS-*teff* straw; EF-*enset* fiber; SB-sugarcane bagasse; CH-coffee hull; CC-NCs-cellulose nanocrystals isolated from commercial cellulose (CC) included for comparison).

4.3.5 Thermal properties

Fig. 4.4. shows the thermal degradation behaviors of CNCs isolated, and their cellulose precursors. A clear difference was observed in the TGA and corresponding DTG (Differential Thermo Gravimetry) curves of cellulose and respective CNCs. The first temperature range between 30-110 °C showed small weight loss (3.9-5.6%) at T_{max} 59-67 °C mainly due to water evaporation (Hemmati et al., 2019). The onset degradation temperature (T_i), the maximum degradation temperature (T_{max}) and maximum weight loss (rate) as well as residue at 550 °C of the CNCs and cellulose precursors are listed in Table 4.3.

Two major degradation regions were observed from the DTG curves of all CNCs. The first degradation with weight loss of 34-38% occurred in the region at 134-300 °C (T_{max} 215-233 °C; (weight loss rate: 0.18-0.21 %/°C), which is mainly due to decomposition of surface sulfate groups and large specific surface area, when compared to the cellulose precursors (T_{max}: 328-346 °C). The other degradation step was recorded in the region 277-465 °C (T_{max}: 335-358 °C) with weight loss of 19-24%, due to breakdown of the interior non-sulfated cellulose crystals (Prado and Spinacé, 2019; Silvério et al., 2013; Xing et al., 2018). As depicted in Fig. 4.4 and Table 4.3, the reduction in thermal stability was more pronounced for the conversion of cellulose to CNCs rather than the partial polymorphic transition from CNC-I to CNC-II. Such a lower degradation temperature in the CNCs may be attributed to the introduction of the negatively charged sulfate half ester groups and a larger number of free ends of chains in CNCs caused by the sulfuric acid hydrolysis The thermal degradation behaviors of CNC-I and CNC-II were similar, and the acid hydrolysis had a slight effect on the thermal degradation behaviors of CNC-I and CNC-II, as reported elsewhere

(Gong et al., 2018, 2017). However, a decrease in thermal stability was also exhibited in cellulose fibers or CNCs upon polymorphic transition from Cellulose I to Cellulose II (Ciolacu and Popa, 2006). Enhanced thermal stability was also reported elsewhere (Nataraj et al., 2022; Yue, 2011) indicating that mercerized samples had better thermal stability properties. All the CNCs exhibited higher char residues at 550 °C than cellulose counterparts due to a dehydration effect of the sulfate group as flame retardants (Rhim et al., 2015; Silvério et al., 2013; Xing et al., 2018). Furthermore, the CNCs also showed slightly higher char residues at 550 °C than CNCs-5% reported in our previous work (Gabriel et al., 2021).

(a)

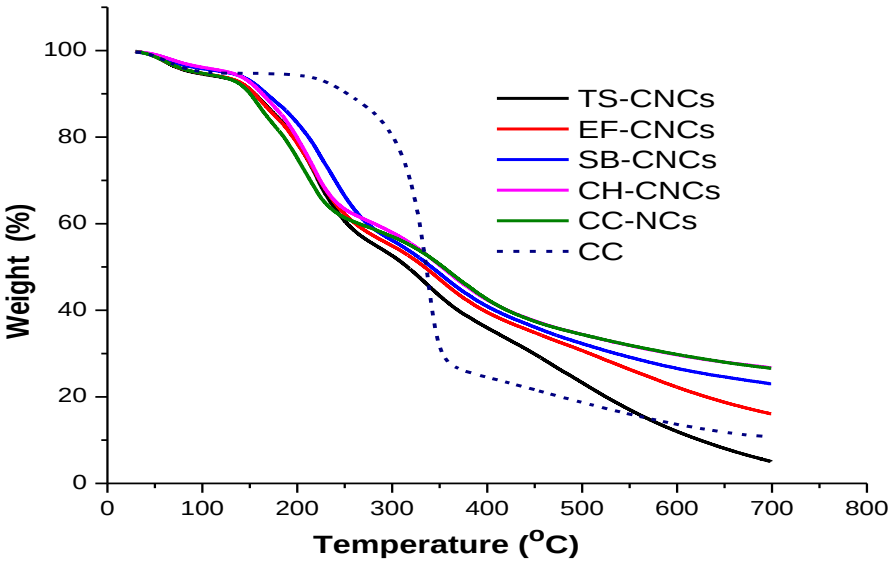

(b)

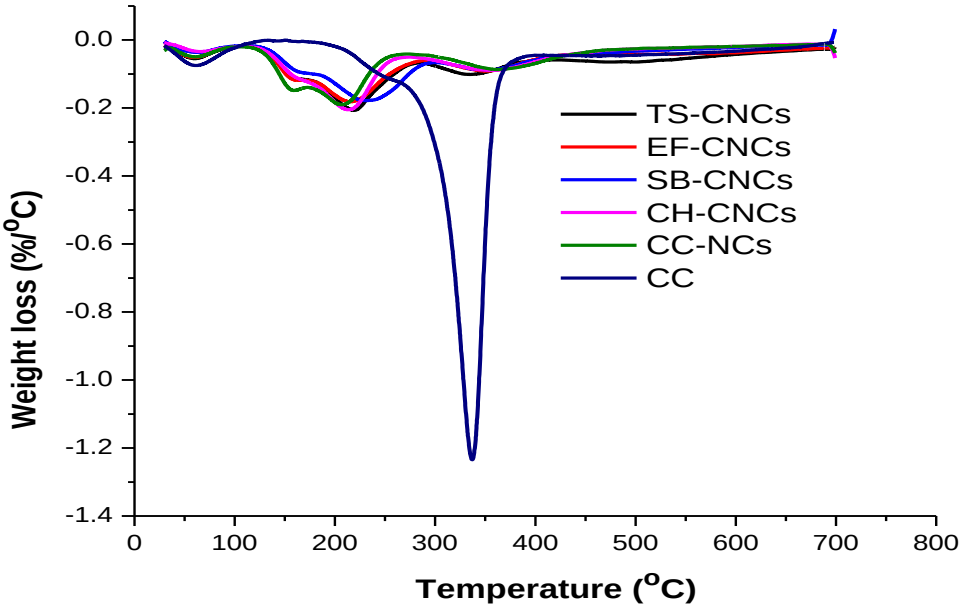
0.0
-0.2
-0.4
-0.6
-0.8
-1.0
-1.2
-1.4
Weight loss (%/°C)
0
100
200
300
400
500
600
700
800
Temperature (°C)
TS-CNCs
EF-CNCs
SB-CNCs
CH-CNCs
CC-NCs
CC

(c)

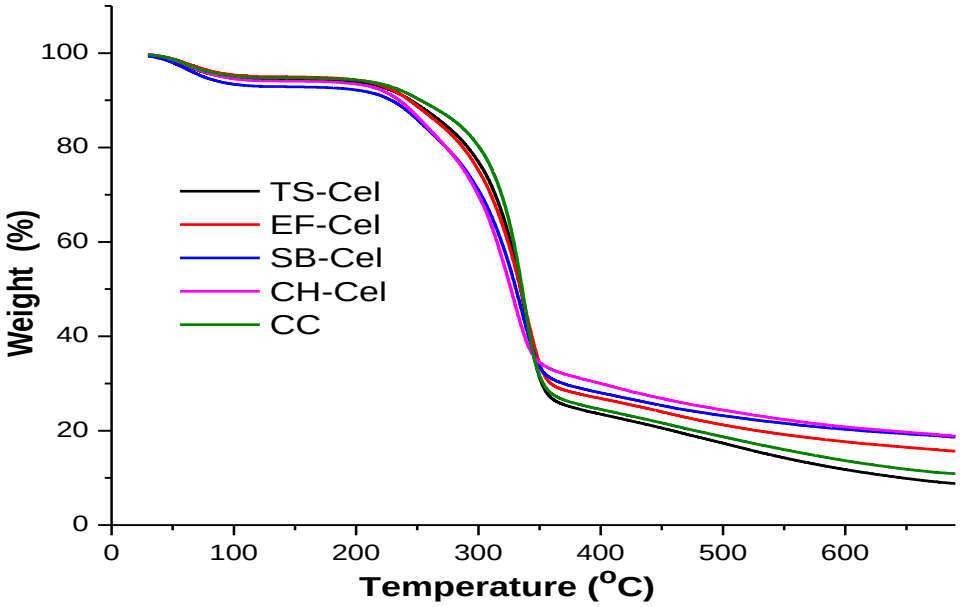
100
80
60
40
20
0
Weight (%)
0
100
200
300
400
500
600
Temperature (°C)
TS-Cel
EF-Cel
SB-Cel
CH-Cel
CC

(d)

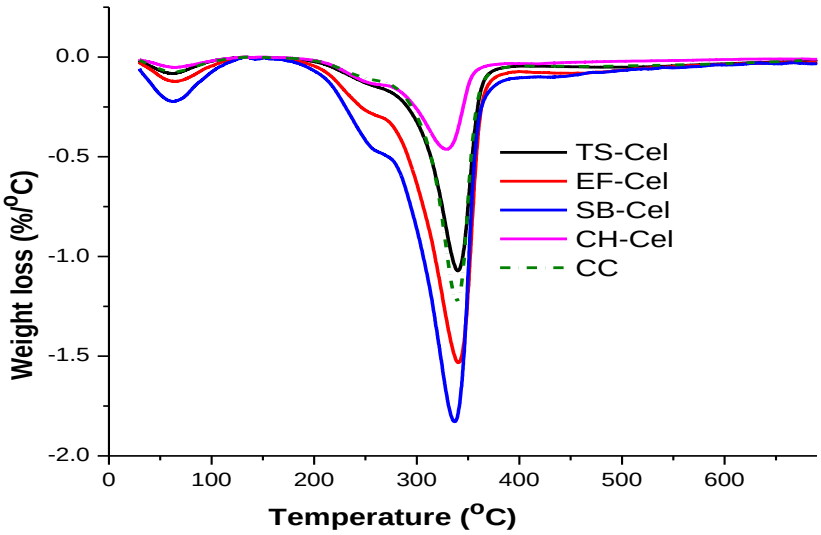

Fig. 4.4: Thermal degradation characteristics of as-isolated CNCs using TGA (a) and DTG (b), and their cellulose precursors using TGA (c) and DTG (d). (Key: CNCs-cellulose nanocrystals; Cel-cellulose; TS-*teff* straw; EF-*enset* fiber; SB-sugarcane bagasse; CH-coffee hull; CC-NCs-cellulose nanocrystals isolated from commercial cellulose (CC) included for comparison).

Table 4.3: Summary of thermogravimetric characteristics of TGA and DTG of the CNCs and cellulose precursors.

Material	ΔT (°C)	T_{max} (°C)	Weight loss (%)	Weight loss rate (%/°C)	T_i (°C)	Residue at 550 °C (%)
TS-CNCs	29.77-110.22	59.94	5.64	0.0548	134.96	16.99
	134.96-283.58	219.16	38.13	0.2069		
	284.72-413.59	334.80	20.38	0.1012		
TS-Cel	29.70-109.04	61.69	6.25	0.1081	207.15	9.73
	207.15-390.23	342.88	47.52	1.0979		
	390.23-550.00	517.18	14.11	0.0797		
EF-CNCs	29.77-109.56	59.04	5.36	0.0510	133.95	26.36
	133.95-287.37	216.65	36.82	0.1815		
	287.37-418.71	335.76	18.78	0.1011		
EF-Cel	29.99-121.38	65.62	3.15	0.0846	210.43	20.66
	210.43-400.22	346.67	69.04	1.6778		
	400.22-550.00	438.86	5.81	0.0637		
SB-CNCs	29.77-105.07	65.91	3.93	0.0367	139.53	29.12
	139.53-300.39	233.27	37.99	0.1779		
	300.39-433.82	351.61	18.55	0.0884		
	29.72-125.25	57.64	4.85	0.1382		

SB-Cel	199.76-399.47	340.68	66.59	1.4264	196.76	20.26
	399.47-550.00	469.58	7.40	0.0759		
CH-CNCs	29.77-108.21	66.69	3.85	0.0339	134.96	31.86
	134.96-272.07	214.15	33.63	0.2050		
	276.57-464.69	357.53	24.04	0.0893		
CH-Cel	29.77-109.00	56.35	5.48	0.0568	282.45	21.56
	282.45-390.20	327.57	46.24	0.4862		
	390.20-550.00	423.13	9.91	0.0392		
CC-NCs	29.77-108.65	59.94	5.29	0.0495	152.56	31.90
	152.56-171.4	158.6	5.52	0.1484		
	142.00-237.01	206.244	28.60	0.1903		
	286.85-478.15	361.67	22.58	0.0868		
CC	30.16-108.49	62.60	4.70	0.0749	268.93	15.91
	268.93-378.50	338.76	62.20	1.2165		
	378.50-550.00	463.49	9.85	0.0470		

(Key: CNCs-cellulose nanocrystals; Cel-cellulose; TS-*teff* straw; EF-*enset* fiber; SB-sugarcane bagasse; CH-coffee hull; CC-NCs-cellulose nanocrystals isolated from commercial cellulose (CC) included for comparison).

4.4 Conclusion

The higher alkaline condition during cellulose extraction resulted in partial polymorphic transition of native cellulose of TS, EF and SB and the respective CNCs into Cellulose II. EF-CNCs (II) and SB-CNCs (II) exhibited reduction of CrIs, yield, length and aspect ratios when compared to CNCs obtained from celluloses pretreated with 5% NaOH. EF-CNCs (II) had the highest CrI and Cellulose II fraction among CNCs containing Cellulose II allomorphs. Morphological and dimensional studies by TEM revealed formation of needle-shaped nano-scaled particles. Two major decomposition processes of the CNCs were recorded at T_{max} 215-233 °C and 335-358 °C. In general, the physicochemical properties of the isolated CNCs were dependent on the source of cellulose, cellulose extraction and acid hydrolysis conditions, but the polymorphic transitions were more dependent on the first two. Lignocellulosic materials with high lignin content such as CH do not easily undergo polymorphic transition even at higher alkaline pretreatment condition. The large-scale use of CH-CNCs may be limited due to poor yield and appearance. From the results, CNCs with Cellulose I and Cellulose II allomorphs can be produced by controlled treatment conditions from the plant byproducts based on their chemical compositions for potential value-added industrial applications.

5 Physicochemical characterization of carboxymethyl cellulose from local agro-industrial byproducts

5.1 Introduction

The increasing demand of green industry has driven the researchers to develop ecofriendly and low-cost materials from biowastes (Naceur Abouloula et al., 2018). The plant biomass consists of cellulose, hemicelluloses, lignin, pectins, gums, mucilages, starch and proteins. Cellulose is the most abundant organic compound on earth. Woody plants and cotton are the major sources of cellulose and cellulose derivatives for industrial use, but cost has made it imperative that other materials be investigated as potential sources (Adel et al., 2011; Chen and Lou, 2014; Nascimento et al., 2016; Saputra et al., 2015; Singh and Singh, 2013). In our previous work (Gabriel et al., 2020), alternative sources of celluloses were explored from TS, EF, SB and CH, abundant lignocellulosic resources in Ethiopia extracted using relatively simple and eco-friendly method. It was also reported that agro-industrial residues have low cost, high availability, and are easy to collect and are attractive alternative materials to wood, cotton, and linter (Nascimento et al., 2016).

The strong inter- and intra-molecular hydrogen bonds have limited the industrial application of cellulose as it neither melts nor dissolves readily in common solvents. Consequently, cellulose is modified mainly chemically to improve process-ability and to produce cellulose derivatives (cellulosics) which can be tailored for specific industrial applications (Adinugraha et al., 2005). The typical chemical modifications of cellulose are esterification and etherification at the hydroxyl groups of cellulose (Kamel et al., 2008). Carboxymethylation of cellulose is a versatile modification by etherification because it provides access to water-swellable or water-soluble polymers and intermediates with various valuable features (Varshney et al., 2006).

Sodium carboxymethyl cellulose (SCMC) is a linear, long chain, water soluble, anionic, semi-synthetic polysaccharide. SCMC is produced by aqueous alkali swollen cellulose reaction with monochloroacetic acid (MCA) in surplus of organic solvent (e.g. isopropanol or ethanol) (Singh and Singh, 2013).

SCMC is among the most widely used natural polymer derivatives in various industries such as food, pharmaceuticals, detergents, toiletries, surgical prosthetics, incontinence, personal hygiene, electrical elements, papermaking, and textile and cosmetic products. In pharmaceutical industries, it is used as viscosity inducing and stabilizing agent in oral liquids, as a tablet binder and

disintegrant, gelling agents, humectants, as a muco-adhesive in self-adhesive ostomy, wound care, and dermatological patches and to absorb wound exudate or transepidermal water and sweat (Hooton, 2009; Zhao et al., 2003).

The quality of the resulting CMC is expressed by several parameters, such as, the DS, purity and the presence of functional groups. The value of DS is affected by several factors, including the type of reaction medium, the concentration of alkali, the concentration of MCA, reaction time and reaction temperature (Hooton, 2009; Khullar et al., 2005; Saputra et al., 2015; Waring and Parsons, 2001).

CMC has been obtained from various (lignocellulosic) materials such as agricultural wastes of spent tea leaves, sugarcane bagasse, coconut fibres, oil palm fibres, dried duckweed and palm kernel cake (Huang et al., 2017), almond shells, almond stems, and fig stems (Moussa et al., 2019), bacterial cellulose (Casaburi et al., 2018; Schlufter and Heinze, 2010), bamboo shaving (Chen and Lou, 2014; Khullar et al., 2007), banana stem and peel (Yuliasmi et al., 2019) and banana pseudo-stem (Adinugraha et al., 2005), corn cobic waste (Singh and Singh, 2013), cotton linters (Haleem et al., 2014; Zhao et al., 2003) and cotton stalk (Zhang et al., 2011), durian rind (Rachtanapun et al., 2012), grapefruit peel (Karataş and Arslan, 2016), *Lantana camara* (Varshney et al., 2006), mesquite tree (Salama et al., 2018), orange peel (Yaşar et al., 2007), paper waste (He et al., 2009; Joshi et al., 2015), pineapple peel (Dai et al., 2019), pomelo peel (Chumee and Seeburin, 2014), recycled newspaper (Ünlü, 2013), rice husk (Abdulhameed et al., 2019), rice straw (Ragheb et al., 2012), seaweed (Lakshmi et al., 2017), sago biomass (Veeramachineni et al., 2016), spruce sulfite pulp (Heinze and Pfeiffer, 1999), water hyacinth (Barai et al., 1997; Saputra et al., 2015), waste textiles (Bidgoli et al., 2014), wheat straw, barley straw, and rice hull (Biswas et al., 2014),

However, so far, to the best of our knowledge, no research has described the preparation and physicochemical characterization of CMC from TS, EF and CH for potential value-added applications. Despite the fact that preparation of CMC from SB was reported elsewhere (Candido and Gonçalves, 2016; Golbaghi et al., 2017), it was considered in this study as a reference material in a new cellulose extraction method we reported in our previous work (Gabriel et al., 2020) and for comparison purpose along with CMC prepared from commercial cellulose (CMC-CC) as well as commercial SCMC (C-SCMC).

The objective of the study was to prepare and characterize CMC obtained from celluloses of TS, EF, SB and CH, abundant and unexploited agro-industrial byproducts locally, and investigate the influence of the source of cellulose and carboxymethylation condition on DS. The chemical functionality, crystallinity, morphology and thermal stability of the CNCs were analyzed using FTIR, XRD, SEM and TGA.

5.2 Materials and methods

5.2.1 Materials

The lignocellulosic resources; namely, TS, EF, SB and CH collected during the previous work (Gabriel et al., 2020) in section 2.2.1 were used. Monochloroacetic acid (Sigma-Aldrich, Germany), glacial acetic acid (Riedel-de Haën), acetone and sodium hydroxide 97% (HiMedia, Mumbai, India), isopropanol 99.5% (Indenta Chemicals, India), HCl 37% (BDH, England), phenolphthalein (Alpha Chemoka, India), formic acid 98% (Central Drug House (P) Ltd. New Delhi, India), commercial SCMC (C-SCMC) (UNI-CHEM Co. Ltd., South Korea), nitric acid 69-70%, commercial cellulose (CC), iodine 99%, methanol 99.9% (LOBA CHEMIE-Laboratory, India) and hydrogen peroxide 30% (CARLO ERBA reagents, France) and ethanol absolute (Fisher Scientific, UK) were used as received.

5.2.2 Cellulose extraction

Celluloses were extracted from plant byproducts: TS, EF, SB and CH according to our previous method in section 2.2.2 following three stages treatment (Gabriel et al., 2020).

5.2.3 Preparation of CMC

First, cellulose fibers were mixed with isopropanol in the proportion of 1/20 (w/v) followed by dropwise addition of 30% NaOH solution (1/4 (w/v) cellulose:NaOH) under stirring for 30 min and continued stirring for another 1 h at 25 °C to form alkali cellulose. Then, MCA in a ratio of 1:1.14 (cellulose:MCA, g/g) was added dropwise to the mixture under stirring for 15 min following preliminary studies. The temperature of the reaction was set at 55 °C for a reaction time of 3.0 h in water bath. Then, the mixture was decanted, and the CMC was dispersed in 40 ml absolute methanol under stirring in order to precipitate CMC and ease drying. After 40 min, pure acetic acid was added dropwise to neutralize the mixture. The mixture was then filtered and washed four times with 40 ml of 70% ethanol and was washed again with 40 ml of absolute methanol to remove

undesired salts. Finally, the CMC was dried in an oven (Kottermann® 2711, Lüdenscheid, Germany) at 60 °C for 12 h (Golbaghi et al., 2017; Joshi et al., 2015; Lakshmi et al., 2017), and the yield was estimated on a dry weight basis considering the initial weight of cellulose fibers and final weight of dried CMC (Yeasmin and Mondal, 2015).

5.2.4 Identification tests and properties of CMC

Solubility, pH, appearance of powder and solution, color, ash values, moisture content of the as-obtained CMC from the four byproducts were determined according to the methods described in different pharmacopeias (BP, 2016b; PhEur, 2013; USP41-NF36, 2019b).

5.2.5 Determination of degree of substitution (DS)

One gram of CMC was weighed and added to 250 mL beaker followed by 50 mL of 95% ethanol and stirred. Then, 5 mL of 2 M nitric acid was added and the mixture stirred for 10 min at room temperature. The mixture was then heated to boiling by using magnetic hot plate for 5 min and stirred further for 20 min and left to settle. After the solution had settled, the solution was filtered and the residue was washed with 100 mL 95% ethanol until the acid and salts were removed. The precipitate was washed with methanol and transferred to beaker and heated until the alcohol was removed. The beaker with the precipitate was dried in the oven at 90 °C for 3 h.

CMC (0.5 g) was weighed in 250 mL Erlenmeyer flask and 100 mL distilled water added and stirred. Twenty-five milliliter 0.5 M sodium hydroxide was added and boiled for about 20 min. Then the heated solution was titrated with 0.3 M HCl by using phenolphthalein as an indicator to observe the color change from Mexican pink (dark pink) to colorless. The DS of CMC was then calculated using the equations below (Haleem et al., 2014; Joshi et al., 2015; Pushpamalar et al., 2006).

$$DS = \frac{0.162XA}{1 - 0.058XA}$$

$$A = \frac{BC - DE}{F}$$

determined using the following equations:

Where:

A: the required weight of alkali per gram of sample; B: the amount of NaOH solution (ml)

C: the normality of NaOH solution; D: the amount of HCl solution (ml)

E: the normality of HCl solution; F: the weight of sample (g)

5.2.6 Rheological properties of CMC

A CAP2000 Viscometer (AMETEK Brookfield, 11 Commerce Blvd, Middleboro, MA 02346 United States) was used to determine the viscosities of the samples at 3% (w/w) varying the shear rate from 5 to 500 rpm.

5.2.7 FTIR spectroscopy studies

FTIR experiments were conducted using a PerkinElmer FTIR spectrometer (L1600400 Spectrum TWO DTGS, SN: 108152, LIantrisant, UK). The FTIR spectra of as-obtained CMC, as well as CMC-CC and C-SCMC were recorded in the range from 4000 to 450 cm^{-1}, with no further sample preparation.

5.2.8 XRD investigations

XRD analyses were performed using an XRD-7000 X-ray Diffractometer MAXima (SHIMADZU Corporation, Japan) at 40 kV, 30 mA with monochromatic Cu-Kα radiation, typically with scan speed of 3.0000 °/min and sampling pitch of 0.0200 °. Data acquired were plotted in Origin Pro 8.5.1 in a 2θ scale from 10 to 40. The as-obtained CMC, as well as CMC-CC and C-SCMC were examined.

The *CrIs* for Cellulose I were determined using the equation proposed by Segal et al. (Segal et al., 1959) (section 2.2.5):

For Cellulose II, the *CrIs* were calculated using the equation mentioned below (Revol et al., 1987):

$$CrI = \frac{(I_{110} - I_{15.0^\circ})}{I_{110}} x100\%$$

Where, I_{110} is the maximum intensity (in arbitrary units) of the diffraction from the 110 plane around 2θ=20°, and $I_{15.0^\circ}$ is the intensity (in arbitrary units) at 2θ=15°.

5.2.9 TGA analyses

TGA was performed using DTG (Differential Thermo Gravimetry)-60H (SHIMADZU Corporation, Japan) to study the degradation characteristics. The as-obtained CMC, as well as CMC-CC and C-SCMC were heated from room temperature to 700 °C at a heating rate of 10 °C/min and a nitrogen gas flow rate of 60 mL/min.

5.2.10 SEM studies

The ESEM images as-obtained CMC, as well as CMC-CC and C-SCMC were obtained using ESEM FEI/Philips XL-30 ESEM (Leuven, Belgium) at an accelerating voltage of 2.00 KV. All the samples were coated with chromium using vacuum sputter prior to SEM analysis.

5.2.11 Statistical analysis

The experiments were conducted in triplicates and the data were presented as the mean ± standard deviation (SD). All data reported in this study were the averages of triplicate determinations, and analyzed using OriginPro 8.5.1 (OriginLab Corporation, MA, USA) and Excel 2016. *P* value of less than 0.05 was considered to be evidence for a significant difference, and a Tukey's test for one-way analysis of variance (ANOVA) was applied when necessary.

5.3 Results and discussions

5.3.1 Properties of as-obtained CMC

CMC was prepared from the celluloses previously extracted from the four agro-industrial byproducts, namely, TS, EF, SB and CH following the two steps of carboxymethylation: first, the alkalization by NaOH then etherification using MCA under heterogeneous conditions (Singh and Singh, 2013; Varshney et al., 2006). Isopropyl alcohol was a solvent of choice medium due to its unique carboxymethylation properties, and it was also used in most other studies (Heinze and Pfeiffer, 1999; Schlufter and Heinze, 2010; Varshney et al., 2006; Yuliasmi et al., 2019), but few other solvents were also employed such as ethanol (Chen and Lou, 2014), benzene/ethanol mixture (Zhao et al., 2003), isopropyl alcohol and isobutanol mixture. The crystalline form of natural cellulose is destroyed in the alkalization step forming amorphous alkalized cellulose (Cell-O-Na^{+}) so that MCA diffuses easily to enhance the carboxymethylation process (Saputra et al., 2015; Zhao et al., 2003). Furthermore, the influence of amount of MCA, reaction media (methanol, isopropyl alcohol, and ethanol) and reaction time on DS was investigated in the preliminary work.

The as-obtained CMC occurred as a white to almost white, tasteless, odorless and free-flowing granular powder. The CMC samples were soluble in water forming highly viscous solution, and film but insoluble in ethanol, acetone, ether and toluene, fulfilling the parameters specified in pharmacopeias (BP, 2016b; PhEur, 2013; USP41-NF36, 2019b).

The yield of as-obtained CMC ranged from 1.28 g/g (for CH-CMC) to 1.55 g/g (for EF-CMC) based on dry weight conditions (Table 5.1). CMC obtained from EF cellulose exhibited the highest DS (1.18) and %carboxymethyl (30.09%), but the least DS (0.714) and %carboxymethyl (20.65%) were observed in SB-CMC (Table 5.1). The yield, DS as well as % carboxymethyl of as-obtained CMC products were dependent on the source of cellulose at similar carboxymethylation condition.

Table 5.1: Properties of CMC obtained from TS, EF, SB and CH.

SN	Sample	DS	%Carboxymethyl	Yield (g/g)
1.	TS-CMC	0.771 ± 0.201	21.83 ± 4.454	1.40 ± 0.050
2.	EF-CMC	1.175 ± 0.098	30.09 ± 1.770	1.55 ± 0.100
3.	SB-CMC	0.714 ± 0.116	20.65 ± 2.704	1.35 ± 0.072
4.	CH-CMC	0.957 ± 0.050	25.96 ± 1.022	1.28 ± 0.067
5.	CMC-CC	0.989 ± 0.089	26.55 ± 1.770	1.29 ± 0.040
6.	C-SCMC	0.741 ± 0.156	21.24 ± 3.540	--

The least DS values were obtained in all as-obtained CMC when 1:0.75 and 1:1.00 ratio of Cellulose: MCA (g/g) was used but the highest DS was observed in EF-CMC when 1:1.14 ratio was followed (Fig. 5.1a). Different DS was obtained for each CMC prepared from the byproducts at similar carboxymethylation conditions. Additionally, a reaction time of 2.50 h yields the least DS for all as-obtained CMC (Fig. 5.1b).

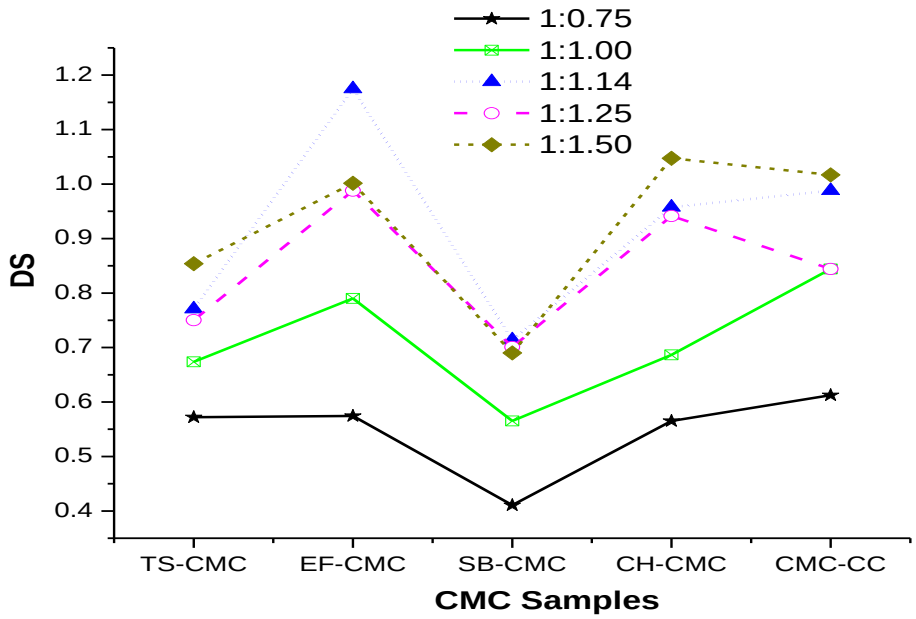

(a)

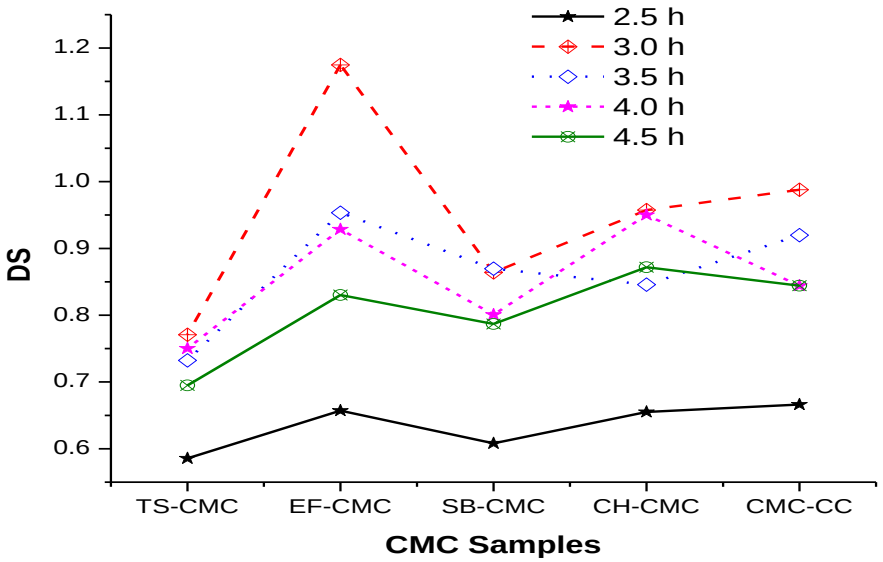

(b)

Fig. 5.1: (a) Effect of amount of MCA (Cellulose: MCA g/g) on DS (NaOH: 30%; Temp: 55 °C; Time: 3.0 h). (b) Effect of reaction time on DS (NaOH: 30%; Temp: 55 °C; Cellulose to MCA:

1:1.14 g/g). (Key: TS-*teff* straw; EF-*enset* fiber; SB-sugarcane bagasse; CH-coffee hull; CC-commercial cellulose; CMC-Carboxymethylcellulose obtained from the celluloses; CMC-CC:-Carboxymethylcellulose obtained from CC included for comparison).

All the samples exhibited a shear thinning behavior as confirmed by decreased viscosity when the shear rate increased from 5 to 500 rpm (Fig. 5.2).

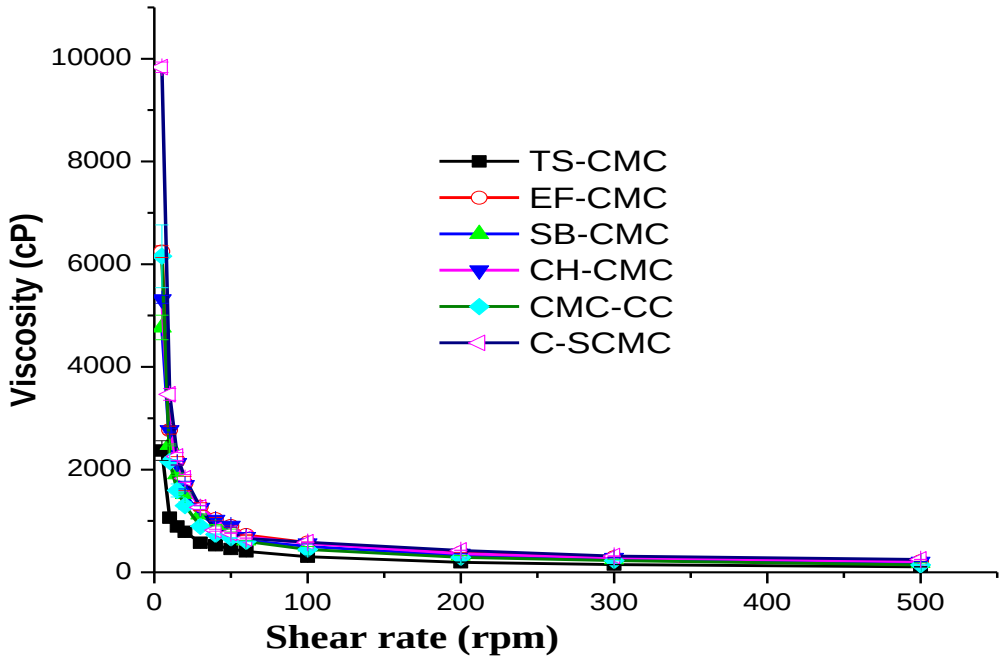

Fig. 5.2: Relationship curve between viscosity and shear rate of the samples. (Key: TS-*teff* straw; EF-*enset* fiber; SB-sugarcane bagasse; CH-coffee hull; CC-commercial cellulose; CMC-Carboxymethylcellulose obtained from the celluloses; CMC-CC:-Carboxymethylcellulose obtained from CC included for comparison).

5.3.2 FTIR spectroscopy properties

Fig. 5.3 shows the FTIR spectra of cellulose and as-obtained CMC from the four plant byproducts, and CMC obtained from CC, and C-SCMC. All the samples showed peaks in the range of 3200-3400 cm^{-1} and 2800-2900 cm^{-1} which are attributed to the stretching vibrations of OH of the polyhydroxylated saccharide backbone and CH groups stretching within each glucose unit, respectively (Naceur Abouloula et al., 2018; Ventura-Cruz and Tecante, 2019; Zhanhong Wang et al., 2019). The appearance of strong absorption bands in the as-obtained CMC around 1600 and

1412 cm^{-1} proved the successful attachment of carboxymethyl groups to the cellulose chains (Biswas et al., 2014; Chumee and Seeburin, 2014; Huang et al., 2017; Klemm et al., 1998; Naceur Abouloula et al., 2018; Veeramachineni et al., 2016). It was also reported elsewhere that the presence of carboxymethyl substituents in CMC was confirmed by the appearance of peaks in the region of 1590-1640 cm^{-1} and 1390-1450 cm^{-1} representing absorption bands of COO and CH_2, respectively (Adinugraha et al., 2005; Basta et al., 2016; Candido and Gonçalves, 2016; He et al., 2009; Heinze and Pfeiffer, 1999; Klemm et al., 1998; Rachtanapun et al., 2012; Ünlü, 2013; Veeramachineni et al., 2016). A band around 1640 cm^{-1} appeared in all cellulose samples which may be due to the bending mode of the absorbed water (Ahuja et al., 2018), but it was not observed in the FTIR spectra of as-obtained CMC as it was probably masked by the carboxymethyl group. The bands around 1329.32 cm^{-1} and 1112.65 cm^{-1} are assigned to OH bending vibration and COC stretching, respectively (Yeasmin and Mondal, 2015).

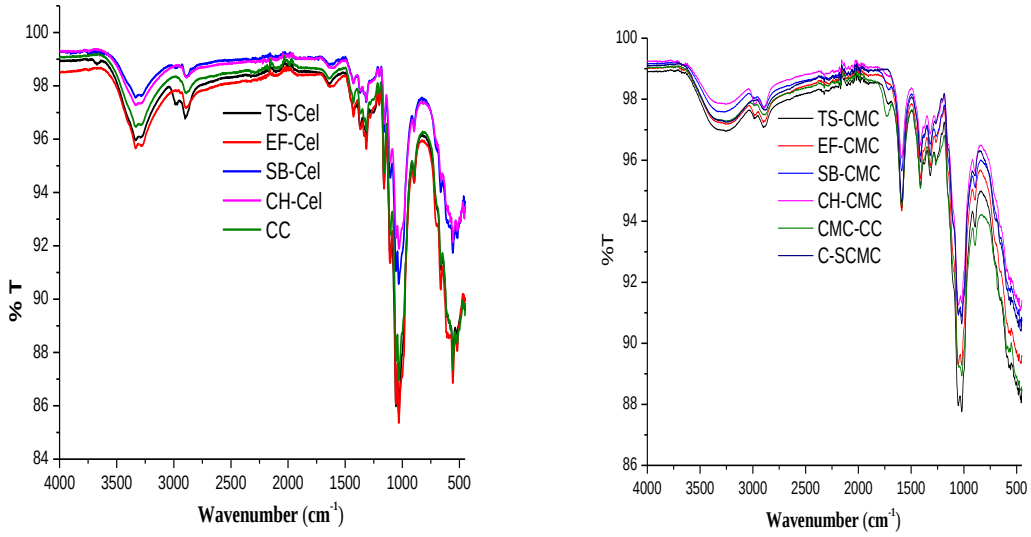

Fig. 5.3: FTIR spectra of the celluloses extracted from the four plant byproducts (left), and the as obtained CMC (right). (Key: TS-*teff* straw; EF-*enset* fiber; SB-sugarcane bagasse; CH-coffee hull; Cel-cellulose extracted from the byproducts; CC-commercial cellulose; CMC- Carboxymethylcellulose obtained from the celluloses; CMC-CC:-Carboxymethylcellulose obtained from CC; and C-SCMC:-Commercial sodium carboxymethyl cellulose, the last three included for comparison).

The peaks at about 1030 cm^{-1} and 890 cm^{-1} are associated with the CO stretching and glycosidic C_1H deformation, a ring vibration, and OH bending (C_1OC_4), showing the β-1,4-glycosidic linkages of each glucose ring of cellulose, respectively (Veeramachineni et al., 2016; Ventura-Cruz and Tecante, 2019). The intensity of the absorption band around 3335 decreases after etherification because of the conversion of Cellulose I to II, significant reduction in crystallinity and/or formation of the amorphous components due to weakening of hydrogen bonding between cellulose chains.

The peaks in the FTIR spectra at 1429, 1315, 1035, and 896 cm^{-1} represented typical cellulose absorption peaks assigned for CH_2 bending, CH_2 rocking, CO stretching and CH or CH_2 bending. Additionally, the peak at 896 cm^{-1} can be attributed to the typical structure of cellulose due to the β-glycosidic linkages of the glucose ring of the cellulose chain (Chieng et al., 2017).

5.3.3 Crystallinity analyses

Fig. 5.4 shows the XRD patterns of cellulose extracted from the four untreated plant byproducts and as-obtained CMC. The XRD peaks of all as-obtained CMC samples showed the broad and typical diffraction signal around 2θ=20°, followed by other strong peaks around 29° and 32° for SB-CMC with low DS, which could be due to presence of metallic impurity. However, all the as-extracted cellulose fibers showed the typical lattice of Cellulose I, with characteristic peaks around 2θ values of 15°, 16°, 22.5° and 34° (Veeramachineni et al., 2016). In another study, a high intensity peak of CMC was observed at 2θ of 19.7, followed by smaller peaks around18.4, 22.7, 25.3, and 28.4° (Basu et al., 2018) .

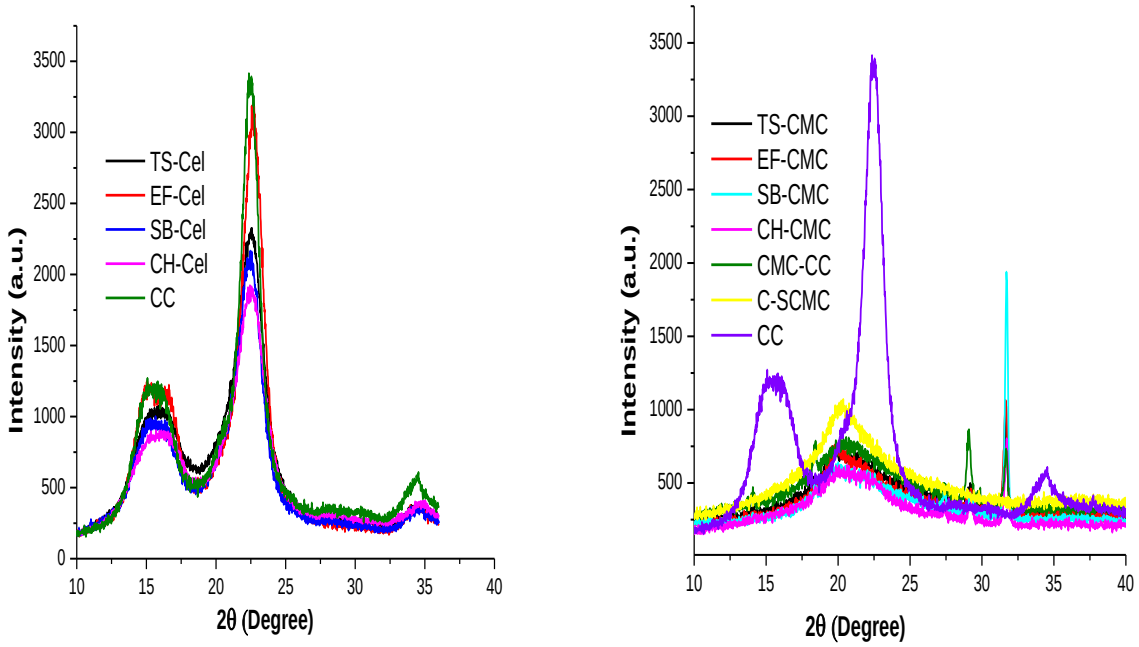

Fig. 5.4: X-ray diffractograms of the celluloses extracted from the four plant byproducts (left), and the as-obtained CMC (right). (Key: TS-*teff* straw; EF-*enset* fiber; SB-sugarcane bagasse; CH-coffee hull; Cel-cellulose extracted from the byproducts; CC-commercial cellulose; CMC- Carboxymethylcellulose obtained from the celluloses; CMC-CC:-Carboxymethylcellulose obtained from CC; and C-SCMC:-Commercial sodium carboxymethyl cellulose, the last three included for comparison).

The CMC samples had peaks of lower intensity than the cellulose precursor samples. The CrIs of the as-obtained CMC (SB-CMC: 55.00%; TS-CMC: 55.23%; CMC-CC: 55.42%; CH-CMC: 60.19%; C-SCMC: 61.50% and EF-CMC: 65.20%) were reduced significantly upon carboxymethylation when compared to the CrIs of the cellulose precursors which ranged from 77.90% (CH-Cel), 78.00% (TS-Cel), 80.92% (SB-Cel), 85.56% (EF-Cel) to 87.23% (CC). This is most likely because of the destruction of the crystalline structure of cellulose and cleavage of hydrogen bonds due to alkalization by NaOH along with swelling prior to the carboxymethylation process (Golbaghi et al., 2017; Singh and Singh, 2013; Tuan Mohamood et al., 2021).

It was also reported that the decrease in the crystallinity could also be due to an increase in the electrostatic interactions between the CMC as a result of the anionic carboxymethyl groups substituted for the OH groups of cellulose (Veeramachineni et al., 2016). Additionally, the

substitution of carboxymethyl group to the backbone of cellulose leads to the transformation of polymorphs cellulose I in cellulose to polymorphs of cellulose II in CMC (Alves et al., 2015; Dai et al., 2019; He et al., 2009; Rashid and Dutta, 2022; Rasid et al., 2021; Veeramachineni et al., 2016). Based on respective diffraction peaks, CMC appears to be more amorphous when compared to cellulose fibers. It was also reported that the crystallinity almost disappeared when the DS increased (Yeasmin and Mondal, 2015).

5.3.4 Thermal stability behaviors

The thermal degradation behaviors of the as-obtained CMC and cellulose precursors are indicated in Figs. 5.5 and 5.6, and Table 5.2. A small weight loss was observed in all samples in the maximum and low-temperature range from 60-70 °C for as-obtained CMC (7-11%) as well as 56-60 °C for the celluloses (3-6%), corresponding to the evaporation of absorbed water (Veeramachineni et al., 2016). The maximum weight loss of as-obtained CMC ranged from 38.92-47.50 % (with a loss rate of 0.4293-0.5993 %/°C), which was lower than that of cellulose precursors (46.24-69.04 %) with a loss rate of 0.4863-0.7625 %/°C). Moreover, a 50% weight loss happened in a relatively lower temperature range of 305.02-327.73 °C for as-obtained CMC when compared to 327.73-341.29 °C for cellulose precursors (Table 5.2). Elsewhere, it was reported that CMC shows two stages of decomposition with lower weight loss and lower temperatures (Salama et al., 2018).

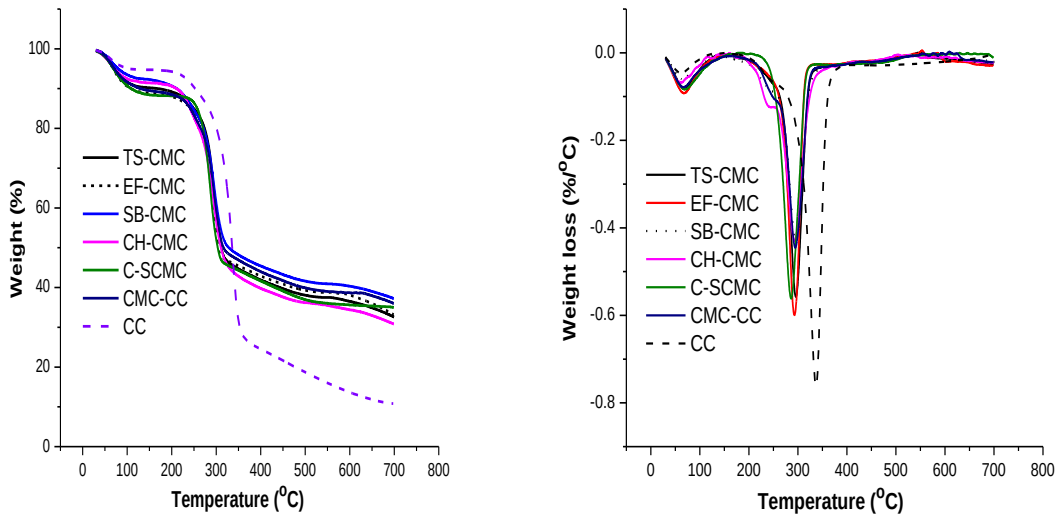

Fig. 5.5: Thermal degradation behaviors: TGA (left) and DTG (right) of as-obtained CMC from the cellulose extracted from the four plant byproducts. (Key: TS-*teff* straw; EF-*enset* fiber; SB-sugarcane bagasse; CH-coffee hull; Cel-cellulose extracted from the byproducts; CC-commercial cellulose; CMC:-Carboxymethylcellulose obtained from the celluloses; CMC-CC:-Carboxymethylcellulose obtained from CC; and C-SCMC:-Commercial sodium carboxymethyl cellulose, the last three included for comparison).

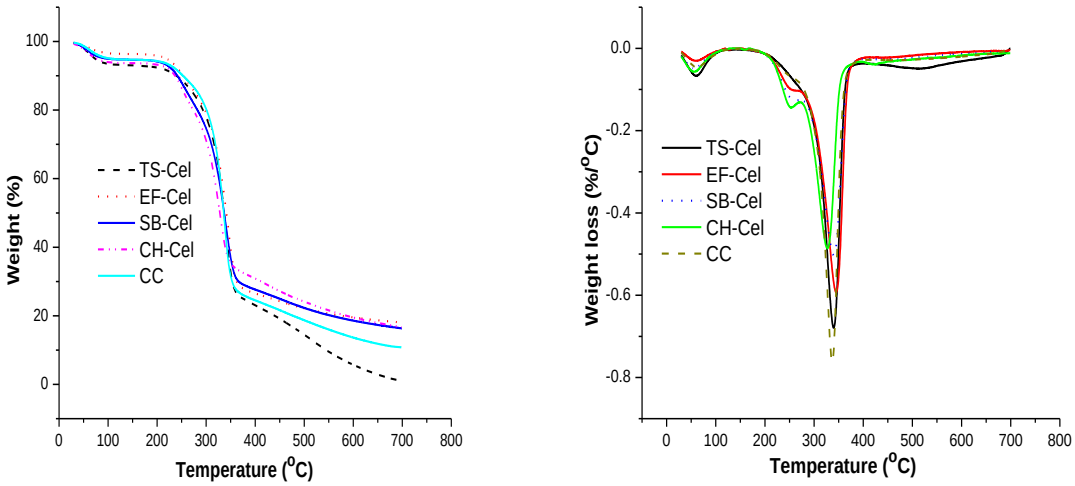

Fig. 5.6: Thermal degradation behaviors: TGA (left) and DTG (right) of celluloses extracted from the four plant byproducts, and CC. (Key: TS-*teff* straw; EF-*enset* fiber; SB-sugarcane bagasse; CH-coffee hull; Cel-cellulose extracted from the byproducts; CC-commercial cellulose; CMC:- Carboxymethylcellulose obtained from the celluloses; CMC-CC:-Carboxymethylcellulose obtained from CC; and C-SCMC:-Commercial sodium carboxymethyl cellulose, the last three included for comparison).

Table 5.2: Summary of thermal characteristics of TGA and DTG of the as-obtained CMC and the cellulose precursors from the four plant byproducts, CC, CMC-CC, and C-SCMC.

Material	**ΔT (°C)**	**T_{max} (°C)**	**Weight loss (%)**	**Weight loss rate (%/°C)**	**$T_{50\%}$ (°C)**	**Residue at 550 °C (%)**	**Residue at 700 °C (%)**
TS-Cel	29.70-109.04	59.94	6.25	0.0668	336.11	9.73	1.16
	207.15-390.23	340.00	47.52	0.6791			
	390.23-550.00	517.18	14.11	0.0797			
TS-CMC	29.77-127.26	69.99	9.22	0.0798	311.49	37.49	32.58
	204.92-331.23	296.21	42.93	0.5570			
	331.23-550.00	390.55	8.56				
	29.99-121.38	59.94	3.15	0.0302			
	210.43-400.22	343.76	69.04	0.5914			

EF-Cel	400.22-550.00	438.86	5.81	0.0637	341.29	20.66	18.07
EF-CMC	29.77-130.61	67.92	10.54	0.0923	305.02	38.72	33.18
	230.05-319.27	293.12	39.14	0.5993			
	319.27-550.00	410.33	8.40	0.0106			
SB-Cel	29.72-125.25	56.77	4.85	0.0490	336.58	20.26	16.31
	199.76-399.47	340.30	66.59	0.5920			
	399.47-550.00	469.58	7.40	0.0759			
SB-CMC	29.77-124.18	65.52	7.02	0.0617	327.73	40.90	37.25
	212.60-332.27	294.75	40.25	0.4322			
	332.27-550.00	396.87	8.74				
CH-Cel	29.77-109.00	56.35	5.48	0.0568	327.73	21.56	16.61
	282.45-390.20	327.57	46.24	0.4862			
	390.20-550.00	423.13	9.91	0.0392			
CH-CMC	29.77-115.92	63.60	7.48	0.0675	308.74	35.51	30.83
	206.24-351.02	292.93	47.50	0.4293			
	351.02-550.00	415.54	7.25	0.0117			
CC	30.16-108.49	62.76	4.70	0.0462	335.82	15.91	10.81
	268.93-378.50	336.95	62.20	0.7625			
	378.50-550.00	463.49	9.85	0.0239			
CMC-CC	29.77-127.62	66.93	10.60	0.0786	316.28	38.98	36.01
	225.50-330.00	294.10	38.92	0.4452			
	330.00-550.00	406.75	9.30				
C-SCMC	29.77-129.50	70.51	10.39	0.0834	303.14	36.05	34.99
	228.61-325.01	285.83	42.18	0.5613			
	325.01-550.00	413.44	9.63				

Key:-ΔT-Temperature change where main weight loss occurs; T_{max}-Maximum degradation (maximum weight loss) temperature; $T_{50\%}$-Degradation temperature where 50% weight loss occurs; TGA-Thermogravimetric analysis; DTG-Differential thermogravimetry; Cel-Cellulose precursor(s); TS-*teff* straw; EF-*enset* fiber; SB-sugarcane bagasse; CH-coffee hull; CMC- carboxymethyl cellulose obtained from the celluloses; CC-Commercial cellulose, C-SCMC:-Commercial sodium carboxymethyl cellulose and CMC-CC:-Carboxymethylcellulose obtained from CC included for comparison).

The maximum degradation temperature (T_{max}) of the as-obtained CMC (285-296 °C) decreased as compared to cellulose (327-340 °C) which may be due to the decarboxylation of COO groups in CMC and the loss of CO_2 (Golbaghi et al., 2017; Lakshmi et al., 2017) as well as decomposition of cellulose, named as the volatilization stage (Basta et al., 2016). Elsewhere, it was reported that the reduction in the thermal stability observed could be associated with the reduction in crystallinity upon carboxymethylation (Casaburi et al., 2018), due to the presence of sodium and interference with crystallinity as the presence of random irregularities produced by the relatively bulky side groups of carboxymethyl substituted on the cellulose backbone (Veeramachineni et al., 2016). Hence, the migration of Na^+ into the cellulose lattice planes disrupts the hydrogen bonded

crystalline region and, therefore, weakens the energy bonding of cellulose, which results in reduced stability of CMC to heat. On contrary, enhanced thermal stability of CMC was reported upon carboxymethylation of cellulose (Golbaghi et al., 2017).

In the last stage of decomposition, the weight loss of all samples was significantly small (< 15%) with slow degradation rates (0.0117-0.0128 %/°C for CMC; 0.0239-0.0797 %/°C for celluloses). At 700 °C, as-obtained CMC exhibited higher residual weights (30.83-37.25%) than cellulose precursors (1.16-18.07%). Higher residual weights of CMC than the cellulose precursors at 700 °C were also observed in different studies (Golbaghi et al., 2017; Salama et al., 2018).

5.3.5 Morphological properties

The surface morphology of extracted celluloses and as-obtained CMC is illustrated in Figs. 5.7, and 5.8. The extracted cellulose samples clearly show unique cellulose structure. The appearance in CMC sample exhibits a very different surface morphology where it is more rod-like (or ribbon shaped), granular, compact, corroded and denser than cellulose (Joshi et al., 2015; Moussa et al., 2019; Veeramachineni et al., 2016; Yeasmin and Mondal, 2015), which is due to the chemical insertion and attachments of reacting species with the pulp. Furthermore, it was reported that the particles obtained after carboxymethylation were nearly clavate in shape and rough (Alves et al., 2015; Klunklin et al., 2021; Veeramachineni et al., 2016; Zhang et al., 2011). However, in studies reported elsewhere (Rasid et al., 2021; Suriyatem et al., 2020), the exterior surface of CMC appeared smooth and less twisted and ruptured when compared with the cellulose precursors. There is no much difference in the diameters of as-obtained CMC (15-27 μm), and the diameters of the cellulose fibers (6-24 μm) (Table 5.3), but much lower than the diameters of the untreated plant byproducts which ranged from 160 μm (TS) to 965 μm (CH) (Gabriel et al., 2020).

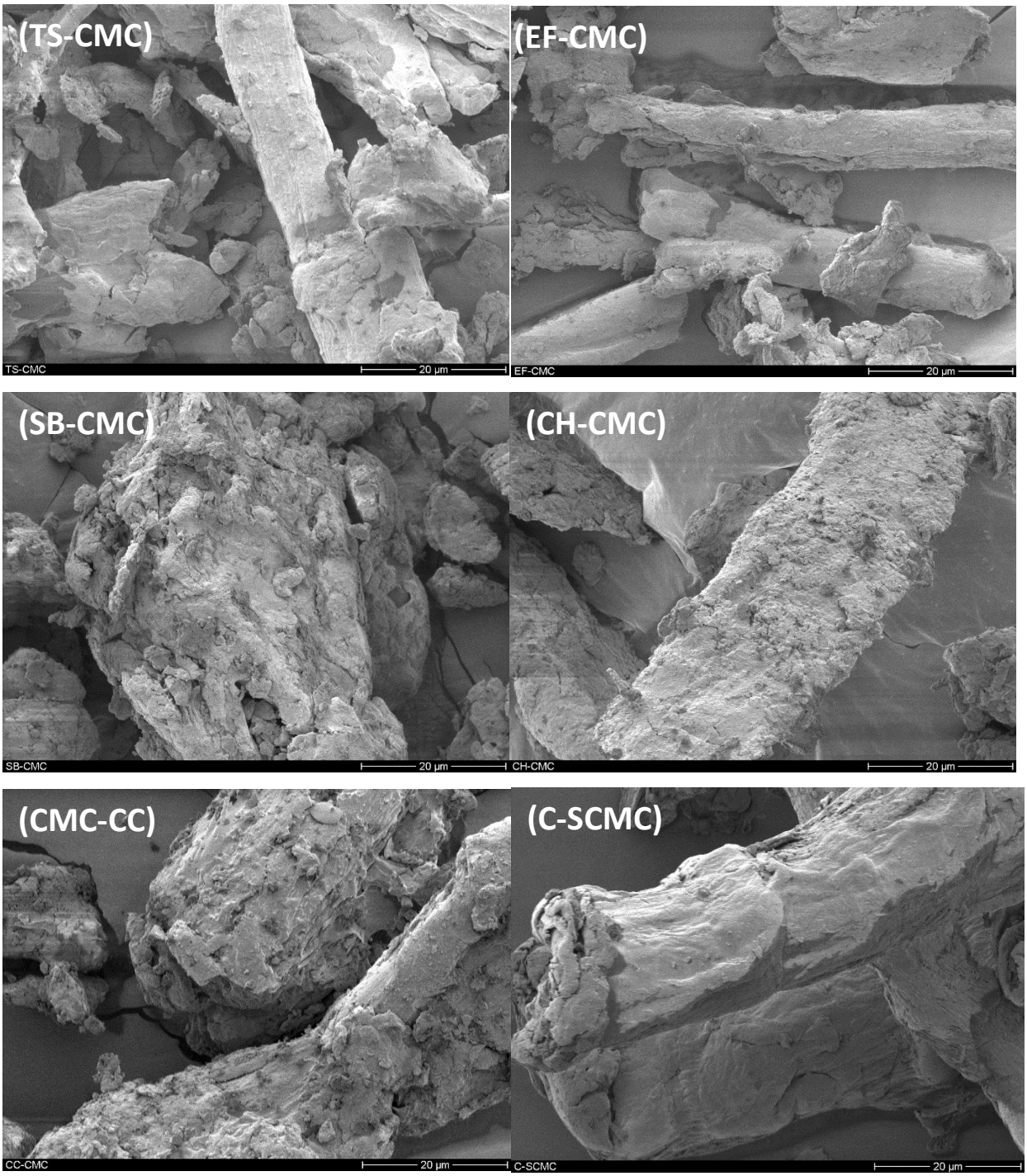

Fig. 5.7: SEM images of as-obtained CMC, CMC-CC and C-SCMC with a scale bar of 20 µm. (Key: TS-*teff* straw; EF-*enset* fiber; SB-sugarcane bagasse; CH-coffee hull; Cel-cellulose extracted from the byproducts; CC-commercial cellulose; CMC:-Carboxymethylcellulose obtained from the celluloses; CMC-CC:-Carboxymethylcellulose obtained from CC; and C-SCMC:-Commercial sodium carboxymethyl cellulose, the last three included for comparison).

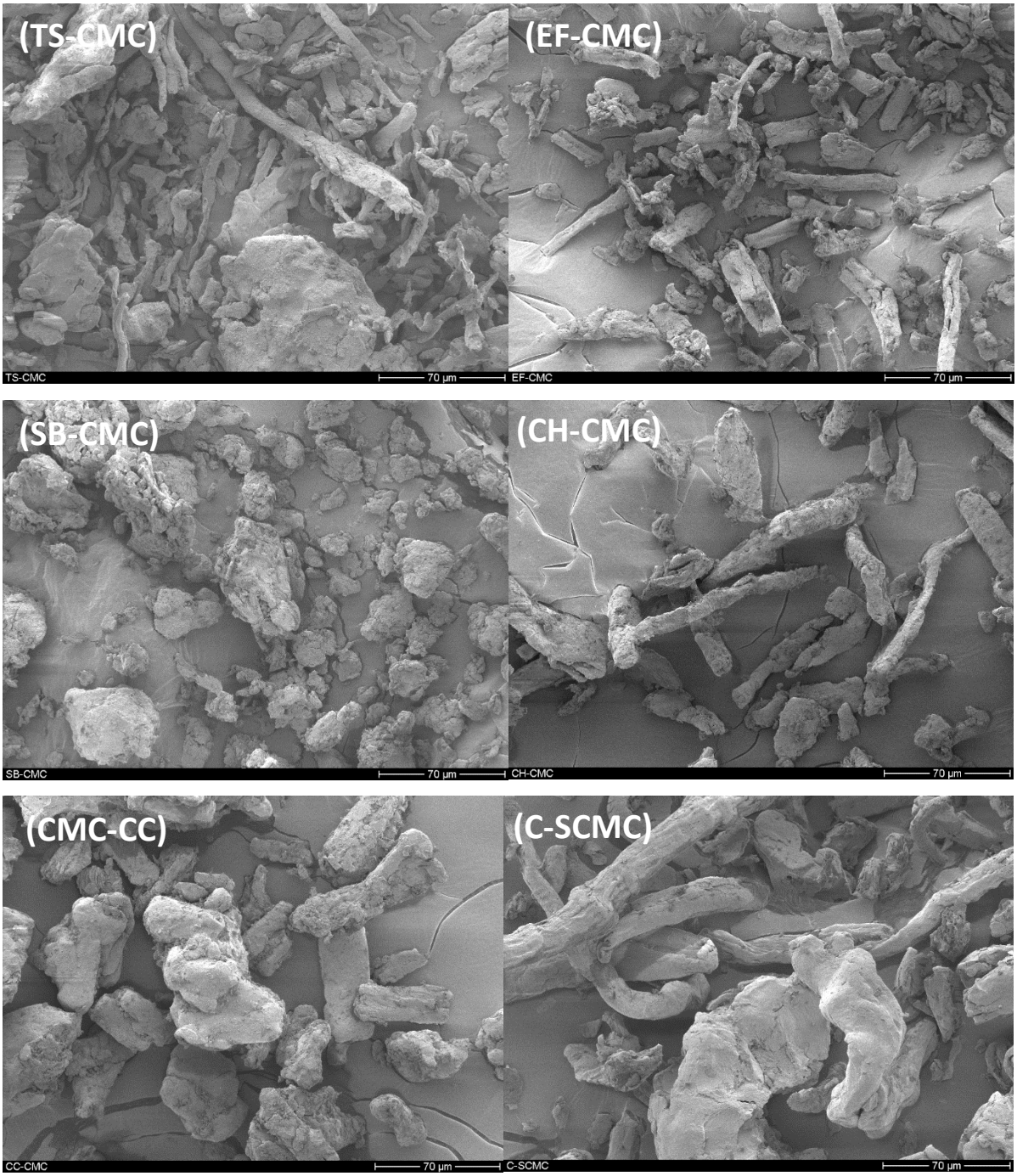

Fig. 5.8: SEM images of as-obtained CMC, CMC-CC and C-SCMC with a scale bar of 70 µm. (Key: TS-*teff* straw; EF-*enset* fiber; SB-sugarcane bagasse; CH-coffee hull; CMC-As-obtained carboxymethyl cellulose; C-SCMC-Commercial sodium carboxymethyl cellulose and CMC-CC-Carboxymethylcellulose obtained from CC included for comparison).

Table 5.3: Average diameters of the as-obtained CMC, respective cellulose precursors, as well as CMC-CC and C-SCMC.

Samples	Diameters, average (µm)					
	TS	EF	SB	CH	CC	C-SCMC
Cellulose precursors (Cel)/CC	6.39 ± 2.24	13.37 ± 2.45	19.19 ± 5.18	24.06 ± 7.37	11.93 ± 3.08	------
As-obtained CMC/CMC-CC and C-SCMC	16.53 ± 7.62	14.99 ± 2.13	25.72 ± 9.64	17.46 ± 4.46	27.15 ± 12.05	26.35 ± 15.14

Key: Cel- celluloses extracted from the four plant byproducts; TS-*teff* straw; EF-*enset* fiber; SB-sugarcane bagasse; CH-coffee hull; CC-commercial cellulose; CMC-Carboxymethylcellulose obtained from the celluloses; CMC-CC - Carboxymethylcellulose obtained from CC; and C-SCMC: Commercial sodium carboxymethyl cellulose, the last three are included for comparison). NB: ImageJ Software was used for the determination of the (average) diameters.

5.4 Conclusion

The isolated celluloses from the four lignocellulosic materials: TS, EF, SB and CH were converted to CMC by etherification using MCA and NaOH. At similar carboxymethylation condition, CMC obtained from EF had the highest DS, %carboxymethyl, and yield. FTIR studies indicated the appearance of new peaks suggesting that the hydroxyl groups of the celluloses were etherified. XRD analysis indicated that the degree of crystallinity of all the as-obtained CMC reduced significantly. The reduction in the thermal stability of CMC was due to the reduction in crystallinity upon carboxymethylation, and a 50% weight loss happened in a temperature range of 305.02-327.73 °C. The physicochemical properties of the as-obtained CMC products were dependent on the source of cellulose and carboxymethylation conditions. Further, the findings of this study could open a way to explore the lignocellulosic materials for the synthesis of CMC for potential value-added application.

6 Nanocellulose-based nanogels for sustained drug delivery: Preparation, characterization and evaluation

6.1 Introduction

Polysaccharide-based nanocarriers such as nanogels have recently received considerable attention in modified drug delivery due to their biocompatibility and biodegradability. Nanogels, three-dimensional hydrogel nanomaterials, have recently received considerable attention as effective nanocarriers in drug delivery systems (Ahmed et al., 2020; Li et al., 2021, 2015; Zhu et al., 2013). Nanogels integrate not only the features and the potential advantages of nanoparticles, but also the attractive features of hydrogels such as high hydrophilicity, high loading capacity, and the potential for biocompatibility and sustaining the release (Ahmed et al., 2020; Demirel and Von Klitzing, 2013; Eckmann et al., 2014; Neamtu et al., 2017; Quinn, 2016; Raemdonck et al., 2009; Zhang et al., 2016).

Despite the potential advantages of nanogels, their preparation methods suffer from several limitations. The most commonly employed methods for fabrication of nanogels are emulsion radical polymerization and seed emulsion polymerization, involving the usage of large amounts of organic solvents and surfactants, which are not eco-friendly and not easily removed from the system (Qian et al., 2014; Yao et al., 2014).

Additionally, most nanogels take long preparation time (> 5 h) (An et al., 2015; Chen et al., 2017; Das et al., 2016; Hassanpour and Bagheri, 2017; Zhao et al., 2016), with particle sizes too large to be used in biomedical fields (Yao et al., 2014) and lower drug loading capacity (LC) and encapsulation efficiency (EE). The sub-200 nm diameter is desirable for nanocarriers to extend their blood circulation time and penetrate into cells (Li et al., 2015). Different attempts have been made to search for new, simple, and green, and surfactant-free nanogel preparation methods avoiding such factors which limit their clinical application as drug delivery systems.

Polyelectrolyte complex coacervation (PEC) is the simplest way to form nanoparticles by mixing oppositely charged macromolecular species, such as polymers, proteins, and colloids in solution (Fares et al., 2018; Sing and Perry, 2020). PEC is considered to be greener approach for preparation of nanomaterials in aqueous media, and amenable for scale up without using harsh chemicals (Otoni et al., 2020). Due to their natural biocompatibility and biodegradability, polysaccharides

and proteins are commonly used to prepare biohybrid colloids via electrostatic interactions for various industrial applications such as food and drug delivery (Li et al., 2015; Wu et al., 2021).

Chitosan-ovalbumin (Yu et al., 2006), lysozyme-dextran (Li et al., 2008), bovine serum albumin-dextran-chitosan (Qi et al., 2010), CMC-lysozyme (Li et al., 2015; Pei et al., 2019; Zhu et al., 2013), pectin, gum Arabic, carrageenan and alginate-low density lipoprotein (LDL) (Zhou et al., 2016) are among such polysaccharide-protein interactions forming nanogels for different applications. CMC was also reported to be self-assembled with branched poly(ethyleneimine) (Yang et al., 2015), and LDL (He et al., 2015; Zhou et al., 2016), as well as grafted with polyacrylic acid using amine-based cross linker (Rajput et al., 2020).

Cellulose, the most abundant polysaccharide in nature, can be obtained from plants, animals, or bacteria. CNCs, celluloses in the form of nanostructures, have gained growing interest due to their attractive characteristics such as abundance, high aspect ratio, surface area, desirable mechanical properties, renewability and biocompatibility as well as ease of functionalization (Trache et al., 2020). CNCs can be etherified to introduce negatively charged carboxymethyl groups to form carboxymethyl nanocellulose (CMNC) like carboxymethylation of cellulose fibers using monochloroacetic acid (MCA) in alkaline media containing isopropyl alcohol (Hooton, 2009).

Proteins, natural polyelectrolytes, possess unique functional properties to encapsulate nutraceuticals (Chen et al., 2006; Zhu et al., 2013). Lysozyme, also known as muramidase, is a 1,4-β-N-acetylmuramidase that degrades the glycosidic bonds in the peptidoglycan of bacterial cell walls. It is widespread in tears, saliva, blood serum, human and cow milk, and avian egg whites (Wu et al., 2015). Hen egg white lysozyme, a small globular protein (129 amino acid residues), attracted many researchers due to its low cost, widespread availability, and application in various colloidal preparations (Wu et al., 2021; Xue and Findenegg, 2012). Lysozyme carries net positive charge at physiological pH and its isoelectric point is at pH 10.7.

Nanogels are well known for their ability to encapsulate different drugs such as insulin (Yao et al., 2014; Zhao et al., 2016), doxorubicin (Hassanpour and Bagheri, 2017; He et al., 2015; Qian et al., 2014; Wen and Oh, 2015), dexamethasone (Jamard et al., 2016), and 5-fluorouracil (Zhu et al., 2013). However, no single work has been reported on comparative loading of drugs based on the

Biopharmaceutics Classification System (BCS) into nanogels except for the work reported by Paulos et al (2019) who developed hydrophobically modified starch-based nanoparticles for loading different drugs.

In this study, three model drugs: acyclovir (Class III, soluble and poorly permeable), carbamazepine (Class II, permeable and poorly soluble), and furosemide (Class IV, poorly soluble and poorly permeable) were selected on the basis of their solubility and permeability profiles. Acyclovir, a well-known antiviral agent with nucleoside analogues for the treatment of herpes viruses such as herpes simplex virus type I/II and varicella zoster, has a poor bioavailability (15-30%), and plasma half-life (2.5 h) (Nair et al., 2014). Various approaches have been reported to improve the bioavailability of acyclovir such as encapsulating in carboxylated cyclodextrin-based nanosponges (Lembo et al., 2013), poly (d, l) lactide nanoparticles (Patel et al., 2014), nanoparticulates of thiolated xyloglucan (Madgulkar et al., 2016), and starch acetate nanoparticles (Paulos et al., 2019), among others. Carbamazepine, an anticonvulsant and antiepileptic tricyclic compound, causes several side-effects such as dizziness, nausea, fatigue, diplopia and headache in long term therapy, associated with the fluctuations in serum concentration. Slow-release preparations of carbamazepine have been shown to reduce these fluctuations and the side-effects (Reunanen et al., 1992). Recently, carbamazepine-loaded nanostructured lipid carriers and nanoparticles were reported to improve the drug bioavailability (Elmowafy et al., 2018; Khan et al., 2020; Scioli Montoto et al., 2018; Zybina et al., 2018). Furosemide, a weakly acidic loop diuretic typically used for oral treatment of hypertension and edema, has poor oral bioavailability of 37–51% (Brater et al., 1982; Shariare et al., 2019). The bioavailability of furosemide was enhanced using different approaches such as microencapsulation of self-microemulsifying system (Zvonar et al., 2010), mucopenetrating nanoparticles (Radwan et al., 2017), polymeric microcontainers (Nielsen et al., 2016), and multicomponent crystal forms (Diniz et al., 2020). A prolonged release system is needed to reduce the administration frequency, increase the compliance of patients, and minimize the associated side effects (Tiwari et al., 2012). Most of the approaches reported thus far involve complex and longer time of preparations, and residues of hazardous organic phases. The resulting micro/nanocarriers were also much larger and polydisperse with lower colloidal stability.

The aim of this study was to prepare nanogels from self-assembled CMNC-lysozyme blends via electrostatic complexation, a simple and eco-friendly preparation approach, for sustained drug delivery. Where important, CMC was included to prepare CMC-based nanogels and compare with CMNC-based nanogels. CNCs, CMC and CMNC were prepared from *enset* fiber, an abundant and renewable lignocellulosic material with high cellulose content (~60 %) (Gabriel et al., 2021, 2020). To the best of our knowledge, CMNC-based nanogels with a simple and green preparation technique for sustained delivery of different BCS class drugs have not been reported and documented elsewhere. Moreover, the effects of weight ratios of CMNC-lysozyme, pH, sonication and heating times, drug loading, and storage conditions on the size and polydispersity index (PDI) of the nanogels were studied.

6.2 Materials and methods

6.2.1 Materials

EF which was previously collected from local market at Kambata Tembaro Zone, South Ethiopia was used in this study (Gabriel et al., 2020). Glacial acetic acid (Riedel-de Haën), sodium hydroxide 97% (HiMedia, Mumbai, India), sulfuric acid 97% (BDH, England), formic acid (98%) (Central Drug House (P) Ltd. New Delhi, India), lysozyme, MCA and dialysis bags (Sigma–Aldrich, USA), and hydrogen peroxide 30% (CARLO ERBA reagents, France) were used as received. Acyclovir (Zhejiang Zhebei Pharmaceutical Co., Ltd, Hangzhou, China) was kindly donated from Cadila Pharmaceuticals PLC, Addis Ababa, Ethiopia, and carbamazepine (Ipca Laboratories Ltd, Mumbai, India) and furosemide (Bajaj Healthcare Ltd, Thane, India) from Ethiopian Pharmaceuticals Manufacturing Factory Sh. Co, Addis Ababa, Ethiopia.

6.2.2 Cellulose extraction

Cellulose was extracted from EF following three-treatment stage according to our previous extraction method (Gabriel et al., 2020) in section 2.2.2.

6.2.3 Isolation of CNCs

The CNCs were isolated from EF based on the method described in our previous work (Gabriel et al., 2021) in section 3.2.3.

6.2.4 Preparation of carboxymethyl nanocellulose (CMNC)

CMNC was prepared from the CNCs of EF cellulose according to the method for preparation of CMC (Golbaghi et al., 2017; Joshi et al., 2015; Lakshmi et al., 2017) as described in section 5.2.3.

6.2.5 Preparation of nanogels

The nanogels were prepared by dissolving CMNC and lysozyme each in distilled water (1 mg/ml) with continuous mixing at room temperature for 4 h and then stored overnight at 4 °C. Then, the lysozyme solution was slowly added into the CMNC solution with vigorous magnetic stirring with various weight ratios (4:1, 4:2, 4:3, 4:4, 3:4, 2:4, 1:4). The coacervates were heated at 75 °C for different times: 15, 30, 45, 60 and 75 min. The pH of the formed nanogels (without sonication) was 5.3 (designated as UNGs0) and sonicated using probe-sonicator (Sonics and Materials Inc. Vibracell, VCX 750, 160 Newtown CT, USA) for 5 min (and designated as UNGs1 or NGs), and further adjusted to pH 7.4 (designated as UNGs2), 8.5, and 10.3 to investigate the influence of pH on the size and PDI. The formed nanogels (NGs) thus obtained were freeze-dried in a lyophilizer for 72 h (Operon Co., Ltd. - Bio-Equip, Siheung city, Gyeonggi-Do, Korea).

6.2.6 Preparation of drug-loaded nanogels

In order to prepare drug-loaded nanogels, acyclovir or furosemide at the concentration of 0.5 mg/ml was added to the mixtures being heated containing the CMNC and lysozyme solutions (1 mg/ml) at 75 °C, whereas carbamazepine solution (10 mg/ml, methanol) at similar concentration (0.5 mg/ml) was added to the mixtures being heated in the last 5 min of the reaction when more hydrophobic portion of lysozyme got exposed. The methanol was removed from the system using gentle heating and rotary evaporator (Xingyang Kori Instrument, Zhengzhou City, China). The drug-loaded nanogels were investigated at pH of 5.3 and 7.4.

6.2.7 Turbidity measurements

Turbidity measurements of the nanogels were conducted using UV/Vis Spectrophotometer (PG Instruments Limited, T92+ equipped with UV-WIN software, Leicestershire, LE17 5BH, UK) at 700 nm.

6.2.8 FTIR spectroscopy

The FTIR spectra of the CMC, CMNC, CNCs, lysozyme, model drugs, unloaded and drug-loaded nanogels were recorded using a Perkin Elmer FTIR spectrometer (L1600400 Spectrum TWO DTGS, SN: 108152, LIantrisant, UK) in the range of 4000 to 450 cm^{-1}, with no further sample preparation.

6.2.9 Morphological investigations

CNC dispersions (0.05% w/w), unloaded and drug-loaded nanogels were deposited on formvar-coated copper grids according to the method mentioned in section 3.2.8. The morphology of cellulose fiber, CMC, CMNC and lysozyme was analyzed using SEM FEI/Philips XL-30 ESEM (Leuven, Belgium), or TESCAN VEGA3 (Brno-Kohoutovice, Czech Republic) as per the method indicated in section 2.3.6.

6.2.10 Particle size and polydispersity index (PDI) analyses

Photon correlation spectroscopy (PCS), a 90Plus Particle Size Analyzer 28 (Brookhaven Instruments Corporation, New York, USA) was employed for measurements of particle size and PDI of the CNCs and nanogels. Prior to measurement, the samples were diluted with distilled water to achieve a count rate of 50–300 kcps. The measurements were made at 25 °C and fixed angle of 90°.

6.2.11 Zeta potential

The zeta potentials of aqueous suspension of CNCs (0.05% w/v), unloaded and drug-loaded nanogels were measured based on the method described in section 3.2.10.

6.2.12 XRD studies

The XRD patterns of CNCs, CMC, CMNC, lysozyme, model drugs, unloaded and drug-loaded nanogels were examined using an XRD-7000 X-ray Diffractometer MAXima (SHIMADZU Corporation, Kyoto, Japan) at 40 kV, 30 mA with monochromatic Cu-Kα radiation, typically with scan speed of 3.0000°/min and sampling pitch of 0.0200°. Origin Pro 8.5.1 was used to plot the data acquired in a 2θ scale from 10 to 40.

6.2.13 Thermal analyses

The Thermogravimetric Analysis (TGA) and Differential Scanning Calorimetery (DSC) of CNCs, CMC, CMNC, lysozyme, unloaded and drug-loaded nanogels were performed using Thermal Analyzer (SDT-Q600, TA Instrument, USA). The samples were heated from room temperature to 700 °C in Alumina pan at a heating rate of 10 °C/min and a nitrogen gas flow rate of 100 ml/min.

6.2.14 UV calibration curves of model drugs

Stock solutions containing 100 μg/ml of acyclovir or frusemide dissolved in phosphate buffer solution (PBS, pH 7.4), or carbamazepine dissolved in methanol (10 mg/ml) and diluted with (PBS, pH 7.4) was prepared to provide 100 μg/ml stock solution. From these stock solutions, eight different concentrations for acyclovir and furosemide (3, 4, 5, 6, 7, 8, 9 and 10 μg/ml), and carbamazepine (0.75, 1.00, 1.25, 1.50, 1.75, 2.00, 2.25 and 2.50 μg/ml) were prepared. The UV absorbance readings of acyclovir, carbamazepine, and furosemide solutions were measured at 254 nm, 284 nm, and 274 nm, respectively using UV/Vis Spectrophotometer (PG Instruments Limited, T92+ equipped with UV-WIN software, Leicestershire, LE17 5BH, UK). The absorbances (Y) versus concentration (X, μg/ml) of solutions were plotted and calibration curves with linear regression equations of: $Y=0.0694X+0.0779$, $R^2= 0.9995$; $Y=0.2691X+0.1315$, $R^2=0.9986$; $Y=0.0610X+0.0424$, $R^2=0.9991$ were respectively obtained for acyclovir, carbamazepine and furosemide (Fig. A7a, b, and c in the Appendix).

6.2.15 Determinations of solubilities and partition coefficients of the model drugs

The aqueous solubilities and partition coefficients of the model drug molecules: acyclovir, carbamazepine and furosemide were determined in distilled water and PBS (7.4) by shake flask method (Paulos et al., 2019; Wasik et al., 1981). The solubilities were investigated by adding an excess amount of each drug in a 100 ml conical flask containing 50 ml of the solvent while stirring. The mixtures were further stirred for 24 h at room temperature, and filtered through 0.45 μm membrane filter. The UV absorbances of the drugs: acyclovir, carbamazepine and furosemide were measured after appropriate dilutions at 254 nm, 284 nm, and 274 nm. For partition coefficient determinations, 50 mg of each drug was added to a 100 ml separatory funnel containing 25 ml of n-octanol saturated with water while stirring. Then, 25 ml of water saturated with n-octanol was added and the mixture was shaken well for 30 min, and left for 24 h at room temperature. The absorbance readings of the drugs in aqueous phase were taken using UV/Vis Spectrophotometer

(PG Instruments Limited, T92+ equipped with UV-WIN software, Leicestershire, LE17 5BH, UK). The amount of the drug in aqueous phase was determined, followed by the amount of the drug in n-octanol phase which was obtained by subtraction.

6.2.16 Drug encapsulation efficiency (EE) and loading capacity (LC)

The drug-loaded nanogels were centrifuged at 10,000 rpm for 20 min in a refrigerated centrifuge (Beckman Coulter Allegra 64R Centrifuge, Ramsey County, Minnesota, USA). Unloaded drugs: acyclovir, carbamazepine, and furosemide in the supernatant solutions were determined by UV/Vis Spectrophotometer (PG Instruments Limited, T92+ equipped with UV-WIN software, Leicestershire, LE17 5BH, UK) at 254 nm, 284 nm, and 274 nm, respectively. The encapsulation efficiency (EE) and loading capacity (LC) were calculated as follows (Azadi et al., 2013, 2012):

$$\mathrm{EE}(\%) = \frac{\text{total weight of drug} - \text{weight of unloaded drug}}{\text{total weight of drug}} \; X \; 100\%$$

$$\mathrm{LC}(\%) = \frac{\text{total weight of drug} - \text{weight of unloaded drug}}{\text{weight of nanogels}} \; X \; 100\%$$

6.2.17 *In vitro* drug release

In vitro drug release study was carried out using dialysis method. Briefly, 10 ml of colloidal dispersions containing drug loaded nanogels were placed into dialysis bags (MWCO 3.5 kDa, Sigma-Aldrich, Saint Louis, Missouri, USA), and dialyzed with 100 ml of PBS (pH 7.4) in a water bath at 100 rpm for 12 h, 37 °C. At appropriate time intervals, 2.5 ml of aliquots of dissolution medium was collected and the same amount of fresh PBS was replenished every time. The amounts of the acyclovir, carbamazepine, and furosemide released were determined at 254 nm, 284 nm, and 274 nm, respectively using UV/Vis Spectrophotometer (PG Instruments Limited, T92+ equipped with UV-WIN software, Leicestershire, UK) (Li et al., 2015).

6.2.18 Short-term stability studies

Stability studies of the produced nanogels were conducted following International Conference on Harmonization (ICH) guideline (ICH, 2003). The nanogels were kept at different conditions, i.e., at ambient storage condition (25 °C/60% relative humidity (RH)), at accelerated condition (40 °C/75% RH) in a stability chamber (Binder® Scientific Laboratory Supplies Ltd, Nottingham,

UK), and in refrigerator (LG, Seoul, South Korea) at 4 ^{o}C for 3 months. Samples were withdrawn at 0, 30, 60, and 90 days for size and PDI measurements.

6.2.19 Statistical analysis

All data reported in this study were the averages of triplicate determinations (but > 10 measurements of TEM images using ImageJ software) and presented as the mean ± standard deviation (SD). Wherever appropriate, the data were subjected to statistical analysis with Origin®, version 8.5 (OriginLab Corporation, Northampton, MA, USA) assisted by MS Excel 2016, following either one-way or two-way analysis of variance (ANOVA) with Tukey's test. *P* value of less than 0.01 was considered to be evidence for a significant difference.

6.3 Results and discussion

6.3.1 Preparation conditions of nanogels

CMNC was obtained from CNCs isolated from EF via etherification using chloroacetic acid. The as-obtained CMNC had a degree of substitution (DS) and yield of 0.65 ± 0.05, and 1.10 ± 0.072 (g/g) using the optimal condition, respectively. The nanogels were prepared by self-assembly via electrostatic interaction between the solutions of CMNC and lysozyme under appropriate conditions. CMNC like CMC is a highly water-soluble anionic polysaccharide. Lysozyme carries a zeta potential of 36.7 mV at an isoelectric point of 10.7 in aqueous solutions, and it is cationic at normal physiological pH.

Aqueous solutions of pure CMNC and pure lysozyme were transparent showing that they did not contain any colloidal aggregates that were large enough to cause significant scattering of light. In all weight ratios investigated, turbid complexes were formed between CMNC and lysozyme, like between CMC and lysozyme but increasing the CMNC concentration at fixed lysozyme concentration led to reduction in turbidity based on UV Absorbance values at 700 nm. This could be due to a change in the size, number, and/or refractive index of the colloidal particles when more polymers such as CMC were added (Pei et al., 2019).

It was also suggested that the less the amount of lysozyme molecules deposited on the chain of CMC, the weaker the complexes are, and scatter light weakly (Li et al., 2015). When the pH of

the complexes was increased to 7.4 and 8.5, the turbidity gradually decreased as confirmed by reduction in absorbance at 700 nm, and instantly disappeared above pH 8.5. But, while heating the complex at least for 15 min, higher turbidity along with higher hydrodynamic sizes (> 300 nm) was observed in CMC-based nanogels as compared to CMNC-based nanogels. The hydrodynamic diameters of the unloaded and drug-loaded CMNC-based nanogels were larger at pH 5.3 (200-300 nm), and reduced to 100-200 nm under probe sonication, and < 110 nm at higher pH values. The size of CMC-based nanogels at pH 5.3 was 355 nm, and reduced to 237 nm upon probe-sonication and to 140 nm by pH adjustment to 7.4 (Fig. 6.1a). Fig. 6.1a and b shows the influence of pH, heating time, and weight ratios of CMNC:lysozyme on the size and PDI of nanogels.

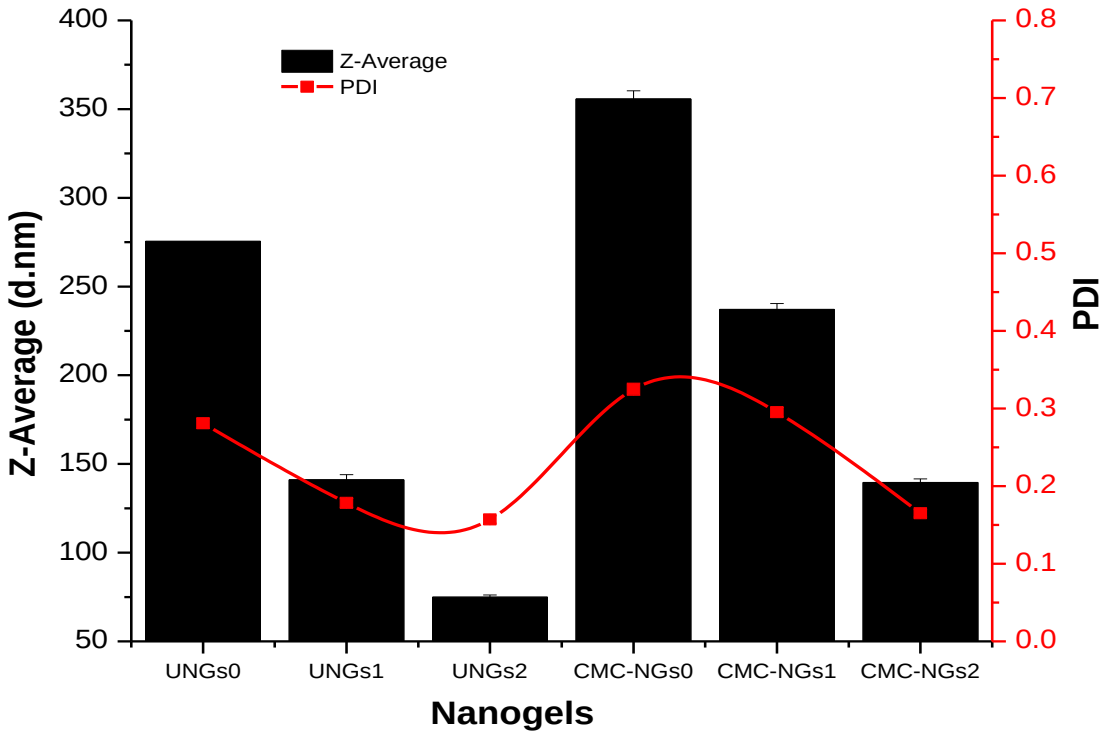

a)

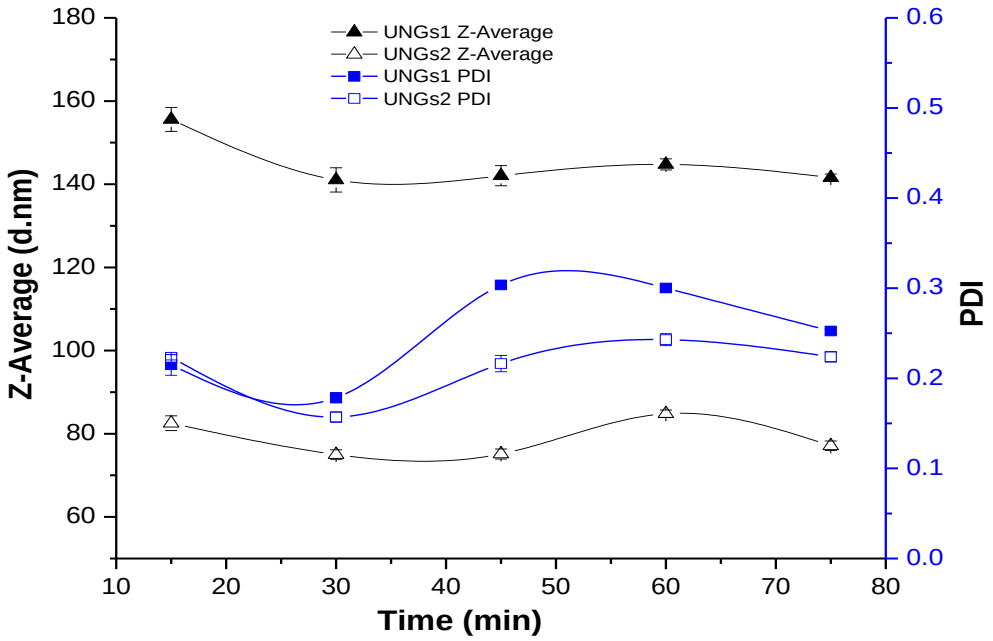
UNGs1 Z-Average
UNGs2 Z-Average
UNGs1 PDI
UNGs2 PDI
Z-Average (d.nm)
PDI
Time (min)
180
160
140
120
100
80
60
0.6
0.5
0.4
0.3
0.2
0.1
0.0
10
20
30
40
50
60
70
80

b)

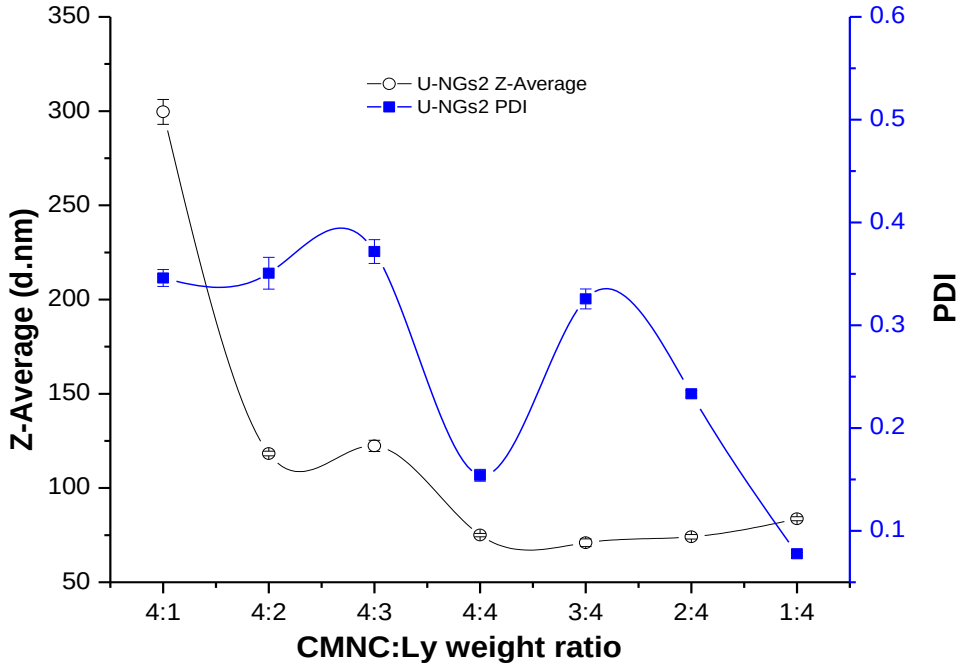
U-NGs2 Z-Average
U-NGs2 PDI
Z-Average (d.nm)
PDI
CMNC:Ly weight ratio
350
300
250
200
150
100
50
0.6
0.5
0.4
0.3
0.2
0.1
4:1
4:2
4:3
4:4
3:4
2:4
1:4

c)

Fig. 6.1: a) Size and PDI of CMNC-based unloaded nanogels (UNGs0, UNGs1, and UNGs2), and CMC-based unloaded nanogels (CMC-NGs0, 1, and 2) obtained at 1:1 weight ratio and 30 min heating time, and influence of b) pH and heating time and c) weight ratios of CMNC:lysozyme on the size and PDI of nanogels. (Key:- CMNC: Carboxymethyl nanocellulose; CMC: Carboxymethyl cellulose; NGs0: unloaded nanogels obtained at pH 5.3; NGs1: unloaded nanogels obtained at pH 5.3 and ultrasonicated; NGs2: unloaded nanogels prepared at pH 7.4). Data are presented as the mean ± SD (n = 3).

Hydrophilic groups of the nanogels get partly protonated and the CMNC becomes less charged at lower pH values such as pH 5.3, resulting in loose electrostatic interaction, followed by larger size. While at pH 7.4 and above, nanogels remained in collapse state through strong electrostatic interaction between the polyelectrolytes, followed by the intramolecular H-bonding for further reduction of the size of the nanogels (Das et al., 2016). However, there is no interaction at a pH above the isoelectric point of lysozyme (pH 12), and therefore no colloidal formation since the lysozyme is no longer positively charged (Wu et al., 2021).

The higher the CMNC concentration, the larger the particle sizes and PDIs of the unheated complexes and as-obtained nanogels like CMC-based complexes and nanogels (Fig. 6.1a), due to either formation of larger individual particles or particle aggregation (Pei et al., 2019). The unheated complexes of CMNC:Lysozyme (1:4 to 3:4) were in nano-scale range (> 300 nm), but no nanoparticle was formed in the complexes when the ratio was fixed at 1:1 to 4:1 (> 1 μm). However, all the unheated complexes were in nano-scale range regardless of the weight ratio when the pH was adjusted to 7.4 and above (to 10.5) with 0.1 M NaOH. When heat was applied to the pH adjusted complexes, nanogels with smaller sizes were formed as compared to pH unadjusted complexes/nanogels.

The CMNC-based nanogels adjusted at a pH of 7.4 had lower particle size than those obtained at lower pH (5.3). CMNC-based nanogels exhibited lower particle size than CMC-based nanogels at all the pH points investigated. All the nanogels obtained without pH adjustment (pH 5.3) exhibited higher particle sizes. Fig. 6.1a shows the PCS results of the nanogels obtained after heating the complexes for 30 min at 75 °C with the varying ratios of CMNC:Lysozyme from 4:1 to 1:4. When the ratios were changed from 4:1 to 1:1, the average size of the nanogels decreased, and then

increased slightly when the ratio of CMNC:Lysozyme ratio varied from 1:1 to 1:4. The PDI of the nanogels also decreased from 0.372 to 0.078 when the ratios were changed from 4:1 to 1:4.

As compared to unheated complexes, heating time (varying from 15 to 75 min) on the formation of nanogels at 75 °C resulted in rapid decrement of particle size and PDI of the CMNC and CMC-based nanogels. However, the reduction of the particle size was more pronounced in pH changes than sonication, and heating time. When the heating time changed from 15 min to 30 min, the average size of nanogels decreased, then increased at 45 min, 60 min and 75 min, which could be attributed to over-denaturation of lysozyme in the nanogels resulting in further exposure of hydrophobic groups and consequently a looser arrangement. Moreover, the PDI of the nanogels seem to increase with longer heating times. Hence, a heating time of between 15 and 30 min appears to be optimal to obtain nanogels of smaller particle size and PDI. Accordingly, after heating the mixture for 30 min, CMNC-based nanogels at pH 7.4 resulted in small average size (< 110 nm) and PDI (< 0.2) for the optimum preparations.

Heating the complex at 75 °C, which is slightly beyond or around the denaturation temperature of lysozyme, facilitates the intermolecular hydrophobic association along with strong electrostatic interaction of CMNC and lysozyme to form stable nanogels. The peptide chains of lysozyme molecules suffer from excessive thermal shock upon heating causing the destruction of hydrogen bonds, which results in a change in the original conformation of lysozyme and the exposure of hydrophobic groups to the surface of the molecules. Herein, the hydrophobic interactions among lysozyme molecules are enhanced so that more aggregates are easily formed. CMNC and lysozyme molecules could be changed from chains to spherical aggregates gradually with the extension of heating period.

The differences in sizes of nanogels measured by TEM and PCS study may be attributed by the fact that the nanogels are in dry state in TEM analysis, and the nanogels are in hydrated state while in PCS experiment, where larger hydrodynamic sizes are typically measured (Sun et al., 2020; Zhao et al., 2016). All the nanogels showed good colloidal stability with the zeta potential values ranging from -24 to -55 mV, and the nanogels prepared at pH 7.4 had higher zeta potential values (-38 to -55 mV) than those nanogels prepared without pH adjustment (pH 5.3) (-24 to -30 mV), as depicted in Fig. 6.2a. This could contribute to their excellent colloidal stability upon storage. The

photographs of unheated complexes as well as unloaded and drug-loaded nanogels are shown in Fig. 6.2b. A clear pattern is observed from the figure that nanogels prepared at pH 7.4 had consistently smaller particle sizes, lower turbidity and higher zeta potentials than those prepared at pH 5.3.

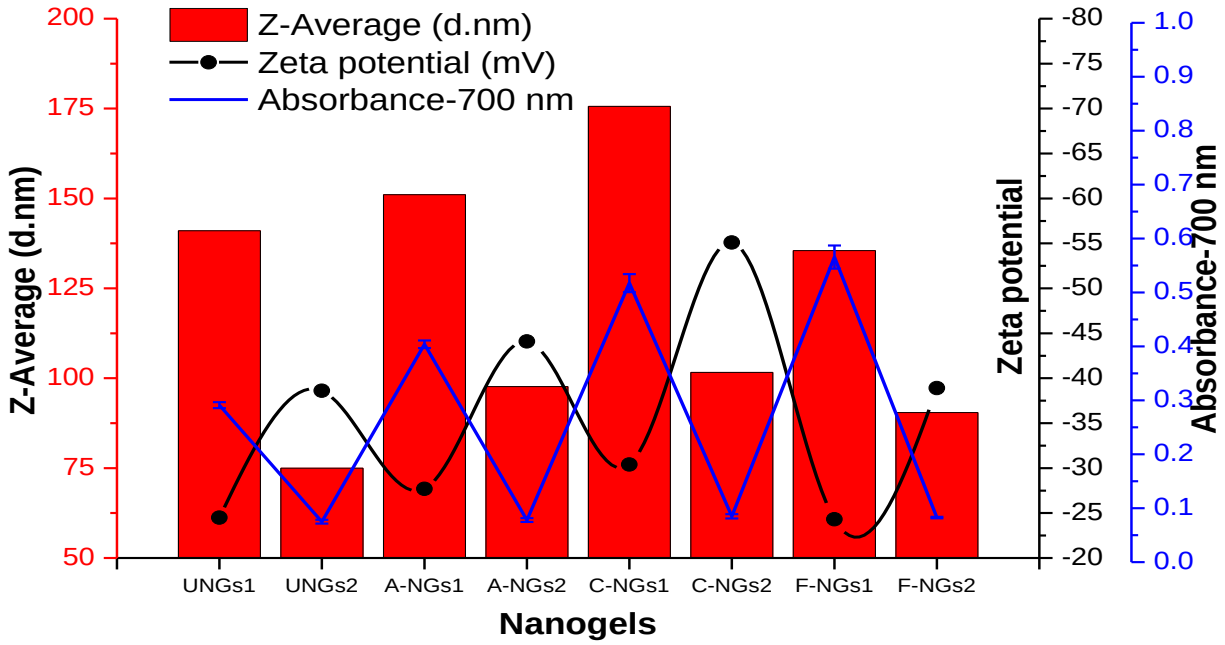

a)

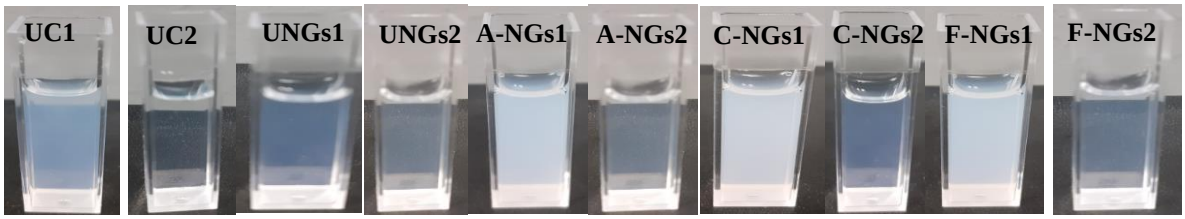

b)

Fig. 6.2: a) Particle size, zeta potential and turbidity of unloaded and drug-loaded nanogels prepared at pH 5.3 and 7.4, and b) photographs of unheated complexes (UC1 and UC2) as well as the nanogels (NG1 and NGs2). (Key: - UC1: Unheated complex; 1, and 2: Complexes or nanogels, prepared at pH 5.3, followed by probe-sonication for 5 min, and pH adjusted at 7.4; UNGs: Unloaded nanogels; A-NGs: Acyclovir loaded nanogels; C-NGs: Carbamazepine loaded nanogels; F-NGs: Furosemide loaded nanogels). Data are presented as the mean ± SD (n = 3).

6.3.2 FTIR spectroscopy studies

Fig. 6.3 shows the FTIR spectra of CNCs, CMNC, lysozyme, and unloaded nanogels. The broad band around 3338 cm^{-1} represents the stretching vibration of OH which contributes to the formation of hydrogen bonds in the cellulose and its derivatives as well as cellulose-based nanogels. The weak band around 2907 cm^{-1} is attributed to the asymmetric stretching vibration of CH in all the materials. The appearance of new bands around 1600 and 1412 cm^{-1} in the CMNC FTIR spectrum is due to the carboxymethyl groups that are incorporated during etherification of CNCs. The peak around 1323 cm^{-1} region of the spectra is due to the in-plane bending vibration of the CH and CO groups of the hexose ring in the cellulose, CNCs, CMC, and CMNC. The peak around 896 cm^{-1} is related to glycosidic C_1H deformation, a ring vibration, and OH bending where these characters infer the β-glycosidic linkages between anhydroglucose units. The high intensity at 1030 cm^{-1} reveals that the degree of crystallinity of CNCs was high due to high cellulose content when compared with CMNC, and corresponding nanogels. In the pure lysozyme FTIR spectrum, the peaks at 1522 cm^{-1} and 1643 cm^{-1} were due to vibrations of secondary NH bonds of the peptide chains and the stretching vibrations of α-helices in the conjugated peptide bonds, respectively.

In the FTIR spectrum of unloaded nanogels, different peaks of CMNC at ~ 1412, 1323, 1030 and 896 cm^{-1} and the two peaks of lysozyme at ~ 1643 and 1522 cm^{-1} still exist, with a slight shift showing strong electrostatic interaction between the carboxyl groups of CMNC and amino groups of lysozymes. Another absorption peaks at ~ 3330 cm^{-1} for OH and weak bands around 2907 cm^{-1} for CH groups of CMNC and lysozyme indicated that the polymer and protein chains were embedded in the resulting nanogels. The loading of the model drugs was confirmed by the characteristic peaks observed in the unloaded nanogels and respective drugs (Fig. A8a and b in the Appendix). Absence of incompatibility in the drug-loaded nanogels, and the physical mixtures of CMNC, lysozyme, and the model drugs was established by the FTIR results as depicted in Fig. A8c, d and e (Appendix).

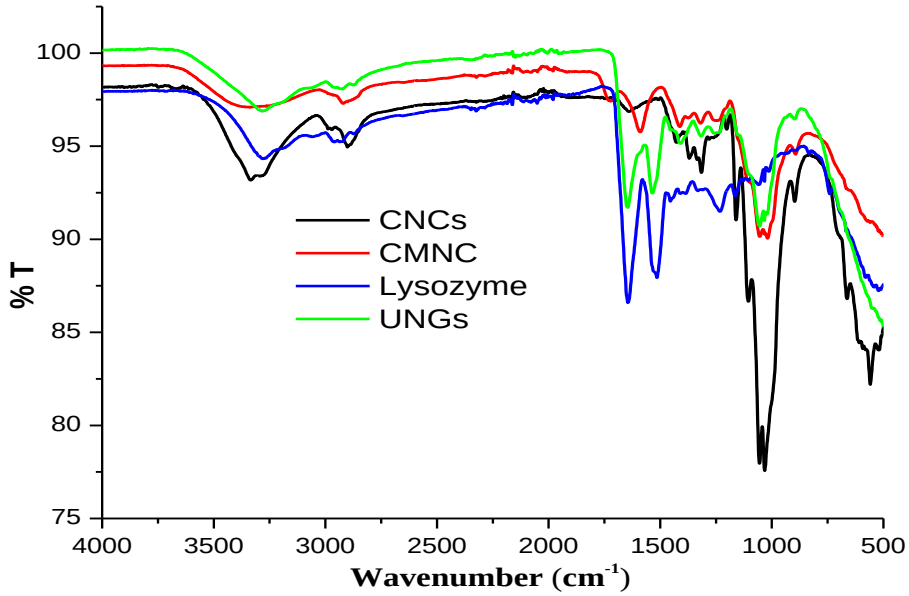

Fig. 6.3: FTIR spectra of CNCs, CMNC, Lysozyme, and UNGs (Key:- CNCs: cellulose nanocrystals; CMNC: carboxymethyl nanocellulose; UNGs: Unloaded nanogels).

6.3.3 Morphological properties

The cellulose extracted from EF had lower average diameter of 13.37 μm than the untreated fiber diameter (258.80 μm). The CNCs isolated from the cellulose fibers exhibited a hydrodynamic size of 157.2 nm with needle shaped structure. However, the diameters increased (14.99 ± 2.13; 13.93 ± 1.62 μm, respectively) after carboxymethylation of the cellulose fibers and CNCs. When the cationic lysozyme solution was mixed with the anionic CMNC solution, a complex was formed due to electrostatic interaction, and when heat was applied at 75 °C, a more stable nanogel with spherical shape was produced. From the TEM investigation, nanogels with diameters ranging from 19-77 nm were obtained. It was observed that when the pH was increased from 5.3 to 7.4, the particle size was significantly reduced from 58-77 to 19-37 nm, as substantiated by the PCS results. Drug loading did not cause much variation in the size of the pH adjusted nanogels. All unloaded and drug-loaded nanogels displayed nearly spherical shape with smooth surface in TEM images shown in Fig.6.4a. The size of the nanogels from the TEM images are also shown in Fig. 6.4b.

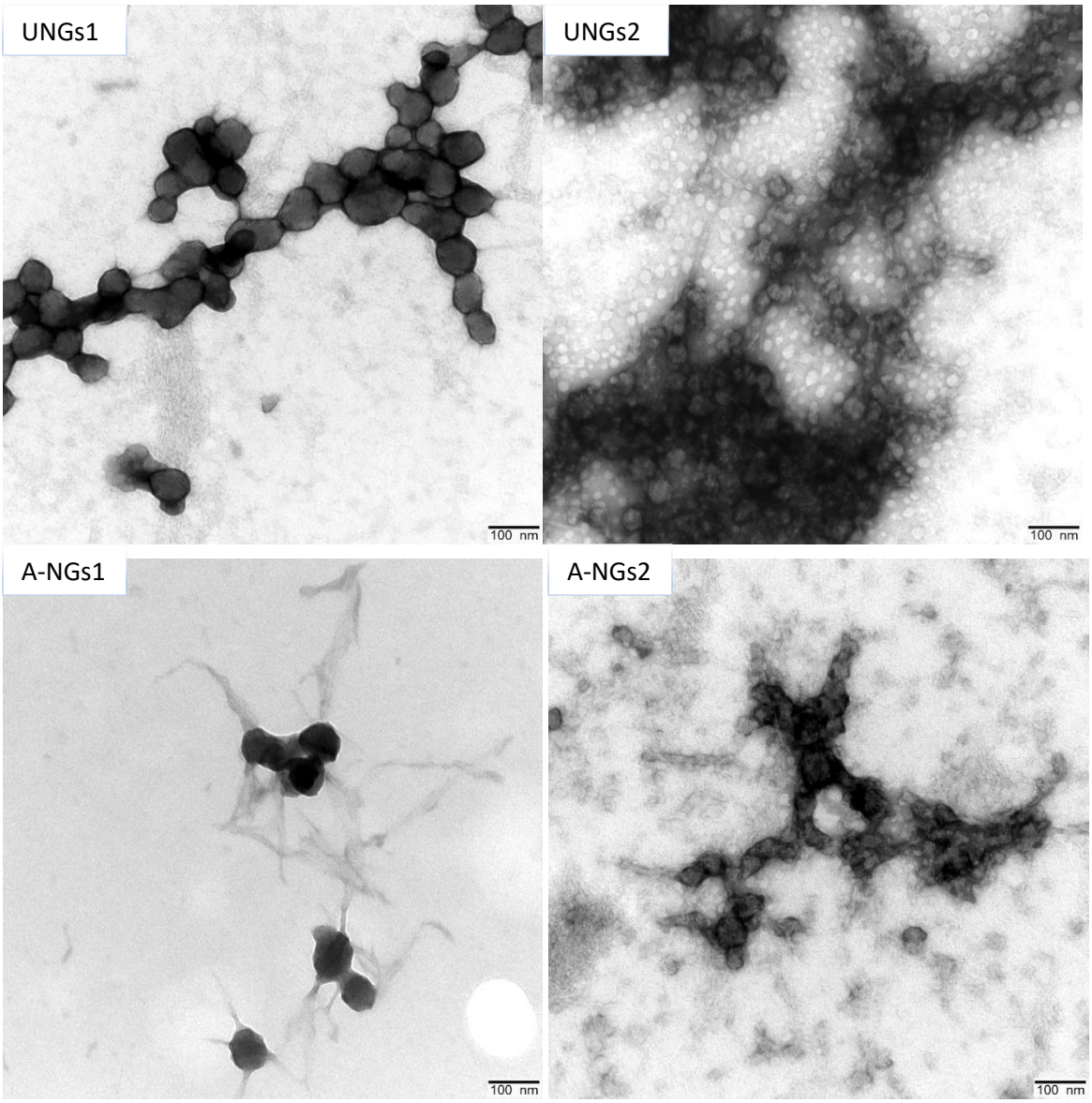
UNGs1
100 nm
UNGs2
100 nm
A-NGs1
100 nm
A-NGs2
100 nm

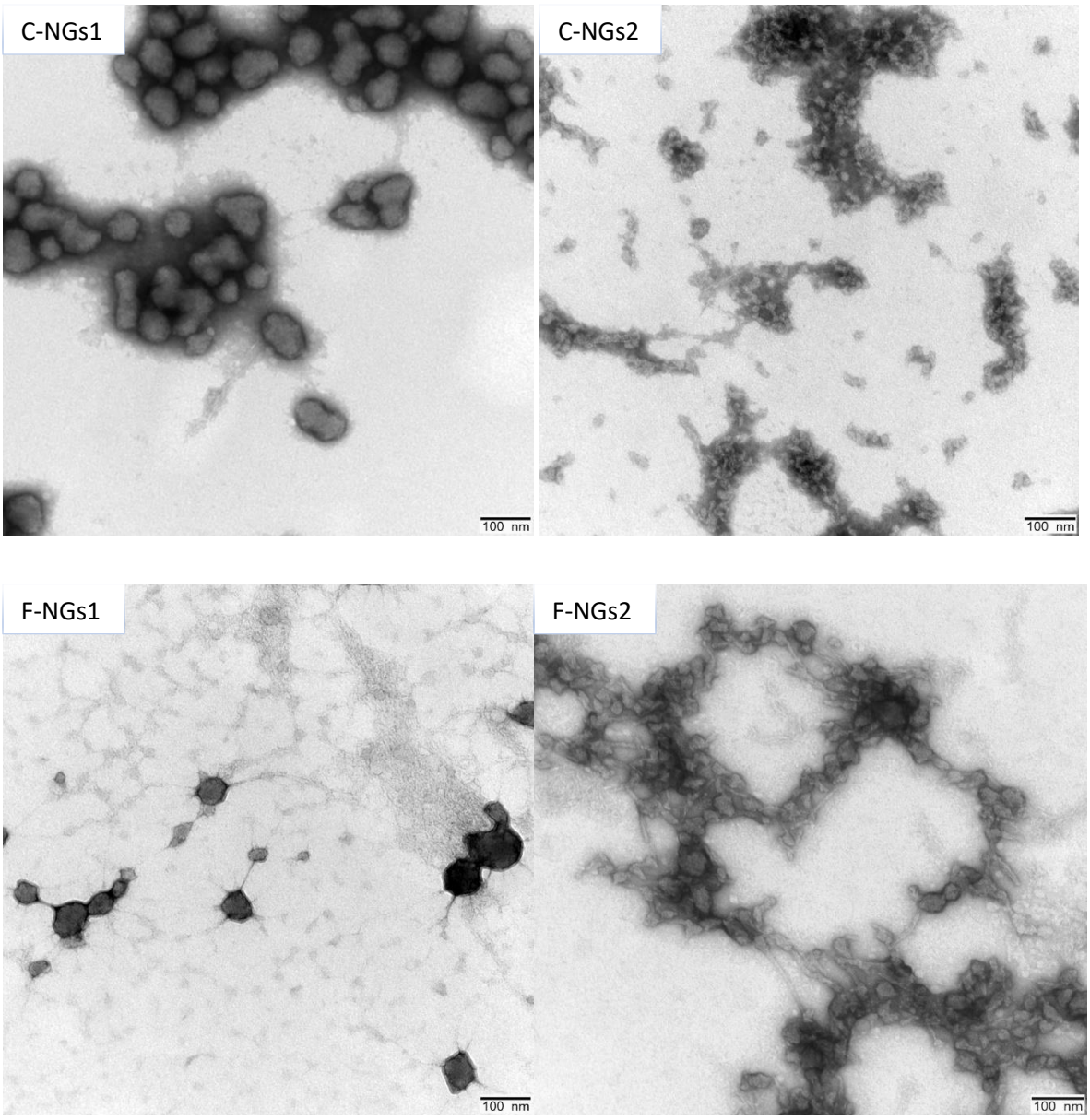

a)

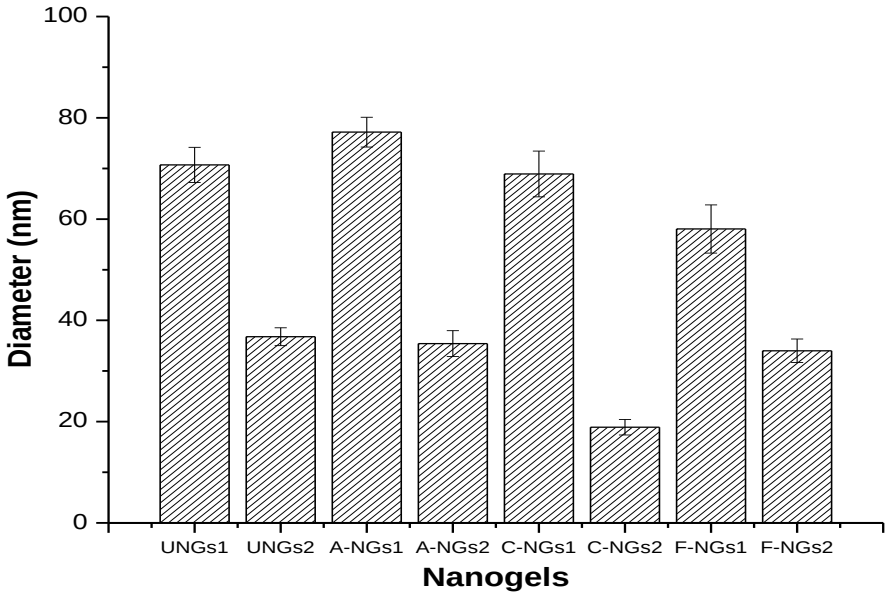

b)

Fig. 6.4: a) Transmission electron micrographs of unloaded and drug-loaded nanogels, b) the size of the nanogels from the TEM images (Key:- 1,and 2: Nanogels, their pH prepared at 5.3 and ultrasonicated, and adjusted at 7.4, respectively; UNGs: Unloaded nanogels; A-NGs: Acyclovir loaded nanogels; C-NGs: Carbamazepine loaded nanogels; F-NGs: Furosemide loaded nanogels). (Bar scale: 100 nm). NB: ImageJ Software was used for the determination of the (average) diameters. Data are presented as the mean ± SD (n > 10).

6.3.4 Crystallinity analyses

The XRD patterns of CNCs, CMNC, lysozyme, model drugs, unloaded nanogels, and drug-loaded nanogels are shown in Fig. 6.5a-c. CNCs exhibited a *CrI* of ~85.6%, with diffraction peaks at 2θ values of 14.9°, 16.3°, 22.4° and 34.4° for planes of $1\bar{1}0$, 110, 200 and 040. However, the crystallinity was reduced/lost by the etherification reaction to form amorphous CMNC. Lysozyme showed a strong diffraction peak at 2θ = 27°, and other peaks were also observed at 2θ = 23° and 38°, due to its crystalline nature. After the electrostatic interaction, the unloaded nanogels showed a flatter hump instead of sharp peaks, confirming their amorphous nature. Other research group also showed loss of crystallinity of low density lipoproteins in nanogels when they are self-assembled with CMC (He et al., 2015). However, in a study reported elsewhere (Borzooeian et

al., 2018), no significant difference occurred in the XRD patterns between the free and conjugated lysozymes, when the lysozymes were conjugated covalently onto the single-walled carbon nanotubes surfaces without causing a phase change and structural denaturation.

The three pure model drugs showed multiple strong diffraction peaks due to their crystal structures. However, the drugs lost their characteristic peaks in the XRD patterns when they are loaded into nanogels, suggesting the formation of amorphous forms of the drugs. In the literature, it was reported that the crystalline drugs were converted to amorphous state in entrapped form in a nanoscale polymeric matrix (He et al., 2015; Thomas et al., 2018).

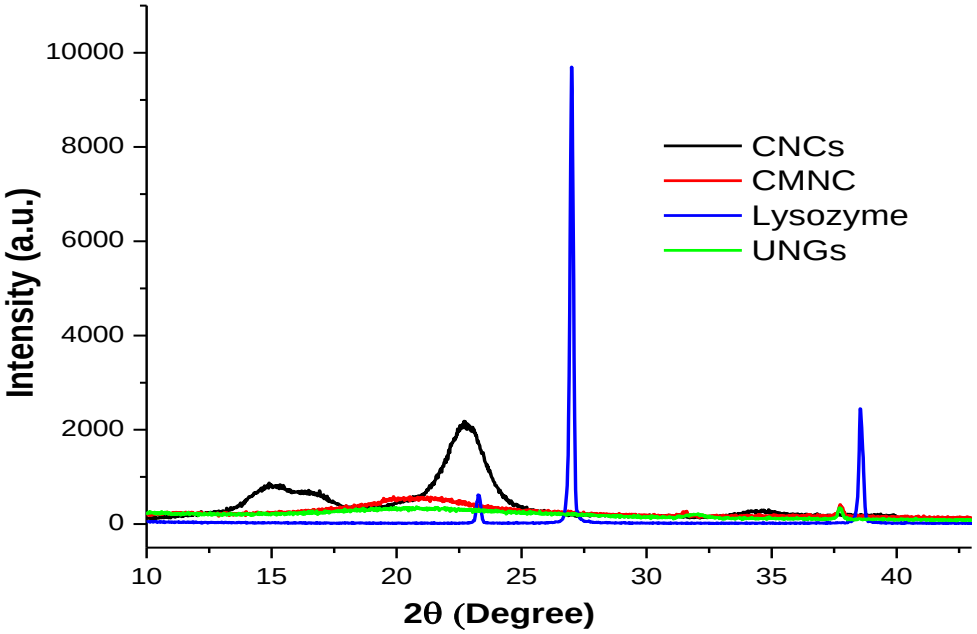

a)

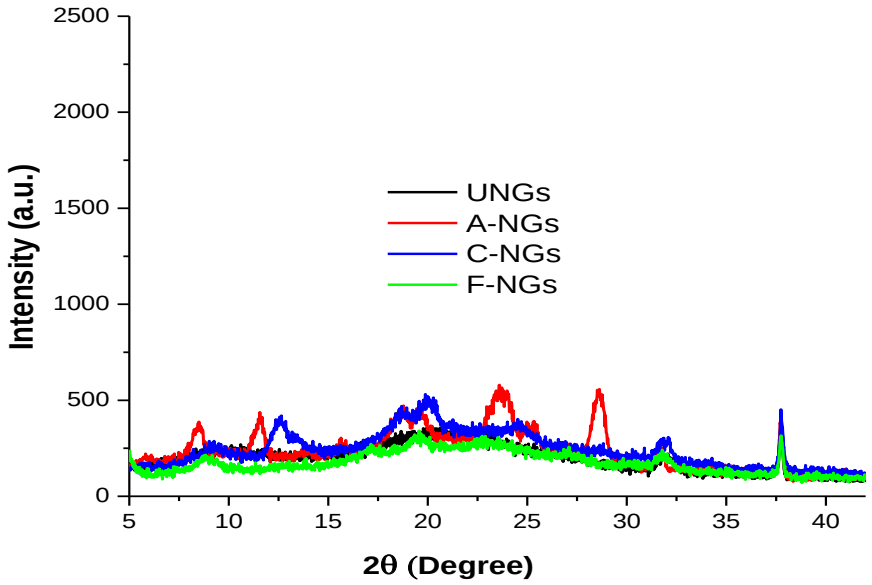

b)

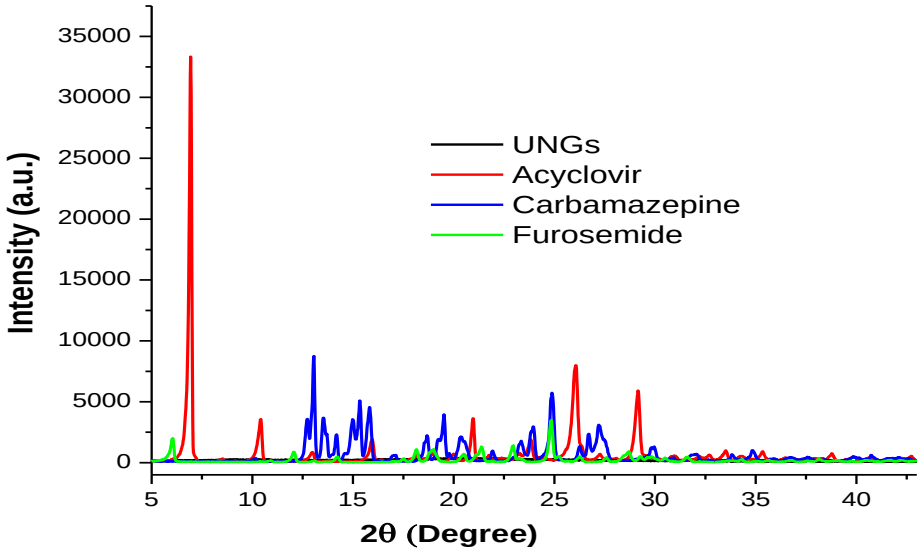

c)

Fig. 6.5: XRD of a) CNCs, CMNC, lysozyme, unloaded nanogels, b) drug-loaded nanogels: A-NGs, C-NGs, and F-NGs, compared to UNGs c) pure drugs: acyclovir, carbamazepine, and furosemide. (Key:- CNCs: cellulose nanocrystals; CMNC: carboxymethyl nanocellulose; UNGs: Unloaded nanogels; A-NGs: Acyclovir loaded nanogels; C-NGs: Carbamazepine loaded nanogels; F-NGs: Furosemide loaded nanogels).

6.3.5 Thermal properties

The TGA/DTG analysis showed that small weight loss was observed in all samples upon heating to 115 °C owing to the elimination of moisture. The CNCs had a two-step decomposition process at T_{max} 207.41 and 364.07°C due to degradation of surface sulfate groups which have large specific surface area, and breakdown of the interior non-sulfated cellulose crystals. The major weight loss (47.06%) of CMNC is observed at maximum degradation temperature (T_{max}) of 308.20°C (rate: 4.8782 %/°C) due to degradation of the polysaccharide backbone (Fig. 6.6a and b, and Table 6.1). As it is clear, the lysozyme has high thermal stability and lost only < 5% of its weight at 700 °C (Table 6.1). In the TGA/DTG curve of lysozyme, only < 2% weight loss was recorded at T_{max} 316.63 °C (rate: 0.1947 %/°C) with the highest residue (> 95%) at 700 °C, and its thermogram is not significant compared to the others. It was also reported elsewhere that lysozyme undergoes three stages of weight loss with a residual weight > 85%. The first two zones showed removal of adsorbed and absorbed water while in the third zone, decomposition of the protein occurred around the melting temperature (Elkordy et al., 2004).

In the thermograms of unloaded nanogels (Fig. 6.6), the major decomposition (~ 50% weight loss) occurred at T_{max} at 300 °C like CMNC and lysozyme. It was reported that such a degradation was due to the decomposition and evaporation of CO and CO_2, and main chain breakdown (Hayati et al., 2020). The results indicated that the presence of lysozyme and CMNC in the nanogels played an important role for the thermal stability of the nanogels (Das et al., 2016). Loading the three model drugs: acyclovir, carbamazepine, and furosemide into the nanogels did not significantly reduce the T_{max} and thermal stability, and at least three weight loss regions were observed in carbamazepine and furosemide loaded nanogels as depicted in Fig. 6.6c and 6d. Some of the peaks observed in the loaded nanogels are related to the melting points of the drugs suggesting that some of the crystalline forms of the drugs still remain in the nanogels even though more of them have been converted into amorphous form.

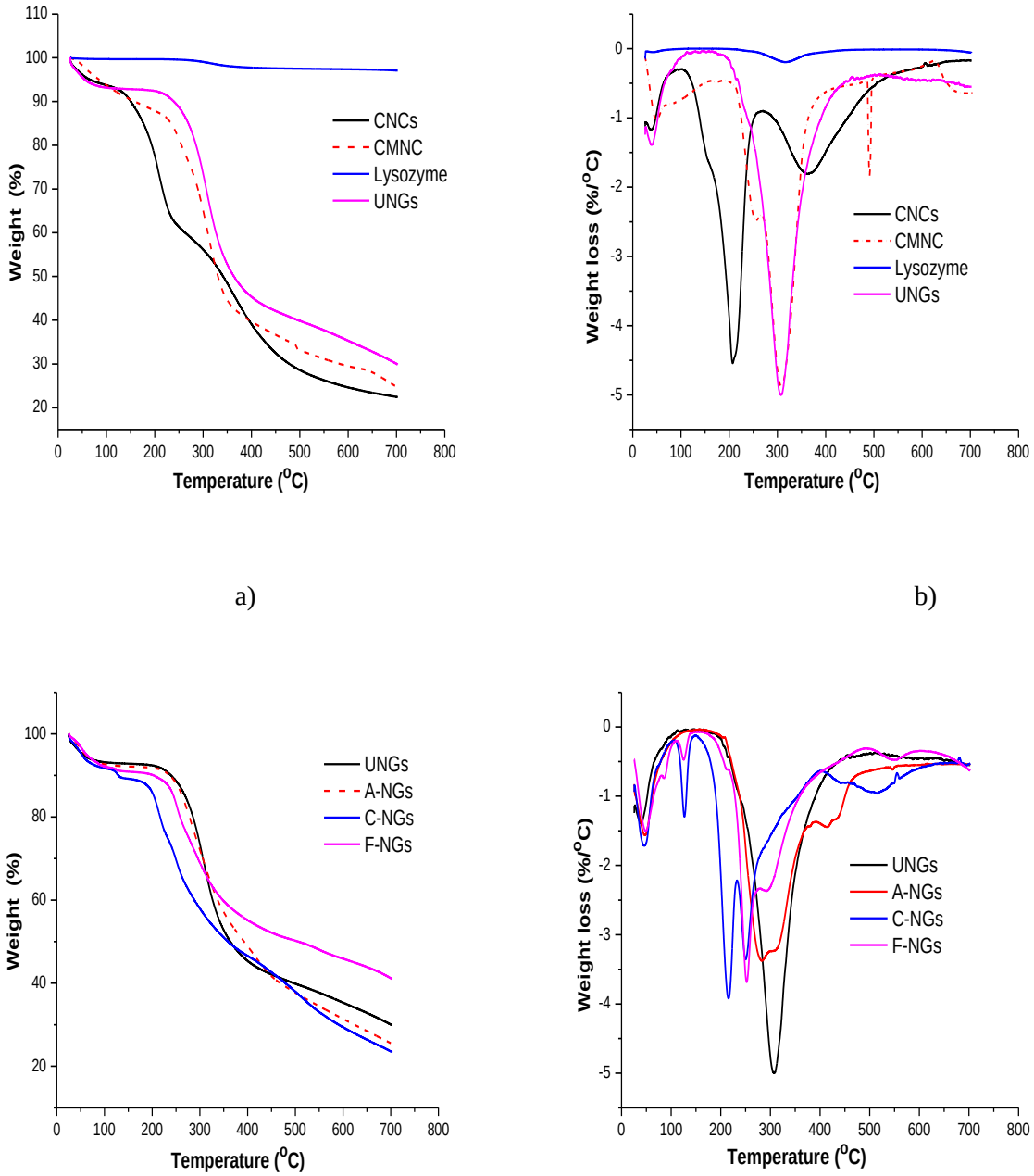

Fig. 6.6: Thermal degradation behaviors: TGA (a) and DTG (b) of CNCs, CMNC, lysozyme, unloaded nanogels (UNGs), and TGA (c) and DTG (d) of drug-loaded nanogels (A-NGs, C-NGs and F-NGs) and UNGs. (Key:- CNCs: cellulose nanocrystals; CMNC: carboxymethyl nanocellulose; UNGs: Unloaded nanogels; A-NGs: Acyclovir loaded nanogels; C-NGs: Carbamazepine loaded nanogels; F-NGs: Furosemide loaded nanogels).

Table 6.1: Summary of TGA and DTG results of CNCs, CMNC, lysozyme, unloaded and drug-loaded nanogels.

Material	ΔT (°C)	T_{max} (°C)	Weight loss (%)	Weight loss rate (%/°C)	$T_{10\%}$; $T_{50\%}$ (°C)	Residue at 700 °C (%)
CNCs	26.55-94.39	39.33	6.08	1.1660	150.47; 341.47	22.47
	117.39-260.17	207.41	32.83	4.5407		
	276.27-542.72	364.07	32.12	1.8092		
CMNC	25.74-112.46	48.65	7.20	1.0438	158.40; 330.72	24.78
	216.27-396.84	308.20	47.06	4.8782		
	486.80-496.89	491.30	1.34	1.8325		
Lysozyme	27.27-64.24	41.74	0.26	0.0494	> 700	97.10
	270.52-361.24	317.79	1.42	0.1941		
UNGs	26.55-94.39	38.33	6.75	1.3840	239.41; 363.74	30.04
	199.24-441.38	306.61	49.87	4.9943		
A-NGs	25.78-101.10	46.65	7.49	1.5618	236.91; 392.67	25.55
	208.50-469.55	284.27	51.76	3.3754		
C-NGs	25.78-101.02	46.19	8.03	1.7135	129.21; 358.90	23.59
	111.02-140.80	125.60	2.17	0.4714		
	175.84-231.82	215.43	13.49	3.9184		
	232.24-296.60	250.66	16.45	3.3555		
F-NGs	25.78-105.60	49.08	7.99	1.5020	203.20; 506.47	41.20
	108.52-143.97	126.61	0.98	1.2923		
	188.92-425.62	252.33	36.99	3.6838		

Key:- ΔT-Temperature change where main weight loss occurs; T_{max}-Maximum degradation (maximum weight loss) temperature; TGA-Thermogravimetric analysis; DTG-Differential thermogravimetry; CNCs: cellulose nanocrystals; CMNC: carboxymethyl nanocellulose; UNGs: Unloaded nanogels; A-NGs: Acyclovir loaded nanogels; C-NGs: Carbamazepine loaded nanogels; F-NGs: Furosemide loaded nanogels.

Fig. 6.7 shows the Differential Scanning Calorimetry (DSC) curves of CNCs, CMNC, lysozyme, unloaded nanogels (UNGs), and drug-loaded nanogels (A-NGs, C-NGs and F-NGs). The DSC thermograms of the samples exhibit an early very small endothermic peak with an enthalpy change observed at 35–110 °C, which is attributed to desorption of moisture trapped in the polysaccharide structure. The DSC profiles of all the samples show an endothermic peak ranged from 211-216 °C. The endothermic peaks of the samples could be due to the breakdown of intramolecular interaction and the decomposition of the chains. The thermal scission of the carboxylate groups in CMNC might result in the evolution of CO_2 from the corresponding cellulose backbone. A broad endothermic peak curve was also observed in the range of 220–300 °C, and it could be assigned

to the partial pyrolysis due to fragmentation of hydroxyl bonds of the CNCs and CMNC. In the case of nanogels, the heat flow intensity gradually increased indicating a better thermal stability. The thermal characterization results were in good agreement with the TGA and XRD results.

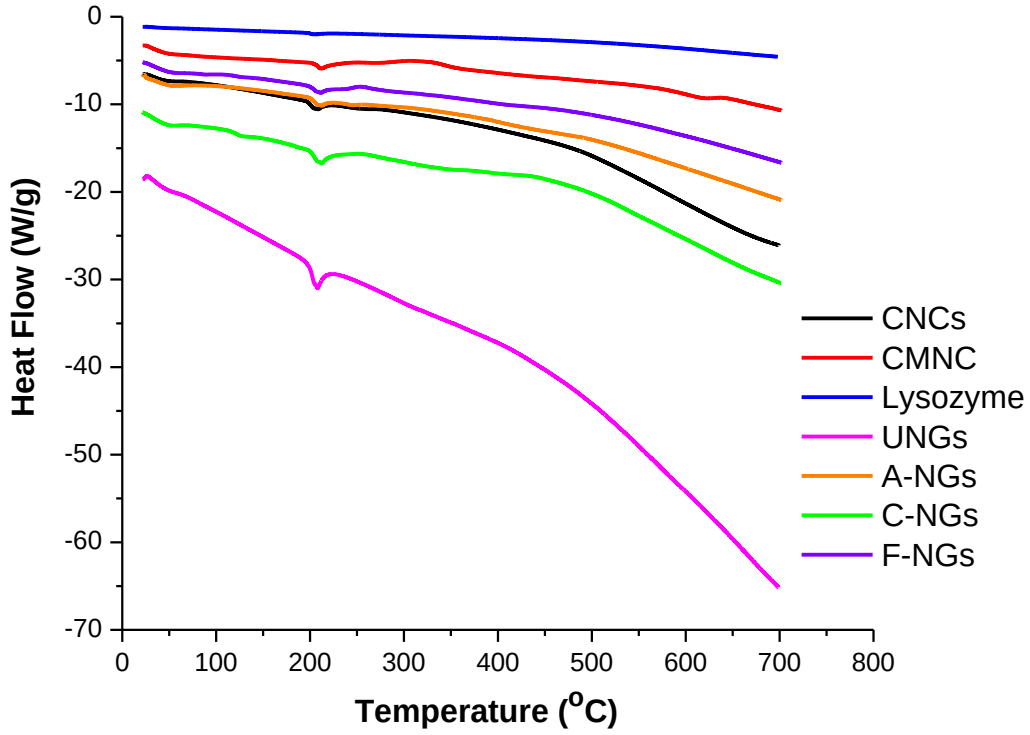

a)

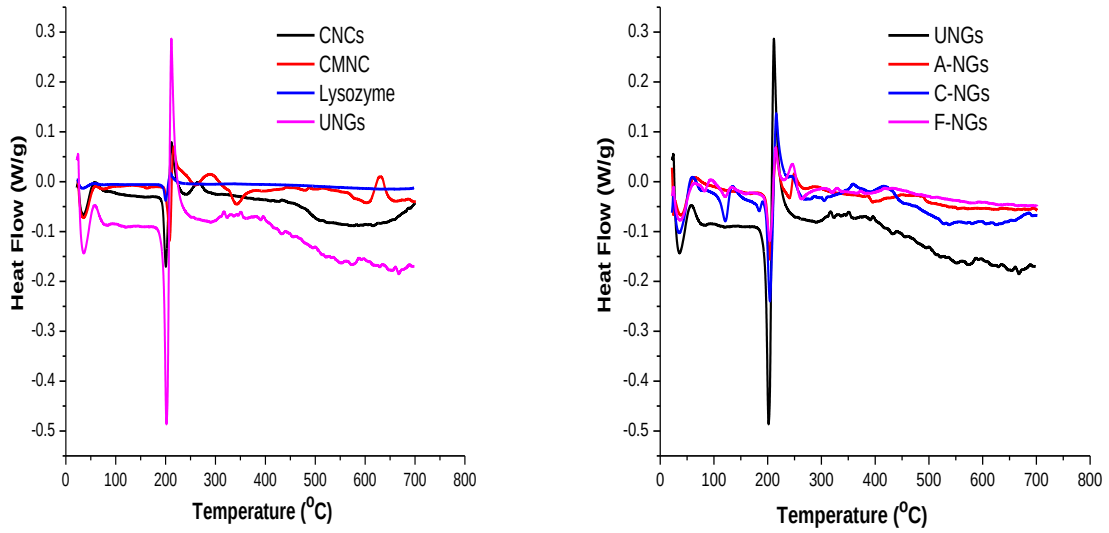

b)

Fig. 6.7: a) DSC curves of CNCs, CMNC, lysozyme, unloaded nanogels (UNGs), and drug-loaded nanogels (A-NGs, C-NGs and F-NGs), and b) the derived DSC curve counterparts (Key:- CNCs: cellulose nanocrystals; CMNC: carboxymethyl nanocellulose; UNGs: Unloaded nanogels; A-NGs: Acyclovir loaded nanogels; C-NGs: Carbamazepine loaded nanogels; F-NGs: Furosemide loaded nanogels).

6.3.6 Drug loading and *in vitro* release studies

The carboxyl groups in the CMNC chains can form hydrogen bonds with the amide groups in the three drug molecules to form intermolecular complexes, as well as the physical entrapment effect when the molecules change from complexes to nanogels during the heating, resulting in a higher drug encapsulation efficiency. The results of EE and LC of the nanogels are shown in Fig. 6.8. When the weight ratio of CMNC:lysozyme was adjusted at 1:1 and the heating temperature was 75 °C, both EE and LC were increased when the heating time was varied from 15 to 30 min. It could be observed that nanogels after heating for 30 min had the highest EE and LC of 62.04 ± 0.2301 - 93.94 ± 0.0135% and 17.73 ± 0.0657 - 26.84 ± 0.004%, respectively. CMC-based nanogels exhibited lower EE (≤ 57.55 ± 0.4322%) and LC (≤ 16.34 ± 0.0315%) when compared with CMNC-based nanogels prepared at similar conditions. Carbamazepine-loaded nanogels had the highest EE and LC when compared with the acyclovir-loaded and furosemide-loaded nanogels. When the heating time was 75 min, both EE and LC decreased due to partial denaturation of

lysozyme and deformation of the nanogels. As a result, less encapsulated model drugs are likely to spread into the solution during centrifugation. Besides, the size of nanogels heated for 15 min is larger than that heated for 30 min because the former gels are of much looser aggregations so the EE and LC decrease, as depicted in Fig. A9 (Appendix).

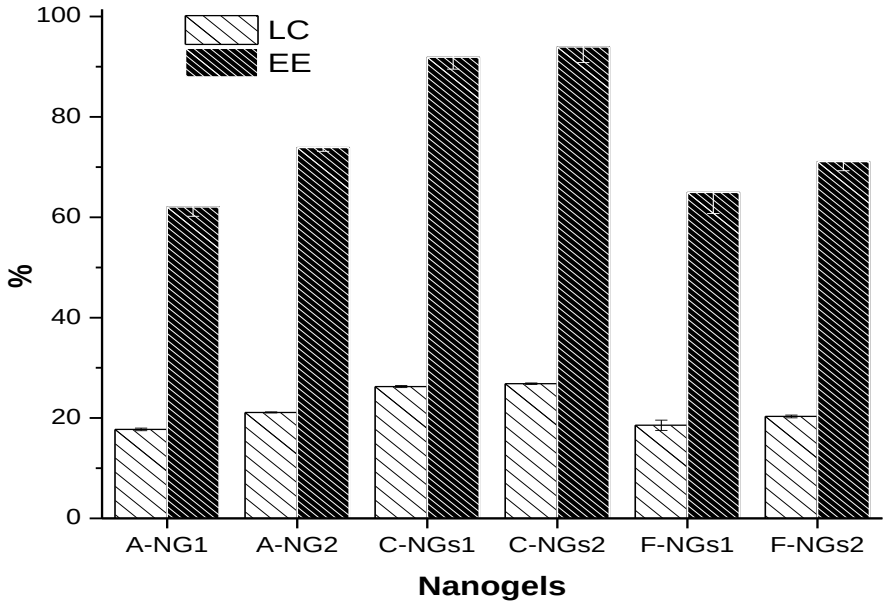

Fig. 6.8: Loading capacity and encapsulation efficiency of the nanogels. (Key:- 1 and 2: Nanogels pH 5.3 and probe-sonicated, and 7.4, respectively; A-NGs: Acyclovir loaded nanogels; C-NGs: Carbamazepine loaded nanogels; F-NGs: Furosemide loaded nanogels). Data are presented as the mean ± SD (*n* = 3).

The cumulative release profiles of the three drugs from the drug-loaded nanogels in PBS (pH 7.4), 37 °C are depicted in Fig. 6.9. The release of the drugs from nanogels prepared at pH 7.4 and 5.3 was sustained over a period of 12 h (48-72%; 60-80%, respectively), showing that the release pattern depended on the preparation condition of the nanogels and the solubility of the drugs. The release of the drugs was consistently more retarded in nanogels prepared at pH 7.4 probably because of the more consolidated assembly resulting from the strong electrostatic interaction between CMNC and lysozyme at this pH and the heating process which helps to cure the CMNC-lysozyme complex into a more rigid structure. The burst release occurred at the first 2 h was attributed to the unincorporated drug molecules located at the surface of the nanogels.

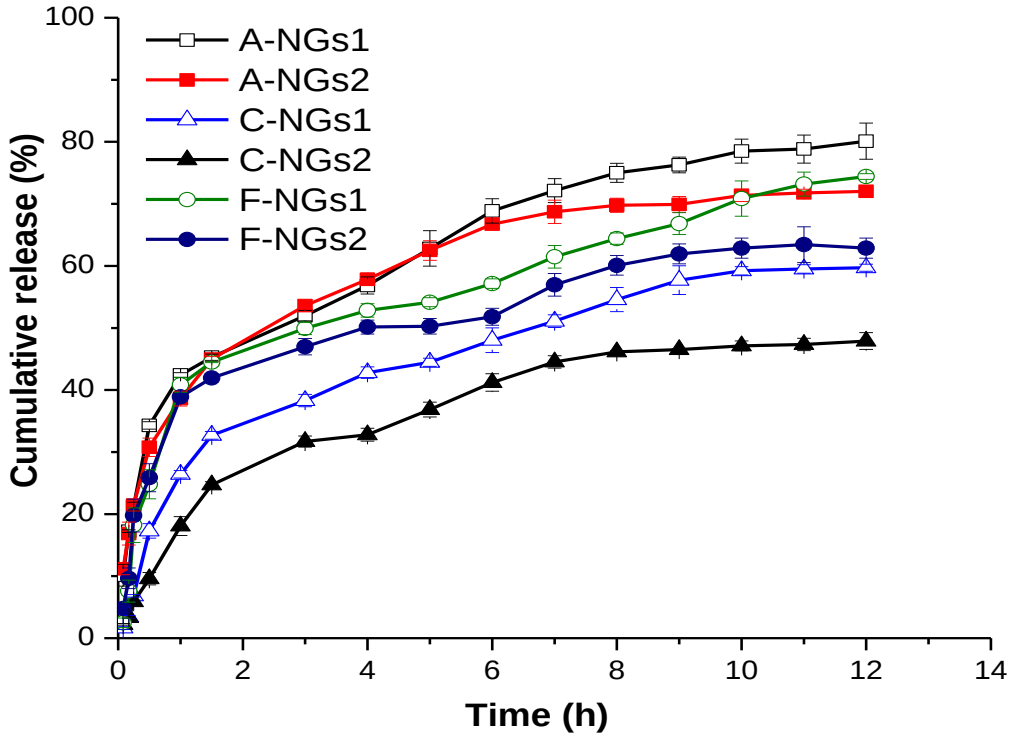

Fig. 6.9: Cumulative *in vitro* release profiles of the three drugs from the drug-loaded CMNC based nanogels for 12 h in PBS (pH 7.4) (Key- 1, and 2: Nanogels, pH 5.3, and adjusted pH 7.4, respectively; A-NGs: Acyclovir loaded nanogels; C-NGs: Carbamazepine loaded nanogels; F-NGs: Furosemide loaded nanogels). Data are presented as the mean ± SD (n = 3).

The release rate of acyclovir was higher when compared with the other two drugs: furosemide and carbamazepine, which could be due to the hydrophilic nature of acyclovir and its small molecular size facilitating the diffusion as well as its higher affinity to the PBS (pH 7.4) medium. Acyclovir is a hydrophilic drug (log p: -1.29 and -1.32, in octanol/water and octanol/PBS (pH 7.4), respectively while carbamazepine and furosemide are hydrophobic drugs (log p: 2.06 and 2.17, and log p: 1.68 and 1.95, respectively), as shown in Table 2. The certificate of analyses of the three model drugs are annexed in the Appendix (Fig. A10).

Table 6.2: Solubilities and partition coefficients of the model drug molecules

Drug molecules	Molecular weight (g/mol)	Solubility at 25 °C (mg/L)		Partition coefficient (log p)	
		Distilled water	PBS (pH 7.4)	Octanol/water	Octanol/PBS (pH 7.4)
Acyclovir	225.20	1,202.7 ± 58.68	1,357.0 ± 52.96	-1.29 ± 0.26	-1.31 ± 0.29
Carbamazepine	236.27	28.6 ± 3.20	27.8 ± 3.65	2.06 ± 0.14	2.17 ± 0.003
Furosemide	330.74	72.9 ± 7.31	79.5 ± 18.59	1.68 ± 0.03	1.95 ± 0.08

Data are presented as mean ± SD (n = 3).

The sustained release pattern of poorly water-soluble drugs: carbamazepine and furosemide from the nanogels is further associated with the enhanced hydrophobic interactions between the drug and the hydrophobic portion of the CMNCs as well as lysozyme, which was induced by the denaturation of lysozyme heating at 75 °C. This interaction could be associated with enhanced partitioning of the hydrophobic drug molecules into the hydrophobic core-shell structure of the nanogels. Carbamazepine and furosemide have also less affinity towards the PBS medium (pH 7.4) due to their hydrophobic nature as evidenced by their high partition coefficients (Table 2). In the following period, the drug release was quite much slower and sustained in carbamazepine, which has the least solubility profile and the highest partition coefficient. The driving forces for drug release from the nanogels may be the effusion of the drugs from the interior of the nanogels, the swelling and the erosion of the nanogels (Eckmann et al., 2014).

6.3.7 Stability profiles of the unloaded and drug-loaded nanogels

Fig. 6.10. shows the particle size and PDI of unloaded and drug-loaded nanogels stored at different temperatures for 3 months. The nanogels showed negligible increment in particle size and PDI at all storage conditions. None of the nanogels indicated any sign of agglomeration or colour change during the storage period. From the stability results, CMNC-based nanogels were stable at all storage conditions during the study period.

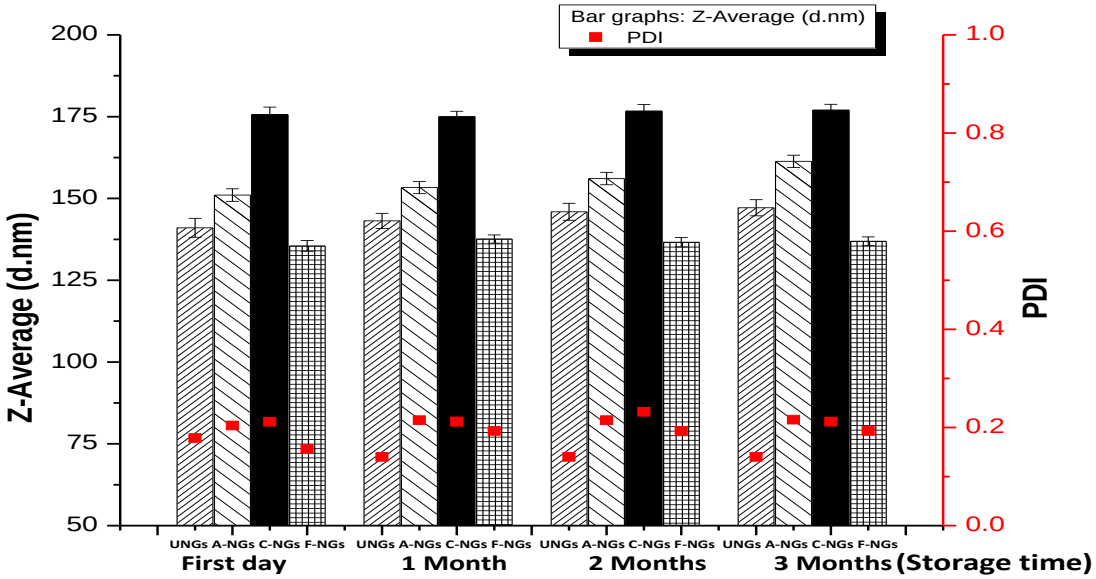
Bar graphs: Z-Average (d.nm)
PDI
Z-Average (d.nm)
PDI
200
175
150
125
100
75
50
1.0
0.8
0.6
0.4
0.2
0.0
UNGs A-NGs C-NGs F-NGs
First day
1 Month
2 Months
3 Months
(Storage time)

a)

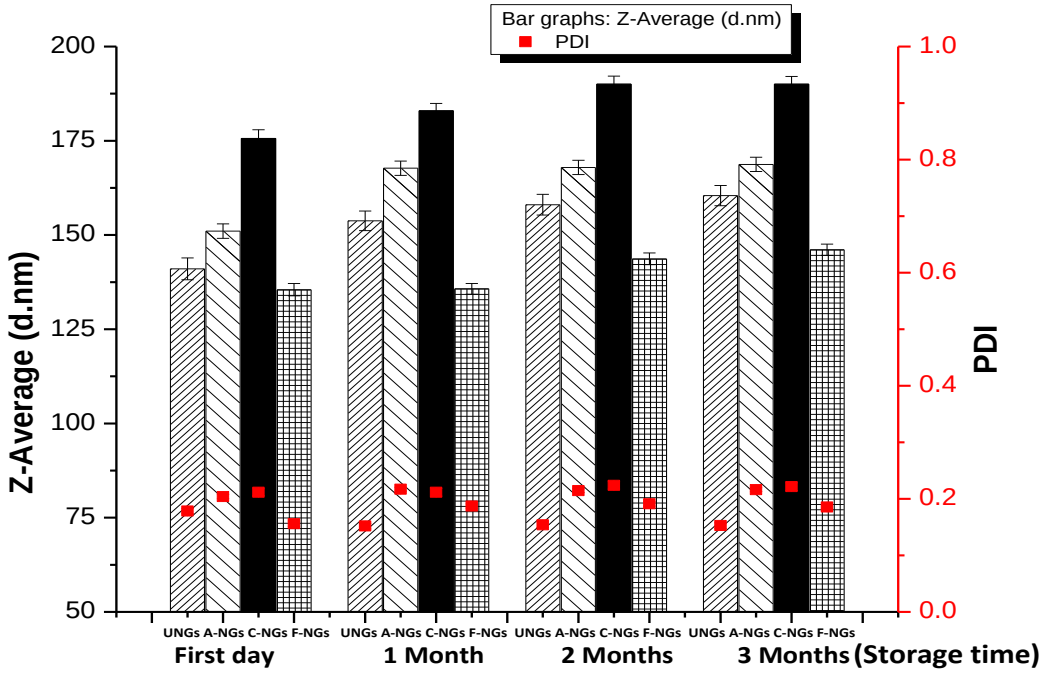
Bar graphs: Z-Average (d.nm)
PDI
Z-Average (d.nm)
PDI
200
175
150
125
100
75
50
1.0
0.8
0.6
0.4
0.2
0.0
UNGs A-NGs C-NGs F-NGs
First day
1 Month
2 Months
3 Months
(Storage time)

b)

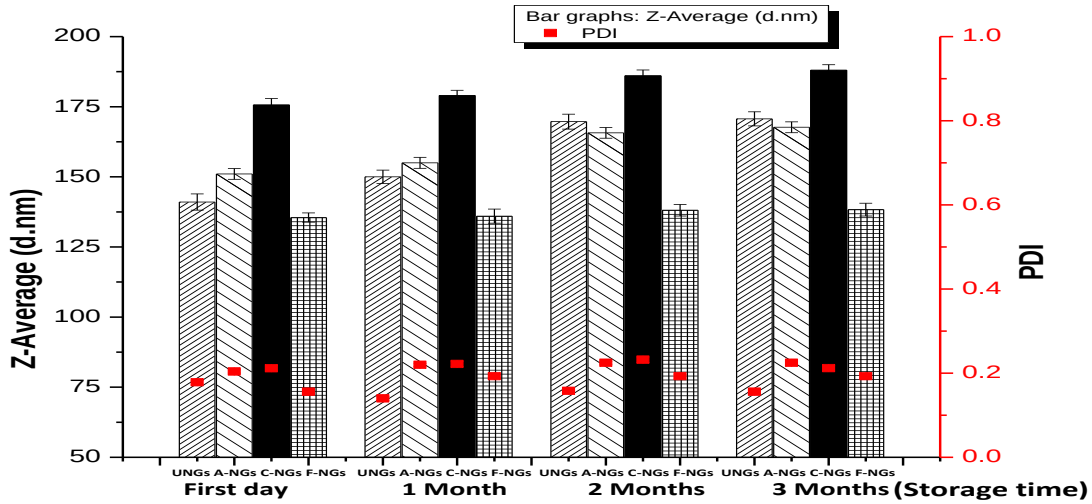

c)

Fig. 6.10: Stability profiles of unloaded and drug-loaded nanogels in terms of particle size and PDI stored at a) 4 °C b) 25 °C and c) 40 °C for 3 months (Key:- NGs: Nanogels, their pH 5.6, followed by ultra-sonication; A-NGs: Acyclovir loaded nanogels; C-NGs: Carbamazepine loaded nanogels; F-NGs: Furosemide loaded nanogels). Data are presented as the mean ± SD (n = 3).

6.4 Conclusion

An optimal condition (a weight ratio of 1:1, pH 7.4, heating at 75 °C for 30 min) was followed for synthesis of the nanogels via electrostatic interaction between anionic CMNC and cationic lysozyme mixture. The prepared nanogels were spherical, amorphous, and colloidally and thermally stable, and had small hydrodynamic size and PDI. CMNC-based nanogels displayed significantly lower particle size than CMC-based nanogels at all pH points (5.3-10.5) investigated ($p < 0.01$). The reduction of the size of nanogels was more pronounced at higher pH values than sonication, and heating times. *In vitro* release studies of the drugs from various BCS classes showed that the nanogels sustained the release, and further governed by the physicochemical properties of the drugs such as solubility and partition coefficient. The unloaded and drug-loaded nanogels remained stable at 4 °C, 25 °C/60% RH and 40 °C/75% RH for at least 3 months. CMNC-based nanogels exhibited lower particle size than CMC-based nanogels at all pH points (5.3-10.5) investigated. This work demonstrated higher drug loading and encapsulation efficiencies, and sustained drug release profiles from nanocellulose-based nanogels prepared using a simple and green self-assembly technique.

Summary

In this study, TS, EF, SB and CH were successfully explored as alternative sources of cellulose, CNCs and CMC with different physicochemical properties, which could be due to variations in cellulose sources and isolation/preparation conditions. Removal of non-cellulosic components in all as-extracted cellulose fibers was confirmed by FTIR, XRD, TGA, and ESEM as well as estimation of the compositions. TEM analyses revealed that CNCs isolated from the four byproducts pretreated with 5% sodium hydroxide had higher aspect ratios (17.32-36.67) with elongated needle-shaped nanoscale structures than CNCs obtained using 17.5% sodium hydroxide at the pretreatment stage (8.95-16.38). Higher alkaline condition, 17.5% sodium hydroxide, might not necessarily contribute to the polymorphic transition in lignocellulosic materials with higher lignin content as evidenced in CH. FTIR studies, XRD and SEM analyses indicated effective etherification, with reduction in the thermal stability in the as-obtained CMC and EF-CMNC. Due to its unique and superior properties such as yield, purity, and crystallinity, EF was selected for preparation of CM(N)C to be included as anionic polysaccharide in the nanogel formulations via self-assembly using cationic lysozyme. Spherical nanogels of small sizes (75-110 nm) and PDI (< 0.2) as well as large zeta potential (-38 to -55 mV) were prepared at optimal condition (at 1:1 weight ratio of CMNC:lysozyme, pH 7.4, and 30-min heating time), with high EE (62-94%) and LC (18-27%), and sustained release profiles. CMNC-based nanogels exhibited superior properties to CMC-based nanogels in terms of size, PDI, zeta potential, LC, and EE ($p < 0.01$). In general, the properties of the (loaded) nanogels depended on the preparation conditions such as weight ratio, pH, sonication, and heating time, as well as properties of the active drug molecules. From the findings, the synthesized nanocellulose-based nanogels following easy and green preparation approach exhibited attractive properties with respect to the size, PDI, zeta potential, shape, thermal stability, EE, LC, and tunability for encapsulating and sustaining different BCS class drugs.

Suggestions for further work

In this research work, nanogels exhibiting desirable properties were obtained via electrostatic interaction between CMNC and lysozyme following a simple and green approach for sustained drug delivery.

Therefore, the following are suggested for further work:

- Conducting cytotoxicity tests for CNCs, CMNC and nanogels; *in vivo* study and establishing *in vitro-in vivo* correlation (IVIVC); real time stability studies for both unloaded and drug loaded nanogels.

List of publications

Gabriel, T., Belete, A., Syrowatka, F., Neubert, R.H.H., Gebre-Mariam, T., 2020. Extraction and characterization of celluloses from various plant byproducts. Int. J. Biol. Macromol. 158, 1248–1258. https://doi.org/10.1016/j.ijbiomac.2020.04.264

Gabriel, T., Belete, A., Hause, G., Neubert, R.H.H., Gebre-Mariam, T., 2021. Isolation and characterization of cellulose nanocrystals from different lignocellulosic residues : A comparative study. J. Polym. Environ. https://doi.org/10.1007/s10924-021-02089-3

List of publishable manuscripts

Gabriel, T., Belete, A., Hause, G., Neubert, R.H.H., Gebre-Mariam, T. Nanocellulose-based nanogels for sustained drug delivery: Preparation, characterization and evaluation. *Submitted to Journal of Drug Delivery Sciences and Technology, Under Review and Preprinted JDDST-D-22-00255, Available at SSRN: https://ssrn.com/abstract=4028236 or http://dx.doi.org/10.2139/ssrn.4028236*

Gabriel, T., Belete, A., Hause, G., Neubert, R.H.H., Gebre-Mariam, T. Is mercerization the only factor for (partial) polymorphic transition of cellulose I to cellulose II in CNCs? *Submitted to Cellulose Chemistry and Technology, and revised.*

Gabriel, T., Belete, A., Neubert, R.H.H., Gebre-Mariam, T. Physicochemical characterization of carboxymethyl cellulose from local agro-industrial byproducts. *Submitted to Bulletin of Materials Science*

Latest developments of cellulose-based nanogels as pharmaceutical nanocarriers. *Ready for submission*

Isolation methods and properties of cellulose nanocrystals from various plant sources: the past, the present and the future. *Under preparation*

References

Abd El-Fattah, M., Hasan, A.M.A., Keshawy, M., El Saeed, A.M., Aboelenien, O.M., 2018. Nanocrystalline cellulose as an eco-friendly reinforcing additive to polyurethane coating for augmented anticorrosive behavior. Carbohydr. Polym. 183, 311–318. https://doi.org/10.1016/j.carbpol.2017.12.084

Abdel-Halim, E.S., 2014. Chemical modification of cellulose extracted from sugarcane bagasse: Preparation of hydroxyethyl cellulose. Arab. J. Chem. 7, 362–371. https://doi.org/10.1016/j.arabjc.2013.05.006

Abdulhameed, A., Mbuvi, H.M., Changamu, E.O., Maingi, F.M., 2019. Microwave synthesis of Carboxymethylcellulose (CMC) from rice husk. IOSR J. Appl. Chem. 12, 33–42. https://doi.org/10.9790/5736-1212013342

Abitbol, T., Rivkin, A., Cao, Y., Nevo, Y., Abraham, E., Ben-Shalom, T., Lapidot, S., Shoseyov, O., 2016. Nanocellulose, a tiny fiber with huge applications. Curr. Opin. Biotechnol. 39, 76–88. https://doi.org/10.1016/j.copbio.2016.01.002

Adel, A.M., Abd El-Wahab, Z.H., Ibrahim, A.A., Al-Shemy, M.T., 2011. Characterization of microcrystalline cellulose prepared from lignocellulosic materials. Part II: Physicochemical properties. Carbohydr. Polym. 83, 676–687. https://doi.org/10.1016/j.carbpol.2010.08.039

Adinugraha, M.P., Marseno, D.W., Haryadi, 2005. Synthesis and characterization of sodium carboxymethylcellulose from cavendish banana pseudo stem (Musa cavendishii LAMBERT). Carbohydr. Polym. 62, 164–169. https://doi.org/10.1016/j.carbpol.2005.07.019

Aguayo, M.G., Pérez, A.F., Reyes, G., Oviedo, C., Gacitúa, W., Gonzalez, R., Uyarte, O., 2018. Isolation and characterization of cellulose nanocrystals from rejected fibers originated in the Kraft Pulping process. Polymers (Basel). 10, 1145–1156. https://doi.org/10.3390/polym10101145

Ahmadzadeh, S., Nasirpour, A., Harchegani, M.B., Hamdami, N., Keramat, J., 2018. Effect of electrohydrodynamic technique as a complementary process for cellulose extraction from bagasse: Crystalline to amorphous transition. Carbohydr. Polym. 188, 188–196. https://doi.org/10.1016/j.carbpol.2018.01.109

Ahmed, S., Alhareth, K., Mignet, N., 2020. Advancement in nanogel formulations provides controlled drug release. Int. J. Pharm. 584, 119435.

https://doi.org/10.1016/j.ijpharm.2020.119435

Ahuja, D., Kaushik, A., Singh, M., 2018. Simultaneous extraction of lignin and cellulose nanofibrils from waste jute bags using one pot pre-treatment. Int. J. Biol. Macromol. 107, 1294–1301. https://doi.org/10.1016/j.ijbiomac.2017.09.107

Al-Dulaimi, A.A., Wanrosli, W.D., 2017. Isolation and characterization of nanocrystalline cellulose from totally chlorine free oil palm empty fruit bunch pulp. J. Polym. Environ. 25, 192–202. https://doi.org/10.1007/s10924-016-0798-z

Alghooneh, A., Mohammad Amini, A., Behrouzian, F., Razavi, S.M.A., 2017. Characterisation of cellulose from coffee silverskin. Int. J. Food Prop. 20, 2830–2843. https://doi.org/10.1080/10942912.2016.1253097

Alves, L., Medronho, B., Antunes, F.E., Fernández-García, M.P., Ventura, J., Araújo, J.P., Romano, A., Lindman, B., 2015. Unusual extraction and characterization of nanocrystalline cellulose from cellulose derivatives. J. Mol. Liq. 210, 106–112. https://doi.org/10.1016/j.molliq.2014.12.010

Alves, R.C., Rodrigues, F., Nunes, M.A., Vinha, A.F., Oliveira, M.B.P.P., 2017. State of the art in coffee processing by-products, in: Galanakis, C.M. (Ed.), Handbook of Coffee Processing By-Products. Academic Press, Elsevier Inc, Chania, Greece, pp. 1–26. https://doi.org/http://dx.doi.org/10.1016/B978-0-12-811290-8.00001-3

An, D., Zhao, D., Li, X., Lu, X., Qiu, G., Shea, K.J., 2015. Synthesis of surfactant-free hydroxypropylcellulose nanogel and its dual-responsive properties. Carbohydr. Polym. 134, 385–389. https://doi.org/10.1016/j.carbpol.2015.08.009

Aristizábal-Marulanda, V., Chacón-Perez, Y., Alzate, C.A.C., 2017. The biorefnery concept for the industrial valorization of coffee processing by-products, in: Galanakis, C.M. (Ed.), Handbook of Coffee Processing By-Products. Elsevier Inc, Chania, Greece, pp. 63–86. https://doi.org/http://dx.doi.org/10.1016/B978-0-12-811290-8.00003-7

Arnata, I.W., Suprihatin, S., Fahma, F., Richana, N., Sunarti, T.C., 2020. Cationic modification of nanocrystalline cellulose from sago fronds. Cellulose 27, 3121–3141. https://doi.org/10.1007/s10570-019-02955-3

Asadian-Birjand, M., Sousa-Herves, A., Steinhilber, D., Cuggino, J.C., Calderon, M., 2012. Functional Nanogels for Biomedical Applications. Curr. Med. Chem. 19, 5029–5043. https://doi.org/10.2174/092986731120902502

Azadi, A., Hamidi, M., Khoshayand, M.R., Amini, M., Rouini, M.R., 2012. Preparation and optimization of surface-treated methotrexate-loaded nanogels intended for brain delivery. Carbohydr. Polym. 90, 462–471. https://doi.org/10.1016/j.carbpol.2012.05.066

Azadi, A., Hamidi, M., Rouini, M.R., 2013. Methotrexate-loaded chitosan nanogels as "Trojan Horses" for drug delivery to brain: Preparation and in vitro/in vivo characterization. Int. J. Biol. Macromol. 62, 523–530. https://doi.org/10.1016/j.ijbiomac.2013.10.004

Baipaywad, P., Udomluck, N., Pyo, S.-G., Park, H.H., Park, H., 2014. Fabrication of nanogels for delivery of molecules. J. Nanosci. Nanotechnol. 14, 7363–7373. https://doi.org/10.1166/jnn.2014.9579

Bano, S., Negi, Y.S., 2017. Studies on cellulose nanocrystals isolated from groundnut shells. Carbohydr. Polym. 157, 1041–1049. https://doi.org/10.1016/j.carbpol.2016.10.069

Barai, B.K., Singhal, R.S., Kulkarni, P.R., 1997. Optimization of a process for preparing carboxymethyl cellulose from water hyacinth (Eichornia crassipes). Carbohydr. Polym. 32, 229–231. https://doi.org/10.1016/S0144-8617(96)00166-X

Basta, A.H., El-Saied, H., El-Deftar, M.M., El-Henawy, A.A., El-Sheikh, H.H., Abdel-Shakour, E.H., Hasanin, M.S., 2016. Properties of modified carboxymethyl cellulose and its use as bioactive compound. Carbohydr. Polym. 153, 641–651. https://doi.org/10.1016/j.carbpol.2016.07.051

Basu, P., Narendrakumar, U., Arunachalam, R., Devi, S., Manjubala, I., 2018. Characterization and Evaluation of Carboxymethyl Cellulose-Based Films for Healing of Full-Thickness Wounds in Normal and Diabetic Rats. ACS Omega 3, 12622–12632. https://doi.org/10.1021/acsomega.8b02015

Begines, B., Ortiz, T., Pérez-Aranda, M., Martínez, G., Merinero, M., Argüelles-Arias, F., Alcudia, A., 2020. Polymeric nanoparticles for drug delivery: Recent developments and future prospects. Nanomaterials 10, 1–41. https://doi.org/10.3390/nano10071403

Benini, K.C.C. de C., Voorwald, H.J.C., Cioffi, M.O.H., Rezende, M.C., Arantes, V., 2018. Preparation of nanocellulose from Imperata brasiliensis grass using Taguchi method. Carbohydr. Polym. 192, 337–346. https://doi.org/10.1016/j.carbpol.2018.03.055

Benito-González, I., López-Rubio, A., Gavara, R., Martínez-Sanz, M., 2019. Cellulose nanocrystal-based films produced by more sustainable extraction protocols from Posidonia oceanica waste biomass. Cellulose 26, 8007–8024. https://doi.org/10.1007/s10570-019-

02641-4

Berhanu, H., Kiflie, Z., Miranda, I., Lourenço, A., Ferreira, J., Feleke, S., Yimam, A., Pereira, H., 2018. Characterization of crop residues from false banana /ensete ventricosum/ in Ethiopia in view of a full-resource valorization. PLoS One 13, 1–21. https://doi.org/10.1371/journal.pone.0199422

Bhattacharya, D., Germinario, L.T., Winter, W.T., 2008. Isolation, preparation and characterization of cellulose microfibers obtained from bagasse. Carbohydr. Polym. 73, 371–377. https://doi.org/10.1016/j.carbpol.2007.12.005

Bickford, R., 2019. Ethiopia Coffee Annual Coffee Annual Report--Global Agricultural Information Network.

Bidgoli, H., Zamani, A., Jeihanipour, A., Taherzadeh, M.J., 2014. Preparation of carboxymethyl cellulose superabsorbents from waste textiles. Fibers Polym. 15, 431–436. https://doi.org/10.1007/s12221-014-0431-5

Biswas, A., Kim, S., Selling, G.W., Cheng, H.N., 2014. Conversion of agricultural residues to carboxymethylcellulose and carboxymethylcellulose acetate. Ind. Crops Prod. 60, 259–265. https://doi.org/10.1016/j.indcrop.2014.06.004

Borrell, J.S., Biswas, M.K., Goodwin, M., Blomme, G., Schwarzacher, T., Heslop-Harrison, J.S., Wendawek, A.M., Berhanu, A., Kallow, S., Janssens, S., Molla, E.L., Davis, A.P., Woldeyes, F., Willis, K., Demissew, S., Wilkin, P., 2019. Enset in Ethiopia: A poorly characterized but resilient starch staple. Ann. Bot. 123, 747–766. https://doi.org/10.1093/aob/mcy214

Borysiak, S., Grząbka-Zasadzińska, A., 2016. Influence of the polymorphism of cellulose on the formation of nanocrystals and their application in chitosan/nanocellulose composites. J. Appl. Polym. Sci. 133, 1–9. https://doi.org/10.1002/app.42864

Borzooeian, Z., Taslim, M.E., Ghasemi, O., Rezvani, S., Borzooeian, G., Nourbakhsh, A., 2018. A high precision method for length-based separation of carbon nanotubes using bio-conjugation, SDS-PAGE and silver staining. PLoS One 13, 1–16. https://doi.org/10.1371/journal.pone.0197972

BP, 2016a. In vitro drug evaluation, in: British Pharmacopoeia Commission - British Pharmacopoeia-The Stationery Office. Crown Copyright 2008.

BP, 2016b. Carmellose (Sodium), in: British Pharmacopoeia Commission - British

Pharmacopoeia-The Stationery Office. Crown Copyright 2015, London, pp. 2015–2016. https://doi.org/http://www.pharmacopoeia.com

Brater, D.G., Seiwell, R., Anderson, S., Burdette, A., Dehmer, G.J., Chennavasin, P., 1982. Absorption and disposition of furosemide in congestive heart failure. Kidney Int. 22, 171–176. https://doi.org/10.1038/ki.1982.149

Candido, R.G., Gonçalves, A.R., 2016. Synthesis of cellulose acetate and carboxymethylcellulose from sugarcane straw. Carbohydr. Polym. 152, 679–686. https://doi.org/10.1016/j.carbpol.2016.07.071

Casaburi, A., Montoya Rojo, Ú., Cerrutti, P., Vázquez, A., Foresti, M.L., 2018. Carboxymethyl cellulose with tailored degree of substitution obtained from bacterial cellulose. Food Hydrocoll. 75, 147–156. https://doi.org/10.1016/j.foodhyd.2017.09.002

César, N.R., Pereira-da-Silva, M.A., Botaro, V.R., de Menezes, A.J., 2015. Cellulose nanocrystals from natural fiber of the macrophyte Typha domingensis: extraction and characterization. Cellulose 22, 449–460. https://doi.org/10.1007/s10570-014-0533-7

Chacko, R.T., Ventura, J., Zhuang, J., Thayumanavan, S., 2012. Polymer nanogels: A versatile nanoscopic drug delivery platform. Adv. Drug Deliv. Rev. https://doi.org/10.1016/j.addr.2012.02.002

Chen, L., Remondetto, G.E., Subirade, M., 2006. Food protein-based materials as nutraceutical delivery systems. Trends Food Sci. Technol. 17, 272–283. https://doi.org/10.1016/j.tifs.2005.12.011

Chen, W., Hou, Y., Tu, Z., Gao, L., Haag, R., 2017. pH-degradable PVA-based nanogels via photo-crosslinking of thermo-preinduced nanoaggregates for controlled drug delivery. J. Control. Release 259, 160–167. https://doi.org/10.1016/j.jconrel.2016.10.032

Chen, W.Q., Lou, D.P., 2014. Synthesis of sodium carboxymethyl cellulose based on pretreated bamboo shaving. Adv. Mater. Res. 997, 169–172. https://doi.org/10.4028/www.scientific.net/AMR.997.169

Cheng, L., Hu, X., Gu, Z., Hong, Y., Li, Z., Li, C., 2019. Characterization of physicochemical properties of cellulose from potato pulp and their effects on enzymatic hydrolysis by cellulase. Int. J. Biol. Macromol. 131, 564–571. https://doi.org/10.1016/j.ijbiomac.2019.02.164

Chieng, B.W., Lee, S.H., Ibrahim, N.A., Then, Y.Y., Loo, Y.Y., 2017. Isolation and

characterization of cellulose nanocrystals from oil palm mesocarp fiber. Polymers (Basel). 9, 1–11. https://doi.org/10.3390/polym9080355

Chumee, J., Seeburin, D., 2014. Cellulose Extraction from Pomelo Peel: Synthesis of Carboxymethyl Cellulose. Int. J. Mater. Metall. Eng. 8, 435–437. https://doi.org/scholar.waset.org/1307-6892/9998337

Ciolacu, D., Popa, V.I., 2006. On the thermal degradation of cellulose allomorphs. Cellul. Chem. Technol. 40, 445–449.

Coelho, C.C.S., Michelin, M., Cerqueira, M.A., Gonçalves, C., Tonon, R. V., Pastrana, L.M., Freitas-Silva, O., Vicente, A.A., Cabral, L.M.C., Teixeira, J.A., 2018. Cellulose nanocrystals from grape pomace: production, properties and cytotoxicity assessment. Carbohydr. Polym. 192, 327–336. https://doi.org/10.1016/j.carbpol.2018.03.023

Collazo-Bigliardi, S., Ortega-Toro, R., Chiralt Boix, A., 2018. Isolation and characterisation of microcrystalline cellulose and cellulose nanocrystals from coffee husk and comparative study with rice husk. Carbohydr. Polym. 191, 205–215. https://doi.org/10.1016/j.carbpol.2018.03.022

Couret, L., Irle, M., Belloncle, C., Cathala, B., 2017. Extraction and characterization of cellulose nanocrystals from post-consumer wood fiberboard waste. Cellulose 24, 2125–2137. https://doi.org/10.1007/s10570-017-1252-7

Dai, H., Ou, S., Huang, Y., Huang, H., 2018. Utilization of pineapple peel for production of nanocellulose and film application. Cellulose 25, 1743–1756. https://doi.org/10.1007/s10570-018-1671-0

Dai, H., Wu, J., Zhang, H., Chen, Y., Ma, L., Huang, H., Huang, Y., Zhang, Y., 2020. Recent advances on cellulose nanocrystals for Pickering emulsions: Development and challenge. Trends Food Sci. Technol. 102, 16–29. https://doi.org/10.1016/j.tifs.2020.05.016

Dai, H., Zhang, Y., Ma, L., Zhang, H., Huang, H., 2019. Synthesis and response of pineapple peel carboxymethyl cellulose-g-poly (acrylic acid-co-acrylamide)/graphene oxide hydrogels. Carbohydr. Polym. 215, 366–376. https://doi.org/10.1016/j.carbpol.2019.03.090

Das, D., Patra, P., Ghosh, P., Rameshbabu, A.P., Dhara, S., Pal, S., 2016. Dextrin and poly(lactide)-based biocompatible and biodegradable nanogel for cancer targeted delivery of doxorubicin hydrochloride. Polym. Chem. 7, 2965–2975. https://doi.org/10.1039/c6py00213g

de Oliveira, J.P., Bruni, G.P., el Halal, S.L.M., Bertoldi, F.C., Dias, A.R.G., Zavareze, E. da R., 2019. Cellulose nanocrystals from rice and oat husks and their application in aerogels for food packaging. Int. J. Biol. Macromol. 124, 175–184. https://doi.org/10.1016/j.ijbiomac.2018.11.205

Debele, T.A., Mekuria, S.L., Tsai, H.C., 2016. Polysaccharide based nanogels in the drug delivery system: Application as the carrier of pharmaceutical agents. Mater. Sci. Eng. C 68, 964–981. https://doi.org/10.1016/j.msec.2016.05.121

Deepa, B., Abraham, E., Cherian, B.M., Bismarck, A., Blaker, J.J., Pothan, L.A., Leao, A.L., de Souza, S.F., Kottaisamy, M., 2011. Structure, morphology and thermal characteristics of banana nano fibers obtained by steam explosion. Bioresour. Technol. 102, 1988–1997. https://doi.org/10.1016/j.biortech.2010.09.030

Delepierre, G., Eyley, S., Thielemans, W., Weder, C., Cranston, E.D., Zoppe, J.O., 2020. Patience is a virtue: Self-assembly and physico-chemical properties of cellulose nanocrystal allomorphs. Nanoscale 12, 17480–17493. https://doi.org/10.1039/d0nr04491a

Demirel, G.B., Von Klitzing, R., 2013. A new multiresponsive drug delivery system using smart nanogels. ChemPhysChem 14, 2833–2840. https://doi.org/10.1002/cphc.201300149

Di Giorgio, L., Salgado, P.R., Dufresne, A., Mauri, A.N., 2020. Nanocelluloses from phormium (Phormium tenax) fibers. Cellulose 27, 4975–4990. https://doi.org/10.1007/s10570-020-03120-x

Dinh Vu, N., Thi Tran, H., Bui, N.D., Duc Vu, C., Viet Nguyen, H., 2017. Lignin and Cellulose Extraction from Vietnam's Rice Straw Using Ultrasound-Assisted Alkaline Treatment Method. Int. J. Polym. Sci. 2017, 1–8. https://doi.org/10.1155/2017/1063695

Diniz, L.F., Carvalho, P.S., Pena, S.A.C., Gonçalves, J.E., Souza, M.A.C., de Souza Filho, J.D., Bomfim Filho, L.F.O., Franco, C.H.J., Diniz, R., Fernandes, C., 2020. Enhancing the solubility and permeability of the diuretic drug furosemide via multicomponent crystal forms. Int. J. Pharm. 587, 119694. https://doi.org/10.1016/j.ijpharm.2020.119694

Ditzel, F.I., Prestes, E., Carvalho, B.M., Demiate, I.M., Pinheiro, L.A., 2017. Nanocrystalline cellulose extracted from pine wood and corncob. Carbohydr. Polym. 157, 1577–1585. https://doi.org/10.1016/j.carbpol.2016.11.036

Du, H., Liu, W., Zhang, M., Si, C., Zhang, X., Li, B., 2019. Cellulose nanocrystals and cellulose nanofibrils based hydrogels for biomedical applications. Carbohydr. Polym. 209, 130–144.

https://doi.org/10.1016/j.carbpol.2019.01.020

Dufresne, A., 2013. Nanocellulose: A new ageless bionanomaterial. Mater. Today 16, 220–227. https://doi.org/10.1016/j.mattod.2013.06.004

Dungani, R., Owolabi, A.F., Saurabh, C.K., Abdul Khalil, H.P.S., Tahir, P.M., Hazwan, C.I.C.M., Ajijolakewu, K.A., Masri, M.M., Rosamah, E., Aditiawati, P., 2017. Preparation and fundamental characterization of cellulose nanocrystal from oil palm fronds biomass. J. Polym. Environ. 25, 692–700. https://doi.org/10.1007/s10924-016-0854-8

Dunlop, M.J., Acharya, B., Bissessur, R., 2018. Isolation of nanocrystalline cellulose from tunicates. J. Environ. Chem. Eng. 6, 4408–4412. https://doi.org/10.1016/j.jece.2018.06.056

Durmaz, E., Ateş, S., 2021. Comparison of properties of cellulose nanomaterials (CNMs) obtained from sunflower stalks. Cellul. Chem. Technol. 55, 755–770.

Eckmann, D.M., Composto, R.J., Tsourkas, A., Muzykantov, V.R., 2014. Nanogel carrier design for targeted drug delivery. J. Mater. Chem. B 2, 8085–8097. https://doi.org/10.1039/c4tb01141d

El Achaby, M., El Miri, N., Hannache, H., Gmouh, S., Ben youcef, H., Aboulkas, A., 2018. Production of cellulose nanocrystals from vine shoots and their use for the development of nanocomposite materials. Int. J. Biol. Macromol. 117, 592–600. https://doi.org/10.1016/j.ijbiomac.2018.05.201

Elkordy, A.A., Forbes, R.T., Barry, B.W., 2004. Stability of crystallised and spray-dried lysozyme. Int. J. Pharm. 278, 209–219. https://doi.org/10.1016/j.ijpharm.2004.02.027

Elmowafy, M., Shalaby, K., Badran, M.M., Ali, H.M., Abdel-Bakky, M.S., Ibrahim, H.M., 2018. Multifunctional carbamazepine loaded nanostructured lipid carrier (NLC) formulation. Int. J. Pharm. 550, 359–371. https://doi.org/10.1016/j.ijpharm.2018.08.062

EP, 2013. Cellulose, Powdered, 8th ed, European Pharmacopoeia – State Of Work Of Pharmeuropa, Harmonisation. Healthcare, European Directorate for the Quality of Medicines and International, (EDQM).

Ernsting, M.J., Tang, W.L., MacCallum, N.W., Li, S.D., 2012. Preclinical pharmacokinetic, biodistribution, and anti-cancer efficacy studies of a docetaxel-carboxymethylcellulose nanoparticle in mouse models. Biomaterials 33, 1445–1454. https://doi.org/10.1016/j.biomaterials.2011.10.061

Esayas, E., C Agon Ass, E., Assefa, S., 2018. Development of wall construction material

stabilized with Enset vegetable fibers for rural housing units. Am. J. Civ. Eng. Archit. 6, 54–62. https://doi.org/10.12691/ajcea-6-2-2

Fan, Q., Jiang, C., Wang, W., Bai, L., Chen, H., Yang, H., Wei, D., Yang, L., 2020. Eco-friendly extraction of cellulose nanocrystals from grape pomace and construction of self-healing nanocomposite hydrogels. Cellulose 27, 2541–2553. https://doi.org/10.1007/s10570-020-02977-2

Fares, H.M., Ghoussoub, Y.E., Delgado, J.D., Fu, J., Urban, V.S., Schlenoff, J.B., 2018. Scattering neutrons along the polyelectrolyte complex/coacervate continuum. Macromolecules 51, 4945–4955. https://doi.org/10.1021/acs.macromol.8b00699

Ferreira, F. V, Mariano, M., Rabelo, S.C., Gouveia, R.F., Lona, L.M.F., 2018. Isolation and surface modification of cellulose nanocrystals from sugarcane bagasse waste: from a micro- to a nano-scale view. Appl. Surf. Sci. 436, 1113–1122. https://doi.org/10.1016/j.apsusc.2017.12.137

Flauzino Neto, W.P., Putaux, J.L., Mariano, M., Ogawa, Y., Otaguro, H., Pasquini, D., Dufresne, A., 2016. Comprehensive morphological and structural investigation of cellulose I and II nanocrystals prepared by sulphuric acid hydrolysis. RSC Adv. 6, 76017–76027. https://doi.org/10.1039/c6ra16295a

Flauzino Neto, W.P., Silvério, H.A., Dantas, N.O., Pasquini, D., 2013. Extraction and characterization of cellulose nanocrystals from agro-industrial residue - Soy hulls. Ind. Crops Prod. 42, 480–488. https://doi.org/10.1016/j.indcrop.2012.06.041

Fortunati, E., Puglia, D., Monti, M., Peponi, L., Santulli, C., Kenny, J.M., Torre, L., 2013. Extraction of cellulose nanocrystals from Phormium tenax fibres. J. Polym. Environ. 21, 319–328. https://doi.org/10.1007/s10924-012-0543-1

French, A.D., 2014. Idealized powder diffraction patterns for cellulose polymorphs. Cellulose 21, 885–896. https://doi.org/10.1007/s10570-013-0030-4

Gabriel, T., Belete, A., Hause, G., Neubert, R.H.H., Gebre-Mariam, T., 2021. Isolation and characterization of cellulose nanocrystals from different lignocellulosic residues : A comparative study. J. Polym. Environ. 29, 2964–2977. https://doi.org/10.1007/s10924-021-02089-3

Gabriel, T., Belete, A., Syrowatka, F., Neubert, R.H.H., Gebre-Mariam, T., 2020. Extraction and characterization of celluloses from various plant byproducts. Int. J. Biol. Macromol. 158,

1248–1258. https://doi.org/10.1016/j.ijbiomac.2020.04.264

Gao, A., Chen, H., Tang, J., Xie, K., Hou, A., 2020. Efficient extraction of cellulose nanocrystals from waste Calotropis gigantea fiber by SO42-/TiO2 nano-solid superacid catalyst combined with ball milling exfoliation. Ind. Crops Prod. 152, 112524. https://doi.org/10.1016/j.indcrop.2020.112524

García-García, D., Balart, R., Lopez-Martinez, J., Ek, M., Moriana, R., 2018. Optimizing the yield and physico-chemical properties of pine cone cellulose nanocrystals by different hydrolysis time. Cellulose 25, 2925–2938. https://doi.org/10.1007/s10570-018-1760-0

Gebre-Mariam, T., Schmidt, P.C., 1996. Isolation and physico-chemical properties of enset starch. Starch/Staerke 48, 208–214. https://doi.org/10.1002/star.19960480603

Gheorghita, R., Anchidin-Norocel, L., Filip, R., Dimian, M., Covasa, M., 2021. Applications of biopolymers for drugs and probiotics delivery. Polymers (Basel). 13. https://doi.org/10.3390/polym13162729

Golbaghi, L., Khamforoush, M., Hatami, T., 2017. Carboxymethyl cellulose production from sugarcane bagasse with steam explosion pulping: Experimental, modeling, and optimization. Carbohydr. Polym. 174, 780–788. https://doi.org/10.1016/j.carbpol.2017.06.123

Gong, J., Li, J., Xu, J., Xiang, Z., Mo, L., 2017. Research on cellulose nanocrystals produced from cellulose sources with various polymorphs. RSC Adv. 7, 33486–33493. https://doi.org/10.1039/c7ra06222b

Gong, J., Mo, L., Li, J., 2018. A comparative study on the preparation and characterization of cellulose nanocrystals with various polymorphs. Carbohydr. Polym. 195, 18–28. https://doi.org/10.1016/j.carbpol.2018.04.039

Haafiz, M.K.M., Hassan, A., Zakaria, Z., Inuwa, I.M., 2014. Isolation and characterization of cellulose nanowhiskers from oil palm biomass microcrystalline cellulose. Carbohydr. Polym. 103, 119–125. https://doi.org/10.1016/j.carbpol.2013.11.055

Habibi, Y., Lucia, L.A., Rojas, O.J., 2010. Cellulose Nanocrystals: Chemistry, Self-Assembly, and Applications. Chem. Rev. 110, 3479–3500.

Hafemann, E., Battisti, R., Marangoni, C., Machado, R.A.F., 2019. Valorization of royal palm tree agroindustrial waste by isolating cellulose nanocrystals. Carbohydr. Polym. 218, 188–198. https://doi.org/10.1016/j.carbpol.2019.04.086

Haleem, N., Arshad, M., Shahid, M., Tahir, M.A., 2014. Synthesis of carboxymethyl cellulose from waste of cotton ginning industry. Carbohydr. Polym. 113, 249–255. https://doi.org/10.1016/j.carbpol.2014.07.023

Hamidi, M., Azadi, A., Rafiei, P., 2008. Hydrogel nanoparticles in drug delivery. Adv. Drug Deliv. Rev. https://doi.org/10.1016/j.addr.2008.08.002

Hassanpour, S., Bagheri, M., 2017. Dual-responsive semi-IPN copolymer nanogels based on poly (itaconic acid) and hydroxypropyl cellulose as a carrier for controlled drug release. J. Polym. Res. 24, 91–100. https://doi.org/10.1007/s10965-017-1246-z

Hastuti, N., Kanomata, K., Kitaoka, T., 2018. Hydrochloric acid hydrolysis of pulps from oil palm empty fruit bunches to produce cellulose nanocrystals. J. Polym. Environ. 26, 3698–3709. https://doi.org/10.1007/s10924-018-1248-x

Hayati, M., Rezanejade Bardajee, G., Ramezani, M., Mizani, F., 2020. Temperature/pH/magnetic triple sensitive nanogel for doxorubicin anticancer drug delivery. Inorg. Nano-Metal Chem. 50, 1189–1200. https://doi.org/10.1080/24701556.2020.1737821

He, L., Liang, H., Lin, L., Shah, B.R., Li, Y., Chen, Y., Li, B., 2015. Green-step assembly of low density lipoprotein/sodium carboxymethyl cellulose nanogels for facile loading and pH-dependent release of doxorubicin. Colloids Surfaces B Biointerfaces 126, 288–296. https://doi.org/10.1016/j.colsurfb.2014.12.024

He, Q., Wang, Q., Zhou, H., Ren, D., He, Y., Cong, H., Wu, L., 2018. Highly crystalline cellulose from brown seaweed Saccharina japonica: isolation, characterization and microcrystallization. Cellulose 25, 5523–5533. https://doi.org/10.1007/s10570-018-1966-1

He, X., Wu, S., Fu, D., Ni, J., 2009. Preparation of sodium carboxymethyl cellulose from paper sludge. J. Chem. Technol. Biotechnol. 84, 427–434. https://doi.org/10.1002/jctb.2057

Heggset, E.B., Chinga-Carrasco, G., Syverud, K., 2017. Temperature stability of nanocellulose dispersions. Carbohydr. Polym. 157, 114–121. https://doi.org/10.1016/j.carbpol.2016.09.077

Heinze, T., Pfeiffer, K., 1999. Studies on the synthesis and characterization of carboxymethylcellulose. Die Angew. Makromol. Chemie 266, 37–45.

Hemmati, F., Jafari, S.M., Kashaninejad, M., Barani Motlagh, M., 2018. Synthesis and characterization of cellulose nanocrystals derived from walnut shell agricultural residues. Int. J. Biol. Macromol. 120, 1216–1224. https://doi.org/10.1016/j.ijbiomac.2018.09.012

Hemmati, F., Jafari, S.M., Taheri, R.A., 2019. Optimization of homogenization-sonication technique for the production of cellulose nanocrystals from cotton linter. Int. J. Biol. Macromol. 137, 374–381. https://doi.org/10.1016/j.ijbiomac.2019.06.241

Hermans, H., Hermans, J.J., Vermaas, D., Weidinger, A., 1948. Deformation mechanism of cellulose gels. IV.* General relationship between orientation of the crystalline and that of the amorphous portion. J. Polym. Sci. 3, 1–9.

Hooton, J., 2009. Carboxymethylcellulose Sodium, in: Rowe, R.C., Sheskey, P.J., Quinn, M.E. (Eds.), Handbook of Pharmaceutical Excipients. the Pharmaceutical Press and and the American Pharmacists Association, London and Chicago, pp. 118–121.

Huang, C.M.Y., Chia, P.X., Lim, C.S.S., Nai, J.Q., Ding, D.Y., Seow, P.B., Wong, C.W., Chan, E.W.C., 2017. Synthesis and characterisation of carboxymethyl cellulose from various agricultural wastes. Cellul. Chem. Technol. 51, 665–672.

ICH, 2003. Stability Testing of new Drug Substances and Products. Int. Conf. Harmon. (ICH), Eur. Med. Agency. https//www.ema.europa.eu/en/documents/scientific-guideline/ich-q-1-r2-stability-testing-new-drug-substances-products-step-5_en.pdf. Accessed 11-09-2020.

Jahan, M.S., Saeed, A., He, Z., Ni, Y., 2011. Jute as raw material for the preparation of microcrystalline cellulose. Cellulose 18, 451–459. https://doi.org/10.1007/s10570-010-9481-z

Jamard, M., Hoare, T., Sheardown, H., 2016. Nanogels of methylcellulose hydrophobized with N-tert-butylacrylamide for ocular drug delivery. Drug Deliv. Transl. Res. 6, 648–659. https://doi.org/10.1007/s13346-016-0337-4

Jin, E., Guo, J., Yang, F., Zhu, Y., Song, J., Jin, Y., Rojas, O.J., 2016. On the polymorphic and morphological changes of cellulose nanocrystals (CNC-I) upon mercerization and conversion to CNC-II. Carbohydr. Polym. 143, 327–335. https://doi.org/10.1016/j.carbpol.2016.01.048

Jmel, M.A., Anders, N., Ben Messaoud, G., Marzouki, M.N., Spiess, A., Smaali, I., 2019. The stranded macroalga Ulva lactuca as a new alternative source of cellulose: Extraction, physicochemical and rheological characterization. J. Clean. Prod. 234, 1421–1427. https://doi.org/10.1016/j.jclepro.2019.06.225

Jordan, J.H., Easson, M.W., Dien, B., Thompson, S., Condon, B.D., 2019. Extraction and characterization of nanocellulose crystals from cotton gin motes and cotton gin waste.

Cellulose 26, 5959–5979. https://doi.org/10.1007/s10570-019-02533-7

Joshi, G., Naithani, S., Varshney, V.K., Bisht, S.S., Rana, V., Gupta, P.K., 2015. Synthesis and characterization of carboxymethyl cellulose from office waste paper: A greener approach towards waste management. Waste Manag. 38, 33–40. https://doi.org/10.1016/j.wasman.2014.11.015

Kabanov, A. V, Vinogradov, S. V, 2009. Nanogels as pharmaceutical carriers: Finite networks of infinite capabilities. Angew. Chemie - Int. Ed. https://doi.org/10.1002/anie.200900441

Kamel, S., Ali, N., Jahangir, K., Shah, S.M., El-Gendy, a. a., 2008. Pharmaceutical significance of cellulose: A review. Express Polym. Lett. 2, 758–778. https://doi.org/10.3144/expresspolymlett.2008.90

Kamelnia, E., Divsalar, A., Darroudi, M., Yaghmaei, P., Sadri, K., 2019. Production of new cellulose nanocrystals from Ferula gummosa and their use in medical applications via investigation of their biodistribution. Ind. Crops Prod. 139, 111538. https://doi.org/10.1016/j.indcrop.2019.111538

Karataş, M., Arslan, N., 2016. Flow behaviours of cellulose and carboxymethyl cellulose from grapefruit peel. Food Hydrocoll. 58, 235–245. https://doi.org/10.1016/j.foodhyd.2016.02.035

Kargarzadeh, H., Ahmad, I., Abdullah, I., Dufresne, A., Zainudin, S.Y., Sheltami, R.M., 2012. Effects of hydrolysis conditions on the morphology, crystallinity, and thermal stability of cellulose nanocrystals extracted from kenaf bast fibers. Cellulose 19, 855–866. https://doi.org/10.1007/s10570-012-9684-6

Kassab, Z., Kassem, I., Hannache, H., Bouhfid, R., Qaiss, A.E.K., El Achaby, M., 2020. Tomato plant residue as new renewable source for cellulose production: extraction of cellulose nanocrystals with different surface functionalities. Cellulose 27, 4287–4303. https://doi.org/10.1007/s10570-020-03097-7

Kaushik, A., Singh, M., 2011. Isolation and characterization of cellulose nanofibrils from wheat straw using steam explosion coupled with high shear homogenization. Carbohydr. Res. 346, 76–85. https://doi.org/10.1016/j.carres.2010.10.020

Keshavarz, M., Kaffashi, B., 2014. The ability of retention, drug release and rheological properties of nanogel bioadhesives based on cellulose derivatives. Pharm. Dev. Technol. 19, 952–959. https://doi.org/10.3109/10837450.2013.846371

Khan, A.U., Malik, N., Arfin, T., 2017. Nanofibrillated Cellulose and Copoly(amino acid) Hydrogel Matrices in Biotechnology and Biomedicine, in: Jawaid, M., Mohammad, F. (Eds.), Nanocellulose and Nanohydrogel Matrices: Biotechnological and Biomedical Applications. Wiley-VCH Verlag GmbH & Co. KGaA, Chennai, pp. 331–353.

Khan, N., Shah, F.A., Rana, I., Ansari, M.M., Din, F. ud, Rizvi, S.Z.H., Aman, W., Lee, G.Y., Lee, E.S., Kim, J.K., Zeb, A., 2020. Nanostructured lipid carriers-mediated brain delivery of carbamazepine for improved in vivo anticonvulsant and anxiolytic activity. Int. J. Pharm. 577, 119033. https://doi.org/10.1016/j.ijpharm.2020.119033

Khoee, S., Asadi, H., 2015. Nanogels: Chemical Approaches to Preparation. Handb. Encapsulation Control. Release 1271–1309. https://doi.org/doi:10.1201/b19038-60

Khullar, R., Varshney, V.K., Heinze, T., Vieira-Nagel, M., Gupta, P.K., Naithani, S., Soni, P.L., 2007. Carboxymethylation of cellulose isolated from bamboo (Dendrocalamus strictus) and its rheology. Cellul. Chem. Technol. 40, 545–552.

Khullar, R., Varshney, V.K., Naithani, S., Heinze, T., Soni, P.L., 2005. Carboxymethylation of cellulosic material (average degree of polymerization 2600) isolated from cotton (gossypium) linters with respect to degree of substitution and rheological behavior. J. Appl. Polym. Sci. 96, 1477–1482. https://doi.org/10.1002/app.21645

Kim, U.J., Eom, S.H., Wada, M., 2010. Thermal decomposition of native cellulose: Influence on crystallite size. Polym. Degrad. Stab. 95, 778–781. https://doi.org/10.1016/j.polymdegradstab.2010.02.009

Klemm, D., Cranston, E.D., Fischer, D., Gama, M., Kedzior, S.A., Kralisch, D., Kramer, F., Kondo, T., Lindström, T., Nietzsche, S., Petzold-Welcke, K., Rauchfuß, F., 2018. Nanocellulose as a natural source for groundbreaking applications in materials science: Today's state. Mater. Today 21, 720–748. https://doi.org/10.1016/j.mattod.2018.02.001

Klemm, D., Heublein, B., Fink, H.P., Bohn, A., 2005. Cellulose: Fascinating biopolymer and sustainable raw material. Angew. Chemie - Int. Ed. https://doi.org/10.1002/anie.200460587

Klemm, D., Philipp, B., Heinze, T., Heinze, U., Wagenknecht, W., 1998. Analytical Methods in Cellulose Chemistry: Section 3.8, in: Comprehensive Cellulose Chemistry. WILEY-VCH Verlag GmbH, Weinheim, Weinheim · NewYork · Chichester · Brisbane · Singapore ·Toronto, pp. 217–222. https://doi.org/10.1002/3527601929.ch3h

Kljun, A., Benians, T.A.S., Goubet, F., Meulewaeter, F., Knox, J.P., Blackburn, R.S., 2011.

Comparative analysis of crystallinity changes in cellulose I polymers using ATR-FTIR, X-ray diffraction, and carbohydrate-binding module probes. Biomacromolecules 12, 4121–4126. https://doi.org/10.1021/bm201176m

Klunklin, W., Jantanasakulwong, K., Phimolsiripol, Y., Leksawasdi, N., Seesuriyachan, P., Chaiyaso, T., Insomphun, C., Phongthai, S., Jantrawut, P., Sommano, S.R., Punyodom, W., Reungsang, A., Ngo, T.M.P., Rachtanapun, P., 2021. Synthesis, characterization, and application of carboxymethyl cellulose from asparagus stalk end. Polymers (Basel). 13, 1–15. https://doi.org/10.3390/polym13010081

Korolovych, V.F., Cherpak, V., Nepal, D., Ng, A., Shaikh, N.R., Grant, A., Xiong, R., Bunning, T.J., Tsukruk, V. V, 2018. Cellulose nanocrystals with different morphologies and chiral properties. Polymer (Guildf). 145, 334–347. https://doi.org/10.1016/j.polymer.2018.04.064

Kupnik, K., Primožič, M., Kokol, V., Leitgeb, M., 2020. Nanocellulose in drug delivery and antimicrobially active materials. Polymers (Basel). 12, 1–40. https://doi.org/10.3390/polym12122825

Laffleur, F., Keckeis, V., 2020. Advances in drug delivery systems: Work in progress still needed? Int. J. Pharm. X 2. https://doi.org/10.1016/j.ijpx.2020.100050

Lakshmi, D.S., Trivedi, N., Reddy, C.R.K., 2017. Synthesis and characterization of seaweed cellulose derived carboxymethyl cellulose. Carbohydr. Polym. 157, 1604–1610. https://doi.org/10.1016/j.carbpol.2016.11.042

Lam, N.T., Chollakup, R., Smitthipong, W., Nimchua, T., Sukyai, P., 2017. Characterization of cellulose nanocrystals extracted from sugarcane bagasse for potential biomedical materials. Sugar Tech 19, 539–552. https://doi.org/10.1007/s12355-016-0507-1

Lee, H., 2018. Teff, A Rising Global Crop: Current Status of Teff Production and Value Chain. Open Agric. J. 12, 185–193. https://doi.org/10.2174/1874331501812010185

Lembo, D., Swaminathan, S., Donalisio, M., Civra, A., Pastero, L., Aquilano, D., Vavia, P., Trotta, F., Cavalli, R., 2013. Encapsulation of Acyclovir in new carboxylated cyclodextrin-based nanosponges improves the agent's antiviral efficacy. Int. J. Pharm. 443, 262–272. https://doi.org/10.1016/j.ijpharm.2012.12.031

Li, C., Obireddy, S.R., Lai, W.F., 2021. Preparation and use of nanogels as carriers of drugs. Drug Deliv. 28, 1594–1602. https://doi.org/10.1080/10717544.2021.1955042

Li, C., Wang, J., Wang, Yiguang, Gao, H., Wei, G., Huang, Y., Yu, H., Gan, Y., Wang,

Yongjun, Mei, L., Chen, H., Hu, H., Zhang, Z., Jin, Y., 2019. Recent progress in drug delivery. Acta Pharm. Sin. B 9, 1145–1162. https://doi.org/10.1016/j.apsb.2019.08.003

Li, J., Yu, S., Yao, P., Jiang, M., 2008. Lysozyme - Dextran Core - Shell nanogels prepared via a green process. Langmuir 24, 3486–3492. https://doi.org/10.1021/la702785b

Li, Z., Xu, W., Zhang, C., Chen, Y., Li, B., 2015. Self-assembled lysozyme/carboxymethylcellulose nanogels for delivery of methotrexate. Int. J. Biol. Macromol. 75, 166–172. https://doi.org/10.1016/j.ijbiomac.2015.01.033

Liao, Q., Shao, Q., Qiu, G., Lu, X., 2012a. Methacrylic acid-triggered phase transition behavior of thermosensitive hydroxypropylcellulose. Carbohydr. Polym. 89, 1301–1304. https://doi.org/10.1016/j.carbpol.2012.04.002

Liao, Q., Shao, Q., Wang, H., Qiu, G., Lu, X., 2012b. Hydroxypropylcellulose templated synthesis of surfactant-free poly(acrylic acid) nanogels in aqueous media. Carbohydr. Polym. 87, 2648–2654. https://doi.org/10.1016/j.carbpol.2011.11.056

Lin, L., Yan, R., Liu, Y., Jiang, W., 2010. In-depth investigation of enzymatic hydrolysis of biomass wastes based on three major components: Cellulose, hemicellulose and lignin. Bioresour. Technol. 101, 8217–8223. https://doi.org/10.1016/j.biortech.2010.05.084

Liu, K., Zheng, D., Zhao, J., Tao, Y., Wang, Y., He, J., Lei, J., Xi, X., 2018. pH-sensitive nanogels based on the electrostatic self-assembly of radionuclide 131-I labeled albumin and carboxymethyl cellulose for synergistic combined chemo-radioisotope therapy of cancer. J. Mater. Chem. B 3, 10715–10722. https://doi.org/10.1039/C8TB01295D

Liu, Y., Wang, H., Yu, G., Yu, Q., Li, B., Mu, X., 2014. A novel approach for the preparation of nanocrystalline cellulose by using phosphotungstic acid. Carbohydr. Polym. 110, 415–422. https://doi.org/10.1016/j.carbpol.2014.04.040

Madgulkar, A., Bhalekar, M.R., Dikpati, A.A., 2016. Improving oral bioavailability of acyclovir using nanoparticulates of thiolated xyloglucan. Int. J. Biol. Macromol. 89, 689–699. https://doi.org/10.1016/j.ijbiomac.2016.02.007

Malucelli, L.C., Lacerda, L.G., Dziedzic, M., da Silva Carvalho Filho, M.A., 2017. Preparation, properties and future perspectives of nanocrystals from agro-industrial residues: a review of recent research. Rev. Environ. Sci. Biotechnol. 16, 131–145. https://doi.org/10.1007/s11157-017-9423-4

Mandal, A., Chakrabarty, D., 2011. Isolation of nanocellulose from waste sugarcane bagasse

(SCB) and its characterization. Carbohydr. Polym. 86, 1291–1299. https://doi.org/10.1016/j.carbpol.2011.06.030

Mansikkamäki, P., Lahtinen, M., Rissanen, K., 2007. The conversion from cellulose I to cellulose II in NaOH mercerization performed in alcohol-water systems: An X-ray powder diffraction study. Carbohydr. Polym. 68, 35–43. https://doi.org/10.1016/j.carbpol.2006.07.010

Mansur, A.A.P., de Carvalho, F.G., Mansur, R.L., Carvalho, S.M., de Oliveira, L.C., Mansur, H.S., 2017. Carboxymethylcellulose/ZnCdS fluorescent quantum dot nanoconjugates for cancer cell bioimaging. Int. J. Biol. Macromol. 96, 675–686. https://doi.org/10.1016/j.ijbiomac.2016.12.078

Mariano, M., Cercená, R., Soldi, V., 2016. Thermal characterization of cellulose nanocrystals isolated from sisal fibers using acid hydrolysis. Ind. Crops Prod. 94, 454–462. https://doi.org/10.1016/j.indcrop.2016.09.011

Mariano, M., El Kissi, N., Dufresne, A., 2014. Cellulose nanocrystals and related nanocomposites: Review of some properties and challenges. J. Polym. Sci. Part B Polym. Phys. 52, 791–806. https://doi.org/10.1002/polb.23490

Melikoğlu, A.Y., Bilek, S.E., Cesur, S., 2019. Optimum alkaline treatment parameters for the extraction of cellulose and production of cellulose nanocrystals from apple pomace. Carbohydr. Polym. 215, 330–337. https://doi.org/10.1016/j.carbpol.2019.03.103

Meng, F., Wang, G., Du, X., Wang, Z., Xu, S., Zhang, Y., 2019a. Extraction and characterization of cellulose nanofibers and nanocrystals from liquefied banana pseudo-stem residue. Compos. Part B Eng. 160, 341–347. https://doi.org/10.1016/j.compositesb.2018.08.048

Meng, F., Zhang, X., Yu, W., Zhang, Y., 2019b. Kinetic analysis of cellulose extraction from banana pseudo-stem by liquefaction in polyhydric alcohols. Ind. Crops Prod. 137, 377–385. https://doi.org/10.1016/j.indcrop.2019.05.025

Meng, L.-Y., Wang, B., Ma, M.-G., Zhu, J.-F., 2017. Cellulose-based Nanocarriers as Platforms for Cancer Therapy. Curr Pharm Des 23, 5292–5300. https://doi.org/10.2174/1381612823666171031111950

Minten, B., Tamru, S., Engida, E., Kuma, T., 2016. Feeding Africa's cities: The case of the supply chain of Teff to Addis Ababa. Econ. Dev. Cult. Change 64, 265–297. https://doi.org/10.1086/683843

Mischnick, P., Momcilovic, D., 2010. Chemical Structure Analysis of Starch and Cellulose Derivatives, Advances in Carbohydrate Chemistry and Biochemistry. Elsevier Inc. https://doi.org/10.1016/S0065-2318(10)64004-8

Mohamad Haafiz, M.K., Eichhorn, S.J., Hassan, A., Jawaid, M., 2013. Isolation and characterization of microcrystalline cellulose from oil palm biomass residue. Carbohydr. Polym. 93, 628–634. https://doi.org/10.1016/j.carbpol.2013.01.035

Morán, J.I., Alvarez, V.A., Cyras, V.P., Vázquez, A., 2008. Extraction of cellulose and preparation of nanocellulose from sisal fibers. Cellulose 15, 149–159. https://doi.org/10.1007/s10570-007-9145-9

Moussa, I., Khiari, R., Moussa, A., Belgacem, M.N., Mhenni, M.F., 2019. Preparation and Characterization of Carboxymethyl Cellulose with a High Degree of Substitution from Agricultural Wastes. Fibers Polym. 20, 933–943. https://doi.org/10.1007/s12221-019-8665-x

Mueller, S., Weder, C., Foster, E.J., 2014. Isolation of cellulose nanocrystals from pseudostems of banana plants. RSC Adv. 4, 907–915. https://doi.org/10.1039/c3ra46390g

Naceur Abouloula, C., Rizwan, M., Selvanathan, V., Abdullah, C.I., Hassan, A., Yahya, R., Oueriagli, A., 2018. A novel application for oil palm empty fruit bunch: extraction and modification of cellulose for solid polymer electrolyte. Ionics (Kiel). 24, 3827–3836. https://doi.org/10.1007/s11581-018-2558-7

Naduparambath, S., Purushothaman, E., 2016. Sago seed shell: determination of the composition and isolation of microcrystalline cellulose (MCC). Cellulose 23, 1803–1812. https://doi.org/10.1007/s10570-016-0904-3

Nair, A.B., Attimarad, M., Al-Dhubiab, B.E., Wadhwa, J., Harsha, S., Ahmed, M., 2014. Enhanced oral bioavailability of acyclovir by inclusion complex using hydroxypropyl-β-cyclodextrin. Drug Deliv. 21, 540–547. https://doi.org/10.3109/10717544.2013.853213

Nang An, V., Chi Nhan, H.T., Tap, T.D., Van, T.T.T., Van Viet, P., Van Hieu, L., 2020. Extraction of high crystalline nanocellulose from biorenewable sources of Vietnamese agricultural wastes. J. Polym. Environ. 28, 1465–1474. https://doi.org/10.1007/s10924-020-01695-x

Nascimento, D.M. do, Dias, A.F., Araújo Junior, C.P. de, Rosa, M. de F., Morais, J.P.S., Figueirêdo, M.C.B. de, 2016. A comprehensive approach for obtaining cellulose

nanocrystal from coconut fiber. Part II: Environmental assessment of technological pathways. Ind. Crops Prod. 93, 58–65. https://doi.org/10.1016/j.indcrop.2016.02.063

Nataraj, D., Hu, C., Reddy, N., 2022. Extraction and Characterization of Nanocellulose From Pongamia Pinnata Oil Meal. Cellul. Chem. Technol. 56, 29–37. https://doi.org/10.35812/cellulosechemtechnol.2022.56.02

Nazir, M.S., Wahjoedi, B.A., Yussof, A.W., Abdullah, M.A., 2013. Eco-friendly extraction and characterization of cellulose from oil palm empty fruit bunches. BioResources 8, 2161–2172. https://doi.org/10.15376/biores.8.2.2161-2172

Neamtu, I., Rusu, A.G., Diaconu, A., Nita, L.E., Chiriac, A.P., 2017. Basic concepts and recent advances in nanogels as carriers for medical applications. Drug Deliv. 24, 539–557. https://doi.org/10.1080/10717544.2016.1276232

Nepomuceno, N.C., Santos, A.S.F., Oliveira, J.E., Glenn, G.M., Medeiros, E.S., 2017. Extraction and characterization of cellulose nanowhiskers from Mandacaru (Cereus jamacaru DC.) spines. Cellulose 24, 119–129. https://doi.org/10.1007/s10570-016-1109-5

Newman, R.H., 1999. Estimation of the lateral dimensions of cellulose crystallites using 13C NMR signal strengths. Solid State Nucl. Magn. Reson. 15, 21–29. https://doi.org/10.1016/S0926-2040(99)00043-0

Nielsen, L.H., Melero, A., Keller, S.S., Jacobsen, J., Garrigues, T., Rades, T., Müllertz, A., Boisen, A., 2016. Polymeric microcontainers improve oral bioavailability of furosemide. Int. J. Pharm. 504, 98–109. https://doi.org/10.1016/j.ijpharm.2016.03.050

Nuruddin, M., Chowdhury, A., Haque, S.A., Rahman, M., Farhad, S.F., Jahan, M.S., Quaiyyum, A., 2011. Extraction and characterization of cellulose microfibrils from agricultural wastes in an integrated biorefinery initiative. Cellul. Chem. Technol. 45, 347–354.

Nuruddin, M., Hosur, M., Uddin, M.J., Baah, D., Jeelani, S., 2016. A novel approach for extracting cellulose nanofibers from lignocellulosic biomass by ball milling combined with chemical treatment. J. Appl. Polym. Sci. 133, 1–10. https://doi.org/10.1002/app.42990

Oh, S.Y., Dong, I.Y., Shin, Y., Hwan, C.K., Hak, Y.K., Yong, S.C., Won, H.P., Ji, H.Y., 2005a. Crystalline structure analysis of cellulose treated with sodium hydroxide and carbon dioxide by means of X-ray diffraction and FTIR spectroscopy. Carbohydr. Res. 340, 2376–2391. https://doi.org/10.1016/j.carres.2005.08.007

Oh, S.Y., Yoo, D. Il, Shin, Y., Seo, G., 2005b. FTIR analysis of cellulose treated with sodium

hydroxide and carbon dioxide. Carbohydr. Res. 340, 417–428. https://doi.org/10.1016/j.carres.2004.11.027

Oliveira, F.B. De, Bras, J., Pimenta, M.T.B., Curvelo, A.A. da S., Belgacem, M.N., 2016. Production of cellulose nanocrystals from sugarcane bagasse fibers and pith. Ind. Crops Prod. 93, 48–57. https://doi.org/10.1016/j.indcrop.2016.04.064

Onofrei, M., Filimon, A., 2016. Cellulose-based hydrogels : Designing concepts, properties, and perspectives for biomedical and environmental applications, in: Polymer Science: Research Advances, Practical Applications and Educational Aspects. pp. 108–120.

Orasugh, J.T., Sarkar, G., Saha, N.R., Das, B., Bhattacharyya, A., Das, S., Mishra, R., Roy, I., Chattoapadhyay, A., Ghosh, S.K., Chattopadhyay, D., 2019. Effect of cellulose nanocrystals on the performance of drug loaded in situ gelling thermo-responsive ophthalmic formulations. Int. J. Biol. Macromol. 124, 235–245. https://doi.org/10.1016/j.ijbiomac.2018.11.217

Otoni, C.G., Queirós, M.V.A., Sabadini, J.B., Rojas, O.J., Loh, W., 2020. Charge matters: Electrostatic complexation as a green approach to assemble advanced functional materials. ACS Omega 5, 1296–1304. https://doi.org/10.1021/acsomega.9b03690

Park, N.M., Choi, S., Oh, J.E., Hwang, D.Y., 2019. Facile extraction of cellulose nanocrystals. Carbohydr. Polym. 223, 115114. https://doi.org/10.1016/j.carbpol.2019.115114

Park, S., Baker, J.O., Himmel, M.E., Parilla, P.A., Johnson, D.K., 2010. Cellulose crystallinity index: Measurement techniques and their impact on interpreting cellulase performance. Biotechnol. Biofuels 3, 1–10. https://doi.org/10.1186/1754-6834-3-10

Patel, P.J., Gohel, M.C., Acharya, S.R., 2014. Exploration of statistical experimental design to improve entrapment efficiency of acyclovir in poly (d, l) lactide nanoparticles. Pharm. Dev. Technol. 19, 200–212. https://doi.org/10.3109/10837450.2013.769566

Paulos, G., Gebre-Mariam, T., Reinhard, N.H., 2019. Fabrication and evaluation of cassava starch acetate nanoparticles loaded with drugs of various BCS classes: Influence of drug solubility and partition coefficient. J Nanomater Mol Nanotechnol 8. https://doi.org/10.4172/2324-8777.1000259

Pei, Y., Li, Z., McClements, D.J., Li, B., 2019. Comparison of structural and physicochemical properties of lysozyme/carboxymethylcellulose complexes and microgels. Food Res. Int. 122, 273–282. https://doi.org/10.1016/j.foodres.2019.03.071

Pereira, P.H.F., Ornaghi Júnior, H.L., Coutinho, L.V., Duchemin, B., Cioffi, M.O.H., 2020. Obtaining cellulose nanocrystals from pineapple crown fibers by free-chlorite hydrolysis with sulfuric acid: physical, chemical and structural characterization. Cellulose 27, 5745–5756. https://doi.org/10.1007/s10570-020-03179-6

PhEur, 2013. Cellulose powder, in: European Pharmacopoeia. European Directorate for the Quality of Medicines & HealthCare (EDQM) and Council of Europe, Strasbourg, France. https://doi.org/http://pharmeuropa.edqm.eu

Poletto, M., Ornaghi Júnior, H.L., Zattera, A.J., 2014. Native cellulose: Structure, characterization and thermal properties. Materials (Basel). 7, 6105–6119. https://doi.org/10.3390/ma7096105

Poletto, M., Pistor, V., J., A., 2013. Structural Characteristics and Thermal Properties of Native Cellulose, in: Van De Ven, T.G.M. (Ed.), Cellulose - Fundamental Aspects. IntechOpen, pp. 45–69. https://doi.org/10.5772/50452

Poletto, M., Zattera, A.J., Forte, M.M.C., Santana, R.M.C., 2012. Thermal decomposition of wood: Influence of wood components and cellulose crystallite size. Bioresour. Technol. 109, 148–153. https://doi.org/10.1016/j.biortech.2011.11.122

Popescu, M., Popescu, C., Lisa, G., Sakata, Y., 2011. Evaluation of morphological and chemical aspects of different wood species by spectroscopy and thermal methods. J. Mol. Struct. 988, 65–72. https://doi.org/10.1016/j.molstruc.2010.12.004

Prado, K.S., Spinacé, M.A.S., 2019. Isolation and characterization of cellulose nanocrystals from pineapple crown waste and their potential uses. Int. J. Biol. Macromol. 122, 410–416. https://doi.org/10.1016/j.ijbiomac.2018.10.187

Pushpamalar, V., Langford, S.J., Ahmad, M., Lim, Y.Y., 2006. Optimization of reaction conditions for preparing carboxymethyl cellulose from sago waste. Carbohydr. Polym. 64, 312–318. https://doi.org/10.1016/j.carbpol.2005.12.003

Qi, J., Yao, P., He, F., Yu, C., Huang, C., 2010. Nanoparticles with dextran/chitosan shell and BSA/chitosan core-Doxorubicin loading and delivery. Int. J. Pharm. 393, 177–185. https://doi.org/10.1016/j.ijpharm.2010.03.063

Qian, H., Wang, X., Yuan, K., Xie, C., Wu, W., Jiang, X., Hu, L., 2014. Delivery of doxorubicin in vitro and in vivo using bio-reductive cellulose nanogels. Biomater. Sci. 2, 220–232. https://doi.org/10.1039/c3bm60176e

Quinn, H.L., 2016. Design and processing of nanogels as delivery systems for peptides and proteins. Ther. Deliv 7, 117–138. https://doi.org/10.4155/tde.15.92

Rachtanapun, P., Luangkamin, S., Tanprasert, K., Suriyatem, R., 2012. Carboxymethyl cellulose film from durian rind. LWT - Food Sci. Technol. 48, 52–58. https://doi.org/10.1016/j.lwt.2012.02.029

Radwan, S.E.S., Sokar, M.S., Abdelmonsif, D.A., El-Kamel, A.H., 2017. Mucopenetrating nanoparticles for enhancement of oral bioavailability of furosemide: In vitro and in vivo evaluation/sub-acute toxicity study. Int. J. Pharm. 526, 366–379. https://doi.org/10.1016/j.ijpharm.2017.04.072

Raemdonck, K., Demeester, J., De Smedt, S., 2009. Advanced nanogel engineering for drug delivery. Soft Matter 5, 707–715. https://doi.org/10.1039/b811923f

Raghav, N., Sharma, M.R., Kennedy, J.F., 2021. Nanocellulose: A mini-review on types and use in drug delivery systems. Carbohydr. Polym. Technol. Appl. 2, 100031. https://doi.org/10.1016/j.carpta.2020.100031

Ragheb, A.A., Nassar, S.H., Abd El-Thalouth, I., Ibrahim, M.A., Shahin, A.A., 2012. Preparation, characterization and technological evaluation of CMC derived from rice-straw as thickening agents in discharge, discharge-resist and burn-out printing. Carbohydr. Polym. 89, 1044–1049. https://doi.org/10.1016/j.carbpol.2012.03.054

Rahimian, K., Wen, Y., Oh, J.K., 2015. Redox-responsive cellulose-based thermoresponsive grafted copolymers and in-situ disulfide crosslinked nanogels. Polym. (United Kingdom) 72, 387–394. https://doi.org/10.1016/j.polymer.2015.01.024

Rajput, R.L., Narkhede, J.S., Mujumdar, A., Naik, J.B., 2020. Synthesis and evaluation of luliconazole loaded biodegradable nanogels prepared by pH-responsive Poly (acrylic acid) grafted Sodium Carboxymethyl Cellulose using amine based cross linker for topical targeting: In vitro and Ex vivo assessment. Polym. Technol. Mater. 59, 1654–1666. https://doi.org/10.1080/25740881.2020.1759633

Rånby, B.G., 1952. The Mercerization of cellulose I. A Phase Transition Study with X-Ray Diffraction. Acta Chem. Scand. 6, 116–127.

Rashid, S., Dutta, H., 2022. Physicochemical characterization of carboxymethyl cellulose from differently sized rice husks and application as cake additive. Lwt-Food Sci. Technol. 154, 112630. https://doi.org/10.1016/j.lwt.2021.112630

Rasid, N.S.A., Zainol, M.M., Amin, N.A.S., 2021. Synthesis and characterization of carboxymethyl cellulose derived from empty fruit bunch, in: Sains Malaysiana. pp. 2523–2535. https://doi.org/10.17576/jsm-2021-5009-03

Reddy, N., Yang, Y., 2006. Properties of high-quality long natural cellulose fibers from rice straw. J. Agric. Food Chem. 54, 8077–8081. https://doi.org/10.1021/jf0617723

Reddy, N., Yang, Y., 2005. Structure and properties of high quality natural cellulose fibers from cornstalks. Polymer (Guildf). 46, 5494–5500. https://doi.org/10.1016/j.polymer.2005.04.073

Reunanen, M., Heinonen, E.H., Nyman, L., Anttila, M., 1992. Comparative bioavailability of carbamazepine from two slow-release preparations. Epilepsy Res. 11, 61–66. https://doi.org/10.1016/0920-1211(92)90022-L

Revol, J.F., Dietrich, A., Goring, D.A.I., 1987. Effect of mercerization on the crystallite size and crystallinity index in cellulose from different sources. Can. J. Chem. 65, 1924–1926.

Rhim, J.W., Reddy, J.P., Luo, X., 2015. Isolation of cellulose nanocrystals from onion skin and their utilization for the preparation of agar-based bio-nanocomposites films. Cellulose 22, 407–420. https://doi.org/10.1007/s10570-014-0517-7

Rosa, M.F., Medeiros, E.S., Malmonge, J.A., Gregorski, K.S., Wood, D.F., Mattoso, L.H.C., Glenn, G., Orts, W.J., Imam, S.H., 2010. Cellulose nanowhiskers from coconut husk fibers: Effect of preparation conditions on their thermal and morphological behavior. Carbohydr. Polym. 81, 83–92. https://doi.org/10.1016/j.carbpol.2010.01.059

Sadeghifar, H., Filpponen, I., Clarke, S.P., Brougham, D.F., Argyropoulos, D.S., 2011. Production of cellulose nanocrystals using hydrobromic acid and click reactions on their surface. J. Mater. Sci. 46, 7344–7355. https://doi.org/10.1007/s10853-011-5696-0

Saha, S., Ghosh, R., 2019. Cellulose nanocrystals from lignocellulosic agro-waste: A comparative study on conventional and ultrasonic assisted preparation methods. Mater. Today Proc. 11, 628–636. https://doi.org/10.1016/j.matpr.2019.03.020

Salama, A., Etri, S., Mohamed, S.A.A., El-Sakhawy, M., 2018. Carboxymethyl cellulose prepared from mesquite tree: New source for promising nanocomposite materials. Carbohydr. Polym. 189, 138–144. https://doi.org/10.1016/j.carbpol.2018.02.016

Saputra, A.H., Hapsari, M., Pitaloka, A.B., 2015. Synthesis and characterization of CMC from water hyacinth cellulose using isobutyl-isopropyl alcohol mixture as reaction medium.

Contemp. Eng. Sci. 8, 1571–1582. https://doi.org/10.12988/ces.2015.511300

Sasaki, Y., Akiyoshi, K., 2010. Nanogel engineering for new nanobiomaterials: From chaperoning engineering to biomedical applications. Chem. Rec. 10, 366–376. https://doi.org/10.1002/tcr.201000008

Schlufter, K., Heinze, T., 2010. Carboxymethylation of bacterial cellulose. Macromol. Symp. 294, 117–124. https://doi.org/10.1002/masy.200900054

Scioli Montoto, S., Sbaraglini, M.L., Talevi, A., Couyoupetrou, M., Di Ianni, M., Pesce, G.O., Alvarez, V.A., Bruno-Blanch, L.E., Castro, G.R., Ruiz, M.E., Islan, G.A., 2018. Carbamazepine-loaded solid lipid nanoparticles and nanostructured lipid carriers: Physicochemical characterization and in vitro/in vivo evaluation. Colloids Surfaces B Biointerfaces 167, 73–81. https://doi.org/10.1016/j.colsurfb.2018.03.052

Segal, L., Creely, J.J., Martin, A.E., Conrad, C.M., 1959. An empirical method for estimating the degree of crystallinity of native cellulose using the X-ray diffractometer. Text. Res. J. 29, 786–794. https://doi.org/10.1177/004051755902901003

Sekine, Y., Endo, H., Iwase, H., Takeda, S., Mukai, S.A., Fukazawa, H., Littrell, K.C., Sasaki, Y., Akiyoshi, K., 2016. Nanoscopic structural investigation of physically cross-linked nanogels formed from self-associating polymers. J. Phys. Chem. B 120, 11996–12002. https://doi.org/10.1021/acs.jpcb.6b06795

Shaheen, T.I., Emam, H.E., 2018. Sono-chemical synthesis of cellulose nanocrystals from wood sawdust using Acid hydrolysis. Int. J. Biol. Macromol. 107, 1599–1606. https://doi.org/10.1016/j.ijbiomac.2017.10.028

Shariare, M.H., Altamimi, M.A., Marzan, A.L., Tabassum, R., Jahan, B., Reza, H.M., Rahman, M., Ahsan, G.U., Kazi, M., 2019. In vitro dissolution and bioavailability study of furosemide nanosuspension prepared using design of experiment (DoE). Saudi Pharm. J. 27, 96–105. https://doi.org/10.1016/j.jsps.2018.09.002

Silvério, H.A., Flauzino Neto, W.P., Dantas, N.O., Pasquini, D., 2013. Extraction and characterization of cellulose nanocrystals from corncob for application as reinforcing agent in nanocomposites. Ind. Crops Prod. 44, 427–436. https://doi.org/10.1016/j.indcrop.2012.10.014

Sing, C.E., Perry, S.L., 2020. Recent progress in the science of complex coacervation. Soft Matter 16, 2885–2914. https://doi.org/10.1039/d0sm00001a

Singh, R.K., Singh, A.K., 2013. Optimization of reaction conditions for preparing carboxymethyl cellulose from corn cobic agricultural waste. Waste and Biomass Valorization 4, 129–137. https://doi.org/10.1007/s12649-012-9123-9

Singh, S., Gaikwad, K.K., Park, S. Il, Lee, Y.S., 2017. Microwave-assisted step reduced extraction of seaweed (Gelidiella aceroso) cellulose nanocrystals. Int. J. Biol. Macromol. 99, 506–510. https://doi.org/10.1016/j.ijbiomac.2017.03.004

Singh, A. V., 2011. Biopolymers in Drug Delivery: A Review. Pharmacologyonline 1, 666–674.

Sivaram, A.J., Rajitha, P., Maya, S., Jayakumar, R., Sabitha, M., 2015. Nanogels for delivery, imaging and therapy. Wiley Interdiscip. Rev. Nanomedicine Nanobiotechnology 7, 509–533. https://doi.org/10.1002/wnan.1328

Smyth, M., García, A., Rader, C., Foster, E.J., Bras, J., 2017. Extraction and process analysis of high aspect ratio cellulose nanocrystals from corn (Zea mays) agricultural residue. Ind. Crops Prod. 108, 257–266. https://doi.org/10.1016/j.indcrop.2017.06.006

Song, K., Ji, Y., Wang, L., Wei, Y., Yu, Z., 2018. A green and environmental benign method to extract cellulose nanocrystal by ball mill assisted solid acid hydrolysis. J. Clean. Prod. 196, 1169–1175. https://doi.org/10.1016/j.jclepro.2018.06.128

Soni, K.S., Desale, S.S., Bronich, T.K., 2016. Nanogels: An overview of properties, biomedical applications and obstacles to clinical translation. J. Control. Release 240, 109–126. https://doi.org/10.1016/j.jconrel.2015.11.009

Soyekwo, F., Zhang, Q.G., Lin, X.C., Wu, X.M., Zhu, A.M., Liu, Q.L., 2016. Facile preparation and separation performances of cellulose nanofibrous membranes. J. Appl. Polym. Sci. 133, 1–12. https://doi.org/10.1002/app.43544

Stinson-Bagby, K.L., Roberts, R., Foster, E.J., 2018. Effective cellulose nanocrystal imaging using transmission electron microscopy. Carbohydr. Polym. 186, 429–438. https://doi.org/10.1016/j.carbpol.2018.01.054

Sukyai, P., Anongjanya, P., Bunyahwuthakul, N., Kongsin, K., Harnkarnsujarit, N., Sukatta, U., Sothornvit, R., Chollakup, R., 2018. Effect of cellulose nanocrystals from sugarcane bagasse on whey protein isolate-based films. Food Res. Int. 107, 528–535. https://doi.org/10.1016/j.foodres.2018.02.052

Sun, M., He, L., Fan, Z., Tang, R., Du, J., 2020. Effective treatment of drug-resistant lung cancer via a nanogel capable of reactivating cisplatin and enhancing early apoptosis. Biomaterials

257. https://doi.org/10.1016/j.biomaterials.2020.120252

Sun, X.F., Sun, R.C., Su, Y., Sun, J.X., 2004. Comparative Study of Crude and Purified Cellulose from Wheat Straw. J. Agric. Food Chem. 52, 839–847. https://doi.org/10.1021/jf0349230

Sun, X.F., Xu, F., Sun, R.C., Fowler, P., Baird, M.S., 2005. Characteristics of degraded cellulose obtained from steam-exploded wheat straw. Carbohydr. Res. 340, 97–106. https://doi.org/10.1016/j.carres.2004.10.022

Suriyatem, R., Noikang, N., Kankam, T., Jantanasakulwong, K., Leksawasdi, N., Phimolsiripol, Y., Insomphun, C., Seesuriyachan, P., Chaiyaso, T., Jantrawut, P., Sommano, S.R., Ngo, T.M.P., Rachtanapun, P., 2020. Physical properties of carboxymethyl cellulose from palm bunch and bagasse agricultural wastes: Effect of delignification with hydrogen peroxide. Polymers (Basel). 12, 1–16. https://doi.org/10.3390/polym12071505

Taflick, T., Schwendler, L.A., Rosa, S.M.L., Bica, C.I.D., Nachtigall, S.M.B., 2017. Cellulose nanocrystals from acacia bark–Influence of solvent extraction. Int. J. Biol. Macromol. 101, 553–561. https://doi.org/10.1016/j.ijbiomac.2017.03.076

Tahara, Y., Sakiyama, M., Takeda, S., Nishimura, T., Mukai, S.A., Sawada, S.I., Sasaki, Y., Akiyoshi, K., 2016. Self-Assembled Nanogels of Cholesterol-Bearing Hydroxypropyl Cellulose: A Thermoresponsive Building Block for Nanogel Tectonic Materials. Langmuir 32, 12283–12289. https://doi.org/10.1021/acs.langmuir.6b02406

Tan, J., Kang, H., Liu, R., Wang, D., Jin, X., Li, Q., Huang, Y., 2011. Dual-stimuli sensitive nanogels fabricated by self-association of thiolated hydroxypropyl cellulose. Polym. Chem. 2, 672–678. https://doi.org/10.1039/c0py00348d

Tan, J.P.K., Tan, M.B.H., Tam, M.K.C., 2010. Application of nanogel systems in the administration of local anesthetics. Local Reg. Anesth. 3, 93–100. https://doi.org/10.2147/LRA.S7977

Tarchoun, A.F., Trache, D., Klapötke, T.M., 2019. Microcrystalline cellulose from Posidonia oceanica brown algae: Extraction and characterization. Int. J. Biol. Macromol. 138, 837–845. https://doi.org/10.1016/j.ijbiomac.2019.07.176

Tena Gashaw, E., Mekbib, F., Ayana, A., 2018. Sugarcane landraces of Ethiopia: Germplasm collection and analysis of regional diversity and distribution. Adv. Agric. 2018, 1–18. https://doi.org/10.1155/2018/7920724

Thomas, D., Latha, M.S., Thomas, K.K., 2018. Synthesis and in vitro evaluation of alginate-cellulose nanocrystal hybrid nanoparticles for the controlled oral delivery of rifampicin. J. Drug Deliv. Sci. Technol. 46, 392–399. https://doi.org/10.1016/j.jddst.2018.06.004

Tiwari, G., Tiwari, R., Bannerjee, S., Bhati, L., Pandey, S., Pandey, P., Sriwastawa, B., 2012. Drug delivery systems: An updated review. Int. J. Pharm. Investig. 2, 2. https://doi.org/10.4103/2230-973x.96920

Tortorella, S., Buratti, V.V., Maturi, M., Sambri, L., Franchini, M.C., Locatelli, E., 2020. Surface-modified nanocellulose for application in biomedical engineering and nanomedicine: A review. Int. J. Nanomedicine 15, 9909–9937. https://doi.org/10.2147/IJN.S266103

Trache, D., Tarchoun, A.F., Derradji, M., Hamidon, T.S., Masruchin, N., Brosse, N., Hussin, M.H., 2020. Nanocellulose: From Fundamentals to Advanced Applications. Front. Chem. 8, 392. https://doi.org/10.3389/fchem.2020.00392

Tsegaye, B., Balomajumder, C., Roy, P., 2019. Alkali pretreatment of wheat straw followed by microbial hydrolysis for bioethanol production. Environ. Technol. (United Kingdom) 40, 1203–1211. https://doi.org/10.1080/09593330.2017.1418911

Tuan Mohamood, N.F.A.Z., Abdul Halim, A.H., Zainuddin, N., 2021. Carboxymethyl cellulose hydrogel from biomass waste of oil palm empty fruit bunch using calcium chloride as crosslinking agent. Polymers (Basel). 13. https://doi.org/10.3390/polym13234056

Ünlü, C.H., 2013. Carboxymethylcellulose from recycled newspaper in aqueous medium. Carbohydr. Polym. 97, 159–164. https://doi.org/10.1016/j.carbpol.2013.04.039

USP41-NF36, 2019a. In vitro drug evaluation, in: The United States Pharmacopeial Convention - U.S. Pharmacopeia National Formulary.

USP41-NF36, 2019b. Carboxymethylcellulose Sodium, in: The United States Pharmacopeial Convention - U.S. Pharmacopeia National Formulary. 12601 Twinbrook Parkway, Rockville, MD 20852, pp. 712–713.

Varma, R., Vasudevan, S., 2022. Synthesis and Characterization of Cellulose and Cellulose Nanocrystals From Dead Seagrass – Towards the Wealth From Waste Concept". Cellul. Chem. Technol. 56, 39–47. https://doi.org/10.35812/cellulosechemtechnol.2022.56.03

Varshney, V.K., Gupta, P.K., Naithani, S., Khullar, R., Bhatt, A., Soni, P.L., 2006. Carboxymethylation of α-cellulose isolated from Lantana camara with respect to degree of

substitution and rheological behavior. Carbohydr. Polym. 63, 40–45. https://doi.org/10.1016/j.carbpol.2005.07.001

Veeramachineni, A.K., Sathasivam, T., Muniyandy, S., Janarthanan, P., Langford, S.J., Yan, L.Y., 2016. Optimizing extraction of cellulose and synthesizing pharmaceutical grade carboxymethyl sago cellulose from Malaysian sago pulp. Appl. Sci. 6, 170–188. https://doi.org/10.3390/app6060170

Ventura-Cruz, S., Tecante, A., 2019. Extraction and characterization of cellulose nanofibers from Rose stems (Rosa spp.). Carbohydr. Polym. 220, 53–59. https://doi.org/10.1016/j.carbpol.2019.05.053

Vinogradov, S., Batrakova, E., Kabanov, A., 1999. Poly(ethylene glycol)–polyethyleneimine NanoGel™ particles: novel drug delivery systems for antisense oligonucleotides. Colloids Surfaces B Biointerfaces 16, 291–304. https://doi.org/10.1016/S0927-7765(99)00080-6

Wada, M., Okano, T., 2001. Localization of Iα and Iβ phases in algal cellulose revealed by acid treatments. Cellulose 8, 183–188. https://doi.org/10.1023/A:1013196220602

Wang, X., Li, H., Cao, Y., Tang, Q., 2011. Cellulose extraction from wood chip in an ionic liquid 1-allyl-3-methylimidazolium chloride (AmimCl). Bioresour. Technol. 102, 7959–7965. https://doi.org/10.1016/j.biortech.2011.05.064

Wang, Zhihao, Dadi Bekele, L., Qiu, Y., Dai, Y., Zhu, S., Sarsaiya, S., Chen, J., 2019. Preparation and characterization of coffee hull fiber for reinforcing application in thermoplastic composites. Bioengineered 10, 397–408. https://doi.org/10.1080/21655979.2019.1661694

Wang, Zhanhong, Yao, Z., Zhou, J., He, M., Jiang, Q., Li, S., Ma, Y., Liu, M., Luo, S., 2019. Isolation and characterization of cellulose nanocrystals from pueraria root residue. Int. J. Biol. Macromol. 129, 1081–1089. https://doi.org/10.1016/j.ijbiomac.2018.07.055

Waring, M.J., Parsons, D., 2001. Physico-chemical characterisation of carboxymethylated spun cellulose fibres. Biomaterials 22, 903–912. https://doi.org/10.1016/S0142-9612(00)00254-4

Wasik, S.P., Tewari, Y.B., Miller, M.M., Martire, D.E., 1981. Octanol/Water Partition Coefficients and Aqueous Solubilities of Organic Compounds, 2nd ed. U.S. Department of Commerce National Bureau of Standards Center for Chemical Physics Chemical Thermodynamics Division, Washington, DC 20234.

Watkins, D., Nuruddin, M., Hosur, M., Tcherbi-Narteh, A., Jeelani, S., 2015. Extraction and

characterization of lignin from different biomass resources. J. Mater. Res. Technol. 4, 26–32. https://doi.org/10.1016/j.jmrt.2014.10.009

Wen, Y., Oh, J.K., 2015. Intracellular delivery cellulose-based bionanogels with dual temperature/pH-response for cancer therapy. Colloids Surfaces B Biointerfaces 133, 246–253. https://doi.org/10.1016/j.colsurfb.2015.06.017

Wen, Y., Oh, J.K., 2014. Dual-stimuli reduction and acidic pH-responsive bionanogels: intracellular delivery nanocarriers with enhanced release. RSC Adv. 4, 229–237. https://doi.org/10.1039/C3RA46072J

Wijaya, C.J., Ismadji, S., Aparamarta, H.W., Gunawan, S., 2019. Optimization of cellulose nanocrystals from bamboo shoots using Response Surface Methodology. Heliyon 5, e02807. https://doi.org/10.1016/j.heliyon.2019.e02807

Wijaya, C.J., Saputra, S.N., Soetaredjo, F.E., Putro, J.N., Lin, C.X., Kurniawan, A., Ju, Y.H., Ismadji, S., 2017. Cellulose nanocrystals from passion fruit peels waste as antibiotic drug carrier. Carbohydr. Polym. 175, 370–376. https://doi.org/10.1016/j.carbpol.2017.08.004

Wu, H., Cao, D., Liu, T., Zhao, J., Hu, X., Li, N., 2015. Purification and characterization of recombinant human lysozyme from eggs of transgenic chickens. PLoS One 10, 1–17. https://doi.org/10.1371/journal.pone.0146032

Wu, L., Zhou, H., Sun, H.J., Zhao, Y., Yang, X., Cheng, S.Z., Yang, G., 2013. Thermoresponsive bacterial cellulose whisker/poly(NIPAM-co-BMA) nanogel complexes: synthesis, characterization, and biological evaluation. Biomacromolecules 14, 1078–1084. https://doi.org/10.1021/bm3019664

Wu, T., Kummer, N., De France, K.J., Campioni, S., Zeng, Z., Siqueira, G., Dong, J., Nyström, G., 2021. Nanocellulose-lysozyme colloidal gels via electrostatic complexation. Carbohydr. Polym. 251, 1–9. https://doi.org/10.1016/j.carbpol.2020.117021

Wüstenberg, T., 2015. Cellulose and Cellulose Derivatives in the Food Industry: Fundamentals and Applications. Wiley-VCH Verlag GmbH & Co. KGaA, Boschstr. 12, 69469 Weinheim, Germany.

Xiao, Y., Liu, Y., Wang, X., Li, M., Lei, H., Xu, H., 2019. Cellulose nanocrystals prepared from wheat bran: Characterization and cytotoxicity assessment. Int. J. Biol. Macromol. 140, 225–233. https://doi.org/10.1016/j.ijbiomac.2019.08.160

Xie, J., Hse, C.Y., De Hoop, C.F., Hu, T., Qi, J., Shupe, T.F., 2016. Isolation and

characterization of cellulose nanofibers from bamboo using microwave liquefaction combined with chemical treatment and ultrasonication. Carbohydr. Polym. 151, 725–734. https://doi.org/10.1016/j.carbpol.2016.06.011

Xing, L., Gu, J., Zhang, W., Tu, D., Hu, C., 2018. Cellulose I and II nanocrystals produced by sulfuric acid hydrolysis of Tetra pak cellulose I. Carbohydr. Polym. 192, 184–192. https://doi.org/10.1016/j.carbpol.2018.03.042

Xue, M., Findenegg, G.H., 2012. Lysozyme as a pH-responsive valve for the controlled release of guest molecules from mesoporous silica. Langmuir 28, 17578–17584. https://doi.org/10.1021/la304152j

Yang, H., Yan, R., Chen, H., Lee, D.H., Zheng, C., 2007. Characteristics of hemicellulose, cellulose and lignin pyrolysis. Fuel 86, 1781–1788. https://doi.org/10.1016/j.fuel.2006.12.013

Yang, H.N., Park, J.S., Jeon, S.Y., Park, K.H., 2015. Carboxymethylcellulose (CMC) formed nanogels with branched poly(ethyleneimine) (bPEI) for inhibition of cytotoxicity in human MSCs as a gene delivery vehicles. Carbohydr. Polym. 122, 265–275. https://doi.org/10.1016/j.carbpol.2014.12.073

Yao, R., Xu, J., Lu, X., Deng, S., 2011. Phase transition behavior of HPMC-AA and preparation of HPMC-PAA nanogels. J. Nanomater. 2011, 1–6. https://doi.org/10.1155/2011/507542

Yao, R.S., Zhang, W.B., Yang, X.Z., Liu, J., Liu, H.T., 2014. HPMC/PAA hybrid nanogels via aqueous-phase synthesis for controlled delivery of insulin. Biomater. Sci. 2, 1761–1767. https://doi.org/10.1039/c4bm00203b

Yaşar, F., Toğrul, H., Arslan, N., 2007. Flow properties of cellulose and carboxymethyl cellulose from orange peel. J. Food Eng. 81, 187–199. https://doi.org/10.1016/j.jfoodeng.2006.10.022

Yeasmin, M.S., Mondal, M.I.H., 2015. Synthesis of highly substituted carboxymethyl cellulose depending on cellulose particle size. Int. J. Biol. Macromol. 80, 725–731. https://doi.org/10.1016/j.ijbiomac.2015.07.040

Yu, H., Qin, Z., Liang, B., Liu, N., Zhou, Z., Chen, L., 2013. Facile extraction of thermally stable cellulose nanocrystals with a high yield of 93% through hydrochloric acid hydrolysis under hydrothermal conditions. J. Mater. Chem. A 1, 3938–3944. https://doi.org/10.1039/c3ta01150j

Yu, S., Hu, J., Pan, X., Yao, P., Jiang, M., 2006. Stable and pH-sensitive nanogels prepared by

self-assembly of chitosan and ovalbumin. Langmuir 22, 2754–2759. https://doi.org/10.1021/la053158b

Yue, Y., 2011. A comparative study of cellulose I and II and fibers and nanocrystals. Louisiana State University LSU Digital Commons.

Yuliasmi, S., Ginting, N., Wahyuni, H.S., Sigalingging, R.T., Sibarani, T., 2019. The effect of alkalization on carboxymethil cellulose synthesis from stem and peel cellulose of banana. Open Access Maced. J. Med. Sci. 7, 3874–3877. https://doi.org/10.3889/oamjms.2019.523

Zhang, G., Zhang, L., Deng, H., Sun, P., 2011. Preparation and characterization of sodium carboxymethyl cellulose from cotton stalk using microwave heating. J. Chem. Technol. Biotechnol. 86, 584–589. https://doi.org/10.1002/jctb.2556

Zhang, H., Chen, Y., Wang, S., Ma, L., Yu, Y., Dai, H., Zhang, Y., 2020. Extraction and comparison of cellulose nanocrystals from lemon (Citrus limon) seeds using sulfuric acid hydrolysis and oxidation methods. Carbohydr. Polym. 238, 116180. https://doi.org/10.1016/j.carbpol.2020.116180

Zhang, H., Zhai, Y., Wang, J., Zhai, G., 2016. New progress and prospects: The application of nanogel in drug delivery. Mater. Sci. Eng. C 60, 560–568. https://doi.org/10.1016/j.msec.2015.11.041

Zhang, J., Li, D., Zhang, X., Shi, Y., 1993. Solvent effect on carboxymethylation of cellulose. J. Appl. Polym. Sci. https://doi.org/10.1002/app.1993.070490420

Zhang, J.L., Wang, P., An, D., Li, X.T., Wu, Q., Zhao, D., Lu, X.H., Qiu, G., 2014. Synthesis of nanogels of poly methyacrylic acid using methyl cellulose as a template. Mater. Sci. Forum 787, 401–406. https://doi.org/10.4028/www.scientific.net/MSF.787.401

Zhang, X., Xiao, N., Wang, H., Liu, C., Pan, X., 2018. Preparation and characterization of regenerated cellulose film from a solution in lithium bromide molten salt hydrate. Polymers (Basel). 8, 614–627. https://doi.org/10.3390/polym10060614

Zhao, D., Shi, X., Liu, T., Lu, X., Qiu, G., Shea, K.J., 2016. Synthesis of surfactant-free hydroxypropyl methylcellulose nanogels for controlled release of insulin. Carbohydr. Polym. 151, 1006–1011. https://doi.org/10.1016/j.carbpol.2016.06.055

Zhao, H., Cheng, F., Li, G., Zhang, J., 2003. Optimization of a process for carboxymethyl cellulose (CMC) preparation in mixed solvents. Int. J. Polym. Mater. Polym. Biomater. 52, 749–759. https://doi.org/10.1080/713743713

Zhou, M., Hu, Q., Wang, T., Xue, J., Luo, Y., 2016. Effects of different polysaccharides on the formation of egg yolk LDL complex nanogels for nutrient delivery. Carbohydr. Polym. 153, 336–344. https://doi.org/10.1016/j.carbpol.2016.07.105

Zhu, K., Ye, T., Liu, J., Peng, Z., Xu, S., Lei, J., Deng, H., Li, B., 2013. Nanogels fabricated by lysozyme and sodium carboxymethyl cellulose for 5-fluorouracil controlled release. Int. J. Pharm. 441, 721–727. https://doi.org/10.1016/j.ijpharm.2012.10.022

Zvonar, A., Berginc, K., Kristl, A., Gašperlin, M., 2010. Microencapsulation of self-microemulsifying system: Improving solubility and permeability of furosemide. Int. J. Pharm. 388, 151–158. https://doi.org/10.1016/j.ijpharm.2009.12.055

Zybina, A., Anshakova, A., Malinovskaya, J., Melnikov, P., Baklaushev, V., Chekhonin, V., Maksimenko, O., Titov, S., Balabanyan, V., Kreuter, J., Gelperina, S., Abbasova, K., 2018. Nanoparticle-based delivery of carbamazepine: A promising approach for the treatment of refractory epilepsy. Int. J. Pharm. 547, 10–23. https://doi.org/10.1016/j.ijpharm.2018.05.023

Appendix

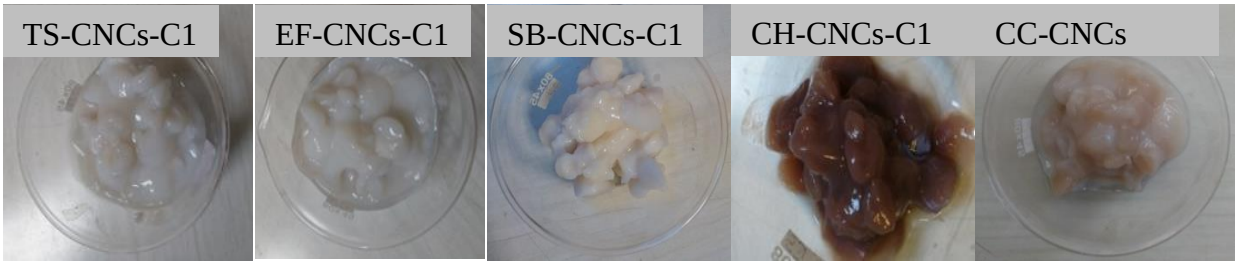

a)

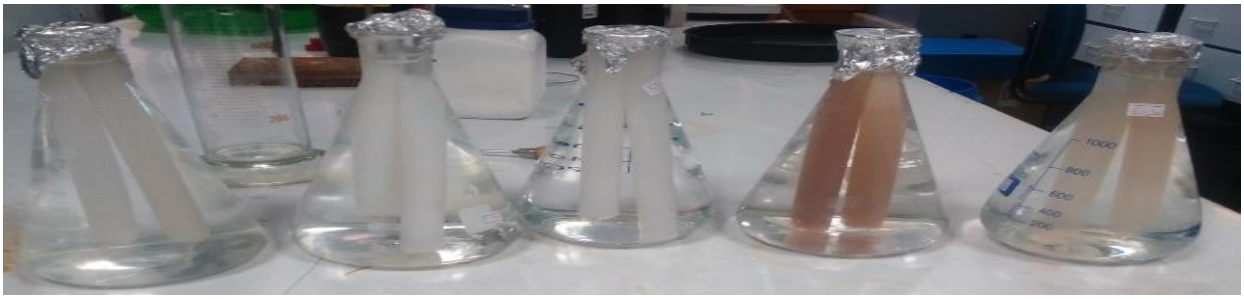

b)

Fig. A1: Photographs of a) CNCs after initial centrifugation b) CNCs during dialysis (TS, EF, SB, CH and CC from left to right).

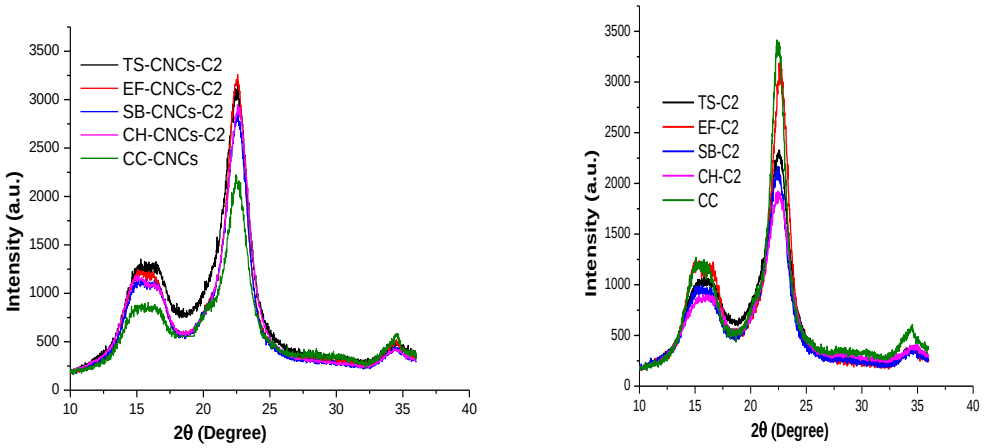

Fig. A2: XRD patterns of CNCs-C2, and the cellulose (C2) precursors. (Key: CNCs-C2-cellulose nanocrystals isolated from C2; C2-cellulose extracted following extraction Condition B; TS-*teff* straw; EF-*enset* fiber; SB-sugarcane bagasse; CH-coffee hull; CC-CNCs-cellulose nanocrystals isolated from commercial cellulose (CC) included for comparison).

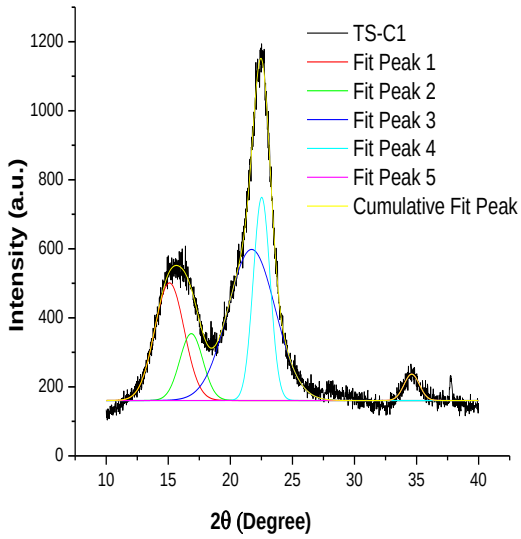
TS-C1
Fit Peak 1
Fit Peak 2
Fit Peak 3
Fit Peak 4
Fit Peak 5
Cumulative Fit Peak
Intensity (a.u.)
2θ (Degree)

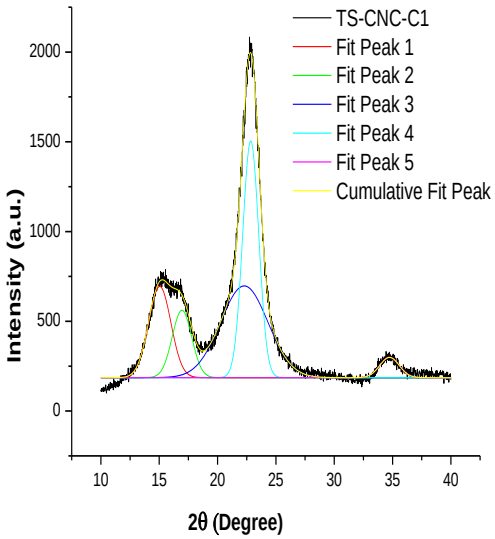
TS-CNC-C1
Fit Peak 1
Fit Peak 2
Fit Peak 3
Fit Peak 4
Fit Peak 5
Cumulative Fit Peak
Intensity (a.u.)
2θ (Degree)

(a)

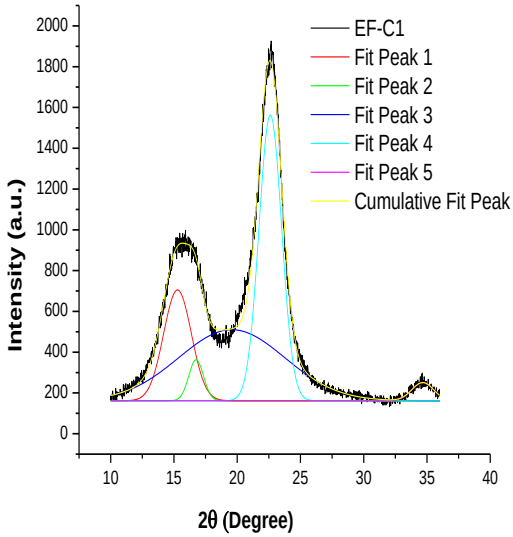
EF-C1
Fit Peak 1
Fit Peak 2
Fit Peak 3
Fit Peak 4
Fit Peak 5
Cumulative Fit Peak
Intensity (a.u.)
2θ (Degree)

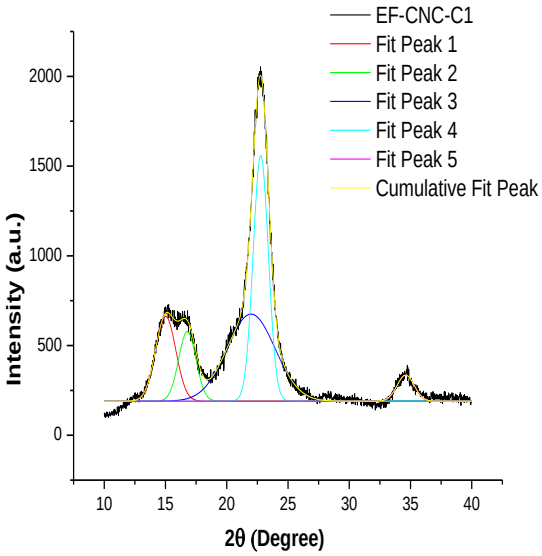
EF-CNC-C1
Fit Peak 1
Fit Peak 2
Fit Peak 3
Fit Peak 4
Fit Peak 5
Cumulative Fit Peak
Intensity (a.u.)
2θ (Degree)

(b)

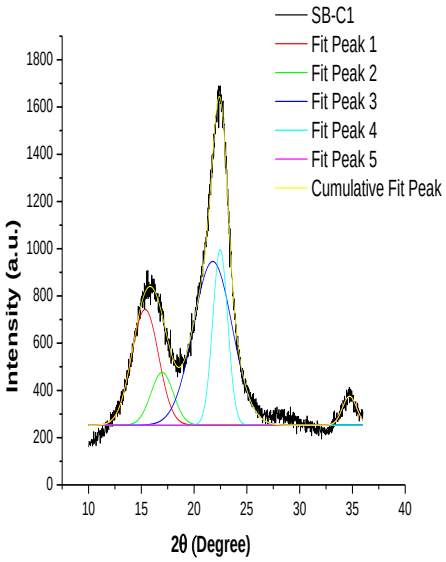
SB-C1
Fit Peak 1
Fit Peak 2
Fit Peak 3
Fit Peak 4
Fit Peak 5
Cumulative Fit Peak
Intensity (a.u.)
2θ (Degree)

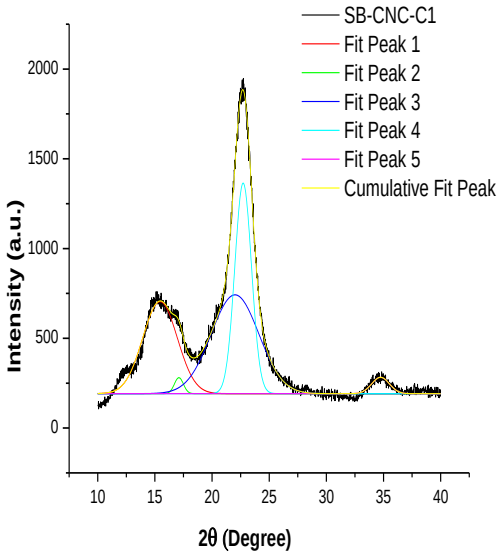
SB-CNC-C1
Fit Peak 1
Fit Peak 2
Fit Peak 3
Fit Peak 4
Fit Peak 5
Cumulative Fit Peak
Intensity (a.u.)
2θ (Degree)

(c)

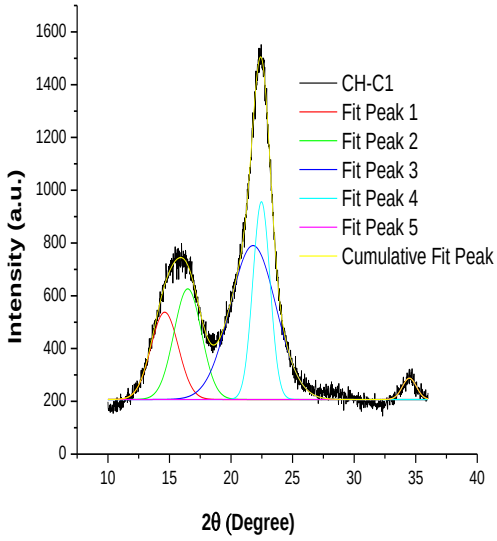
CH-C1
Fit Peak 1
Fit Peak 2
Fit Peak 3
Fit Peak 4
Fit Peak 5
Cumulative Fit Peak
Intensity (a.u.)
2θ (Degree)

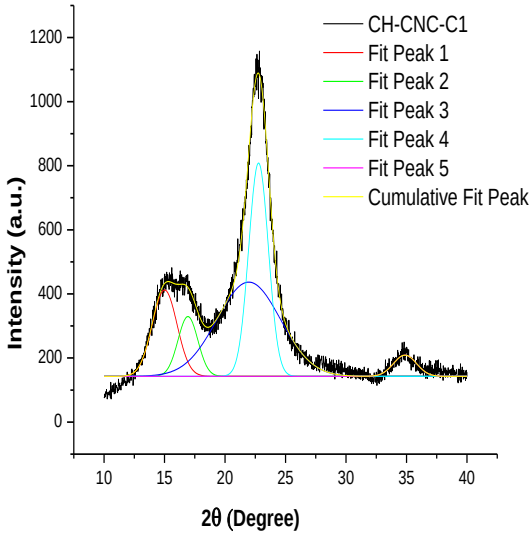
CH-CNC-C1
Fit Peak 1
Fit Peak 2
Fit Peak 3
Fit Peak 4
Fit Peak 5
Cumulative Fit Peak
Intensity (a.u.)
2θ (Degree)

(d)

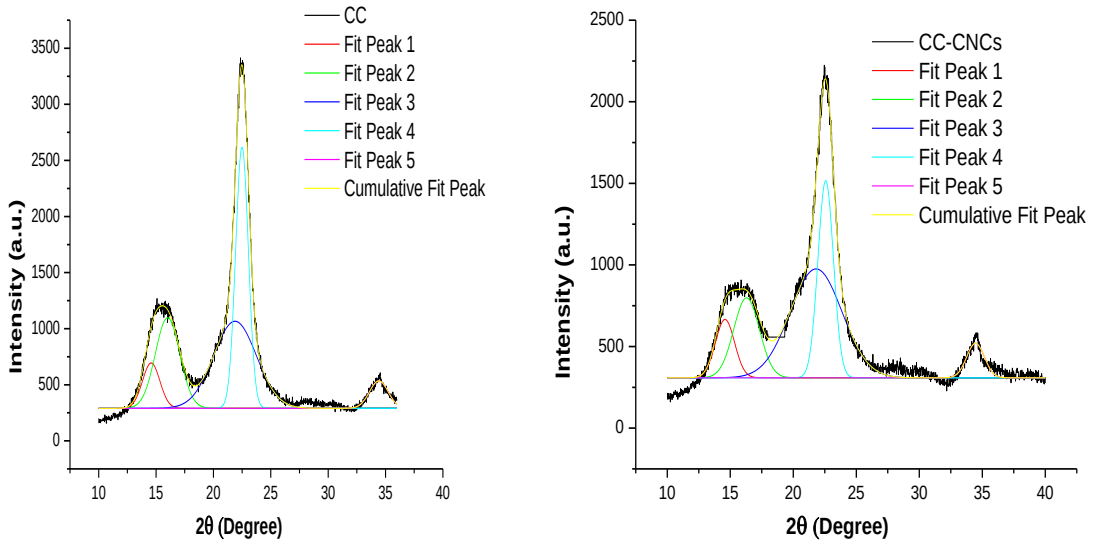

(e)

Fig. A3: Deconvoluted XRD patterns of the cellulose precursors (left) and as-obtained CNCs-C1 (right) from TS (a), EF (b), SB (c), CH (d) and CC (e). (Key: CNCs-C1-cellulose nanocrystals isolated from C1; C1-Cellulose extracted using extraction Condition A; TS-*teff* straw; EF-*enset* fiber; SB-sugarcane bagasse; CH-coffee hull; CC-CNCs-cellulose nanocrystals isolated from commercial cellulose (CC) included for comparison).

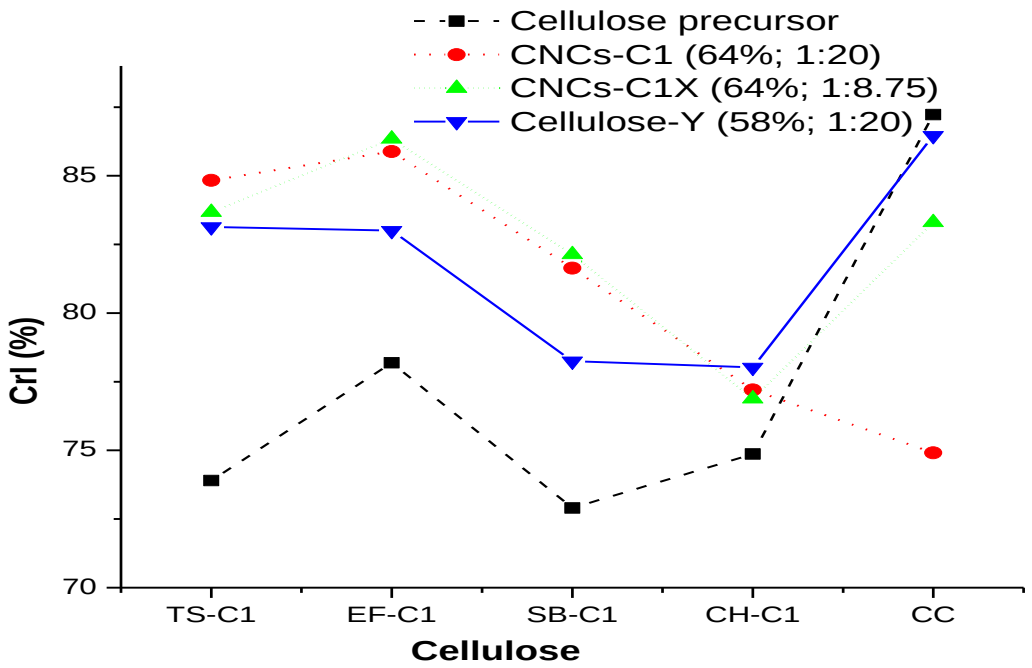

Fig. A4: Influence of sulfuric acid ratio and concentration on CrI of hydrolyzed cellulose using cellulose (C1) from each byproduct and CC as precursor (Preliminary work). (Key: CNCs-C1-cellulose nanocrystals isolated from C1 using 64% (w/w) sulfuric acid (1:20); CNCs-C1X and CC-NCsX-cellulose nanocrystals obtained using 64% wt/wt sulfuric acid (1:8.75 g/mL); Cellulose-Y-cellulose hydrolyzed using 58% (w/w) sulfuric acid (1:20); C1-cellulose extracted following extraction condition A; TS-*teff* straw; EF-*enset* fiber; SB-sugarcane bagasse; CH-coffee hull; CC- commercial cellulose included for comparison).

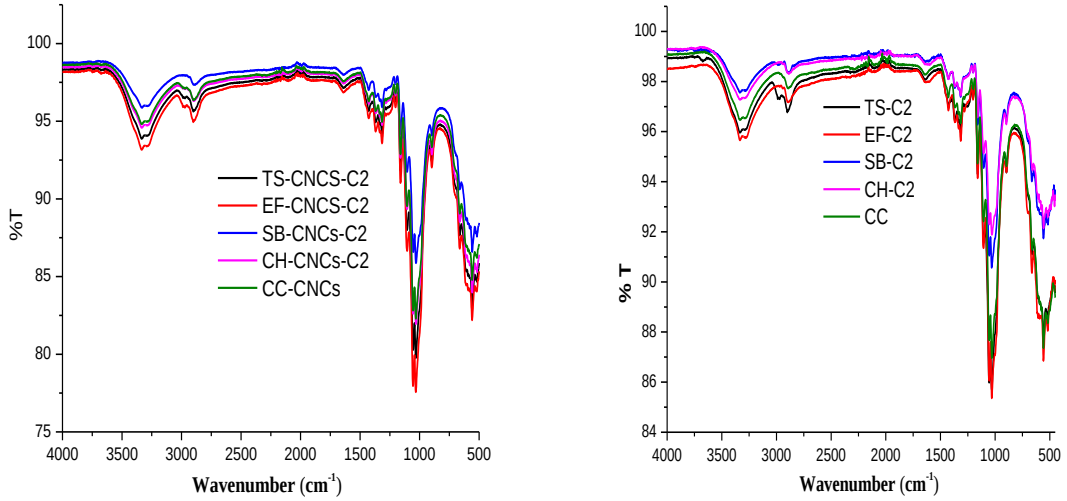

Fig. A5: FTIR spectra of CNCs-C2, and cellulose (C2) precursors. (Key: CNCs-C2-cellulose nanocrystals isolated from C2; C2-cellulose extracted following extraction Condition B; TS-*teff* straw; EF-*enset* fiber; SB-sugarcane bagasse; CH-coffee hull; CC-CNCs-cellulose nanocrystals isolated from commercial cellulose (CC) included for comparison).

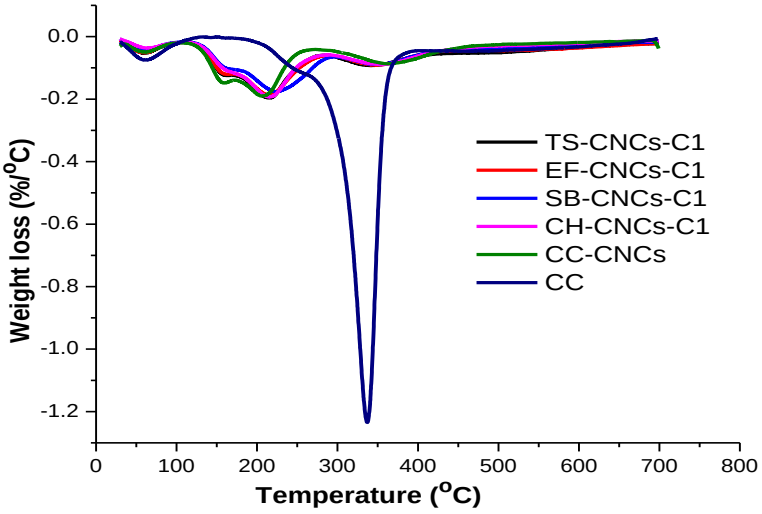

Fig. A6: DTG curve of as-obtained CNCs-C1 from the celluloses extracted from the four plant byproducts, CC-CNCs, and CC. (Key: CNCs-C1-cellulose nanocrystals isolated from C1; C1-Cellulose extracted using extraction Condition A; TS-*teff* straw; EF-*enset* fiber; SB-sugarcane bagasse; CH-coffee hull; CC-CNCs-cellulose nanocrystals isolated from commercial cellulose (CC) included for comparison).

Table A1: Summary of TGA and DTG results of the as-obtained CNCs-1, and cellulose (C1) precursors.

SN	Material	ΔT (°C)	T_{max} (°C)	Weight loss (%)	Weight loss rate (%/°C)	T_i (°C)	Residue at 550 °C (%)
	TS-C1	29.7-108.73	61.30	5.47	0.0855	239.95	16.17
		239.95-384.70	352.03	70.34	1.1420		
		384.70-550.00	509.51	6.22	0.0283		
	TS-CNCs-C1	34.99-109.36	59.94	5.72	0.0531	146.70	21.95
		146.70-254.81	216.08	31.56	0.1963		
		287.84-430.25	342.59	20.96	0.0926		
	EF-C1	30.71-119.27	61.19	5.66	0.1916	221.40	20.44
		221.40-383.70	341.78	65.22	1.5790		
		383.70-550.00	434.99	7.20	0.0687		
	EF-CNCs-C1	29.77-108.63	59.64	5.40	0.0518	112.80	24.89
		112.80-289.40	215.36	38.36	0.1866		
		289.40-439.85	348.1	21.04	0.0916		
	SB-C1	29.72-121.48	60.28	6.28	0.1475	205.22	19.28
		205.22-399.20	340.30	68.41	1.6756		
		399.20-550.00	476.44	5.59	0.0547		
		29.77-108.33	61.04	4.48	0.04155		
		153.86-273.95	224.49	32.45	0.1760		

SB-CNCs-C1	297.7-430.26	354.68	18.71	0.0893	153.86	27.71
CH-C1	29.77-119.01	57.42	5.66	0.0554	284.37	22.47
	284.37-391.15	329.73	50.39	0.5795		
	391.15-550.00	417.98	7.04	0.0277		
CH-CNCs-C1	29.77-107.33	63.81	4.05	0.0364	152.18	30.48
	152.18-253.82	216.65	29.07	0.1927		
	288.12-504.18	355.94	25.40	0.0889		
CC	30.16-108.49	62.60	4.70	0.0749	268.93	15.91
	268.93-378.50	338.76	62.20	1.2165		
	378.50-550.00	463.49	9.85	0.0470		
CC-CNCs	29.77-108.65	59.94	5.29	0.0495	152.56	31.90
	152.56-171.4	158.6	5.52	0.1484		
	142.00-237.01	206.244	28.60	0.1903		
	286.85-478.15	361.67	22.58	0.0868		

Key:- ΔT-Temperature change where main weight loss occurs; T_{max}-Maximum degradation (weight-loss) temperature; T_i-Initial degradation temperature (Onset temperature). CNCs-C1-cellulose nanocrystals isolated from C1; C1-cellulose extracted following extraction Condition A; TS-teff straw; EF-enset fiber; SB-sugarcane bagasse; CH-coffee hull; CC-CNCs-cellulose nanocrystals isolated from commercial cellulose (CC) included for comparison).

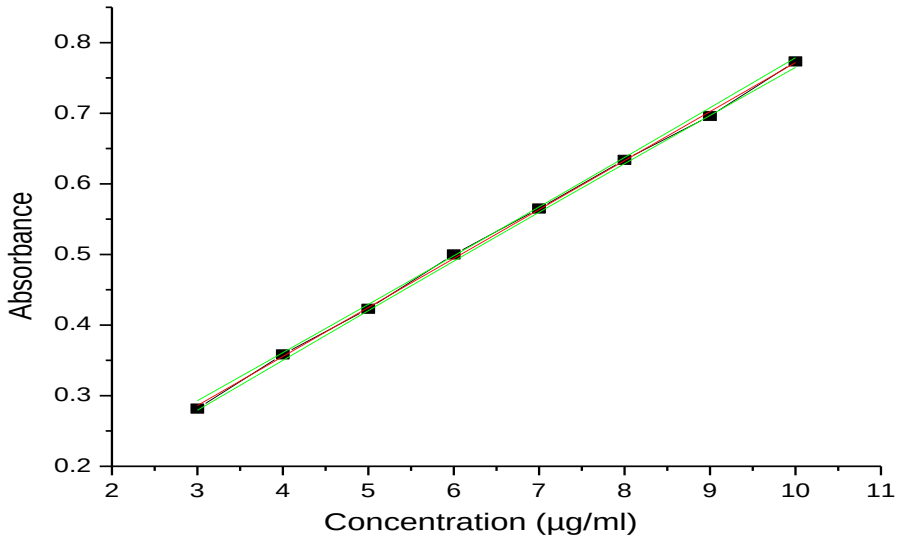

a) Acyclovir at 254 nm with 95% confidence bands for mean, (Y=0.0694X+0.0779; R^2=0.9995).

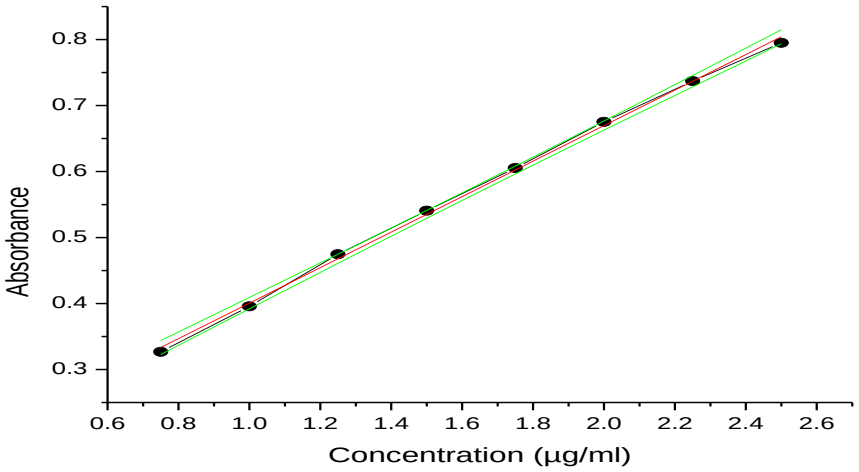

b) Carbamazepine at 284 nm with 95% confidence bands for mean, (Y=0.2691X+0.13152; R^2=0.9986).

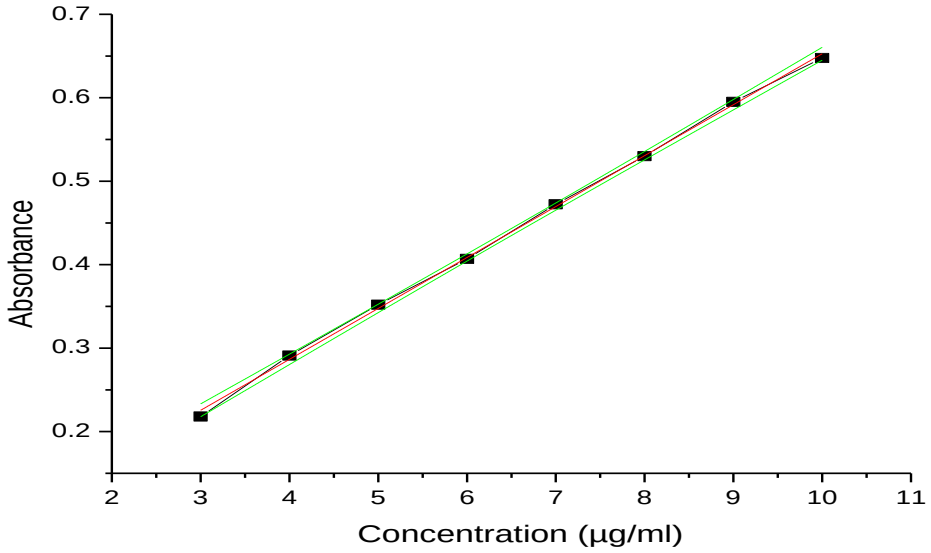

c) Furosemide at 274 nm with 95% confidence bands for mean, (Y=0.0610X+0.0424; R^2=0.9991).

Fig. A7: The UV absorption calibration curves of a) acyclovir b) carbamazepine and c) furosemide. Where, Y is absorbance and X is concentration (µg/ml) of the drug solutions. Data are presented as the mean ± SD (*n* = 3).

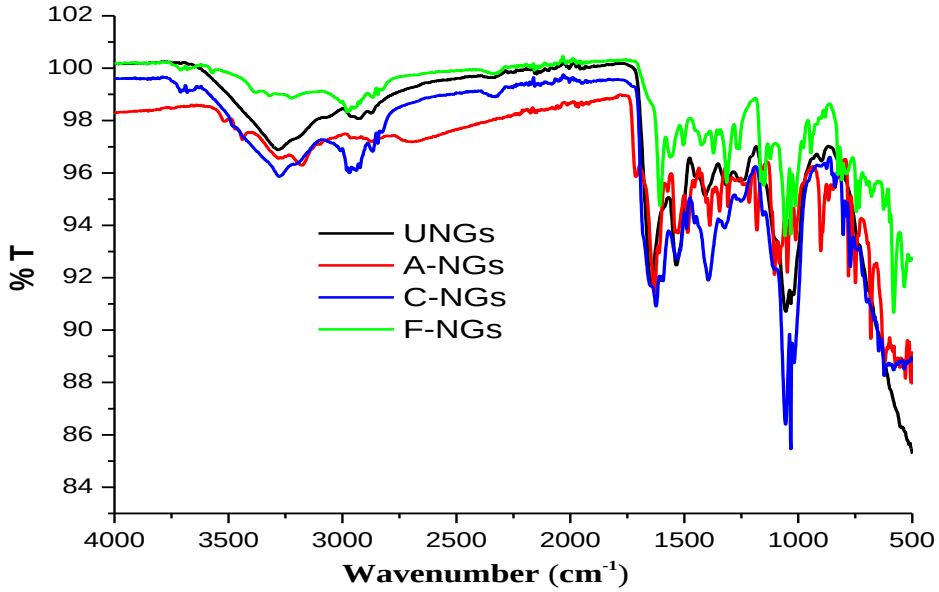

a)

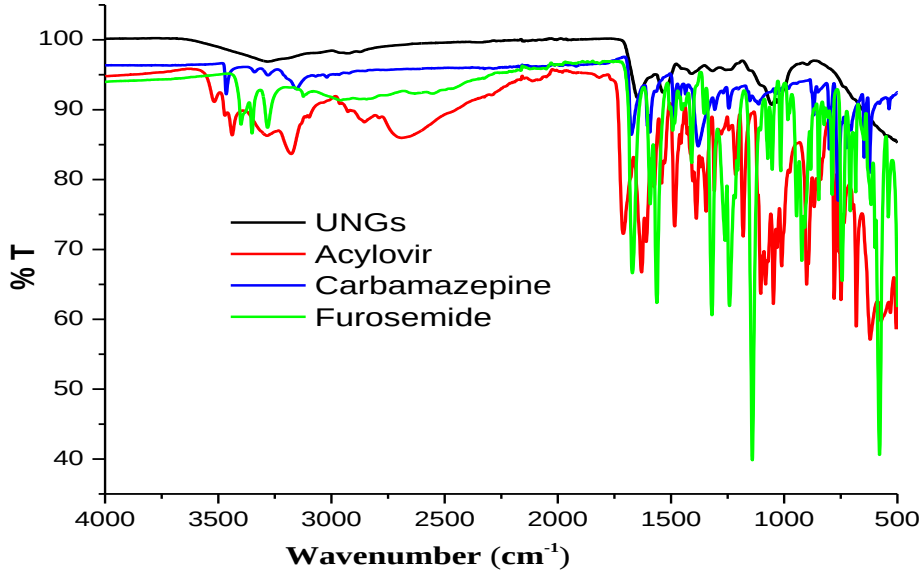

b)

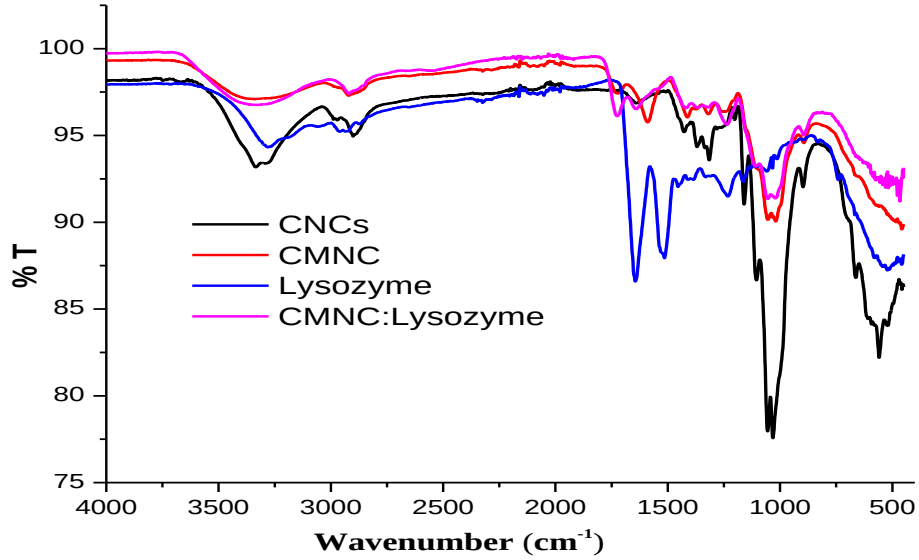
100
95
90
85
80
75
% T
CNCs
CMNC
Lysozyme
CMNC:Lysozyme
4000
3500
3000
2500
2000
1500
1000
500
Wavenumber (cm-1)

c)

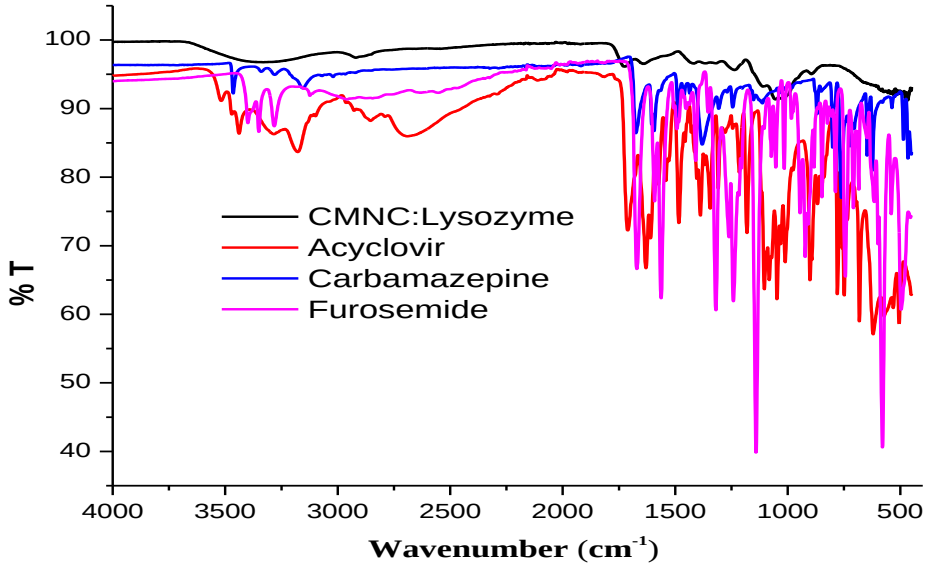
100
90
80
70
60
50
40
% T
CMNC:Lysozyme
Acyclovir
Carbamazepine
Furosemide
4000
3500
3000
2500
2000
1500
1000
500
Wavenumber (cm-1)

d)

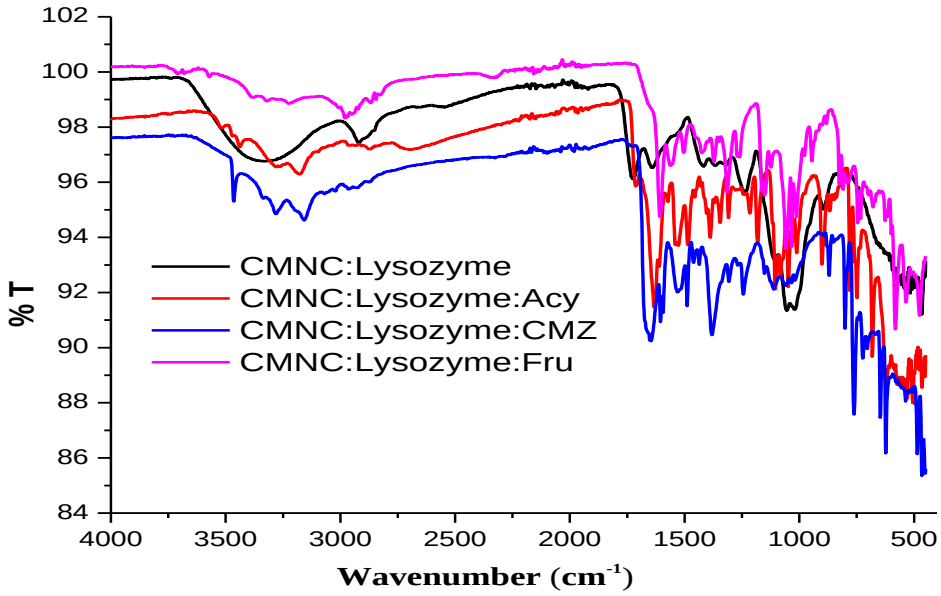

e)

Fig. A8: FTIR spectra of a) UNGs and drug-loaded nanogels, b) UNGs and free model drugs, c) physical mixture of CMNC and Lysozyme (weight ratio of 1:1) in comparison with FTIR spectra of CNCs, CMNC and Lysozyme, d) the physical mixture with respect to FTIR spectra of pure drugs, e) physical mixture of CMNC and Lysozyme, with respect to FTIR spectra of physical mixture containing the drugs (Key:- CNCs: cellulose nanocrystals; CMNC: carboxymethyl nanocellulose; UNGs: Unloaded nanogels; A-NGs: Acyclovir loaded nanogels; C-NGs: Carbamazepine loaded nanogels; F-NGs: Furosemide loaded nanogels; CMNC:Lysozyme-Physical mixture at a ratio of 1:1; CMNC:Lysozyme:Acy, CMZ, and Fru-Physical mixture containing CMNC, Lysozyme and Acyclovir, Carbamazepine, and Furosemide, respectively at weight ratios of 1:1:1).

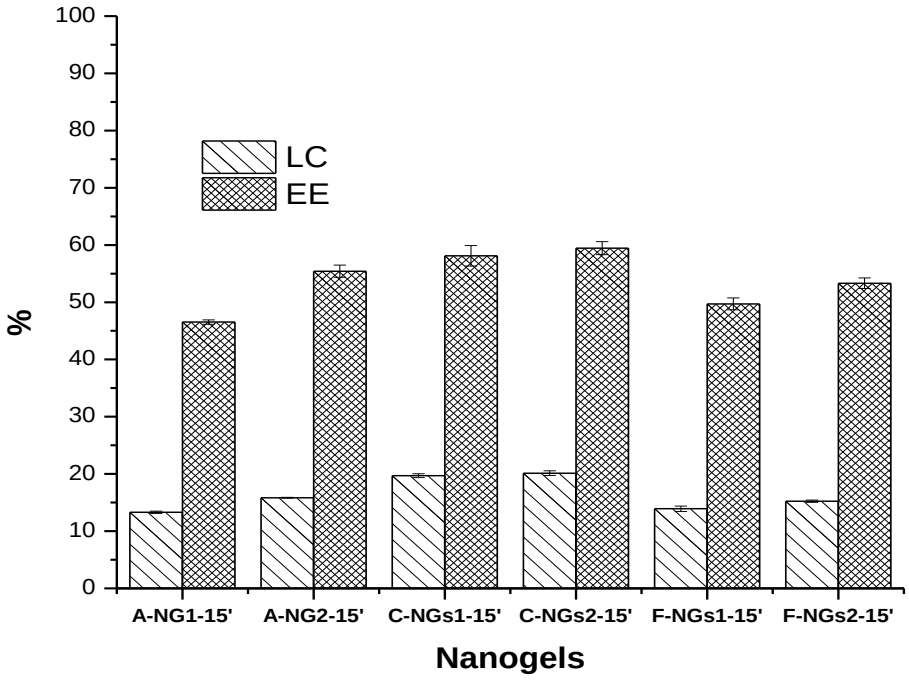

Fig. A9: Loading capacity and encapsulation efficiency of the nanogels prepared at 15 min heating time. (Key:- 1 and 2: Nanogels pH 5.3 and probe-sonicated, and 7.4, respectively; A-NGs: Acyclovir loaded nanogels; C-NGs: Carbamazepine loaded nanogels; F-NGs: Furosemide loaded nanogels). Data are presented as the mean ± SD (n = 3).

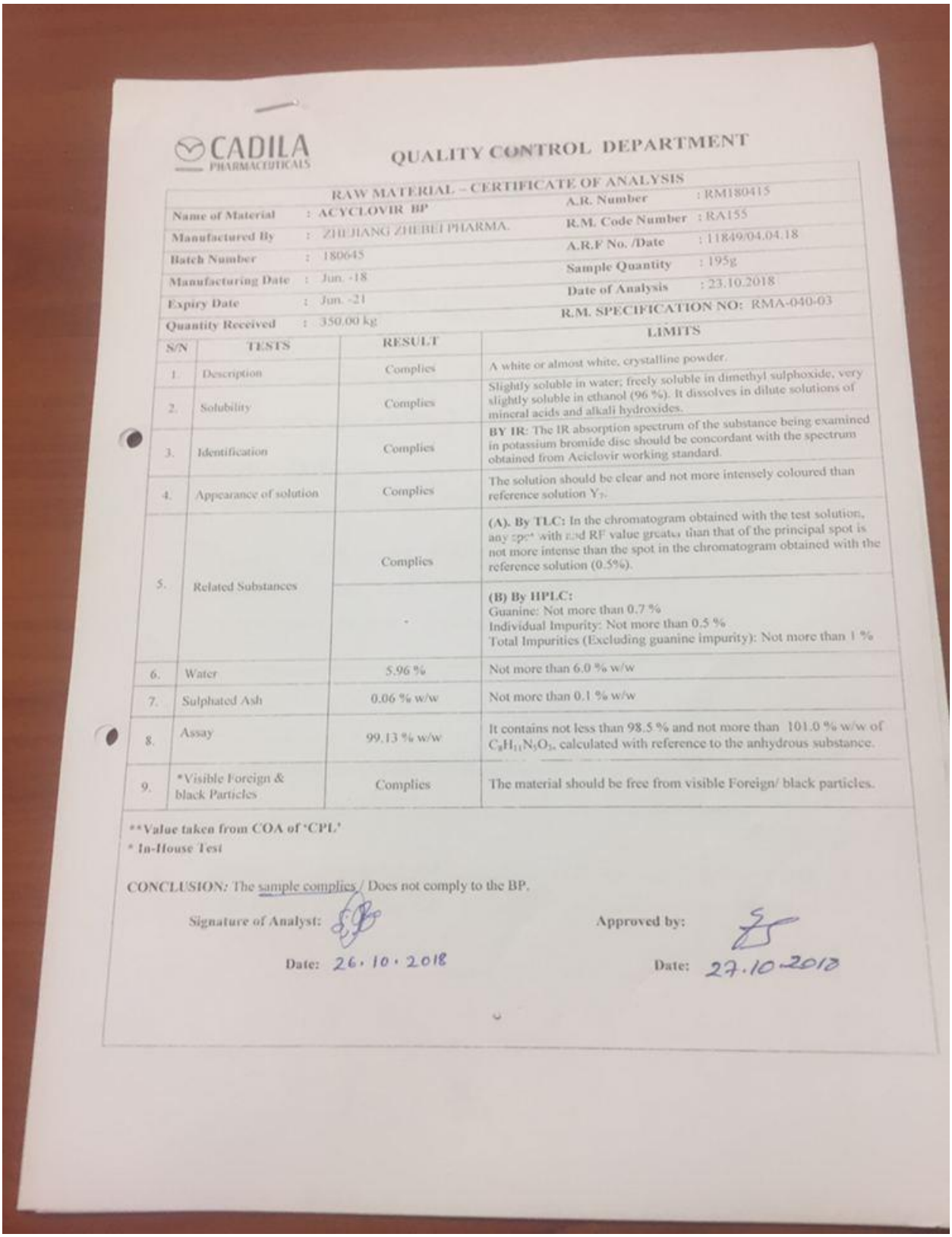

CADILA PHARMACEUTICALS

QUALITY CONTROL DEPARTMENT

RAW MATERIAL – CERTIFICATE OF ANALYSIS

Name of Material	: ACYCLOVIR BP	A.R. Number	: RM180415
Manufactured By	: ZHEJIANG ZHEBEI PHARMA.	R.M. Code Number	: RA155
Batch Number	: 180645	A.R.F No. /Date	: 11849/04.04.18
Manufacturing Date	: Jun. -18	Sample Quantity	: 195g
Expiry Date	: Jun. -21	Date of Analysis	: 23.10.2018
Quantity Received	: 350.00 kg	R.M. SPECIFICATION NO:	RMA-040-03

S/N	TESTS	RESULT	LIMITS
1.	Description	Complies	A white or almost white, crystalline powder.
2.	Solubility	Complies	Slightly soluble in water; freely soluble in dimethyl sulphoxide, very slightly soluble in ethanol (96 %). It dissolves in dilute solutions of mineral acids and alkali hydroxides.
3.	Identification	Complies	**BY IR**: The IR absorption spectrum of the substance being examined in potassium bromide disc should be concordant with the spectrum obtained from Aciclovir working standard.
4.	Appearance of solution	Complies	The solution should be clear and not more intensely coloured than reference solution Y_7.
5.	Related Substances	Complies	**(A). By TLC:** In the chromatogram obtained with the test solution, any spot with a Rf value greater than that of the principal spot is not more intense than the spot in the chromatogram obtained with the reference solution (0.5%).
		-	**(B) By HPLC:** Guanine: Not more than 0.7 % Individual Impurity: Not more than 0.5 % Total Impurities (Excluding guanine impurity): Not more than 1 %
6.	Water	5.96 %	Not more than 6.0 % w/w
7.	Sulphated Ash	0.06 % w/w	Not more than 0.1 % w/w
8.	Assay	99.13 % w/w	It contains not less than 98.5 % and not more than 101.0 % w/w of $C_8H_{11}N_5O_3$, calculated with reference to the anhydrous substance.
9.	*Visible Foreign & black Particles	Complies	The material should be free from visible Foreign/ black particles.

**Value taken from COA of 'CPL'
* In-House Test

CONCLUSION: The sample complies / Does not comply to the BP.

Signature of Analyst: **Approved by:**

Date: 26.10.2018 **Date:** 27.10.2018

a)

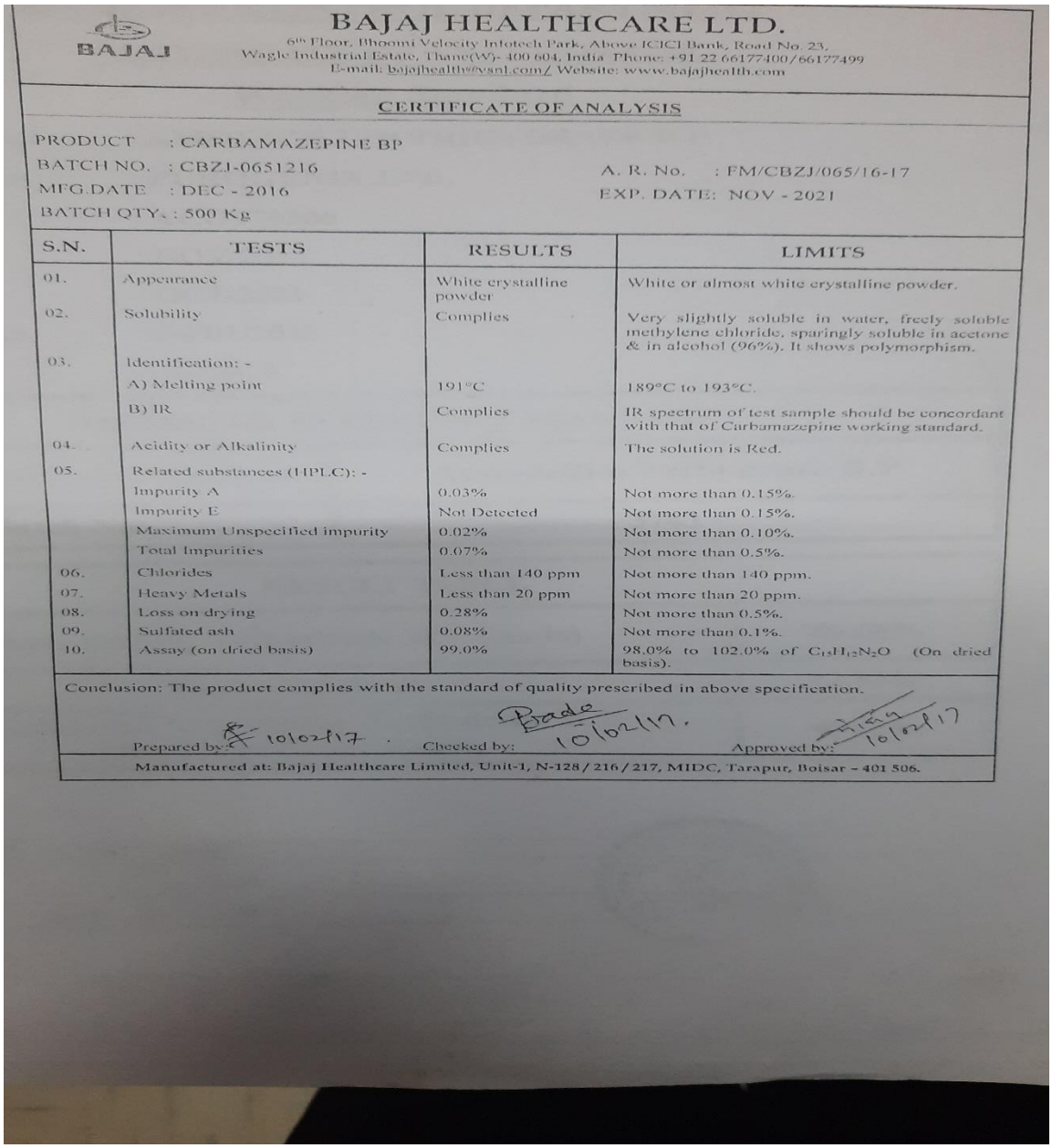

BAJAJ

BAJAJ HEALTHCARE LTD.

6th Floor, Bhoomi Velocity Infotech Park, Above ICICI Bank, Road No. 23,
Wagle Industrial Estate, Thane(W)- 400 604, India. Phone: +91 22 66177400/66177499
E-mail: bajajhealth@vsnl.com/ Website: www.bajajhealth.com

CERTIFICATE OF ANALYSIS

PRODUCT : CARBAMAZEPINE BP
BATCH NO. : CBZJ-0651216
MFG.DATE : DEC - 2016
BATCH QTY. : 500 Kg

A. R. No. : FM/CBZJ/065/16-17
EXP. DATE: NOV - 2021

S.N.	TESTS	RESULTS	LIMITS
01.	Appearance	White crystalline powder	White or almost white crystalline powder.
02.	Solubility	Complies	Very slightly soluble in water, freely soluble methylene chloride, sparingly soluble in acetone & in alcohol (96%). It shows polymorphism.
03.	Identification: -		
	A) Melting point	191°C	189°C to 193°C.
	B) IR	Complies	IR spectrum of test sample should be concordant with that of Carbamazepine working standard.
04.	Acidity or Alkalinity	Complies	The solution is Red.
05.	Related substances (HPLC): -		
	Impurity A	0.03%	Not more than 0.15%.
	Impurity E	Not Detected	Not more than 0.15%.
	Maximum Unspecified impurity	0.02%	Not more than 0.10%.
	Total Impurities	0.07%	Not more than 0.5%.
06.	Chlorides	Less than 140 ppm	Not more than 140 ppm.
07.	Heavy Metals	Less than 20 ppm	Not more than 20 ppm.
08.	Loss on drying	0.28%	Not more than 0.5%.
09.	Sulfated ash	0.08%	Not more than 0.1%.
10.	Assay (on dried basis)	99.0%	98.0% to 102.0% of $C_{15}H_{12}N_2O$ (On dried basis).

Conclusion: The product complies with the standard of quality prescribed in above specification.

Prepared by: 10/02/17 Checked by: 10/02/17 Approved by: 10/02/17

Manufactured at: Bajaj Healtheare Limited, Unit-1, N-128 / 216 / 217, MIDC, Tarapur, Boisar – 401 506.

b)

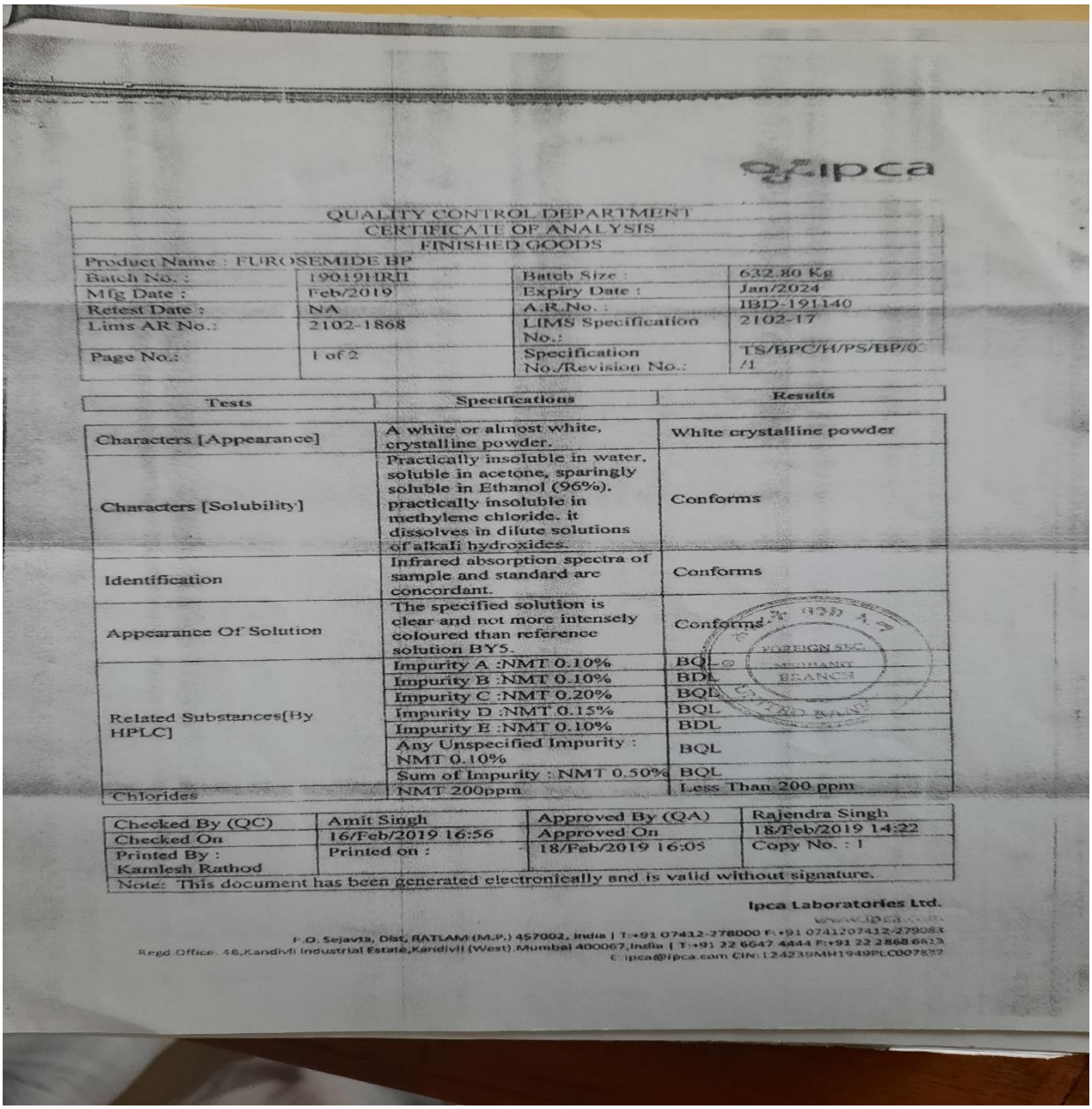

ipca

QUALITY CONTROL DEPARTMENT
CERTIFICATE OF ANALYSIS
FINISHED GOODS

Product Name : FUROSEMIDE BP

Batch No. :	19019HRII	Batch Size :	632.80 Kg
Mfg Date :	Feb/2019	Expiry Date :	Jan/2024
Retest Date :	NA	A.R.No. :	IBD-191140
Lims AR No.:	2102-1868	LIMS Specification No.:	2102-17
Page No.:	1 of 2	Specification No./Revision No.:	TS/BPC/H/PS/BP/0 /1

Tests	Specifications	Results
Characters [Appearance]	A white or almost white, crystalline powder.	White crystalline powder
Characters [Solubility]	Practically insoluble in water, soluble in acetone, sparingly soluble in Ethanol (96%), practically insoluble in methylene chloride, it dissolves in dilute solutions of alkali hydroxides.	Conforms
Identification	Infrared absorption spectra of sample and standard are concordant.	Conforms
Appearance Of Solution	The specified solution is clear and not more intensely coloured than reference solution BY5.	Conforms
Related Substances[By HPLC]	Impurity A :NMT 0.10%	BQL
	Impurity B :NMT 0.10%	BDL
	Impurity C :NMT 0.20%	BQL
	Impurity D :NMT 0.15%	BQL
	Impurity E :NMT 0.10%	BDL
	Any Unspecified Impurity : NMT 0.10%	BQL
	Sum of Impurity : NMT 0.50%	BQL
Chlorides	NMT 200ppm	Less Than 200 ppm

Checked By (QC)	Amit Singh	Approved By (QA)	Rajendra Singh
Checked On	16/Feb/2019 16:56	Approved On	18/Feb/2019 14:22
Printed By : Kamlesh Rathod	Printed on :	18/Feb/2019 16:05	Copy No. : 1

Note: This document has been generated electronically and is valid without signature.

Ipca Laboratories Ltd.

P.O. Sejavta, Dist. RATLAM (M.P.) 457002, India | T:+91 07412-278000 F:+91 07412-279083
Regd Office: 48,Kandivli Industrial Estate,Kandivli (West),Mumbai 400067,India | T:+91 22 6647 4444 F:+91 22 2868 6833
E: ipca@ipca.com CIN: L24239MH1949PLC007837

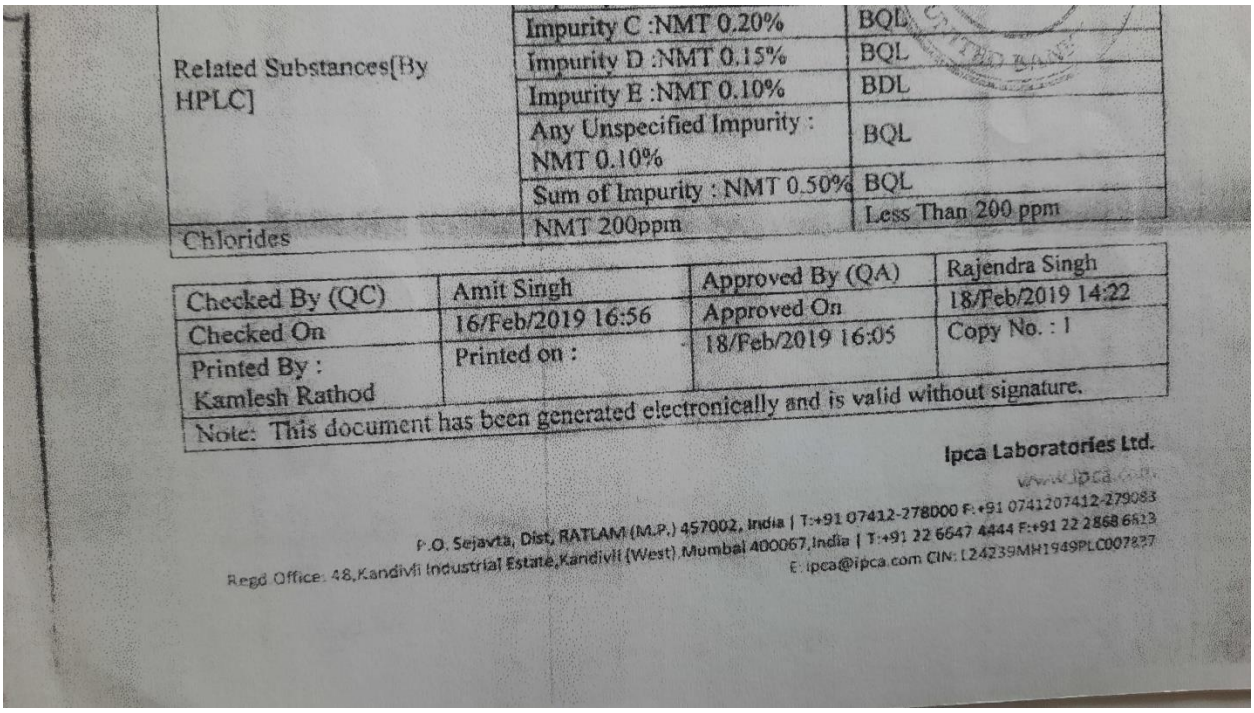

Related Substances[By HPLC]	Impurity C :NMT 0.20%	BQL
	Impurity D :NMT 0.15%	BQL
	Impurity E :NMT 0.10%	BDL
	Any Unspecified Impurity : NMT 0.10%	BQL
	Sum of Impurity : NMT 0.50%	BQL
Chlorides	NMT 200ppm	Less Than 200 ppm

Checked By (QC)	Amit Singh	Approved By (QA)	Rajendra Singh
Checked On	16/Feb/2019 16:56	Approved On	18/Feb/2019 14:22
Printed By : Kamlesh Rathod	Printed on :	18/Feb/2019 16:05	Copy No. : 1

Note: This document has been generated electronically and is valid without signature.

Ipca Laboratories Ltd.

P.O. Sejavta, Dist. RATLAM (M.P.) 457002, India | T:+91 07412-278000 F:+91 07412-279083
Regd Office: 48,Kandivli Industrial Estate,Kandivli (West) Mumbai 400067,India | T:+91 22 6647 4444 F:+91 22 2868 6513
E: ipca@ipca.com CIN: L24239MH1949PLC007827

c)

Fig. A10: Certificate of analyses of model drugs: a) Acyclovir, b) Carbamazepine, and c) Furosemide raw materials.

Front pages of published articles

International Journal of Biological Macromolecules 158 (2020) 1248–1258

Contents lists available at ScienceDirect

International Journal of Biological Macromolecules

journal homepage: http://www.elsevier.com/locate/ijbiomac

Extraction and characterization of celluloses from various plant byproducts

Tesfaye Gabriel [a], Anteneh Belete [a], Frank Syrowatka [b], Reinhard H.H. Neubert [c,d], Tsige Gebre-Mariam [a,*]

[a] Department of Pharmaceutics and Social Pharmacy, School of Pharmacy, College of Health Sciences, Addis Ababa University, P. O. Box 1176, Addis Ababa, Ethiopia
[b] Interdisciplinary Centre of Materials Science, Martin Luther University Halle-Wittenberg, 06120 Halle (Saale), Germany
[c] Department of Pharmaceutical Technology and Biopharmaceutics, Institute of Pharmacy, Martin Luther University Halle-Wittenberg, 06120 Halle (Saale), Germany
[d] Institute of Applied Dermatopharmacy, Martin Luther University Halle-Wittenberg, 06120 Halle (Saale), Germany.

ARTICLE INFO

Article history:
Received 17 January 2020
Received in revised form 11 April 2020
Accepted 29 April 2020
Available online 11 May 2020

Keywords:
Plant byproducts
Cellulose
Chlorine-free extraction, Teff straw, Enset fiber, Cofee hull

ABSTRACT

Celluloses were extracted from teff straw (TS), enset fiber (EF), sugarcane bagasse (SB) and coffee hull (CH), agro-industrial byproducts generated in large quantities in Ethiopia. The present study aimed to explore these plant byproducts as alternative sources of cellulose for potential industrial applications, using various eco-friendly chlorine-free treatment conditions to obtain an optimum cellulose extraction condition. The byproducts and the as-extracted celluloses were analyzed for chemical compositions, yield, chemical functionality, crystallinity, thermal stability and morphology. EF yielded the highest cellulose content (60.0%), whereas CH the least (35.5%). FTIR spectra and ESEM morphological studies of the celluloses indicated progressive removal of non-cellulosic constituents. XRD analyses showed EF cellulose had the highest crystallinity index (CrI) (85.56%), crystallite size (5.52 nm), and proportion of crystallite interior chains of 200 plane (0.629), exhibiting unique physicochemical properties. The byproducts and the as-extracted celluloses showed Cellulose I_β crystal lattice, while celluloses from EF and SB also displayed (partial) polymorphic transition into Cellulose II. TGA studies revealed enhanced stability of the as-extracted celluloses. On the basis of the physicochemical characteristics of the celluloses, all the byproducts studied could be considered as alternative sources of cellulose for potential value-added industrial applications.

1. Introduction

Lignocellulosic-based materials in the green industry have received much attention because they are abundant, relatively cheaper, and eco-friendly [1,2]. A large amount of cellulosic waste is generated by agro-industries, [3] and utilizing these cellulose-rich byproducts can address both ecological and economic concerns [4].

Cellulose is the most abundant polysaccharide produced in nature by plants and microorganisms [4,5]. Celluloses are obtained from the major conventional sources such as cotton and wood. These sources have been used for years in the production of cellulose and its derivatives for different industrial applications mainly in pharmaceutical, textile and paper industries. However, the overutilization of such sources by competing industries, such as energy and construction, and/or deforestations globally has increased the need for alternative cellulose sources from herbaceous plants, agricultural crops and/or non-woody plants [6,7].

Teff (*Eragrostis tef* (Zucc.) Trotter) is among the most widely cultivated staple cereal crops in Ethiopia and its grains are rich in starch. Ethiopia is the largest *teff* producer in the world and *teff* straw (TS) is the solid waste byproduct. Traditionally, TS is used as a binding material for muddy walls of huts and fodder for livestock [8,9]. *Enset* (*Ensete ventricosum* (Welw.) Cheesman), known as *false banana* due to its striking resemblance to the banana plant, is also a traditional staple crop in the South and South-West Ethiopia. *Enset* fiber (EF) is harvested from the leaves, pseudostems, and the inner inflorescence stalks of *enset* plant as a byproduct of *kocho*. Traditionally, EF is used in the production of sacks and ropes for house and fence constructions [10,11]. Sugarcane is a tall perennial grass of the genus Saccharum, Family Poaceae, and sugarcane bagasse (SB) is the byproduct obtained from sugarcane after sucrose extraction and bioethanol production [12]. Coffee, the most popular beverage and the second-largest traded good after crude oil worldwide, traces its origin to the mountains of Ethiopia [13,14]. Coffee hull (CH) is agro-industrial residue available in huge quantities in coffee processing enterprises across Ethiopia, which is among the top 5 coffee producing countries in the world [15].

* Corresponding author.
E-mail addresses: tesfaye.gabriel@aau.edu.et (T. Gabriel), anteneh.belete@aau.edu.et (A. Belete), frank.syrowatka@cmat.uni-halle.de (F. Syrowatka), reinhard.neubert@pharmazie.uni-halle.de (R.H.H. Neubert), tsige.gmariam@aau.edu.et (T. Gebre-Mariam).

https://doi.org/10.1016/j.ijbiomac.2020.04.264
0141-8130/

Journal of Polymers and the Environment
https://doi.org/10.1007/s10924-021-02089-3

ORIGINAL PAPER

Isolation and Characterization of Cellulose Nanocrystals from Different Lignocellulosic Residues: A Comparative Study

Tesfaye Gabriel[1,4] · Anteneh Belete[1] · Gerd Hause[2] · Reinhard H. H. Neubert[3,4] · Tsige Gebre-Mariam[1]

Accepted: 2 February 2021

Abstract
Recently, cellulose nanocrystals (CNCs) have captured the interest of researchers and industries. In this study, CNCs were isolated from four abundant lignocellulosic byproducts: *teff* (*Eragrostis tef*, Poaceae) straw, *enset* (*Ensete ventricosum*, Musaceae) fiber (EF), sugarcane (*Saccharum officinarum*, Poaceae) bagasse and coffee (*Coffea arabica*, Rubiaceae) hull (CH). Cellulose fibers were obtained using chlorine-free extraction with 5% sodium hydroxide pretreatment followed by delignification (with formic acid, acetic acid and hydrogen peroxide) and bleaching (with alkaline hydrogen peroxide). CNCs were then isolated following hydrolysis of the cellulose fibers with 64% sulfuric acid. The as-obtained CNCs were investigated and characterized in terms of yield, crystallinity, chemical functionality, morphology, particle size, zeta potential (ZP) and thermal stability. The CNCs displayed a typical crystal lattice of I_{β}-type based on XRD patterns, d-spacings and Z-values. The highest yield (~70%), CrI (~86%), and crystal size (~6 nm) were observed in EF–CNCs, and the least in CH–CNCs (yield: ~25%, CrI: ~77%, crystal size: ~4 nm). FTIR spectra of all CNCs indicated typical chemical composition of cellulose. TEM observations revealed that the CNCs were needle-shaped nanoscale structures with different aspect ratios (17.32–36.67) and dimensions (average length: 154.28–193.06 nm; diameter: 5.16–11.79 nm), while the DLS measurements provided the hydrodynamic sizes, 96.96–184.90 nm. The thermal studies by TGA/DTG revealed the CNCs had a two-step decomposition process at T_{max} 215–225 °C and 340–355 °C. This study showed that the CNCs isolated exhibited high crystallinity, aspect ratio, colloidal and thermal stability although differences were observed due to variations in cellulose sources.

Keywords Cellulose nanocrystals · Teff straw · Enset fiber · Sugarcane bagasse · Coffee hull

Approval by Institutional Review Board, CHS

ADDIS ABABA UNIVERSITY, COLLEGE OF HEALTH SCIENCES (IRB)
አዲስ አበባ ዩኒቨርስቲ ጤናሳይንስ ኮሌጅ
Institutional Review Board

ANNEX 3
Form AAUMF 03-008

IRB's Decision

Meeting No: 08/2020 Meeting Date: August 26,2020
Protocol number: 071/20/SoP

Protocol Title: Fabrication of Cellulose-Based Nanogels Reinforced with Cellulose Nanocrystals from Local Plant By products for Controlled Drug Delivery		
Principal Investigator:	Tesfaye Gabriel	
Institute:	College of Health Sciences, AAU	
Elements Reviewed (AAUMF 01-008)	☑ Attached	☐ Not attached
Review of Revised Application ☐ Yes ☐ No	Date of Previous review:	
Decision of the meeting:	☑Approved ☐Approved with Recommendation ☐Resubmission ☐ Disapproved	

I. Elements approved-
1. Protocol Version No: 2
2. Protocol Version Date:
3. Informed consent Version No. 2
4. Informed Consent Version Date:

II. Obligations of the PI-
1. Should comply with the standard international & national scientific and ethical guidelines
2. All amendments and changes made in protocol and consent form needs IRB approval
3. The PI should report SAE within 10 days of the event
4. End of the study, including manuscripts and thesis works should be reported to the IRB
5. The PI should report non-compliance and unanticipated events

Institution Review Board (IRB) Approval: Period from: November 19, 2020 to November18, 2021

Follow up report expected in

3 Months ___ 6 months ___ 9 months ___✔___ one year ____

Chairperson, IRB
Dr. Adamu Addissie

Signature _____
Date: 19/11/2020

Institutional Review Board Office (IRB) Faculty of Medicine ADDIS ABABA UNIVERSITY

Tesfaye Gabriel Dalalo
(BPharm, MSc in Pharmaceutics)

Tesfaye Gabriel Dalalo Synthesis, Characterization and Evaluation of Nanocellulose-based Nanogels from Local Sources

Synthesis, Characterization and Evaluation of Nanocellulose-based Nanogels from Local Sources for Sustained Drug Delivery

A Dissertation Presented in Partial Fulfilment of the Requirements for the Degree Doctor of Philosopy (PhD) in Pharmaceutics

Advisors: Prof. Dr. Tsige Gebre-Mariam
Prof. Dr. h. c. Reinhard H. H. Neubert
Dr. Anteneh Belete

Tesfaye Gabriel Dalalo
(BPharm, MSc in Pharmaceutics)

March 2022
Addis Ababa,Ethiopia